EXPERIMENTAL AND NUMERICAL STUDY OF MODULAR HYDRO TURBINE BASED ON CANAL FLOW

A Thesis submitted to Gujarat Technological University

for the Award of

Doctor of Philosophy

in

Mechanical Engineering

by

Mehta Amit Umeshbhai

(Enrollment Number - 189999919026)

under supervision of

Dr. Pankajkumar P. Gohil

Associate Professor,

Department of Mechanical Engineering,

Sarvajanik College of Engineering and Technology, Surat



GUJARAT TECHNOLOGICAL UNIVERSITY

AHMEDABAD

October – 2026

© Mehta Amit Umeshbhai

DECLARATION

I declare that the thesis entitled **"EXPERIMENTAL AND NUMERICAL STUDY OF MODULAR HYDRO TURBINE BASED ON CANAL FLOW"** submitted by me for the degree of Doctor of Philosophy is the record of research work carried out by me during the period from **July-2018** to **October-2026** under the supervision of **"Dr. Pankajkumar P. Gohil"** and this has not formed the basis for the award of any degree, diploma, associateship, fellowship, titles in this or any other University or other institution of higher learning.

I further declare that the material obtained from other sources has been duly acknowledged in the thesis. I shall be solely responsible for any plagiarism or other irregularities, if noticed in the thesis.

Signature of the Research Scholar: ..... Date: **16/10/2026**

Name of Research Scholar: **Mehta Amit Umeshbhai**

Place: **Gujarat Technological University, Ahmedabad, Gujarat, India**

CERTIFICATE

I certify that the work incorporated in the thesis **"EXPERIMENTAL AND NUMERICAL STUDY OF MODULAR HYDRO TURBINE BASED ON CANAL FLOW"** submitted by **Mr. Mehta Amit Umeshbhai (Enrollment Number - 189999919026)** was carried out by the candidate under my supervision/guidance. To the best of my knowledge: (i) the candidate has not submitted the same research work to any other institution for any degree/diploma, Associateship, Fellowship or other similar titles (ii) the thesis submitted is a record of original research work done by the Research Scholar during the period of study under my supervision, and (iii) the thesis represents independent research work on the part of the Research Scholar.

Signature of Supervisor:  ..... Date: **16/10/2026**

Name of Supervisor: **Dr. Pankajkumar P. Gohil**

Place: **Sarvajanik College of Engineering and Technology, Surat, Gujarat, India**

COURSE-WORK COMPLETION CERTIFICATE

This is to certify that **Mr. Mehta Amit Umeshbhai** enrolment number - **189999919026** is enrolled for PhD program in the branch **Mechanical Engineering** of Gujarat Technological University, Ahmedabad.

(Please tick the relevant option(s))

☐ He has been exempted from the course-work (successfully completed during M.Phil Course)

☐ He has been exempted from Research Methodology Course only (successfully completedduring M.Phil Course)

☑ He has successfully completed the PhD course work for the partial requirement for the award of PhD Degree. His performance in the course work is as follows-

Grade Obtained in Research Methodology [PH001]	Grade Obtained in Self-Study Course/ Contact Program [PH002]
BC	**AB**

Supervisor's Sign: .....

Name of Supervisor: **Dr. Pankajkumar P. Gohil**

ORIGINALITY REPORT CERTIFICATE

It is certified that PhD Thesis titled **"EXPERIMENTAL AND NUMERICAL STUDY OF MODULAR HYDRO TURBINE BASED ON CANAL FLOW"** by **Mr. Mehta Amit Umeshbhai (Enrollment Number - 189999919026)** has been examined by us. We undertake the following:

a. Thesis has significant new work / knowledge as compared already published or are under consideration to be published elsewhere. No sentence, equation, diagram, table, paragraph or section has been copied verbatim from previous work unless itis placed under quotation marks and duly referenced.

b. The work presented is original and own work of the author (i.e. there is no plagiarism). No ideas, processes, results or words of others have been presented as Author own work.

c. There is no fabrication of data or results which have been compiled / analyzed.

d. There is no falsification by manipulating research materials, equipment or processes,or changing or omitting data or results such that the research is not accurately represented in the research record.

e. The thesis has been checked using **Turnitin** (copy of originality report attached) and found within limits as per GTU Plagiarism Policy and instructions issued from time to time (i.e. permitted similarity index <= 10%).

Signature of the Research Scholar: ..... Date: **16/10/2026**

Name of Research Scholar: **Mr. Mehta Amit Umeshbhai**

Signature of Supervisor: ..... Date: **16/10/2026**

Name of Supervisor: **Dr. Pankajkumar P. Gohil**

Place: **Gujarat Technological University, Ahmedabad**

Plagiarism Report

Amit Thesis

ORIGINALITY REPORT

6%	0%	6%	%
SIMILARITY INDEX	INTERNET SOURCES	PUBLICATIONS	STUDENT PAPERS

PRIMARY SOURCES

1	Anuj Kumar, R.P. Saini. "Performance analysis of a single stage modified Savonius hydrokinetic turbine having twisted blades", Renewable Energy, 2017 Publication	1%
2	Tamer Nabil, Tamer M. Mansour. "Power Extraction from Pico Hydro Turbines Installed in Water Pipelines", Journal of Energy Engineering, 2022 Publication	1%
3	Anuj Kumar, R.P. Saini. "Performance analysis of a Savonius hydrokinetic turbine having twisted blades", Renewable Energy, 2017 Publication	1%
4	Dhruvin L. Shukla, Smit A. Chodvadiya, Sangam S. Jena, Henish A. Mangukiya, Satyam P. Dubey, Jesika S. Jariwala. "Experimental performance assessment of square pyramid solar still using organic nanofluid and thermal storage material", Applied Thermal Engineering, 2026 Publication	1%

5	Jnana Ranjan Khuntia, Kamalini Devi, Sarjati Sahoo, Bhabani Shankar Das, K. K. Khatua. "Chapter 2 CFD Simulation of Non-prismatic Compound Channels Using k–ε and k–ω Turbulence Models", Springer Science and Business Media LLC, 2025 Publication	1 %
6	Natvarbhai, Chaudhari Vimalkumar. "Design, Development and Experimental Investigation on Savonius Hydrokinetic Turbine.", Gujarat Technological University Publication	1 %
7	C.M. Niebuhr, M. van Dijk, V.S. Neary, J.N. Bhagwan. "A review of hydrokinetic turbines and enhancement techniques for canal installations: Technology, applicability and potential", Renewable and Sustainable Energy Reviews, 2019 Publication	1 %
8	Iacopo Carnacina, Mawada Abdellatif, Manolia Andredaki, James Cooper, Darren Lumbroso, Virginia Ruiz-Villanueva. "River Flow 2024", CRC Press, 2025 Publication	1 %
9	"Fluid Mechanics and Fluid Power (Vol. 3)", Springer Science and Business Media LLC, 2023 Publication	1 %

Ph.D. THESIS NON-EXCLUSIVE LICENSE TO GUJARAT TECHNOLOGICAL UNIVERSITY

In consideration of being a Research Scholar at Gujarat Technological University, and in the interests of the facilitation of research at the University and elsewhere, I, **Mr. Mehta Amit Umeshbhai** having Enrollment Number **189999919026** hereby grant a non- exclusive, royalty free and perpetual license to the University on the following terms:

a. The University is permitted to archive, reproduce and distribute my thesis, in whole orin part, and/or my abstract, in whole or in part (referred to collectively as the "Work") anywhere in the world, for non-commercial purposes, in all forms of media;

b. The University is permitted to authorize, sub-lease, sub-contract or procure any of the acts mentioned in paragraph (a);

c. The University is authorized to submit the Work at any National / International Library, under the authority of their "Thesis Non-Exclusive License";

d. The Universal Copyright Notice (©) shall appear on all copies made under the authorityof this license;

e. I undertake to submit my thesis, through my university, to any Library and Archives. Any abstract submitted with the thesis will be considered to form part of the thesis.

f. I represent that my thesis is my original work, does not infringe any rights of others, including privacy rights, and that I have the right to make the grant conferred by this non-exclusive license.

g. If third party copyrighted material was included in my thesis for which, under the termsof the Copyright Act, written permission from the copyright owners is required, I have obtained such permission from the copyright owners to do the acts mentioned in paragraph (a) above for the full term of copyright protection.

h. I understand that the responsibility for the matter as mentioned in the paragraph (g) rests with the authors / me solely. In no case shall GTU have any liability for any acts /

omissions / errors / copyright infringement from the publication of the said thesis or otherwise.

i. I retain copyright ownership and moral rights in my thesis, and may deal with the copyright in my thesis, in any way consistent with rights granted by me to my university in this non-exclusive license.

j. GTU logo shall not be used /printed in the book (in any manner whatsoever) being published or any promotional or marketing materials or any such similar documents.

k. The following statement shall be included appropriately and displayed prominently in the book or any material being published anywhere: "The content of the published work is part of the thesis submitted in partial fulfilment for the award of the degree of Ph.D.in **Mechanical Engineering** of the "Gujarat Technological University".

l. I further promise to inform any person to whom I may hereafter assign or license my copyright in my thesis of the rights granted by me to my University in this nonexclusive license. I shall keep GTU indemnified from any and all claims from the Publisher(s) or any third parties at all times resulting or arising from the publishing or use or intended use of the book / such similar document or its contents.

m. I am aware of and agree to accept the conditions and regulations of Ph.D. including all policy matters related to authorship and plagiarism.

Date: **16/10/2026**



Place: **GTU, Ahmedabad** Signature of the Research Scholar

Recommendation of the Supervisor: **Recommended**

Recommendation of the Co-Supervisor (if any): **N.A.**



Signature of Supervisor

THESIS APPROVAL FORM

The viva-voce of the PhD Thesis submitted by **Mr. Mehta Amit Umeshbhai** (Enrollment Number - **189999919026**) entitled **"EXPERIMENTAL AND NUMERICAL STUDY OF MODULAR HYDRO TURBINE BASED ON CANAL FLOW"** was conducted on **16/10/2026** at **11:30 A.M.** at Gujarat Technological University.

(Please tick any one of the following options)

☑ The performance of the candidate was satisfactory. We recommend that he/she be awarded the PhD degree.

☐ Any further modifications in research work recommended by the panel after 3 months from the date of first viva-voce upon request of the Supervisor or request of Independent Research Scholar after which viva-voce can be re-conducted by the same panel again.

(Briefly specify the modifications suggested by the panel)

☐ The performance of the candidate was unsatisfactory. We recommend that he/she should not be awarded the PhD degree.

(The panel must give justifications for rejecting the research work)

Dr. Pankajkumar P. Gohil

Name and Signature of Supervisor with Seal

Dr. S. K. Singal

1) (External Examiner 1) Name and Signature

Dr. Jatinkumar R. Patel

2) (External Examiner 2) Name and Signature

ABSTRACT

The depletion of fossil fuel supply due to excessive usage and its negative environmental repercussions are the main factors driving the search for creative, sustainable methods of producing clean energy. The conventional electricity produced by the hydroelectric plant is generally unaffordable and inaccessible to rural and isolated people. Given the catastrophic effects of climate change and the world's continually increasing demand for power, it is critical to quickly accelerate this trend and transition to a portfolio dominated by renewable energy that significantly lowers carbon emissions within the next ten years. Utilizing proven and affordable renewable energy conversion technologies, such solar, hydro, and wind turbines, to quickly grow utility-scale renewable energy projects and markets is a major way to do this. The hydrokinetic turbine (HKT), which generates electricity from open water channels, is the most cost-effective solution for meeting these locations' power needs. Using the potential of rivers, canals, and oceans to generate electricity is also a clean, sustainable, and practical solution.

In the first stage of this research work, for identifying a potential HKT study site, a comparative numerical assessment of various turbulence models was carried out at trapezoidal open canal situated on Tapi River, Surat, Gujarat, India. Various flow parameters like longitudinal velocity along the depth and width as well as secondary vectors were discussed with different turbulence models such as $k-\varepsilon$ Standard, $k-\varepsilon$ Renormalization group (RNG), $k-\varepsilon$ Realizable, $k-\omega$ Standard and $k-\omega$ shear stress transport (SST). For predicting the potential HKT installation and understanding the flow physics phenomena, velocity vectors as well as water power density were analysed. The simulation results were validated using the experiments performed at the site. Based on the results, the $k-\omega$ SST model found to be more accurate providing the potential site for HKT installation. The potential site is capable enough to provide the flow velocity (U_m) of

0.42 m/s, with estimated power generation of 1.2 kW.

Based on the obtained canal flow, in the second stage comparative analysis of Savonius HKT (SHKT) and Michell-Banki HKT (MBHKT) was carried out in a canal. These HKTs are most viable for ease at fabrication and maintenance too. Additionally, they are suitable for low magnitude velocity of flow. For numerical analysis, the $k-\omega$ SST turbulence model has been selected to the Reynolds-Averaged Navier–Stokes (RANS) solver with two different inlet U_m of 0.42 m/s and 1.06 m/s for a wide range of 0.1 to 1.0 tip speed ratio (TSR). Based on the investigation, the maximum power coefficient ($C_{P,max}$) obtained was 0.0648 and 0.0721 at 0.6 TSR for SHKT and; 0.1121 and 0.1249 at 0.4 TSR for MBHKT, at 0.42 m/s and 1.06 m/s velocity, respectively. Additionally, the fluid flow visualisations surrounding the rotors have been examined and discussed for comparing the performance of HKTs. Because of these characteristics, the MBHKT provides a straightforward, reliable, and clog resistant cross-flow option for decentralized zero-head hydrokinetic power generation.

In the next stage, an experimental study of MBHKT was performed at state-of-the-art open channel testing facility established at Fluid Mechanics and Fluid Machine Laboratory, Sardar Vallabhbhai National Institute of Technology, Surat, Gujarat, India. The numerical simulation was validated with the experimental results for MBHKT fully submerged (100% immersion) and partially submerged (75% and 50% immersion) at different velocities. Based on the experimental study, the $C_{P,max}$ obtained was 0.1846 at 1.03 TSR; 0.1523 at 1.08 TSR; and 0.1425 at 0.79 TSR, of 100%, 75% and 50% immersion, respectively. Similarly, during the numerical simulation the $C_{P,max}$ found was 0.2270 at 1.03 TSR; 0.1723 at 1.08 TSR; and 0.1659 at 0.79 TSR, of 100%, 75% and 50% immersion, respectively.

In the final stage of the present investigation, the numerical optimization of three different blade profiles (profile 1 – flat, profile 2 – round and profile 3 – sharp edged) was

performed for open channel testing facility established at Fluid Mechanics and Fluid Machine Laboratory, Sardar Vallabhbhai National Institute of Technology, Surat, Gujarat, India. Moreover, based on the optimum blade profile obtained the various augmentations combining the nozzle and diffuser were also numerically simulated to find out the optimum design of augmentation. The results show that the blade profile-3 (sharp-edged) provided the superior performance across the different U_m, achieving the $C_{P,max}$ of 0.2517 at 1.03 TSR. Furthermore, the $C_{P,max}$ of blade profile-1 (flat) and blade profile-2 (round) were 0.1915 and 0.1050 at 1.03 TSR. The augmentation systems can accelerate the water flow in open channels, especially in low-velocity regions. Based on the numerical investigation, performance of the augmentation system-3 was found better than other three augmentation systems. The $C_{P,max}$ of augmentation system-3 with sharp-edged blade profile was found 0.5520 at 1.03 TSR. Comparing, the $C_{P,max}$ of augmentation system-1, augmentation system-2 and augmentation system-4 was found to be 0.4180, 0.5252 and 0.5314 at 1.03 TSR. Also, performance of the MBHKT with augmentation system-3 was 2.2 times higher that of the without augmentation.

The experimental and numerical results obtained under the present study will be useful to identify a potential site and find maximum potential region over a canal area. Additionally, the outcome of the present study may support the design and deployment of modular HKTs with capacity specific configurations at suitable water potential sites, thereby enhancing adaptability and efficiency of hydrokinetic energy utilisation.

ACKNOWLEDGEMENT

I would like to express my deepest gratitude and sincere thanks to **Dr. Pankajkumar P. Gohil,** my supervisor and mentor for his/her invaluable guidance, constant encouragement, and unwavering support throughout my doctoral research. I am truly grateful for of his time, patience, and dedication to mentoring me with every stage of my study. His unwavering encouragement, technical expertise, and assurance of my skills enabled me to overcome several challenges and complete this work effectively. I express my sincere gratitude to my DPC members, **Dr. Vimal K. Patel** and **Dr. Gaurangkumar C. Chaudhari** for their invaluable advice, constructive suggestions, and continuous support during my research work. Their insightful remarks, critical evaluations, and encouragement have considerably improved the development and success of my research work.

I would like to express my sincere appreciation to **Dr. Dhruvin L. Shukla** for the valuable support and assistance provided throughout my research work and thesis preparation. I express my special thanks to **Mr. Balwant D. Patel, Mr. Sandip Patil, Mr. Vishal Talekar**, and **Mr. Chaitanya Desai** for help in experimentation work; without them, it was next to impossible during my research work. I express deep sense of regards to **Dr. Samip P. Shah, Dr. Parth Shah and Dr. Satish Dokiparti** for sharing their knowledge with me. I am very much thankful to **Mr. Pratik Patel** and his team, who has helped me in developing the experimental set up. I would like to express my sincere gratitude to the authorities and staff of the **Fluid Mechanics and Fluid Machine Laboratory, Sardar Vallabhbhai National Institute of Technology, Surat, Gujarat, India** for providing the necessary laboratory facilities, equipment, and technical support required for conducting this research. I am grateful to my home institution, Sarvajanik college of engineering and Technology, Surat for support throughout my research work. I am also grateful to **Dr. Nitin N. Vibhakar, Dr. Mayank M. Dalal, Dr. Jigar Sevalia** and other staff members of Sarvajanik college of Engineering and Technology, Surat for encouragement and support in my research work.

I would like to express my heartfelt gratitude to my parents **Late Umeshbhai V. Mehta** and **Mrs. Bhanuben U. Mehta, my wife Dr. Nidhi A. Mehta, my son Parv A. Mehta and my sisters, Arti K. Mehta** and **Mamta C. Patel** for their unconditional love, constant encouragement, and unwavering support throughout my doctoral journey.

Last but not the least, I humble thanks The God Almighty for every success in my life.

Mehta Amit Umeshbhai

TABLE OF CONTENTS

TITLE PAGE

DECLARATION i

CERTIFICATE ii

COURSE-WORK COMPLETION CERTIFICATE iii

ORIGINALITY REPORT CERTIFICATE iv

Ph.D. THESIS NON-EXCLUSIVE LICENSE TO GUJARAT TECHNOLOGICAL UNIVERSITY vii

THESIS APPROVAL FORM ix

ABSTRACT x

ACKNOWLEDGEMENT xiii

TABLE OF CONTENTS xiv

LIST OF ABBREVIATION xix

LIST OF SYMBOLS xx

LIST OF FIGURES xxii

LIST OF TABLES xxvii

LIST OF APPENDICES xxviii

CHAPTERS

1. INTRODUCTION 1

1.1 Energy Scenario and Need of Hydrokinetic Turbine 1

1.2 Cross Flow Hydrokinetic Turbine 3

1.2.1 Savonius Hydrokinetic Turbine 4

1.2.2 Michell-Banki Hydrokinetic Turbine 6

1.3 Modular Hydrokinetic Turbine 8

1.4 Introduction to Computational Fluid Dynamics 9

1.5 Outline of the Thesis 12

2. LITERATURE REVIEW, PROBLEM STATEMENT AND OBJECTIVES OF PRESENT WORK **13**

2.1. Literature Review 13

2.1.1 Site Selection 13

2.1.2 Hydrokinetic Turbine 15

2.2. Problem Statement 32

2.3. Objectives of the Present Work 33

2.4. Brief Methodology of the Thesis 34

3. EXPERIMENTAL AND NUMERICAL STUDY OF THE CANAL FLOW **35**

3.1 Experimental Study 35

3.1.1 Hydrokinetic Turbine Site Selection 35

3.1.2 Field Data Measurement 36

3.1.3 Discharge Measurement 40

3.2 Numerical Methodology 44

3.2.1 Geometry 44

3.2.2 Meshing of Computational Domain 45

3.2.3 Boundary Conditions 48

3.2.4 Turbulence Models 48

3.3 Results and Discussion 48

3.3.1 Longitudinal Velocity Profile along the Water Depth 49

3.3.2 Longitudinal Velocity Profile along the Canal Width 52

3.3.3 Secondary Flow Vector Plot at XY Plane 54

3.3.4 Velocity Contour and Water Power Density 56

3.4 Potential Region for Hydrokinetic Turbine Installation 60

3.5 Statistical Error Analysis 63

4. NUMERICAL STUDY OF HYDROKINETIC TURBINES BASED ON THE CANAL FLOW **65**

4.1 Numerical Methodology 65

4.1.1 Geometry 65

4.1.2 Performance Parameters 68

4.1.3 Computation Domain 68

4.1.4 Meshing of Computational Domain 69

4.1.5 Boundary Conditions 72

4.1.6 Validation 74

4.2 Results and Discussion 75

4.2.1 Performance Characteristics Curves 75

4.2.2 Field Visualizations 81

5. EXPERIMENTAL AND NUMERICAL STUDY OF MICHELL-BANKI HYDROKINETIC TURBINE IN OPEN CHANNEL 89

5.1 Experimental Work 89

5.1.1 Fabrication of Michell-Banki Hydrokinetic Turbine 89

5.1.2 Experimental Test Rig 91

5.1.3 Instrumentation Details 91

5.1.4 Methodology 92

5.1.5 Uncertainty Analysis 93

5.1.5.1 Statistical Uncertainty 93

5.1.5.2 Experimental Uncertainty 95

5.2 Numerical Methodology 96

5.3 Results and Discussion 98

5.3.1 Performance Characteristics Curves 98

5.3.2 Field Visualizations 104

6. OPTIMIZATION AND AUGMENTATION OF MICHELL-BANKI HYDROKINETIC TURBINE IN OPEN CHANNEL BY NUMERICAL APPROACH 110

6.1 Numerical Methodology 110

6.2 Results and Discussion 117

6.2.1 Blade Profiles 117

6.2.2 Augmentation Systems 127

7. CONCLUSION 138

8. SCOPE OF FUTURE WORK 143

REFERENCES 145

LIST OF RESEARCH PUBLICATION 161

APPENDICES 162

LIST OF ABBREVIATION

3-D	Three-dimensional
ANFIS	Adaptive neuro-fuzzy inference systems
ANN	Artificial neural networks
CFD	Computational fluid dynamics
HKT	Hydrokinetic turbine
MBHKT	Michell-Banki hydrokinetic turbine
MNRE	Ministry of New and Renewable Energy
MPE	Mean percentage error
MRF	Multiple reference frame
N-S	Navier–Stokes
PCM	Propeller current metres
RANS	Reynolds-Averaged Navier–Stokes
RMSE	Root mean square error
RNG	Renormalization group
SHKT	Savonius hydrokinetic turbine
SMM	Sliding mesh method
SST	Shear stress transport
TSR	Tip speed ratio

LIST OF SYMBOLS

Symbols

A_s	HKT swept area (projected frontal area perpendicular to the incoming flow) in m^2
C_P	Power coefficient
C_T	Torque coefficient
D	Rotor diameter in mm
d	Blade diameter in mm
D_1	Rotor outer diameter in mm
D_2	Rotor inner diameter in mm
D_e	End plate diameter in mm
e	Overlap distance in mm
H	Rotor height in mm
H/D	Aspect ratio
P	Power in W
R_b	Radius of blade in mm
T	Torque in N·m
t_b	Blade thickness in mm
t_e	End plate thickness in mm
U	Flow velocity/ Longitudinal velocity in Z direction in m/s
u	Lateral velocity in X direction in m/s
v	Vertical velocity in Y direction in m/s

Greek Symbols

β_1	Inlet blade angle in degree
β_2	Outlet blade angle in degree
ρ	Density in kg/m^3
δ	Central blade angle in degree
ω	Angular velocity in rad/s

Subscripts

available	Available
exp	Experimental
m	Mean
max	Maximum
model	Model
S	Swept
turbine	HKT

LIST OF FIGURES

Fig. 1.1	Energy consumption trend in world's major energy customers during 1990- 2030	2
Fig. 1.2	Types of HKTs	4
Fig. 1.3	Conventional SHKT	5
Fig. 1.4	Conventional MBHKT	7
Fig. 1.5	Modular HKT	9
Fig. 3.1	Favourable sections for HKT installation	36
Fig. 3.2	Raw topographic data of the whole Ukai canal	37
Fig. 3.3	Different location of Ukai left bank main canal for discharge measurement	38
Fig. 3.4	Schematic dimensional drawing of mounting structure for PCMs	40
Fig. 3.5	Actual photographic view of the (a) PCM and (b) velocity measurement	41
Fig. 3.6	Locations of vertical and horizontal lines selected for velocity measurements in the canal	43
Fig. 3.7	Longitudinal velocity along water depth at the different vertical lines	43
Fig. 3.8	Longitudinal velocity along width of canal at the different horizontal lines	44
Fig. 3.9	3-D Computational stationary fluid domain of the canal	45
Fig. 3.10	Different views of 3-D Computational stationary fluid domain	45
Fig. 3.11	3-D computational fluid domain meshing (a) whole canal (b) cut section (c) edge meshing of canal side wall	47
Fig. 3.12	Grid independency test	47

Fig. 3.13	Longitudinal velocity profile at (a) X0, (b) X1', (c) X2', (d) X3' (e) X1, (f) X2, (g) X3	51
Fig. 3.14	Longitudinal velocity profile at (a) Y1, (b) Y2, (c) Y3, (d) Y4 (e) Y5	53
Fig. 3.15	Secondary flow vector at outlet for (a) $k-\varepsilon$ Standard, (b) $k-\varepsilon$ RNG, (c) $k-\varepsilon$ Realizable, (d) $k-\omega$ Standard and (e) $k-\omega$ SST	55
Fig. 3.16	Velocity contour at outlet for (a) $k-\varepsilon$ Standard, (b) $k-\varepsilon$ RNG, (c) $k-\varepsilon$ Realizable, (d) $k-\omega$ Standard and (e) $k-\omega$ SST	57
Fig. 3.17	Water power density for (a) $k-\varepsilon$ Standard, (b) $k-\varepsilon$ RNG, (c) $k-\varepsilon$ Realizable, (d) $k-\omega$ Standard and (e) $k-\omega$ SST	59
Fig. 3.18	The maximum potential region	60
Fig. 4.1	Flow chart of approach used for HKTs analysis in canal	66
Fig. 4.2	Schematic and geometrical parameters of (a) SHKT and (b) MBHKT	67
Fig. 4.3	3-D computation domain of canal with stationary zone and rotating zone of (a) SHKT and (b) MBHKT	70
Fig. 4.4	Meshing of the computational fluid domain of (a) whole canal, (b) SHKT, and (c) MBHKT	71
Fig. 4.5	Grid independency test for (a) SHKT and (b) MBHKT	72
Fig. 4.6	Various boundary conditions for computational domain	73
Fig. 4.7	Turbulence models comparison with previously published result by T. Hayashi et al.	75
Fig. 4.8	Variation of C_T and C_P with TSR for (a) SHKT and (b) MBHKT	79
Fig. 4.9	Variation of C_T and C_P with TSR for all the HKTs at (a) U_m = 0.42 m/s and (b) U_m = 1.06 m/s	80
Fig. 4.10	Field visualizations for SHKT at U_m = 0.42 m/s (a) pressure contours, (b) velocity contours, (c) velocity vectors, and (d) velocity streamline	83

Fig. 4.11	Field visualizations for SHKT at U_m = 1.06 m/s (a) pressure contours, (b) velocity contours, (c) velocity vectors, and (d) velocity streamline	84
Fig. 4.12	Field visualizations for MBHKT at U_m = 0.42 m/s (a) pressure contours, (b) velocity contours, (c) velocity vectors, and (d) velocity streamline	87
Fig. 4.13	Field visualizations for MBHKT at U_m = 1.06 m/s (a) pressure contours, (b) velocity contours, (c) velocity vectors, and (d) velocity streamline	88
Fig. 5.1	(a) Photographic view and (b) Schematic view of the MBHKT	90
Fig. 5.2	Photographic view of the experimental test setup	90
Fig. 5.3	Proximity sensor	91
Fig. 5.4	Torque sensor	91
Fig. 5.5	MBHKT immersion conditions for experiments	93
Fig. 5.6	Flow chart of approach used for MBHKT analysis in laboratory	96
Fig. 5.7	3-D computation domain of MBHKT at (a) fully submerged (100% immersion), (b) partially submerged at 75% immersion, and (c) partially submerged at 50% immersion (d) the whole domain	97
Fig. 5.8	Variation of C_T with TSR for different immersion conditions	100
Fig. 5.9	Variation of C_P with TSR for different immersion conditions	101
Fig. 5.10	Variation of $P_{turbine}$ with U_m for different immersion conditions	103
Fig. 5.11	Field visualizations for MBHKT at 100% immersion (a) pressure contours, (b) velocity contours, (c) velocity vectors, and (d) velocity streamline	107
Fig. 5.12	Field visualizations for MBHKT at 75% immersion (a) pressure contours, (b) velocity contours, (c) velocity vectors, and (d) velocity	108

streamline

Fig. 5.13 Field visualizations for MBHKT at 50% immersion (a) pressure contours, (b) velocity contours, (c) velocity vectors, and (d) velocity streamline 109

Fig. 6.1 Flow chart of approach used for MBHKT optimization and augmentation 110

Fig. 6.2 Computation domain of MBHKTs with different blade profiles 113

Fig. 6.3 Augmentation systems of MBHKT 113

Fig. 6.4 Computation domain of various augmentation systems of MBHKT 114

Fig. 6.5 Meshing of the computational fluid domain of (a) stationary domain, (b) blade profile-1, (c) blade profile-2, and (d) blade profile-3 116

Fig. 6.6 Meshing of the computational fluid domain of various augmentation systems 117

Fig. 6.7 Variation of C_T with TSR for different blade profiles 118

Fig. 6.8 Variation of C_P with TSR for different blade profiles 119

Fig. 6.9 Variation of $P_{turbine}$ with TSR for different blade profiles 120

Fig. 6.10 Field visualizations for blade profile-1 (flat profile) of MBHKT (a) pressure contours, (b) velocity contours, (c) velocity vectors, and (d) velocity streamline 124

Fig. 6.11 Field visualizations for blade profile-2 (round profile) of MBHKT (a) pressure contours, (b) velocity contours, (c) velocity vectors, and (d) velocity streamline 125

Fig. 6.12 Field visualizations for blade profile-3 (sharp-edged profile) of MBHKT (a) pressure contours, (b) velocity contours, (c) velocity vectors, and (d) velocity streamline 126

Fig. 6.13	Variation of C_T with TSR for different augmentation systems	127
Fig. 6.14	Variation of C_P with TSR for different augmentation systems	128
Fig. 6.15	Variation of $P_{turbine}$ with U_m for different augmentation systems	129
Fig. 6.16	Field visualizations for augmentation system-1 (a) pressure contours, (b) velocity contours, (c) velocity vectors, and (d) velocity streamline	134
Fig. 6.17	Field visualizations for augmentation system-2 (a) pressure contours, (b) velocity contours, (c) velocity vectors, and (d) velocity streamline	135
Fig. 6.18	Field visualizations for augmentation system-3 (a) pressure contours, (b) velocity contours, (c) velocity vectors, and (d) velocity streamline	136
Fig. 6.19	Field visualizations for augmentation system-4 (a) pressure contours, (b) velocity contours, (c) velocity vectors, and (d) velocity streamline	137
Fig. B.1	% error in local velocity at location X0 along the water depth	165
Fig. B.2	% error in local velocity at location X1' along the water depth	165
Fig. B.3	% error in local velocity at location X2' along the water depth	166
Fig. B.4	% error in local velocity at location X3' along the water depth	166
Fig. B.5	% error in local velocity at location X1 along the water depth	167
Fig. B.6	% error in local velocity at location X2 along the water depth	167
Fig. B.7	% error in local velocity at location X3 along the water depth	168
Fig. B.8	% error in local velocity at location Y1 along the water depth	168
Fig. B.9	% error in local velocity at location Y2 along the water depth	169
Fig. B.10	% error in local velocity at location Y3 along the water depth	169
Fig. B.11	% error in local velocity at location Y4 along the water depth	170
Fig. B.12	% error in local velocity at location Y5 along the water depth	170

LIST OF TABLES

Table 2.1	Summary of work done on SHKT	17
Table 2.2	Summary of work done on MBHKT	28
Table 3.1	Geometric data of Ukai left bank main canal	37
Table 3.2	Qualitative multi-criteria site selection matrix for HKT installation	39
Table 3.3	Standard uncertainty in discharge measurement	42
Table 3.4	Possible HKTs installation for given potential region	61
Table 4.1	Boundary conditions for 3-D computational domain of canal	73
Table 5.1	Statistical uncertainty at different immersion levels	94
Table 5.2	Experimental uncertainty at different immersion levels	95
Table 5.3	Boundary conditions for 3-D computational domain of MBHKT	98
Table 5.4	Performance parameters values at different immersion levels	99
Table 6.1	Boundary conditions for 3-D computational domain of various blade profiles and argumentation systems of MBHKT	114
Table 6.2	Performance parameters values for different blade profiles	120
Table 6.3	Performance parameters values for various augmentation systems	130

LIST OF APPENDICES

Appendix A: Turbulence Models 162

Appendix B: Statistical Error Analysis 165

CHAPTER – 1

INTRODUCTION

1.1 Energy Scenario and Need of Hydrokinetic Turbine

The current demand for energy resources is primarily caused by the expanding population and the rising standard of living in developing nations. A decades-long trend of increasing energy consumption is evident in the overall amount of energy utilized worldwide. India being the 5th world's largest economy [1], the supply and demand of energy in India plays a big role in global development. India is a major participant in the global energy market. India's growing industrialization and urbanization provide significant problems for the country's energy sector and policymakers. States and rural and urban areas differ significantly in terms of energy usage and service quality. India's per capita energy consumption is far lower than half of the global average. Over 900 million Indians had an electrical connection in 2019, indicating that almost all homes now have access to electricity [2,3]. As shown in Fig. 1.1, due to strong economic growth, China and India account for 51% of incremental world primary energy demand in 2006-2030 [4]. In the 1990s, China consumed 4200 million tonnes of equivalent energy, which could increase to 8000 million tonnes in the 2030s. In contrast, India's energy consumption increased from 6100 million tonnes in the 1990s to 11000 million tonnes by 2030, nearly doubling.

The primary drivers behind the hunt for innovative, sustainable ways to produce clean energy are the depletion of fossil fuel supplies brought on by excessive consumption and its detrimental effects on the environment. Fossil fuels' share of primary energy consumption has been seen to have dropped from 87% to 85% between 1995 and 2015, and it is anticipated that consumption will further decline to 78% by 2035 [5]. Renewable energy sources have increased their share of the world's energy production in recent years, adding about 2179

GW (or almost 34% of installed power capacity worldwide).

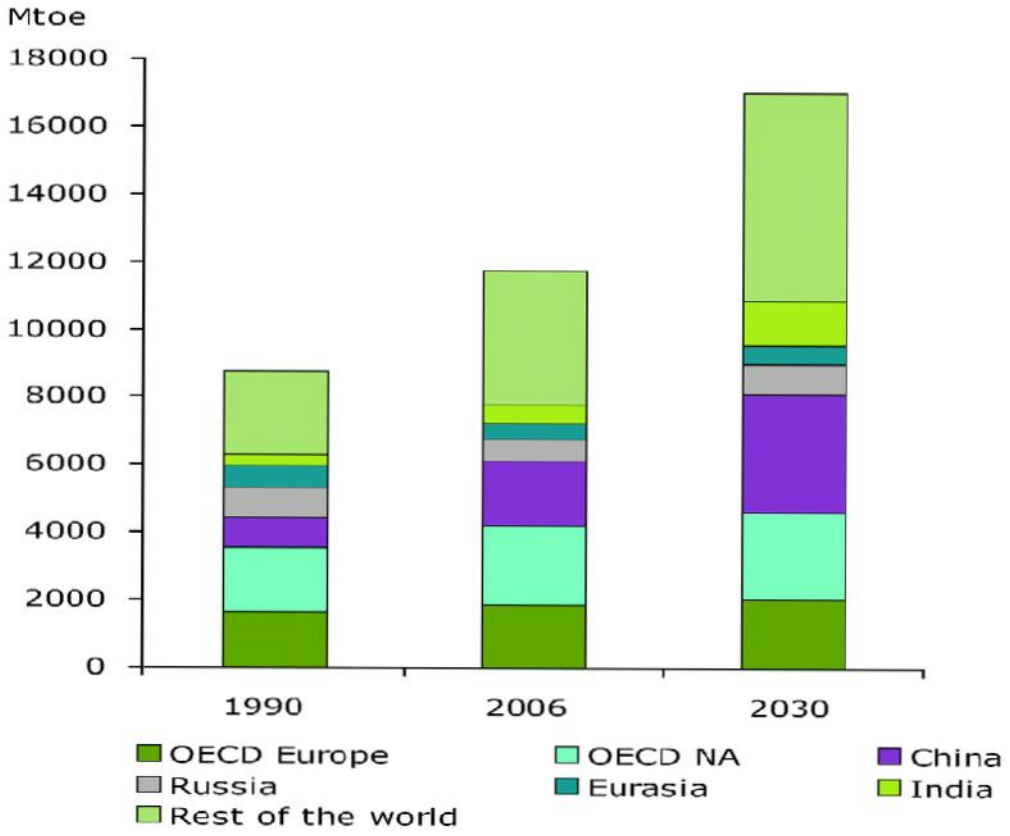


Fig. 1.1. Energy consumption trend in world's major energy customers during 1990-2030 [3].

The largest contributor, accounting for around 1151 GW, or almost 18% of the installed power capacity worldwide, is hydropower [6,7]. However, almost 1.5 billion people globally lack access to enough power, particularly in underdeveloped and emerging communities [8]. In general, rural and remote people cannot afford or access the conventional energy generated by the hydropower plant. It is imperative to swiftly accelerate this trend and shift to a renewable energy-dominant portfolio that drastically lowers carbon emissions within the next ten years, given the climate change catastrophe and the world's steadily rising need for electricity. This can be accomplished in large part by employing established and reasonably priced renewable energy conversion technologies, such as solar, hydro, and wind turbines, to rapidly expand utility-scale renewable energy projects and markets. Hydrokinetic turbine (HKT), which is the best option for electrical generation to

meet the power requirements within a reasonable cost for these places, is the production of electrical energy from open water channels. Using the potential of rivers, canals, and oceans to generate electricity is also a clean, sustainable, and practical solution.

According to a Ministry of New and Renewable Energy (MNRE) assessment, India has 21133.65 MW of potential for small hydropower, or run-of-the-river, throughout the country [9]. If arranged in an array with adequate spacing, several HKTs may be an effective option for harnessing the available hydrokinetic energy potential and generating clean and sustainable electricity for grid supply. Like wind turbines, HKT systems are a type of "zero-head" hydropower in which energy is drawn from the kinetic energy of flowing water rather than the potential energy of falling water. These systems can be set up in streams or rivers that run freely [10]. Many of the issues with more conventional kinds of hydropower, like large civil works expenditures and the requirement for a feasible and exploitable potential energy head, are avoided by HK energy production by utilizing this energy source. Although HK technologies are among the earliest types of hydropower, their development may be separated into several periods, starting with the traditional era that gave rise to the waterwheel concept and ending with the more recent empirical era marked by modernized pilot plants and testing. With multiple HK development projects emerging within river, tidal, and wave energy systems, the technology progress is currently in its growing phase [11]. HKTs don't require a reservoir or spillway, making them comparatively simple designs. According to preliminary research, these devices have a negligible environmental impact, and their ease of use makes installation and maintenance reasonably priced. Because of their simplicity, these systems might be useful in isolated or rural locations.

1.2 Cross Flow Hydrokinetic Turbine

The two types of HKTs: axial-flow turbines and cross-flow turbines are illustrated in Fig. 1.2. Turbines that rotate parallel to or at an angle to the direction of water flow are

known as axial-flow turbines. The rotor of these turbines might contain two, three, or more blades. These turbines use disk-type rotors. These turbines are best utilized in maritime and oceanic environments. The axial-flow turbine is propelled by the lift (vertical) component. These turbines have higher efficiency and mor stable torque with self-starting capacity. On the other hand, their manufacturing cost is high improper handling of debris. HKTs whose rotational axis is perpendicular to the direction of water flow are known as cross-flow turbines. These turbines make better use of available space than axial-flow turbines since their rotors are cylindrical in shape. The cost of manufacturing is minimal, but it also varies according to the kind of rotor. These turbines are easily swept in shallow depths since their diameter is greater than their depth. They manage debris by diverting incoming material. One side of the river or channel may have a generator. Because these turbines don't need sealing arrangements, their production costs are reduced. Although, these turbines have lower efficiency and fluctuating torque [12,13].

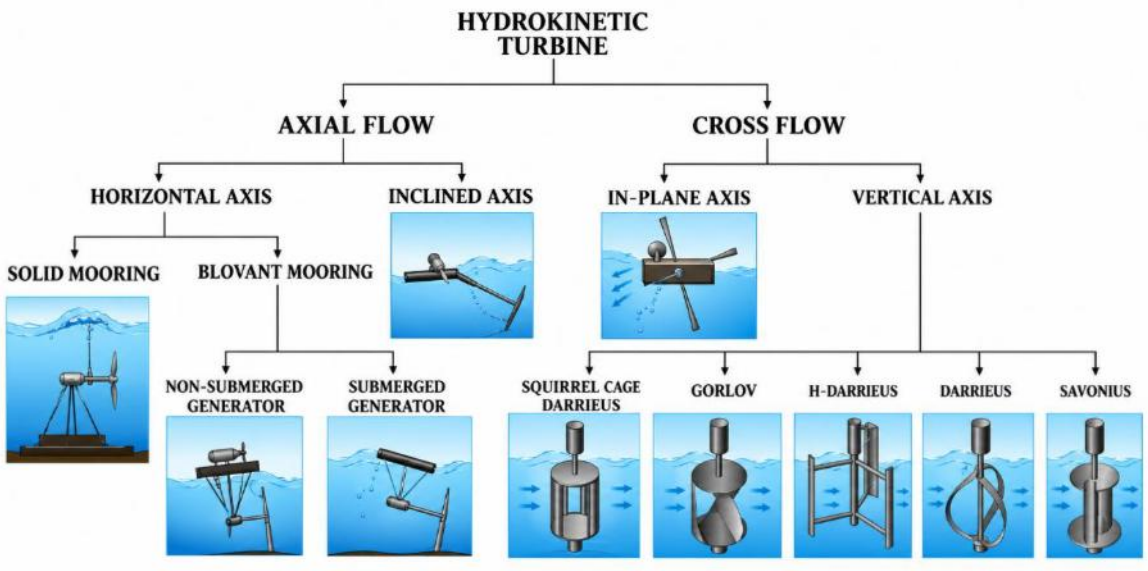


Fig. 1.2. Types of HKTs [14].

1.2.1 Savonius Hydrokinetic Turbine

In 1920, Sigurd J. Savonius developed drag-based and "S" shaped HKT known as Savonius hydrokinetic turbine (SHKT) [15]. The design of SHKT was originated from

cutting cylinder along its axis into two halves and then putting the two halve surfaces sideways as shown in Fig. 1.3. Since the turbine can receive flow from any direction, it does not require a flow orientation mechanism, making it suitable for applications in rivers, canals, and tidal streams where flow conditions may vary. The operating principle of the SHKT is based on drag force. When flowing water strikes the turbine blades, a greater drag force acts on the concave side of the blade compared to the convex side, producing a net torque that causes the rotor to rotate. The continuous difference in drag force between the advancing and returning blades sustains the rotational motion of the turbine. The rotating shaft can then be connected to a generator to convert mechanical energy into electrical power. The SHKT usually operates at relatively low rotational speeds but provides high starting torque, allowing it to start rotating even at low water velocities without requiring external assistance. This self-starting capability makes the SHKT suitable for applications where water flow is inconsistent or relatively slow.

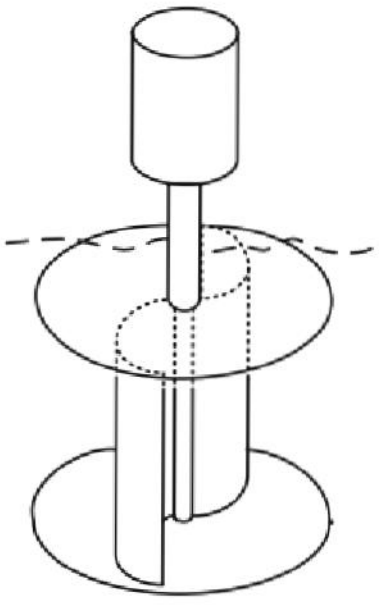


Fig. 1.3. Conventional SHKT [13].

The SHKT offers several advantages that make it suitable for small-scale and decentralized energy generation systems. Its simple structure reduces manufacturing complexity and cost, while its straightforward design enables easy installation and

maintenance. The SHKT can be constructed using locally available materials, which further reduces production costs and makes it practical for rural and remote areas. Furthermore, the SHKT operates efficiently under low water velocity conditions and can function under varying flow directions without complex control systems. The lower rotational speed of the SHKT also contributes to reduced noise and a lower risk to aquatic life compared to some high-speed turbine systems. Due to these characteristics, the SHKT can serve as an alternative energy source for applications such as rural electrification, water pumping, and standalone power systems.

Despite its advantages, the SHKT also has certain limitations that affect its overall performance. Since it operates primarily on the drag principle, its energy conversion efficiency is generally lower than that of lift-based turbines. The blade moving against the direction of flow experiences a resisting force known as negative torque, which decreases the net output power of the turbine. Additionally, the relatively low rotational speed may require the use of gear systems or transmission mechanisms when coupling the turbine to electrical generators. The SHKT may also experience fluctuations in torque during operation, affecting output stability. Nevertheless, due to its robust construction, reliability, and ability to operate under a wide range of flow conditions, the SHKT remains a practical and promising technology for extracting renewable energy from flowing water resources.

1.2.2 Michell-Banki Hydrokinetic Turbine

In the early 20th century, three scientists Anthony Michell, Donát Bánki, and Fritz Ossberger developed the cross flow Michell-Banki hydrokinetic turbine (MBHKT) [16]. It is considered an impulse-type turbine in which water energy is converted into mechanical energy by directing a jet of water onto the turbine blades. The MBHKT consists of a cylindrical runner with numerous curved blades arranged around its periphery, enclosed within a casing and nozzle arrangement that guides the water flow toward the runner as

depicted in Fig. 1.4.

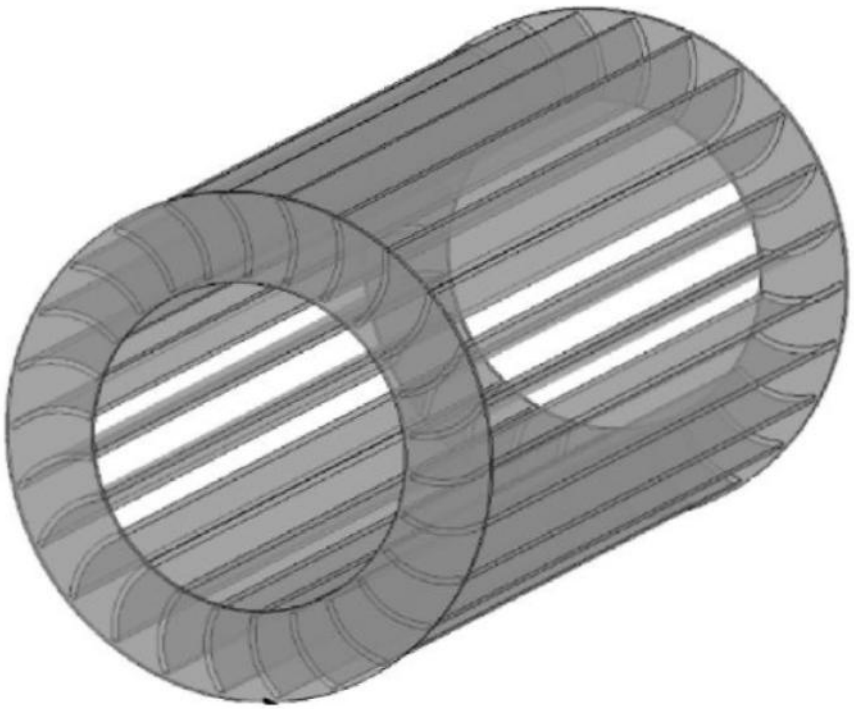


Fig. 1.4. Conventional MBHKT [17].

The working principle of the MBHKT involves a unique double-pass flow mechanism. Water enters the turbine through a nozzle and strikes the runner blades at a specific angle, transferring its kinetic energy and causing the runner to rotate. Unlike many conventional turbines, the water passes through the runner twice before exiting the system. During the first stage, water enters from the outer circumference and moves toward the center of the runner, transferring a portion of its energy to the blades. The water then crosses the runner and passes through the blades again while moving from the inner region toward the outer side, allowing additional energy extraction. This double interaction between water and blades improves the utilization of the available energy and contributes to the turbine's operational effectiveness. The rotating shaft of the turbine is connected to a generator for converting mechanical energy into electrical power.

The MBHKT possesses several advantages that make it suitable for small and medium-scale hydropower applications. The turbine has a relatively simple design and can be

manufactured using conventional fabrication techniques, reducing production and maintenance costs. It is capable of maintaining acceptable efficiency over a wide range of water flow rates and operating conditions, making it highly adaptable in locations where water availability varies seasonally. The turbine also has good self-cleaning characteristics because water continuously passes through the runner, reducing the accumulation of debris and sediments. Due to these characteristics, the MBHKT is commonly employed in micro-hydropower plants, rural electrification systems, and isolated energy applications.

Despite its advantages, the MBHKT also has certain limitations. The efficiency of the turbine is generally lower than some high-performance turbines designed for specific operating conditions, such as Pelton or Francis turbines. Performance can decrease if the nozzle geometry and flow conditions are not properly optimized. Energy losses may occur because of turbulence, friction, and improper water flow distribution across the blades. The turbine may also require careful design considerations to achieve maximum energy extraction and stable operation. Nevertheless, because of its reliability, ease of construction, low maintenance requirements, and ability to operate efficiently under varying flow conditions, the MBHKT remains a practical and effective option for sustainable hydropower generation, particularly in remote and rural regions.

1.3 Modular Hydrokinetic Turbine

Standard modular HKTs are developed based on the concept of integrating standardized and interchangeable components into hydropower systems to improve flexibility, reduce cost, and simplify implementation. Rather than designing every system uniquely for a specific site, the modular approach uses predefined components that can be combined according to operational requirements and environmental conditions. These modules generally include power generation units, support structures, foundation systems, and passage components for water, sediment transport, aquatic life, and recreational

activities. The modular concept aims to create a more adaptable hydropower system while reducing engineering complexity and minimizing the extensive customization normally required for conventional hydropower projects.

The modular design strategy provides several advantages for HKT applications by improving installation efficiency and reducing overall project lifecycle costs. Standardized modules can simplify manufacturing, transportation, maintenance, and replacement processes while enhancing reliability and operational predictability. In addition, modular systems are designed to maintain environmental compatibility by reducing disturbances to natural river systems and preserving ecological functions such as fish migration, sediment transport, and natural water movement. The use of modular structures also supports scalability, where multiple units can be integrated to increase energy output based on site requirements. However, proper site classification and careful module selection are necessary to ensure optimum performance and compatibility with environmental and operational conditions. The various examples of modular turbines are shown in Fig. 1.5.

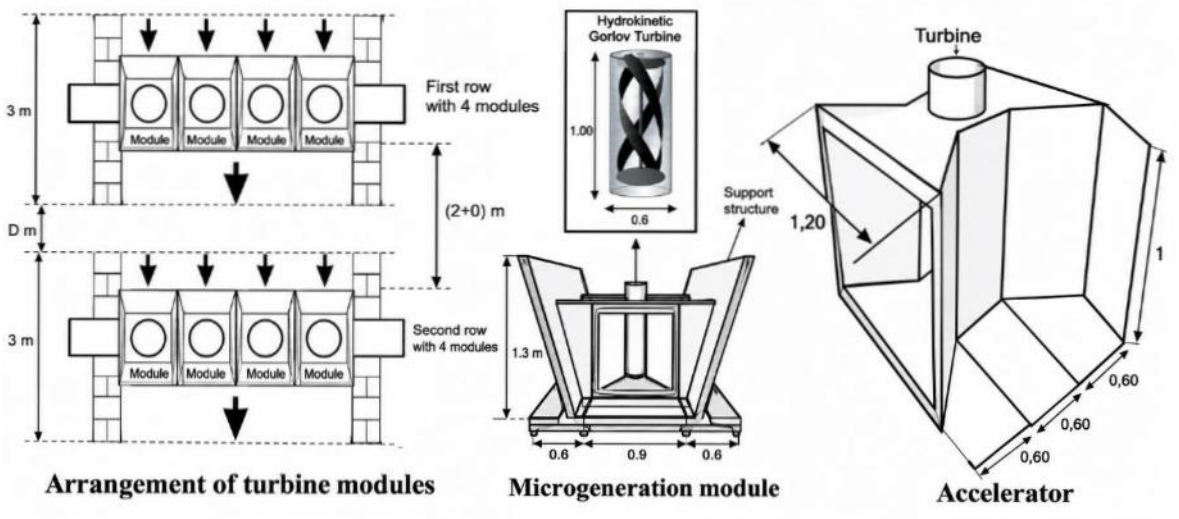


Fig. 1.5. Modular HKT [18].

1.4 Introduction to Computational Fluid Dynamics

Because of the flow separation and wake creation, the flow field surrounding the HKTs is complex and time-dependent. Using conventional methods like the stream tube model,

which is based on blade element momentum theory, it is challenging to describe this type of intricate unsteady flow physics. Additionally, artificial neural networks (ANN), fuzzy logic, and genetic algorithms are examples of soft computing techniques that show promise in predicting the power factor of various energy systems. Additionally, compared to other soft computing methods, the ANFIS provides an efficient way to predict the power output. The most effective method available today for resolving a variety of industrial and non-industrial fluid flow issues is Computational Fluid Dynamics (CFD). Creating the computational domain, dividing it into smaller areas for solving the equations, choosing appropriate boundary conditions, and allocating appropriate values to modelling parameters are prerequisites for carrying out numerical simulation of any phenomenon.

CFD has become an effective numerical approach for investigating the hydrodynamic performance of HKTs. HKTs extract kinetic energy directly from flowing water without requiring significant hydraulic head. Due to the complex interaction between rotating blades and surrounding fluid, CFD techniques are widely used to understand flow behaviour, pressure distribution, wake formation, and turbine performance characteristics. Numerical simulation offers advantages over experimental testing by reducing development cost and allowing detailed visualization of fluid phenomena that may be difficult to measure experimentally. The CFD procedure for HKT analysis generally involves geometry creation, computational domain development, mesh generation, selection of physical and turbulence models, implementation of boundary conditions, solution procedures, convergence assessment, and post-processing of numerical results. Proper implementation of these steps is essential for obtaining reliable simulation outcomes.

The CFD simulation process begins with the development of the HKT geometry, which generally includes the blades, hub, and shaft. The turbine model is then placed within a computational domain representing the surrounding water region. The domain dimensions

are selected carefully to minimize boundary effects and ensure realistic flow conditions. Following geometry creation, the computational domain is discretized into small elements through a meshing process. Mesh quality significantly affects the accuracy of numerical results. A finer mesh is usually generated near blade surfaces to accurately capture pressure gradients and boundary layer effects. Inflation layers are also applied near wall regions to improve near-wall flow prediction. To ensure reliability of results, a mesh independence study is commonly performed. The fluid flow is governed by conservation equations of mass and momentum, commonly referred to as the Navier–Stokes (N-S) equations. Since HKT operation generally involves turbulent flow conditions, an appropriate turbulence model must be selected. Generally, $k-\varepsilon$ Standard, $k-\varepsilon$ Renormalization group (RNG), $k-\varepsilon$ Realizable, $k-\omega$ Standard and $k-\omega$ shear stress transport (SST) turbulence models were employed. The N-S equation for a turbulent flow of an incompressible Newtonian fluid and standard equations for each models are given in Appendix A. Boundary conditions are then applied to define operating conditions of the simulation. A velocity inlet condition is specified at the upstream boundary, while a pressure outlet condition is applied at the downstream region. Blade surfaces are generally treated using no-slip wall conditions. Rotational effects of the turbine are represented using techniques such as the Multiple Reference Frame (MRF) or Sliding Mesh Method (SMM). The governing equations are solved numerically using the finite volume method through an iterative procedure. Convergence is achieved when residual values of continuity and momentum equations reach acceptable limits and monitored parameters such as torque and power become stable. After convergence, post-processing is performed to analyse flow characteristics and turbine performance. Parameters including velocity contours, pressure distribution, and streamlines are evaluated to determine the effectiveness of the HKT design.

1.5 Outline of the Thesis

Chapter 1 describes the current energy scenario pertaining in India and world. It emphasises the need of the HKTs for rapidly moving world energy requirements. Furthermore, the pros and cons of the SHKT, MBHKT and emergence of modular HKT are signified.

Chapter 2 elaborates the literature survey of the work done on site selection of HKTs and performance improvement in SHKT as well as MBHKT in chronological order with highlight of the current research work. The conscious definition of the objectives that were achieved during the entire Ph.D. study is presented along with the identification of the problem statement and research gap.

In the **Chapter 3**, the field data measurement of canal along with the experimental discharge measurement is illustrated. The in-depth numerical methodology with geometry, meshing, applied boundary conditions is explained. In the end, the numerical simulation results are presented with the statistical error analysis.

Chapter 4 of the thesis comprehensively demonstrates the numerical study of the HKTs using the canal flow. The HKT performance characteristics curves with the clear flow filed visualisations are also depicted.

Chapter 5 of the thesis demonstrates the procedure that was employed during the experiment test of the MBHKT in open laboratory channel. It also covers the fabrication of the MBHKT with the instruments that were used during experimentation. The same results were utilised to validate the numerical simulations results.

The numerical optimization of MBHKT with different profiles of the blades is represented in **Chapter 6**. Based on the optimum blade profiles various augmentations were also evaluated for optimum output. In **Chapter 7**, the summary of the work is presented in the form of conclusions as well as scope for the future work.

CHAPTER – 2

LITERATURE REVIEW, PROBLEM STATEMENT AND OBJECTIVES OF PRESENT WORK

2.1 Literature Review

This section represents the brief overview of numerical, theoretical, and experimental work done by the researchers.

2.1.1 Site Selection

Many researchers have attempted to identify about the favourable site for HKT in various canal sections. An analytical, experimental, and CFD methods are to be applied for this analysis. When studying turbulent flows in open channels, hydraulic engineers frequently use CFD and experimental studies to comprehend the different flow components [19–24]. In the early stage of development, Shnipov [25] discovered the primary regularities of the distribution of the three-dimensional (3-D) field of mean velocities, kinematic eddy viscosity, and Reynolds stresses over the cross section of rectilinear trapezoidal open channels. Yang et al. [26] studied the mechanism of the dip phenomenon, which occurs when the maximum velocity appears below the free surface in relation to the secondary currents in open-channel flows. They have developed the new log-law for predicting the dip phenomena at the free surface of water. Yang and Lim [27] developed the analytical model for computing the boundary shear stress in trapezoidal channels. In contrast to rectangular open channels, a trapezoidal channel has zero local boundary shear stress at the water's surface, and as the base angle increases, the maximum shear approaches the bed. Taking this equation as based many authors have tried to develop various models for predicting the velocity distribution, dip phenomena and boundary shear stress [19,28–30]. An effort is made to create a numerical technique to forecast the flow in river bends (curves) in the

research article by Kamel et al. [31]. Their approach makes use of the 3-D non-linear $k-\varepsilon$ model for a compound channel that meanders and has a rectangular cross-section for HKT installation. Furthermore, downstream of hydro power plant were assessed for HKT installation using the power curve by Holanda et al. [32]. A correlation of 0.96 was achieved by creating a power curve for the simulated velocities and measured flow rates. A design velocity of 2.35 m/s was defined, the velocity was estimated, and the energy density was computed using the curve. An integrated hydrokinetic energy index for HKT site selection was developed by Fouz et al. [33]. This novel index comprises not only the geometrical parameters and flow characteristics of particular site, but also includes costs and environmental aspects. Similar attention was also given to flow characteristics determination by various authors using the high quality turbulence models [24,34,35]. Song et al. [36] used an efficient numerical method based on actual geometry statistics to study the turbulent flows in simplified Dragon type river channels with a constant critical curvature and various single-short-branch characteristics. Based on the simulations performed using RNG $k-\varepsilon$ model, they found that the location shift of the main and branch channels' greatest flow impact under various circumstances to direct the strategic positioning of river engineering structures. The performance of several low Reynolds number turbulence models was compared to direct numerical simulations by Gorji et al. [37] and found that $k-\varepsilon$ yield the accurate predictions for the wall shear stress of open channels. Previous studies have explored spillway performance using numerical, experimental, and optimization approaches. CFD based analyses highlight the influence of geometry on energy dissipation and discharge [38], while AI-based optimization methods improve hydraulic efficiency and reduce costs [39]. Additionally, air entrainment studies and advanced particle-based models emphasize accurate prediction of cavitation behaviour and complex free-surface flows [40]. Recently in 2026, Benoumessad et al. [41] modelled the flow velocity profiles for irregular shaped

open channels using the $k-\varepsilon$ simulation model. The principal flow in the curved segment first moves toward the inner bank before being redirected toward the outer bank by centrifugal force. Elevation close to the outside wall and depression close to the inner wall indicate a significant rotational displacement in the free surface.

2.1.2 Hydrokinetic Turbine

There are numerous researchers who have worked to improve the performance of SHKT and MBHKT by varying its parameters, such as blade shape, no. of blades, adding external components, blade angle, and so on. Kumar and Saini [42,43] optimised the blade arc angle, blade twist angle and blade shape factor of single stage SHKT using numerical analysis. They found that at 0.9 tip speed ratio (TSR) and mean flow velocity (U_m) of 2 m/s, the maximum power coefficient ($C_{P,max}$) of 0.426 was obtained for 150° blade arc angle and 0.6 blade shape factor; while 0.390 for 12.5° blade twist angle. Talukdar et al. [44] evaluated the performance of SHKT by varying the no. of blades (two and three); shape of blade (semi-circular and elliptical) and depth of immersion (100% fully submerged and 60% partially submerged). The two bladed semi-circular fully submerged SHKT imparts the highest $C_{P,max}$ of 0.28 at 0.89 TSR. A novel deflector plate added SHKT with NACA6409 blades instead of conventional semi-circular blades were numerically investigated by Chaudhari and Shah [45]. Their study found that the $C_{P,max}$ for NACA6409 blades SHKT and conventional SHKT with deflector is 0.227 at 0.8 TSR and 0.25 at 0.8 TSR, respectively. Also, NACA6409 blades SHKT with deflector has a lesser performance than conventional SHKT with deflector. Shanegowda et al. [46] numerically investigated the performance of SHKT for straight and curved (30°, 60° and 90°) bend channels. The most efficient bend condition is 30° with $C_{P,max}$ of 0.24 at 1 TSR. Mereke et al. [47] evaluated the performance of MBHKT in conjunction with nozzle and diffuser attachment for ultra-low head application. The speed of conventional MBHKT obtained was 344 rpm, while 1025 rpm was obtained for MBHKT

with nozzle and diffuser attachment. For small hydro power plants, the applicability of reaction MBHKT was evaluated Lukes et al. [48] using ANSYS CFX. The rotational speed of 220 rpm with an efficiency of 79.43% was obtained for the design parameters. The summary of work done by various researchers for SHKT and MBHKT is tabulated in Table 2.1 and Table 2.2.

Table 2.1

Summary of work done on SHKT.

Sr. No.	Methodology	Parameters Studied	Range of Parameters	Optimum Value(s) of Parameter			Reference
				TSR	C_P	C_T	
1.	Numerical	Airfoil-Bladed SHKT Use deflector Vertical axis	NACA6409 No. of blades = 2 U_m = 1.0 m/s TSR = 0.7 to 1.1	0.8	0.227	0.284	Chaudhari and Shah [45]
2.	Experimental	Use deflector plate Advancing blade (α) and returning blade (β) angles Flow velocity Inclined axis	No. of blades = 3 U_m = 1.37-2.28 m/s α = 35° and 15° β = 107°, 60° and 21° TSR = 0.0-1.3	0.8	0.24	0.29	Jeeva et al. [49]
3.	Numerical	Effect of placing a turbine	No. of blades = 2	0.9	0.17	0.19	Shashikumar et al.

Sr. No.	Methodology	Parameters Studied	Range of Parameters	Optimum Value(s) of Parameter			Reference
				TSR	C_P	C_T	
		Vertical axis	TSR = 0.7-1.3 U_m = 0.5 m/s				[50]
4.	Experimental Numerical	Helical SHKT SHKT arranged in array Spacing between Various SHKT Flow velocity Vertical axis	No. of blades = 2 Spacing between Various SHKT = 3D (D = rotor diameter), 3.5D, 4D, 4.5D, 5D, and 5.5D U_m = 1-3 m/s TSR = 0.25-1.2	0.9	0.396	0.44	Nag and Sarkar [51]
5.	Experimental	Unique vane shape Vertical axis	No. of blades = 2 U_m = 0.85 m/s TSR = 0.3-1.7	0.8	0.17	0.21	Patel et al. [52]

Sr. No.	Methodology	Parameters Studied	Range of Parameters	Optimum Value(s) of Parameter			Reference
				TSR	C_P	C_T	
6.	Numerical	Use barrier Length of the barrier Vertical axis	No. of blades = 2 U_m = 0.48 m/s TSR = 0.4, 0.8 and 1.2	0.8	0.292	0.365	Alizadeh et al. [53]
7.	Numerical	Blade Profile Flow velocity Vertical axis	No. of blades = 2 U_m = 0.3-0.8 m/s TSR = 0.4-1.2	1	0.43	0.43	Anthony and Roy [54]
8.	Experimental Numerical	Twisted blade SHKT Use deflector Three configurations of the deflector system Vertical axis	No. of blades = 2 U_m = 0.86 m/s	0.78	0.195	0.25	Mosbahi et al. [55]

Sr. No.	Methodology	Parameters Studied	Range of Parameters	Optimum Value(s) of Parameter			Reference
				TSR	C_P	C_T	
9.	Numerical	S shape blade Flow velocity Vertical axis	No. of blades = 2 U_m = 0.5-3.0 m/s TSR = 0.2-1.3	0.8	0.246	0.308	Ramadan et al. [56]
10.	Numerical	SHKT New conventional SHKT New proposed SHKT Vertical axis	No. of blades = 2 U_m = 0.48 and 1.0 m/s TSR = 0.2-1.3	0.98	0.28	0.29	Alipour et al. [57]
11.	Experimental Numerical	Blade profile Rotor angle (θ) Flow velocity Horizontal axis	No. of blades = 2 θ = 0°, 36°, 72°, 108°, 128° and 144° U_m = 1.3-4.0 m/s TSR = 0.1-0.7	0.5	0.164	0.328	Zhang et al. [58]

Sr. No.	Methodology	Parameters Studied	Range of Parameters	Optimum Value(s) of Parameter			Reference
				TSR	C_P	C_T	
12.	Experimental Numerical	Modified and Helical SHKT Use flume Duct angle Flow velocity Vertical axis	No. of blades = 2 Duct angle = 20°–32° U_m = 1.0-3.0 m/s TSR= 0.0-1.25	0.714	0.108	0.156	Nag and Sarkar [59]
13.	Numerical	Use thick deflector plate Deflector shape and position Vertical axis	TSR = 0.8 to 1.2	1.1	0.24	0.22	Kerikous and Thevenin [60]
14.	Experimental Numerical	Use deflector system Helical SHKT Different configurations of deflector system	No. of blades = 3 U_m = 0.86 m/s	0.7	0.14	0.20	Mosbahi et al. [61]

Sr. No.	Methodology	Parameters Studied	Range of Parameters	Optimum Value(s) of Parameter			Reference
				TSR	C_P	C_T	
15.	Experimental Numerical	Use duct and augmentation channel Flow velocity Horizontal axis	No. of blades = 3 U_m = 0.5, 1.15 and 2.15 m/s TSR = 1.0-5.0	3.5	0.53	0.29	Goundar et al. [62]
16.	Numerical	Use an impinging jet duct design Flow velocity Vertical axis	No. of blades = 2 U_m = 0.3-1.5 m/s	0.61	0.5	0.82	Thakur et al. [63]
17.	Experimental Numerical	Effect of no. of blades and blade shape Semi-circular and elliptical blade profiles	No. of blades = 2 and 3 Immersion = 100%, 80% and 60% U_m = 0.8 m/s	0.89	0.28	0.31	Talukdar et al. [44]

Sr. No.	Methodology	Parameters Studied	Range of Parameters	Optimum Value(s) of Parameter			Reference
				TSR	C_P	C_T	
		Submerge conditions Vertical axis	TSR = 0.2-1.4				
18.	Experimental	Different geometry of the channel Use of hump, Deflector plate and side wall plate Vertical axis	No. of blades = 2 U_m = 0.46 and 0.56 m/s TSR = 0.4-1.6	1.1	0.49	0.45	Patel et al. [64]
19.	Theoretical	Pressure Impulse momentum Principle Vertical axis	No. of blades = 2 U_m = 0.589 m/s TSR = 0.3-1.1	0.5	0.14	0.28	Patel et al. [65]
20.	Numerical	Blade twist angle	No. of blades = 2	0.9	0.39	0.43	Kumar and Saini

Sr. No.	Methodology	Parameters Studied	Range of Parameters	Optimum Value(s) of Parameter			Reference
				TSR	C_P	C_T	
		Vertical axis	Blade twist angle = 0°-25°				[42]
			U_m = 0.5-2.0 m/s				
			TSR = 0.5-1.0				
21.	Numerical	Blade arc angle	No. of blades = 2	0.9	0.426	0.473	Kumar and Saini
		Blade shape factor	Blade arc angle = 110°-150°				[43]
		Vertical axis	Blade shape factor = 0.0-0.6				
			U_m = 0.5-2.0 m/s				
			TSR = 0.5-1.0				
22.	Numerical	Use ducted nozzle	No. of blades = 2	0.73	0.25	0.34	Elbatran et al. [66]
		Six configurations of ducted nozzle	TSR = 0.6-1.1				
		Vertical axis					

Sr. No.	Methodology	Parameters Studied	Range of Parameters	Optimum Value(s) of Parameter			Reference
				TSR	C_P	C_T	
23.	Experimental	Overlap ratio Vertical axis	No. of blades = 4 Overlap ratio = 0 and 0.2 U_m = 0.82 m/s TSR = 0.0-1.0	0.5	0.19	0.38	Thiyagaraj et al. [67]
24.	Numerical	Use Deflector Deflector position Flow velocity Vertical axis	No. of blades = 2 β = 90°, 101°, 123° and 137° U_m = 0.3-1.5 m/s TSR = 0.4-0.9	0.578	0.54	0.93	Basumatary and Biswas [68]
25.	Experimental	Overlap ratio Aspect ratio Vertical axis	No. of blades = 2 Overlap ratio = 0.0-0.174 Aspect ratio = 0.211-0.637 U_m = 0.46 m/s	0.6	0.20	0.33	Patel et al. [69]

Sr. No.	Methodology	Parameters Studied	Range of Parameters	Optimum Value(s) of Parameter			Reference
				TSR	C_P	C_T	
			TSR = 0.3-1.2				
26.	Numerical	New configuration with quarter blades Vertical axis	U_m = 6.0-10.17 m/s TSR = 0.6-0.74	0.66	0.2266	0.3433	Sharma and Sharma [70]
27.	Experimental	A novel drag-driven vertical axis Turbine configurations	U_m = 0.77-1.22 m/s TSR= 0.05-0.8	0.441	0.132	0.299	Harries et al. [71]
28.	Numerical	Multi-Stage of rotor with variable diameter of rotor Vertical axis	No. of blades = 2 No. of stages = 3 Diameter of each stage = 0.15, 0.16 and 0.17 m Height of each stage (h) =	0.8	0.32	0.40	Kumar and Saini [72]

Sr. No.	Methodology	Parameters Studied	Range of Parameters	Optimum Value(s) of Parameter			Reference
				TSR	C_P	C_T	
			0.050, 0.100 and 0.112 m U_m = 2.0 m/s TSR = 0.4-1.1				
29.	Experimental Numerical	Low flow velocity Flow velocity Vertical axis	No. of blades = 3 U_m = 0.3-0.9 m/s TSR = 0.6-1.0	0.77	0.39	0.51	Sarma et al. [73]
30.	Experimental	Use deflector plates Distance from rotor center (Z) Angle from the horizontal axis (α) Vertical axis	Z = R and 1.8R (rotor radius (R)) α = 15°-60° TSR = 0.6-1.2	1.1	0.35	0.32	Golecha et al. [74]

Sr. No.	Methodology	Parameters Studied	Range of Parameters	Optimum Value(s) of Parameter			Reference
				TSR	C_P	C_T	
31.	Experimental	Use deflector plate Modified blade profile Deflector plate positions Multi-Stage of rotor Vertical axis	No. of blades = 2 No. of stages = 1-3 TSR = 0.6-1.2	0.82	0.21	0.26	Golecha et al. [75]

Table 2.2

Summary of work done on MBHKT.

Sr. No.	Methodology	Parameters Studied	Range of Parameters	Optimum Value(s) of Parameter			Reference
				TSR	C_P	C_T	
1.	Numerical	Use diffuser augmented and dual rotor Vertical axis	No. of blades = 23 Volume flow rate	--	0.594	--	Mereke et al. [47]

Sr. No.	Methodology	Parameters Studied	Range of Parameters	Optimum Value(s) of Parameter			Reference
				TSR	C_P	C_T	
			= 1 m³/s				
2.	Numerical	Use novel close-ended deflector and various rotors i.e., straight blade, H-Darrieus, SHKT and MBHKT Vertical axis	No. of blades = 17 U_m = 0.56 m/s TSR = 0.0-1.3	1.3	0.42	0.32	Mohammed et al. [76]
3.	Experimental	Use bidirectional diffuser augmented channel and twin lower and upper cross flow turbines Horizontal axis	No. of blades = 26 U_m = 0.2 m/s TSR = 0.0-2.2	0.7	0.612	0.874	Elbatran et al. [77]
4.	Numerical	Use augmented channel Internal diameter Inlet blade angle (β_1)	No. of blades = 30 Internal diameter = 800-1200 mm	1	0.89	0.89	Gaba and Bhowmick [78]

Sr. No.	Methodology	Parameters Studied	Range of Parameters	Optimum Value(s) of Parameter			Reference
				TSR	C_P	C_T	
		Horizontal axis	β_1 = 24°-30° U_m = 2.5 m/s TSR = 0.8-1.2				
5.	Experimental Numerical	Use bidirectional diffuser augmented channel and twin lower and upper cross flow turbines Use NACA0025 for Nozzle shape effects of blades' inlet and outlet angles Diameter ratio (D_i/D_o) Horizontal axis	No. of blades = 26 Blade inlet angle (β_1) = 15°-60° Blade outlet angle (β_2) = 75°-120° D_i/D_o = 0.677-0.736 U_m = 1 m/s TSR = 0.0-2.2	0.7	0.612	0.874	Elbatran et al. [17]

Sr. No.	Methodology	Parameters Studied	Range of Parameters	Optimum Value(s) of Parameter			Reference
				TSR	C_P	C_T	
6.	Numerical	Use bidirectional diffuser-augmented channels system and twin lower and upper cross flow turbines Use NACA0025 for Nozzle shape Horizontal axis	No. of blades = 26 U_m = 1 m/s TSR = 0-1.2	0.5	0.52	1.04	Elbatran et al. [79]
7.	Numerical	Use ducted nozzle Vertical axis	No. of blades = 30 U_m = 0.65-3.25 m/s TSR = 1.0-3.5	3.5	0.56	0.16	Goundar et al. [80]
8.	Numerical	Use augmentation channel, single turbine and number of equally spaced turbines Horizontal axis	No. of blades = 26 U_m = 2.5 m/s TSR = 0.15-2.7	1.3	0.51	0.39	Kim et al. [81]

2.2 Problem Statement

Few researchers have focused on MBHKT, despite the abundance of literature reviews accessible for SHKT performance improvement. The majority of study to date has focused on MBHKT performance through numerical analysis; nevertheless, there is a dearth of literature based on experimental examination. Additionally, research on the MBHKT's performance is conducted for water channels such rivers and irrigation canals. The majority of the work has been done on various nozzle settings and blade shapes for other HKTs. Investigating the best blade and nozzle parameter values for MBHKT that are appropriate for the given hydro potential location is therefore necessary. Additionally, the literature review that is currently accessible concentrates on using these HKTs horizontally to harness energy. The main objectives of this study are to evaluate the performance of vertical axis MBHKT in terms of torque coefficient (C_T) and C_P for various conditions and locations.

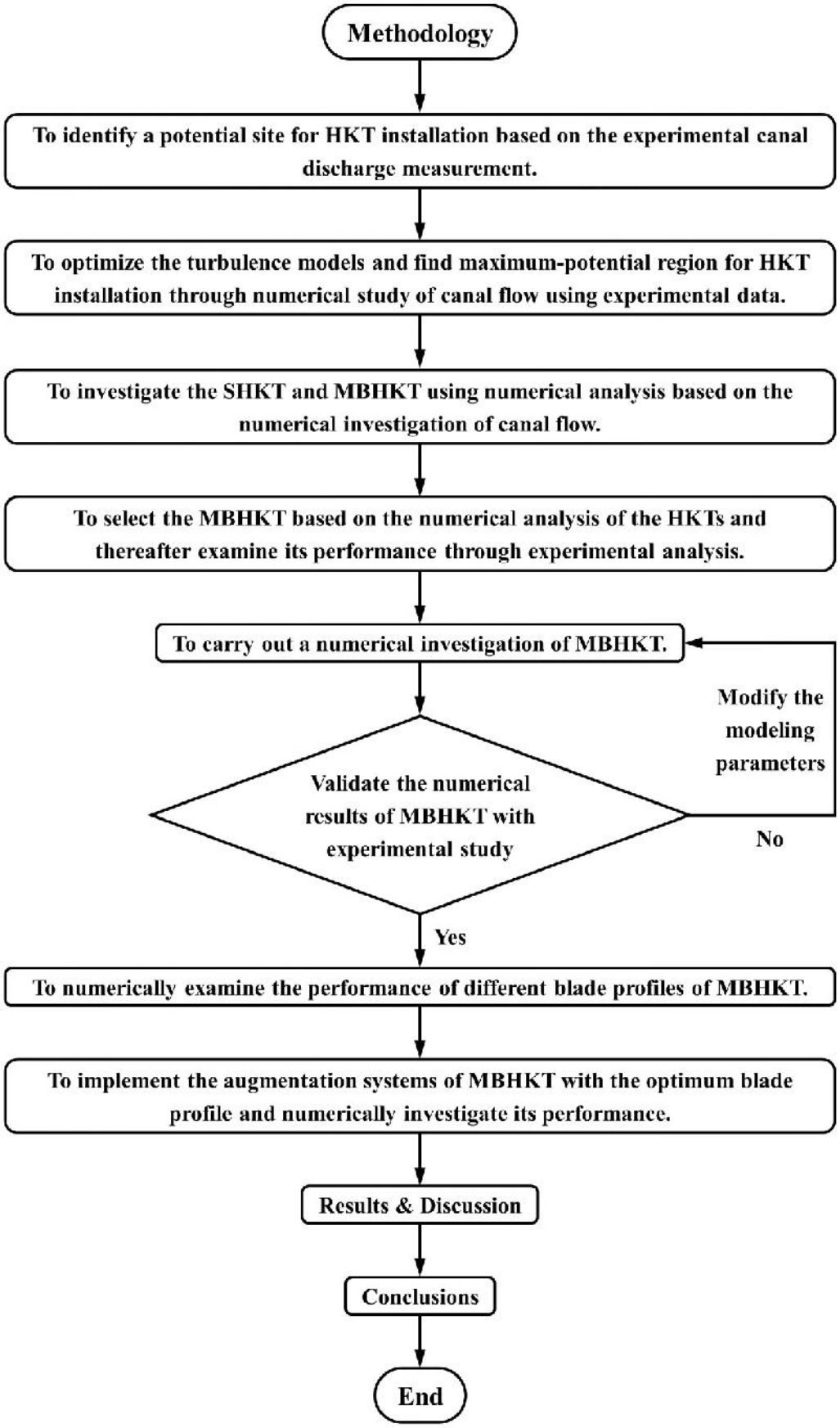
To fill the research gap and to explore the practical feasibility of actual system, the performance of MBHKT was evaluated in four stages of this research work. In the first stage, the actual experimental velocity of the actual canal flow was measured. Also, with the help of the comparative assessment of various turbulence models, the potential HKT installation site was determined. In the second stage, using the obtained canal flow and preferred HKT installation site, the comparative analysis of SHKT and MBHKT was carried out in a canal. In the third stage, experimental study of MBHKT was performed at state-of-the-art open channel testing facility established at Fluid Mechanics and Fluid Machine Laboratory, Sardar Vallabhbhai National Institute of Technology, Surat, Gujarat, India. In the final and forth stage of the present investigation, the numerical optimization of three different blade profiles (profile 1 – flat, profile 2 – round and profile 3 – sharp edged) was performed for the open channel testing facility. Additionally, based on the optimum blade profile, the various augmentations combining the nozzle and diffuser were also numerically simulated

to find out the optimum augmentation design.

2.3 Objectives of the Present Work

1. To identify a suitable HKT installation site and comparative assessment of turbulence models in open channel flow.
2. To analyse flow characteristics and water power density for prediction of hydrokinetic energy potential.
3. To perform comparative numerical evaluation of SHKT and MBHKT for optimal performance under canal flow conditions.
4. To experimentally validate the performance of the MBHKT under different flow conditions.
5. To optimize MBHKT blade profiles for enhancing overall turbine performance.
6. To develop and evaluate flow augmentation systems for improving MBHKT performance in open channel.

2.4 Brief Methodology of the Thesis



CHAPTER – 3

EXPERIMENTAL AND NUMERICAL STUDY OF THE CANAL FLOW

In the first stage of this research work, an identification of a potential HKT study site and a comparative assessment of various turbulence models was carried out at trapezoidal open canal situated on Tapi River, Surat, Gujarat, India.

3.1 Experimental Study

3.1.1 Hydrokinetic Turbine Site Selection

HKTs have certain operational challenges, i.e., depending on the type of turbine and its direction, a minimum water flow speed of 1 to 3 m/s is typically required. The site should be at least two meters deep and three meters wide [82]. Debris in the stream, low energy capacity and efficiency, the lack of indigenous technology, and the complexity, importation, and inability to adjust current technology to site specifications. Higher velocities are typically accessible more easily at sites at existing narrowed sections (such as flume sections or outlets of syphon). As a result of these problems, these technologies are still in their infancy and have limited applicability [83]. The pre-commercial phase of HKTs technology development is currently ongoing. despite the fact that the HKTs are still in their infancy. Fig. 3.1 shows a favourable installation sections in various canal sections. When choosing sections like these, a number of problems might arise, including excessive construction of dams (raising the risk of flooding because of the obstruction) or stopping the infrastructures operate (prior to installation), as the additional obstruction may cause the hydrodynamic effects in areas at risk. Thus, the optimal installation option is still to choose a place where a smaller portion of the cross section is used for the HK installation and there is a greater available velocity along a uniform section.

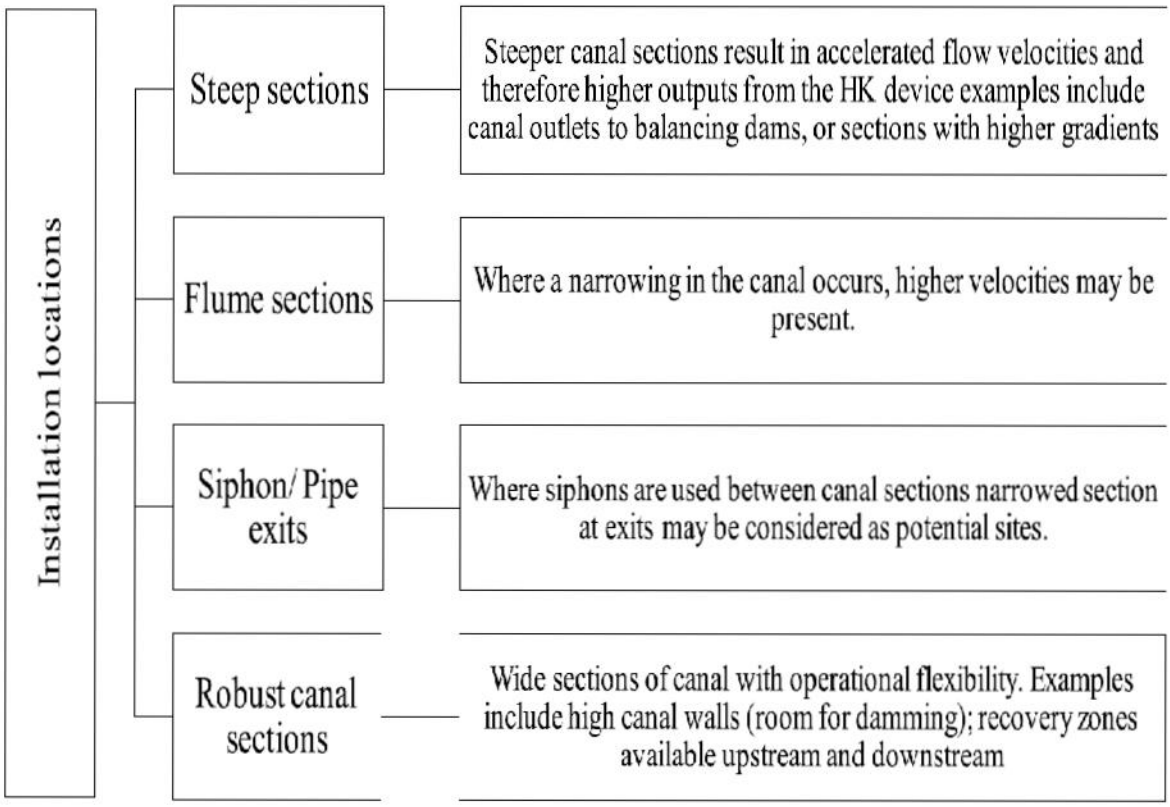


Fig. 3.1. Favourable sections for HKT installation [84].

3.1.2 Field Data Measurement

Under the present work, the canal originating from Ukai Mini Hydro known as Ukai Left Bank Main Canal Surat, Gujarat, India is considered for bathymetric filed data measurement. Fig. 3.2 shows the raw topographic data of the whole canal. This canal is having total length of 121 km and total area of 62225 km^2 covering total of 224 villages across the Gujarat, India [85]. Table 3.1 shows the geometric data of the Ukai left bank main canal. An advance visit was conducted near the area of Ukai Mini Hydro and Ukai left bank main canal in December 2020 to identify suitable sites for discharge measurement, standard method for each measurement (IEC 60041), and necessary site preparation. A number of locations were identified as of potential installation: near to Mini Hydro about 1.5 km (Location-1) and about 3.3 km (Location-2), aqueduct canal near to Ukai thermal power plant (Location-3), near to vadi ashram road (Location-4 and Locaion-5) as shown in Fig. 3.3.

Table 3.1

Geometric data of Ukai left bank main canal [85].

Parameters	Value
Top width of the canal	18.5 m
Top width of the water level	15.5 m
Height of the canal	4 m
Full supply depth of the canal	3 m
Height of the free board	1 m
Bed width of the canal	6.5 m
Side slop of the canal	1.5:1
Discharge capacity of the canal	35 m^3/s (1236 cusec)

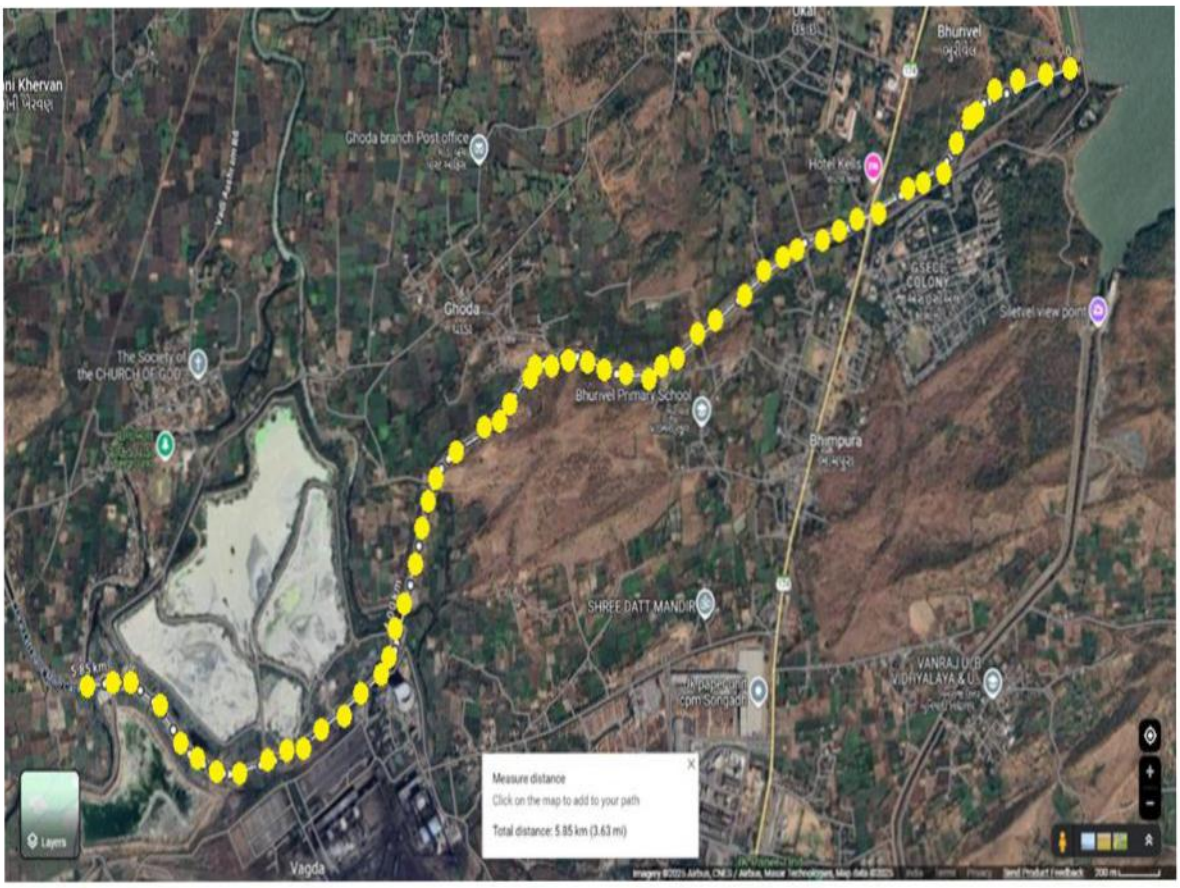


Fig. 3.2. Raw topographic data of the whole Ukai canal.



Fig. 3.3. Different location of Ukai left bank main canal for discharge measurement.

Table 3.2

Qualitative multi-criteria site selection matrix for HKT installation.

Criteria	Location-1	Location-2	Location-3	Location-4	Location-5
Mean flow velocity	Medium	High	High	Medium	Low
Flow uniformity	Low	High	Medium	Medium	Low
Turbulence intensity	Medium	Low	High	Low	Medium
Bed shear stability	Medium	High	Medium	Low	Low
Constructability	High	High	Medium	Medium	High
Debris risk	Medium	Low	High	High	Medium
Operational stability	Medium	High	Medium	Low	Medium

A qualitative multi-criteria assessment was conducted to evaluate potential turbine installation sites based on hydraulic and practical considerations as shown in Table 3.2. In this matrix, "High" represents favourable conditions for turbine performance, while "Low" indicates less suitable conditions. At Location-4, the canal has maximum turbulence as it is connected with drainage. While Locaiton-5 has intermittent flow as it was operated only during the irrigational requirement. The canal alignment is straight from Location-1 to Location-3, and the channel's flow was comparatively disturbance free. Location-2 consistently exhibited favorable conditions, including high flow velocity, uniformity, and operational stability with relatively low turbulence and debris risk, leading to its selection for HKT installation. Therefore, Location-2 was considered to be the ideal location in the canal for in depth analysis of field data. The field measurements were conducted at the Ukai Left Bank Main Canal, Surat, Gujarat, India, during December 2020. The flow velocity measurements were carried out at the selected Location-2 using five propeller current meters (PCMs) (Make National Instruments Corporation, Model No. 1009) to characterize the flow

conditions and identify the suitability of the location for HKT installation. The Ukai left bank main canal has a trapezoidal cross section, therefore the PCM were mounted vertically on cylindrical pipe, set on the equidistance between the water-free surface level and the canal bed, as per the dimensional drawing shown in Fig. 3.4. The velocities were measured by horizontally moving the PCMs mounting structure. A microcontroller-based data logger was used to simultaneously record the readings (number of revolutions) of the PCM. Each PCMs calibration equation had been entered into the data logger. The data logger computes and records the average water velocity at all 37 points along a vertical line at the end of each 120-second integration period. During the measuring procedure, a number of observations were taken at each width in order to average out any random error. It was found that the flow velocities range in between 0.25 m/s and 0.61 m/s. The actual photographic view of the PCM structure and measurement is shown in Fig. 3.5 (a) and (b).

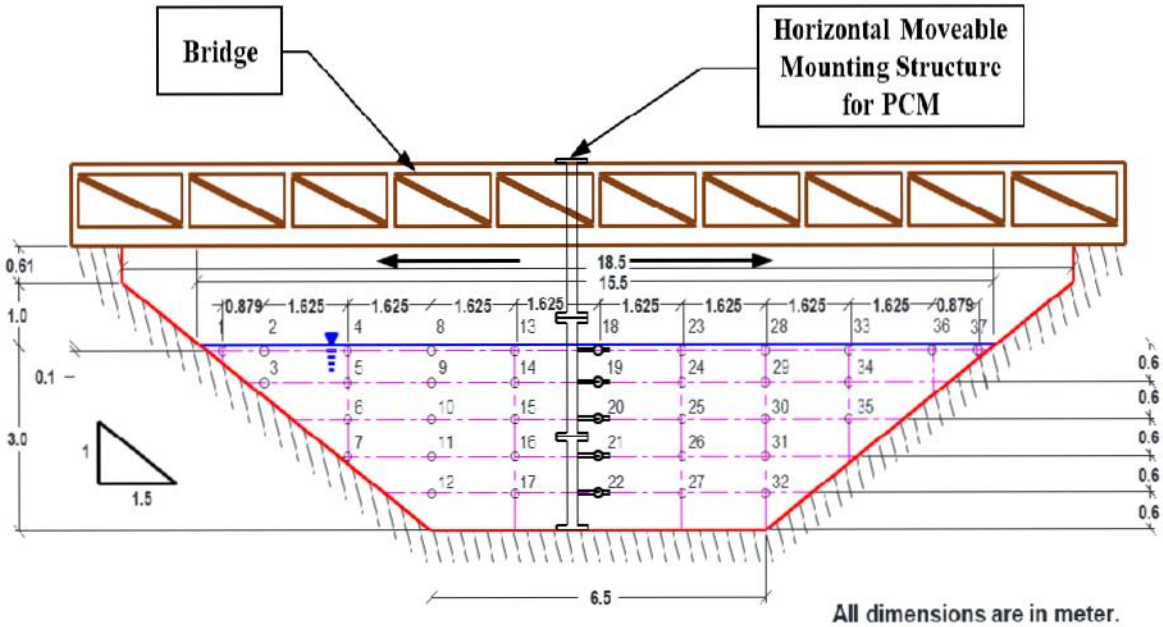


Fig. 3.4. Schematic dimensional drawing of mounting structure for PCMs.

3.1.3 Discharge Measurement

The velocity-area segmentation method [86] was used to determine the discharge based on the velocity measured as per IEC 60041 using PCM as described in Section 3.2. It

was found that the discharge through the canal was 14 m^3/s ($\approx$ 495 cusec). Additionally, the canal's average velocity was 0.42 m/s. An assessment of uncertainty in discharge measurement as per ISO 748:2007 [87] is mentioned in Table 3.3. The total standard uncertainty in discharge measurement was found to be 4.27%.



(a)



(b)

Fig. 3.5. Actual photographic view of the (a) PCM and (b) velocity measurement.

Table 3.3

Standard uncertainty in discharge measurement.

Uncertainty in Discharge Measurement	Standard Uncertainty (%)
Uncertainty due to the width measure	0.15
Uncertainty due to the depth measure	0.65
Uncertainty due to the measurement point number	2.5
Uncertainty due to the PCM measurement duration	10
Uncertainty due to the point velocity measure	1.5
Uncertainty due to the number of verticals	4.2
Total uncertainty	4.27

The velocity profiles have been studied along both vertical and horizontal lines at key velocity magnitude locations as shown in Fig. 3.6. The whole channel width is divided into seven critical points along the vertical lines: the centre (X0), at a distances of 1.625 m, 3.25 m, and 4.875 m to the right of X0 (X1, X2, X3), as well as the same distances to the left (X1', X2', X3'). Additionally, five significant points along the horizontal lines are investigated at 0.6 m (Y1), 1.2 m (Y2), 1.8 m (Y3), 2.4 m (Y4), and 3 m (Y5) water depth above the canal bed. Longitudinal velocity along water depth at the different vertical lines is drawn in Fig. 3.7. It can be seen as velocity reaches a maximum value at the water's surface from zero at the channel's inversion. The maximum average velocity of 0.4460 m/s was obtained at location X1 while minimum average velocity was 0.1990 m/s at X3. Similarly, longitudinal velocity along width of canal at the different horizontal lines is depicted in Fig. 3.8. At the free water's surface (Y5), the maximum velocity was found to be 0.61 m/s at middle of the width of the canal (X0). At the location Y1 to Y4 as we move towards the X3 point from the centre line X0, the maximum velocity was obtained. This can be understood as in this region the canal has bend due to which the more centrifugal effect is observed.

Furthermore, as we move towards the Y5 (free water surface), the region of velocity distribution is increased accompanied along the width of the canal.

To assess the potential HKT site selection, the obtained results are compared against the various turbulence models' predictions and maximum velocity region was determined in further sections.

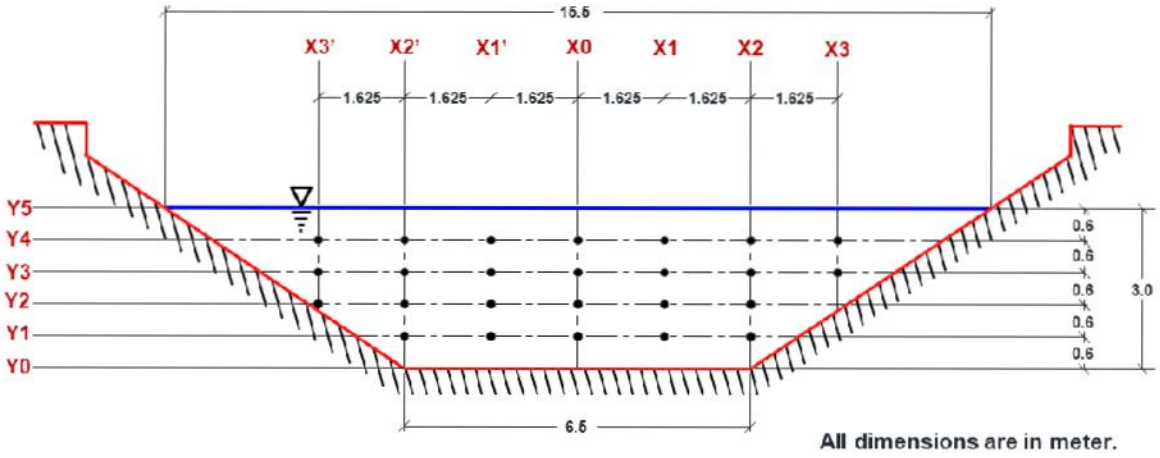


Fig. 3.6. Locations of vertical and horizontal lines selected for velocity measurements in the canal.

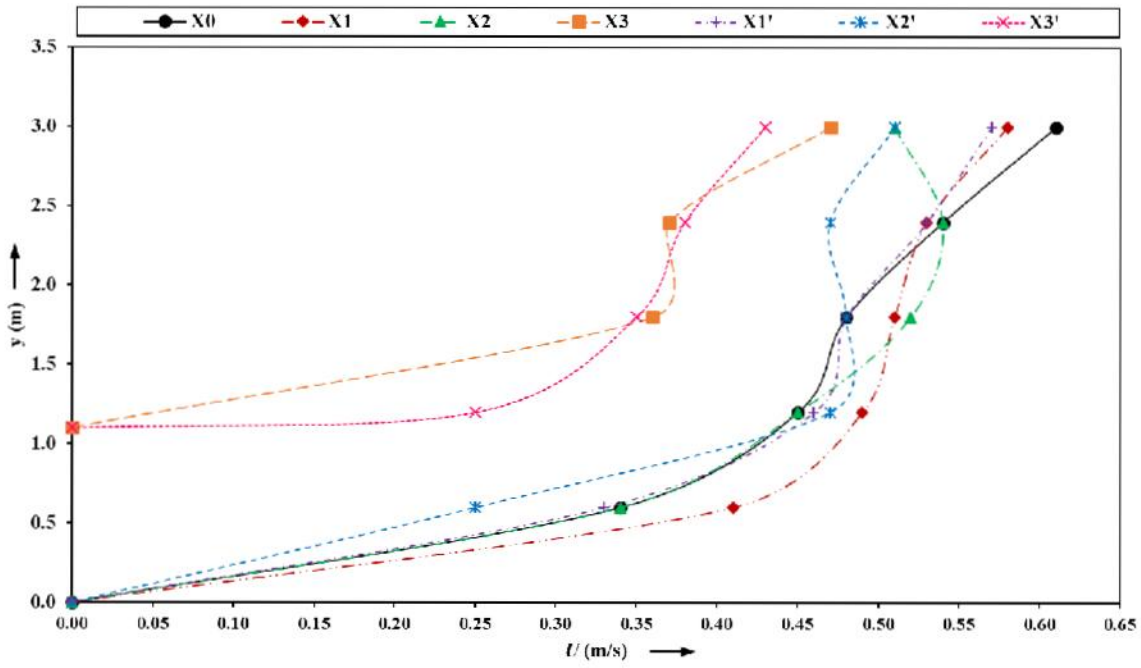


Fig. 3.7. Longitudinal velocity along water depth at the different vertical lines.

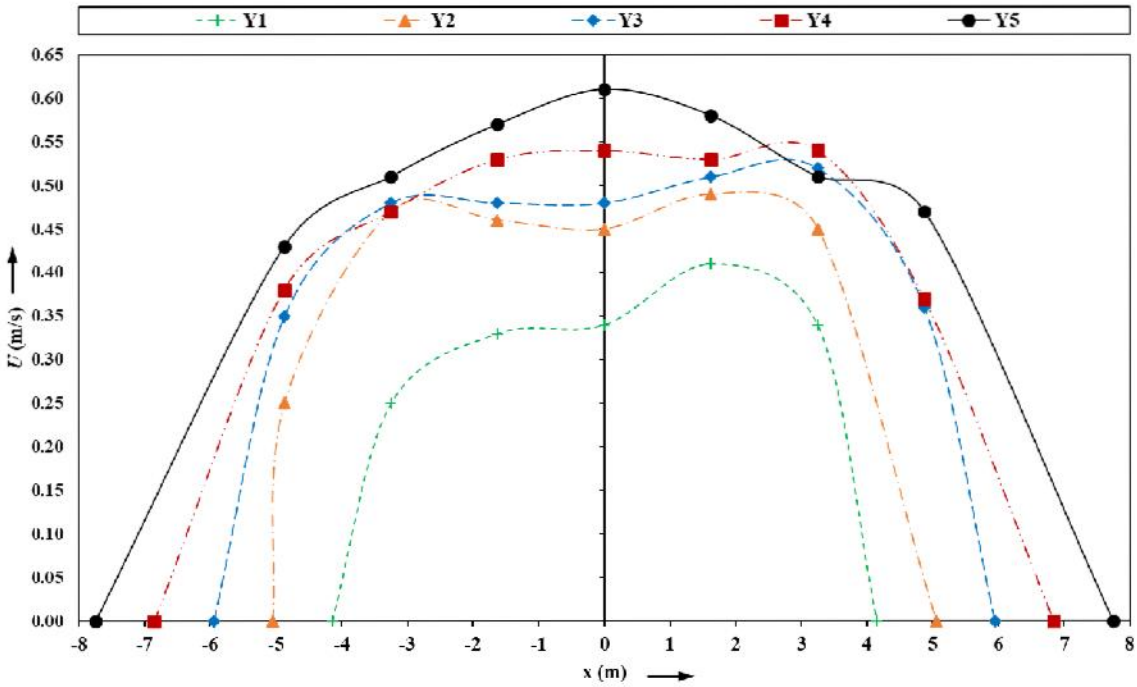


Fig. 3.8. Longitudinal velocity along width of canal at the different horizontal lines.

3.2 Numerical Methodology

Creating the computational domain, dividing it into smaller areas for solving the equations, choosing appropriate boundary conditions, and allocating appropriate values to modelling parameters are prerequisites for carrying out numerical simulation.

3.2.1 Geometry

In this study, 3-D model of canal was constructed and verified by experimental test. ANSYS 2020 R1 "Design Modeler" was used to create a 3-D computational stationary domain of canal using the parameters specified in Fig. 3.9. The channel's width, depth, and lengths are taken into account in the X, Y, and Z directions, respectively. A 3-D computational stationary domain of a canal's material is considered as fluid domain. After the domain is constructed, the geometry is given the proper domain names to suit the respective boundary conditions. This process is called "physics module setup". These domains are identified as Inlet, Canal Bed, Canal Side Wall, Water Free Surface, and Outlet as shown in Fig. 3.10.

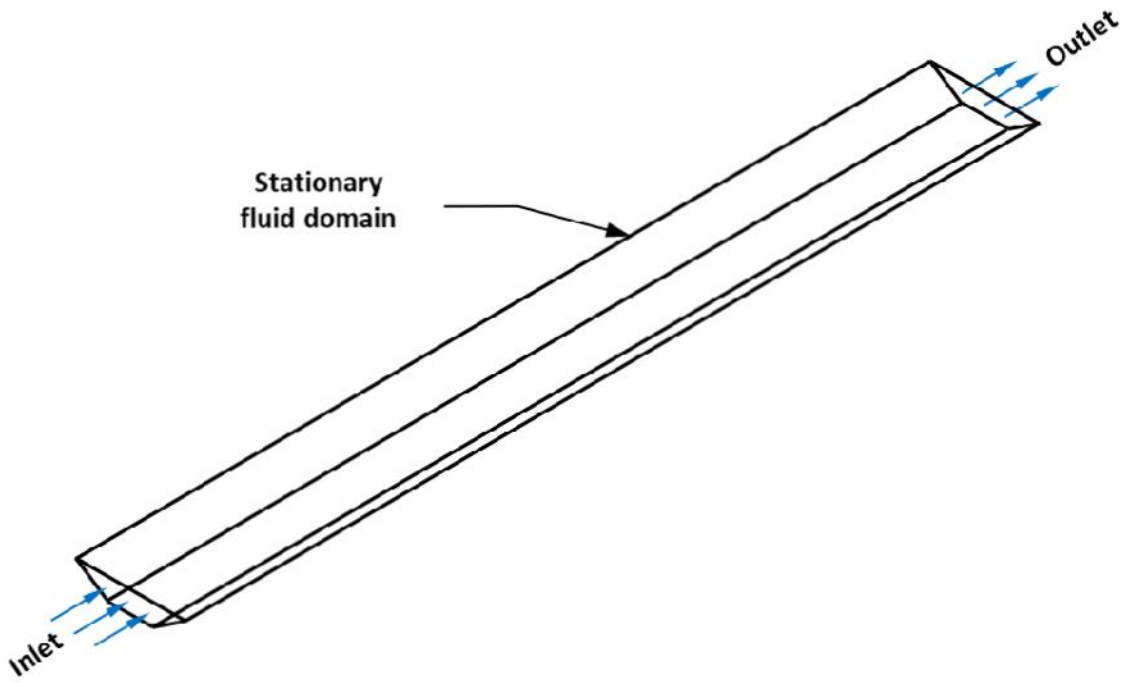


Fig. 3.9. 3-D Computational stationary fluid domain of the canal.

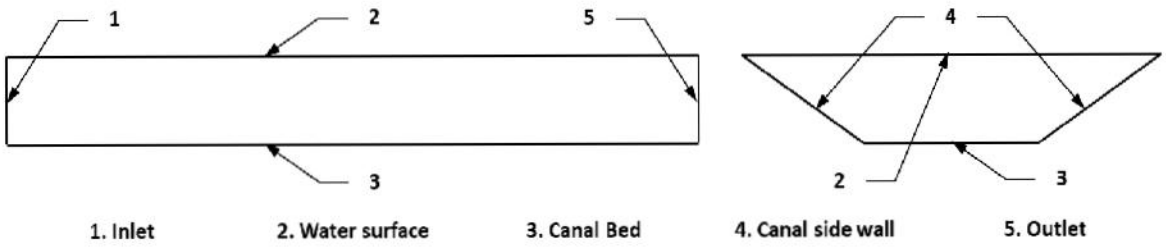
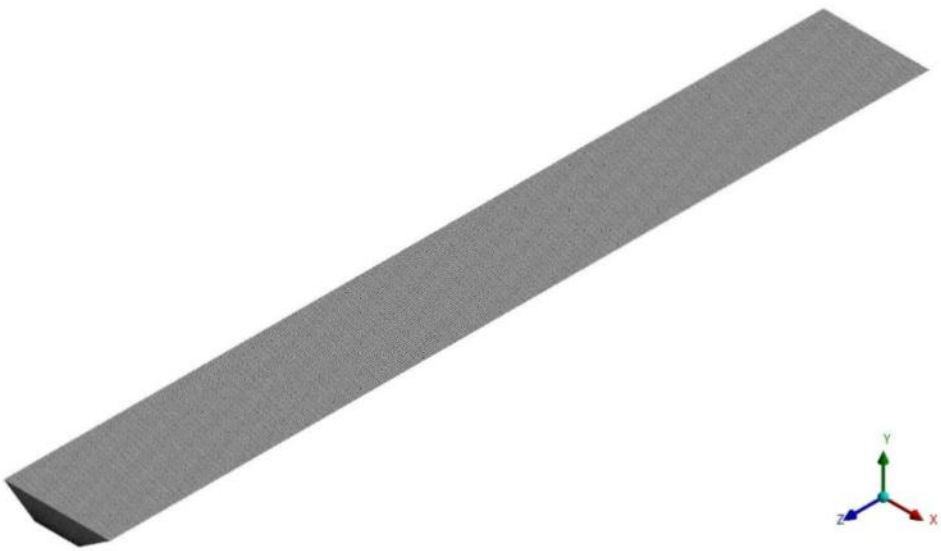


Fig. 3.10. Different views of 3-D Computational stationary fluid domain.

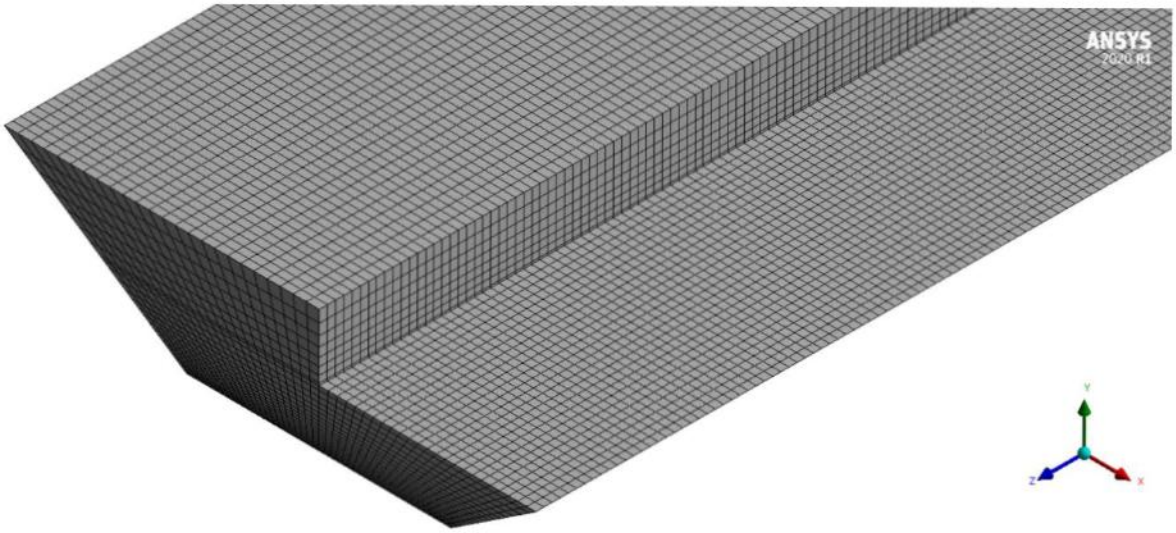
3.2.2 Meshing of Computational Domain

The convergence and stability of the numerical solution depend on the construction of an appropriate computing mesh. To apply the partial differential equations governing fluid flow to each subdomain and solve them using one of the three methods - finite volume, finite element, and finite difference, meshing entails dividing the fluid domain into smaller sub-domains. An estimated solution of the entire fluid domain is then generated by assembling the solutions found in each of the domain's cells. The finite volume approach is the foundation of ANSYS MESH. The final 3-D computational fluid domain meshing of canal was depicted in Fig. 3.11 (a). As shown in cut section of canal Fig. 3.11 (b), a structured

mesh with hexahedral elements was taken into account to produce mesh for the entire flow domain. The structured hexahedral mesh offers better accuracy for viscous calculations because it can handle cells in the boundary layer with extremely high aspect ratio cells [88,89]. The edge meshes were generated on the side wall of the domain depicted in Fig. 3.11 (c). Computational cell sizes are reduced in the vicinity of the canal bed and side walls to produce more accurate findings. In the interior areas of the channel, the cell sizes are larger. Grid independence test was performed on the entire domain using six different mesh elements: 806400, 1029672, 1395324, 1978200, 2548980, and 3186680. According to the findings, a grid element was defined as an estimated 1395324 elements, beyond which the discharge varied small. Grid independence test was performed on the entire domain using six different mesh elements as shown in Fig. 3.12. According to the findings, an estimated 1.39 million grid elements were selected for the study beyond which the discharge varied very small. Mesh refinement was applied near the bed and side walls to capture boundary layer effects. Also, the skewness of 0.29 with orthogonal quality of 0.86 was obtained for selected elements. Consequently, the y+ value in this research is regarded as being around at one.



(a)



(b)



(c)

Fig. 3.11. 3-D computational fluid domain meshing (a) whole canal (b) cut section (c) edge meshing of canal side wall.

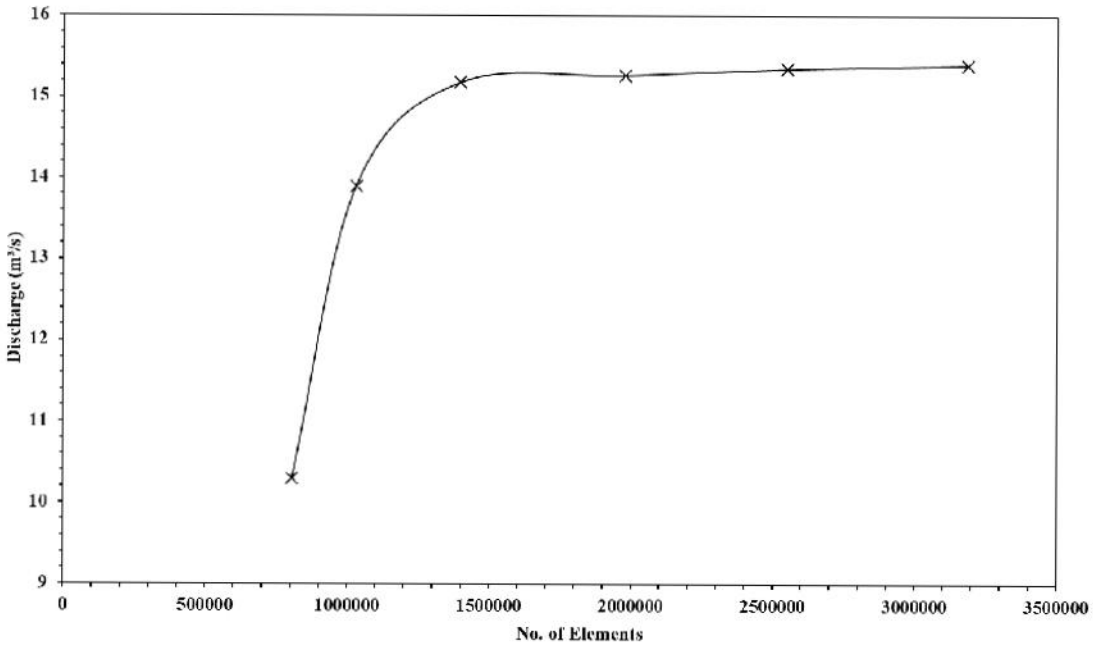


Fig. 3.12. Grid independency test.

3.2.3 Boundary Conditions

Considering the steady state flow of water, a uniform velocity inlet was specified at the inlet, while a pressure outlet condition was applied at the outlet. Both the canal side walls and the bottom of the model (canal bed) had walls as their boundary condition, and it was considered that these walls were stationary. The moving wall was used as a boundary condition on the top surface of the model (water surface), representing steady free-surface flow conditions. With the use of a finite volume discretization method, steady incompressible N-S equations were solved using ANSYS FLUENT, where the resulting mesh is imported, as a flow solver. In the case of water flow, turbulence was seen as critically important and needs to be properly accounted for. Several models are available to address the turbulence issue in the simulation. Therefore, selecting an appropriate turbulence model is necessary. For analysing all the gradients, the cell based least-squares approach is taken into consideration. For all residual of the momentum, continuity, and turbulence equations, the convergence conditions were set up as 1×10^{-5}.

3.2.4 Turbulence Models

In this investigation, $k-\varepsilon$ Standard, $k-\varepsilon$ RNG, $k-\varepsilon$ Realizable, $k-\omega$ Standard and $k-\omega$ SST turbulence models were employed. Using a 2^{nd} order upwind scheme for all convection terms, such as the momentum equation, turbulent dissipation rate, turbulent kinetic energy, and a SIMPLE pressure-velocity coupled solver, the CFD investigation was performed out in order to obtain results that are more accurate.

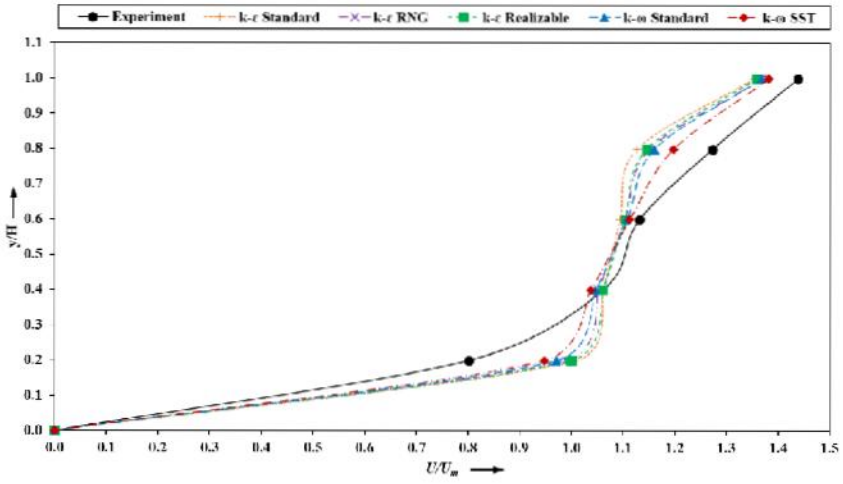
3.3 Results and Discussion

This section presents and discusses comprehensive numerical results. The validation of different turbulence models' results is done against the experimental results. The flow parameters like longitudinal depth and width velocity, depth averaged velocity and secondary current are presented along with the velocity vectors. The statistical error analysis

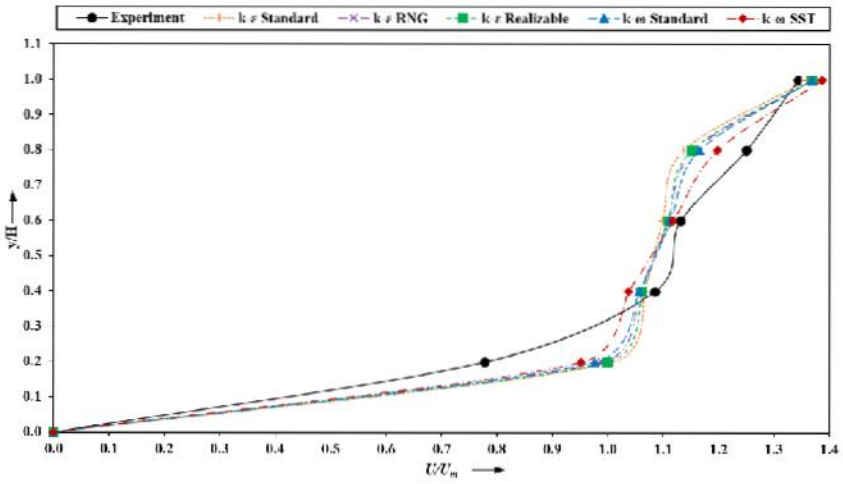
is also included for predicting its effectiveness accordance to the data.

3.3.1 Longitudinal Velocity Profile along the Water Depth

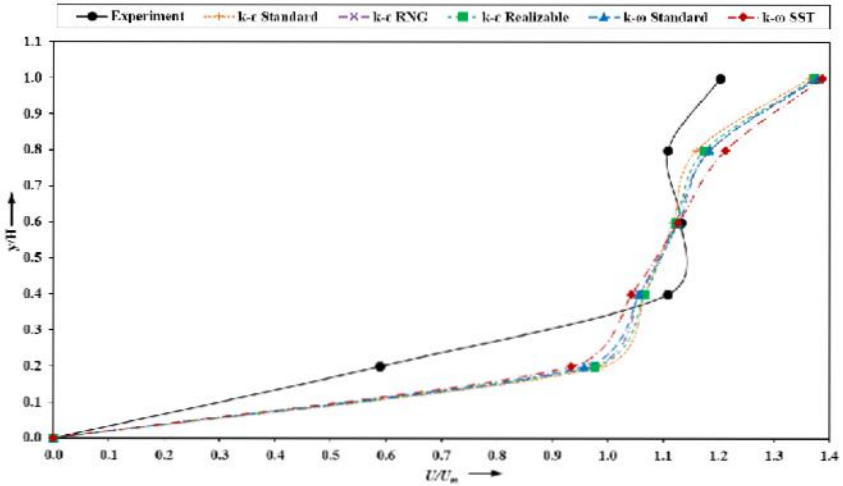
For a better understanding of the change in velocity across the flow depth of a canal, longitudinal velocity profiles for each of the turbulence models are discussed in this section with a comparison of the experimental and numerical results. Seven vertical locations (X3', X2', X1', X0, X1, X2, X3) at outlet of domain are selected to plot these profiles. The ratio of local longitudinal velocity to the mean flow velocity ($^{U}/_{U_m}$) is taken into account for dimensionless analysis. The results of the $^{U}/_{U_m}$ along water depth for seven different vertical sections are shown in Fig. 3.13 (a) to (g) respectively. It has been observed that the deviation for all turbulence models results from experimental one is least at the mid-water depth region while it is larger for lowest water depth at all vertical locations. Furthermore, in compare to all locations along the water depth, X0 location (at centre) has least variation in the velocity profile while, the X3 and X3' locations have the most amount of error. This can be understood as at the centre location X0, the wall effects are not considered in compare to the extreme end locations X3 and X3'. Also the actual canal is found to be slightly curved in the experimental study, while the canal domain modelled as straight domain in the numerical study. From Figs. 12 to 18, it is observed that the $k-\omega$ SST model is predicting the accurate longitudinal velocity profiles in all the vertical positions followed by $k-\omega$ standard, $k-\varepsilon$ realizable, $k-\varepsilon$ RNG and $k-\varepsilon$ standard. The isotropic nature of the turbulent fluctuations is a drawback of the k–ε standard model. As a result, the $k-\varepsilon$ standard model produces inaccurate predictions in turbulent fluid flows [90,91]. The $k-\omega$ SST model is the blend of $k-\omega$ standard model and the $k-\varepsilon$ model. Now, the standard $k-\omega$ model accurately predicts the flow near canal wall and the $k-\varepsilon$ model precisely simulates the flow away from the canal wall and bed.


Experiment
k-ε Standard
k-ε RNG
k-ε Realizable
k-ω Standard
k-ω SST
y/H
U/U∞

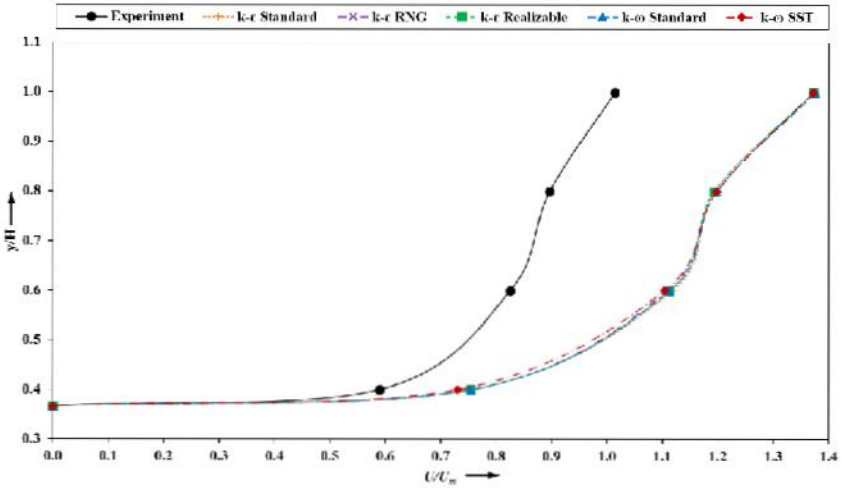
(a)


Experiment
k ε Standard
k ε RNG
k ε Realizable
k ω Standard
k ω SST
y/H
U/U∞

(b)


Experiment
k-ε Standard
k-ε RNG
k-ε Realizable
k-ω Standard
k-ω SST
y/H
U/U∞

(b)


Experiment
k-ε Standard
k-ε RNG
k-ε Realizable
k-ω Standard
k-ω SST
y/H
U/U∞

(d)

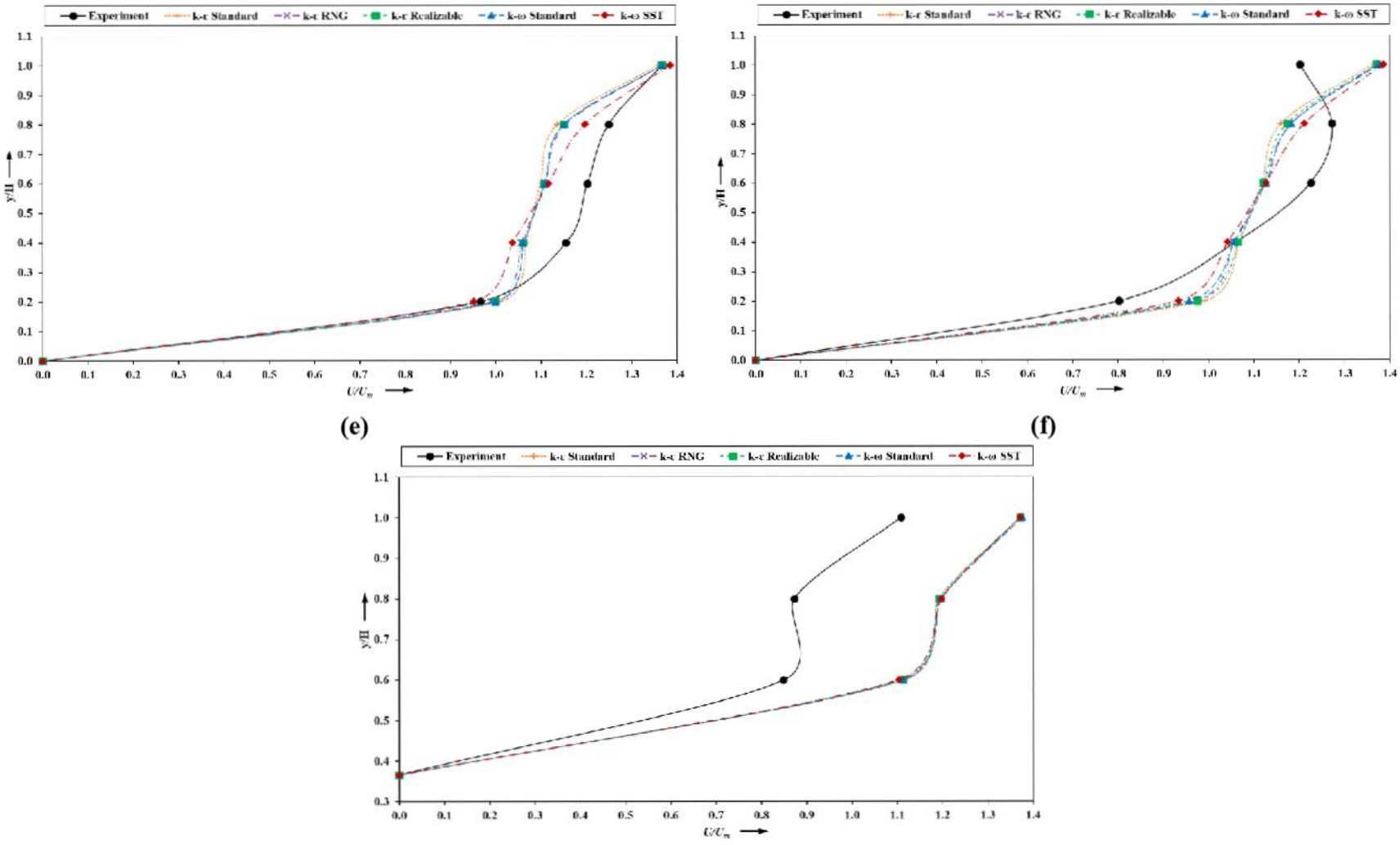
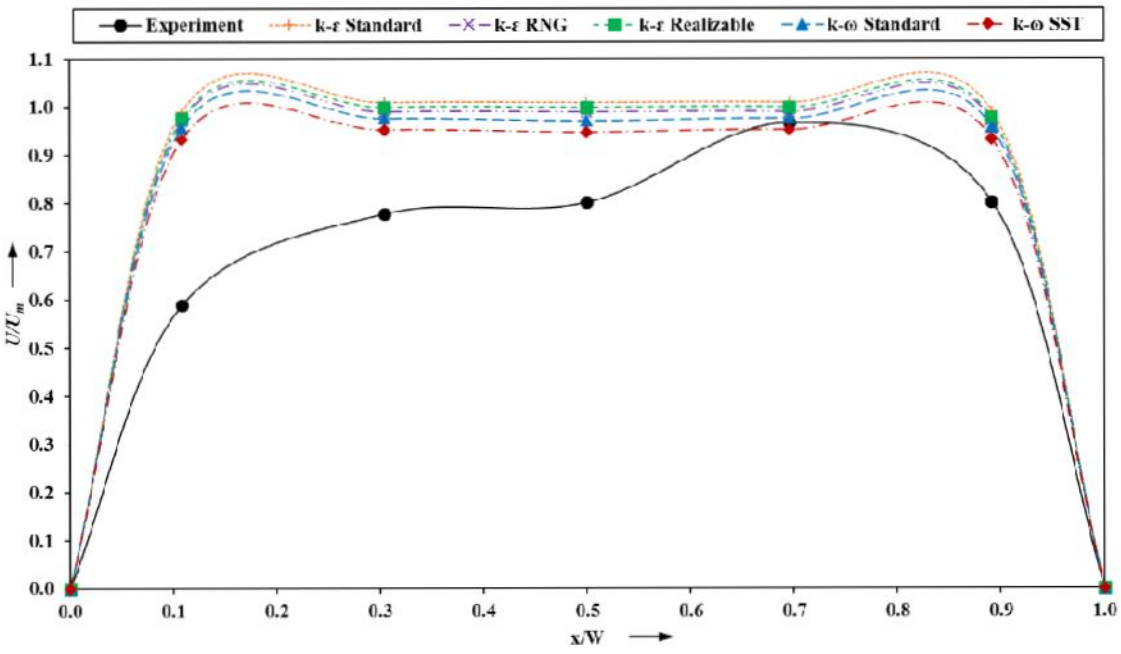


Fig. 3.13. Longitudinal velocity profile at (a) X0, (b) X1', (c) X2', (d) X3' (e) X1, (f) X2, (g) X3.

3.3.2 Longitudinal Velocity Profile along the Canal Width

When attempting to get a knowledge of the flow characteristics of the canal flow, it is helpful to conduct an investigation into the velocity profile along the canal width. It can also provide information about the flow behaviour, including the existence of turbulent areas, eddies, and other characteristics that influence the flow characteristics. The simulation results of the longitudinal velocity profile carried out throughout the canal width are shown in Fig. 3.14 (a) to (e), which include five different water depth compared with experimental results. In comparison to other turbulence models, the $k-\omega$ SST model is capable of accurately forecasting longitudinal velocity profiles at Y1, Y3, Y4, and Y5 horizontal positions, while the $k-\varepsilon$ realizable model predicts the velocity profile at the Y2 position more accurately with experimental results. When applied to a boundary layer or separated flows, a $k-\varepsilon$ realizable turbulence model performs more effectively. The coefficient of the $k-\varepsilon$ realizable model is provided in an approach that is dependent on the properties of turbulence and mean flow.



(a)

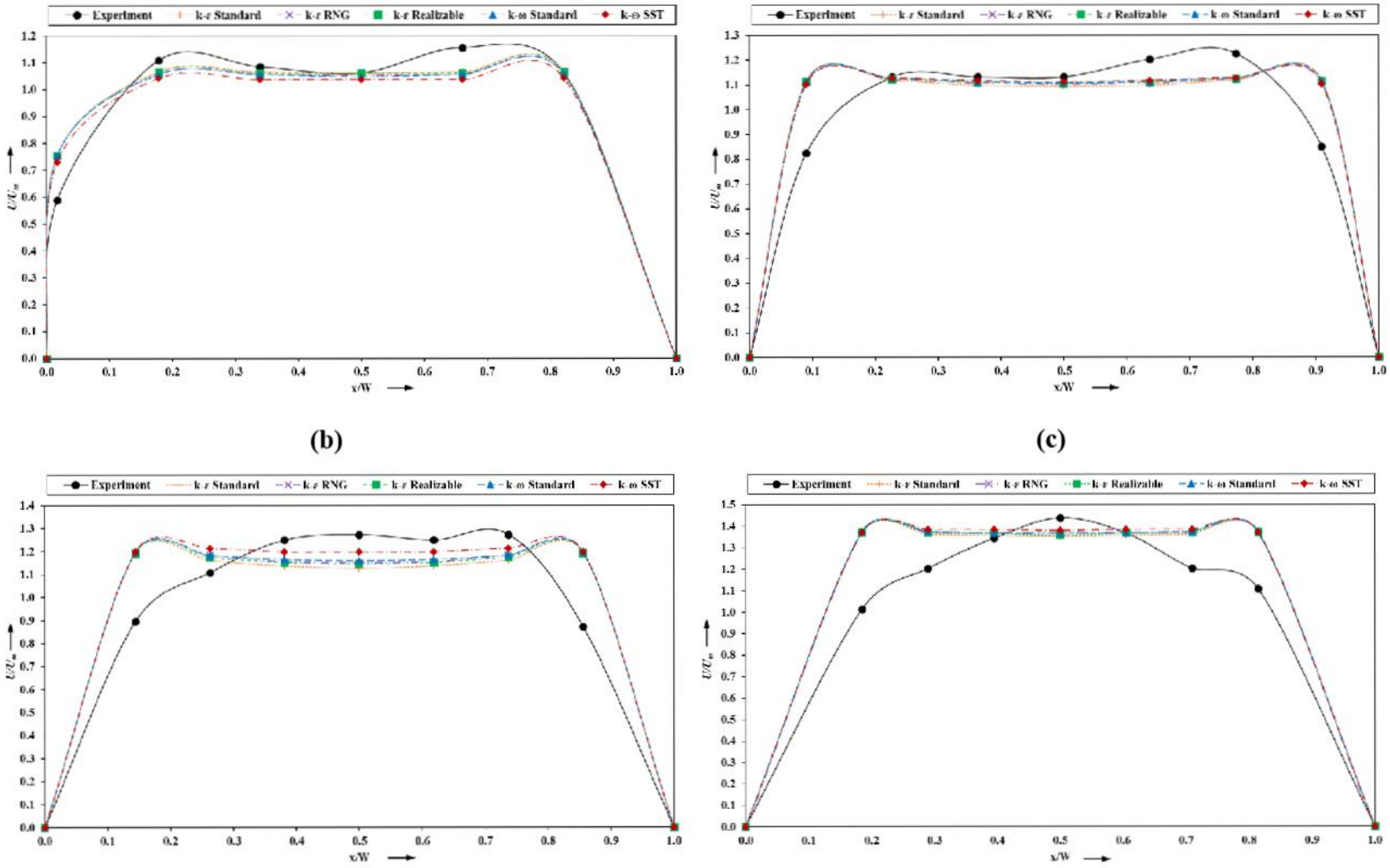
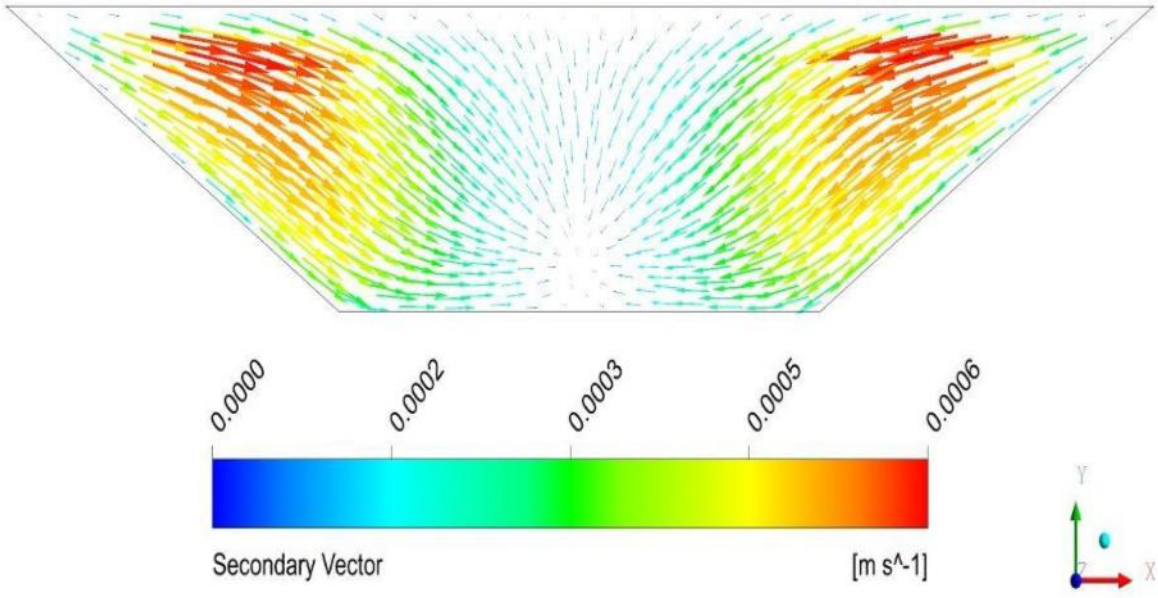


Fig. 3.14. Longitudinal velocity profile at (a) Y1, (b) Y2, (c) Y3, (d) Y4 (e) Y5.

3.3.3 Secondary Flow Vector Plot at XY Plane

The calculation of secondary flow vectors involves the use of the equation $\sqrt{{u_m}^2 + {v_m}^2}$, where u_m represents the mean lateral velocity (in X direction) and v_m represents the mean vertical velocity (in Y direction). This secondary flow resists the longitudinal velocity of fluid in Z direction. In Fig. 3.15, the outcomes of secondary flow vectors are shown for different turbulence models. All turbulence models estimated the greatest magnitude to be around 0.0006 m/s. It is observed that the canal trapezoidal cross-section results in the formation of two secondary current vortices converging towards the canal mid-section. The maximum momentum fluid has been carried from the side walls towards the canal's centre by these two pair of vortices. However, high secondary velocity magnitudes are seen at a considerable distance from the canal's midsection and free surface. This indicates the development of secondary currents, leading to the velocity dip phenomenon. Near to the side walls, the intensity exhibits a significant increase, and the secondary currents are directed downward as a result of the resistance presented by the side walls.



(a)

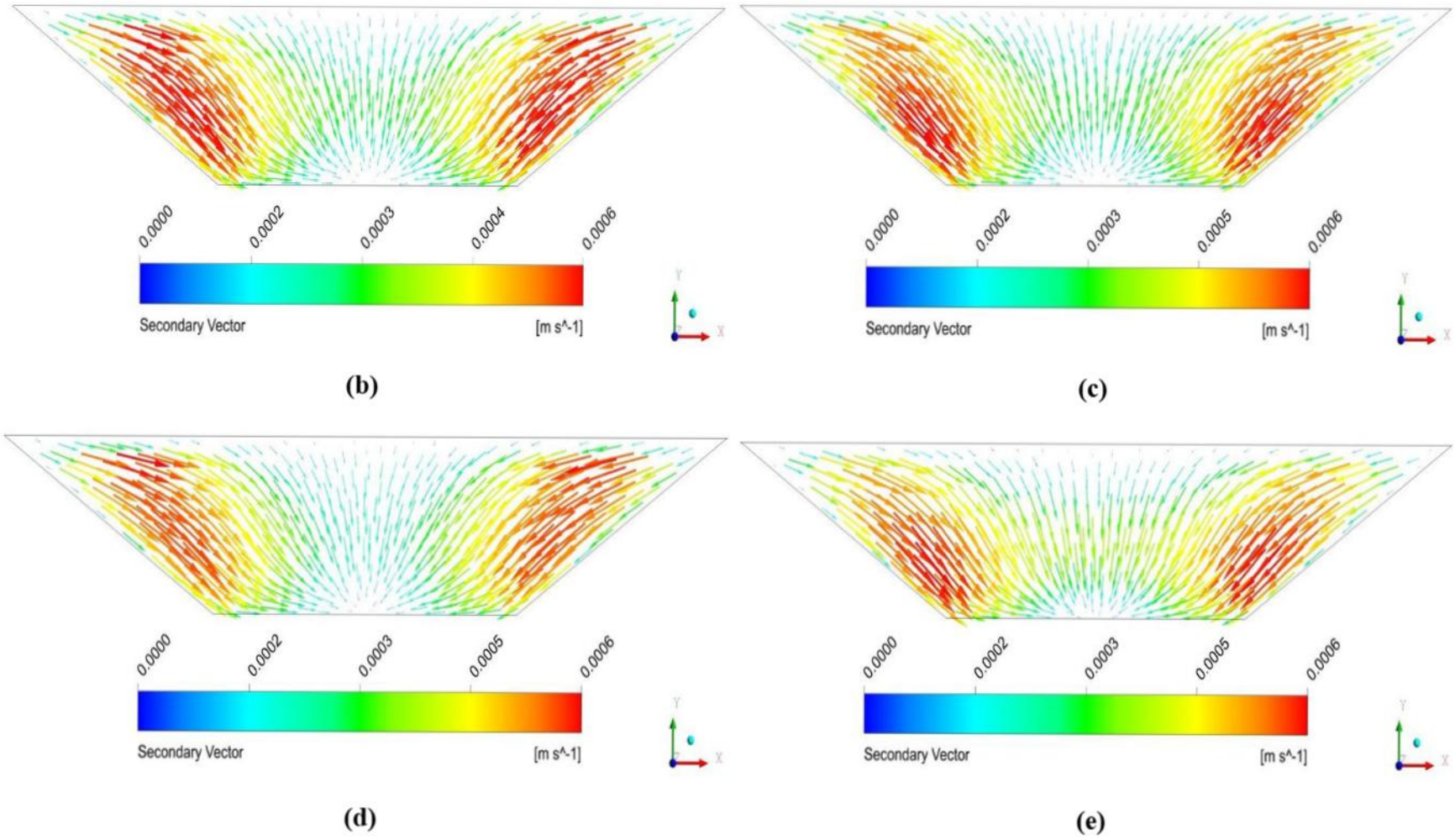
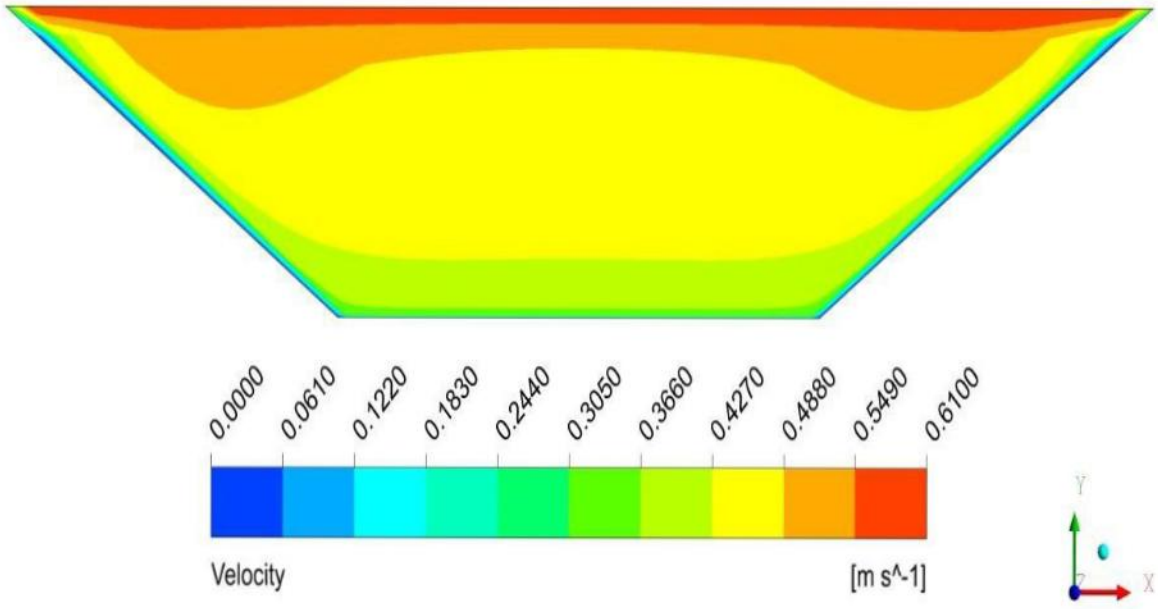


Fig. 3.15. Secondary flow vector at outlet for (a) $k-\varepsilon$ Standard, (b) $k-\varepsilon$ RNG, (c) $k-\varepsilon$ Realizable, (d) $k-\omega$ Standard and (e) $k-\omega$ SST.

3.3.4 Velocity Contour and Water Power Density

Based on the simulation results, Fig. 3.16 shows velocity contour at outlet while Fig. 3.17 shows the water power density available at canal cross section by various turbulence models. It is observed that the longitudinal flow velocity and power density was found to be maximum near the water surface region, while both the values decrease at the canal's side wall and bed. This is because the longitudinal flow's velocity interacts with the wall, creating friction and causing the wall to experience shear stress. The highest values after the water free surface are observed at two points equally spaced from the midpoint towards the wall, and the profiles do not feature many significant gradients. The accuracy of predicting the velocity and power density at various locations is found to be more in case of $k-\omega$ SST model in compare to the other models. This can be understood as in other model prediction less contour lines are found in compare the more contour lines for $k-\omega$ SST model. The assumptions and model constants used to model shear stress terms account for the variations in velocity output produced by various models.



(a)

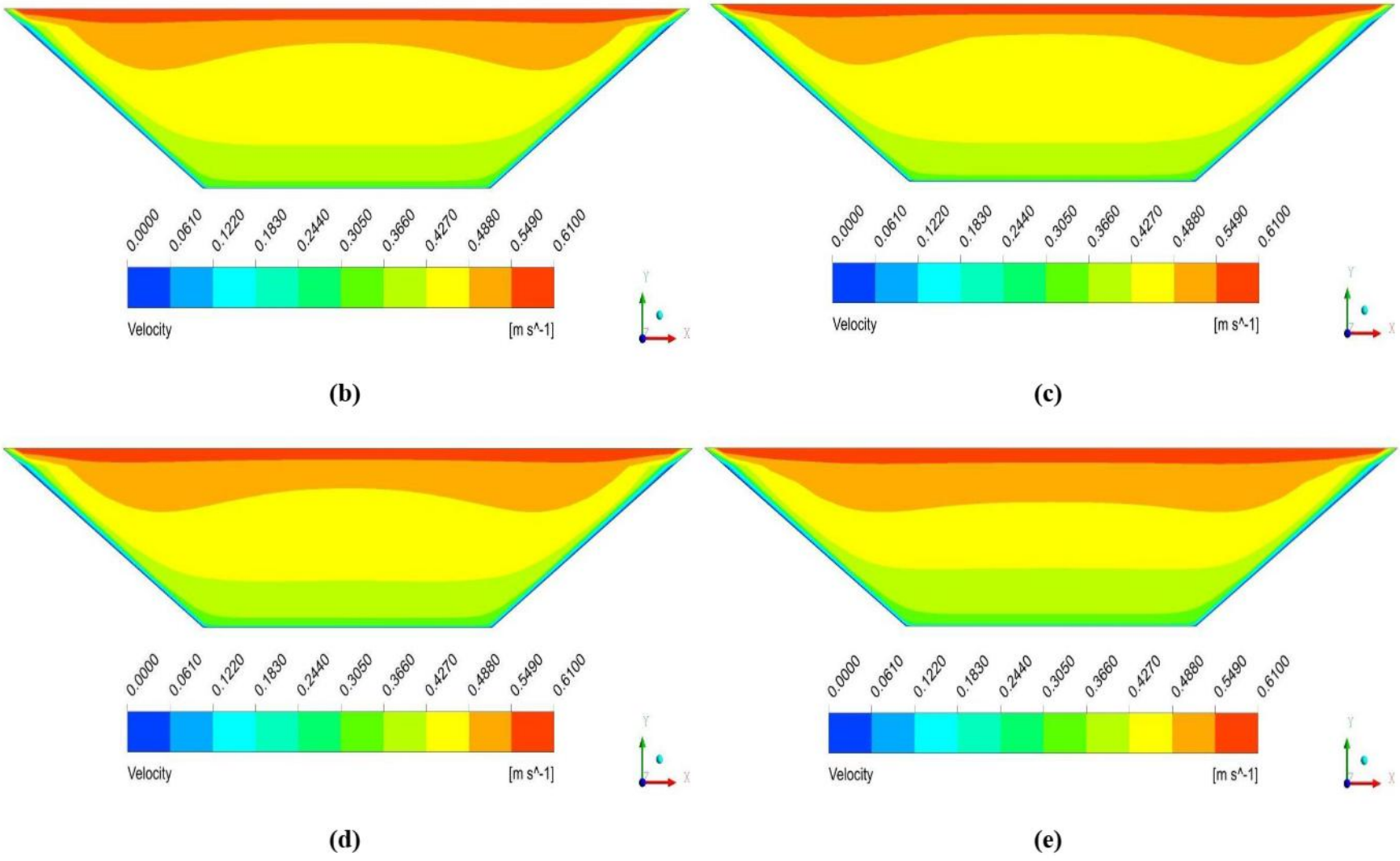
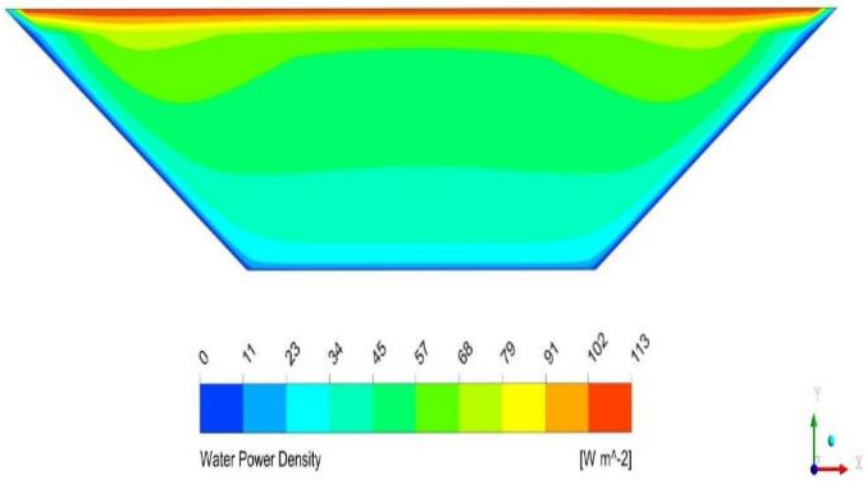
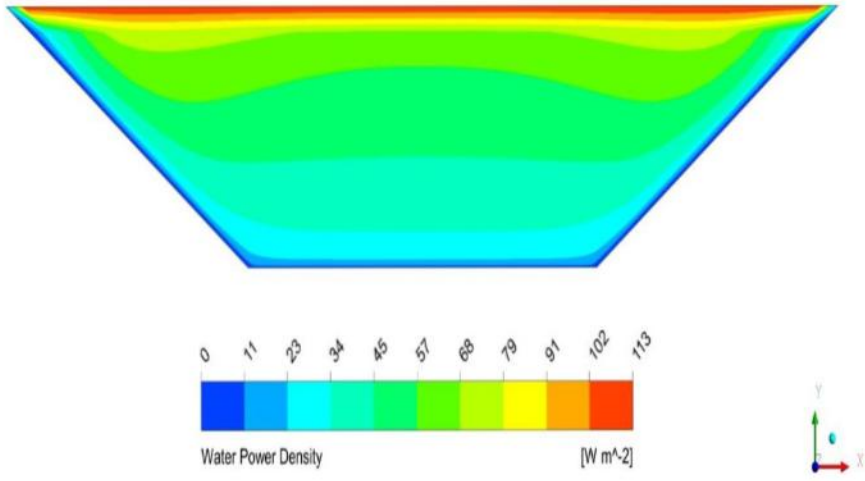


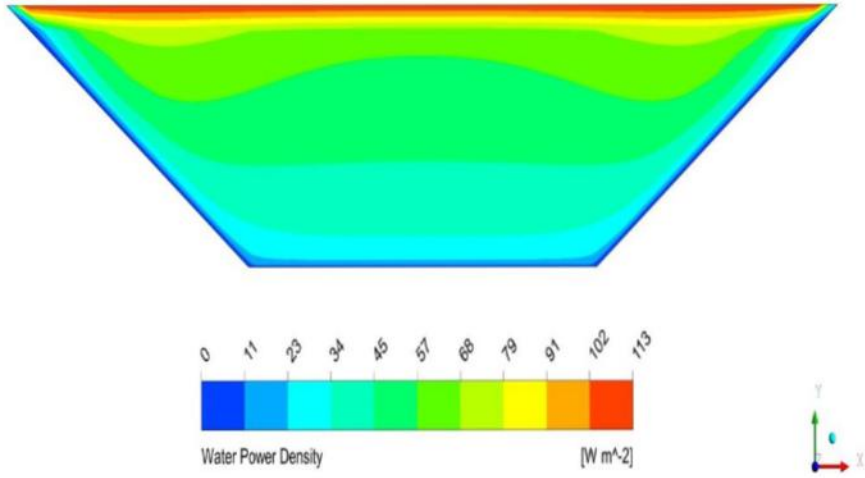
Fig. 3.16. Velocity contour at outlet for (a) $k-\varepsilon$ Standard, (b) $k-\varepsilon$ RNG, (c) $k-\varepsilon$ Realizable, (d) $k-\omega$ Standard and (e) $k-\omega$ SST.


0 11 23 34 45 57 68 79 91 102 113
Water Power Density
[W m^-2]

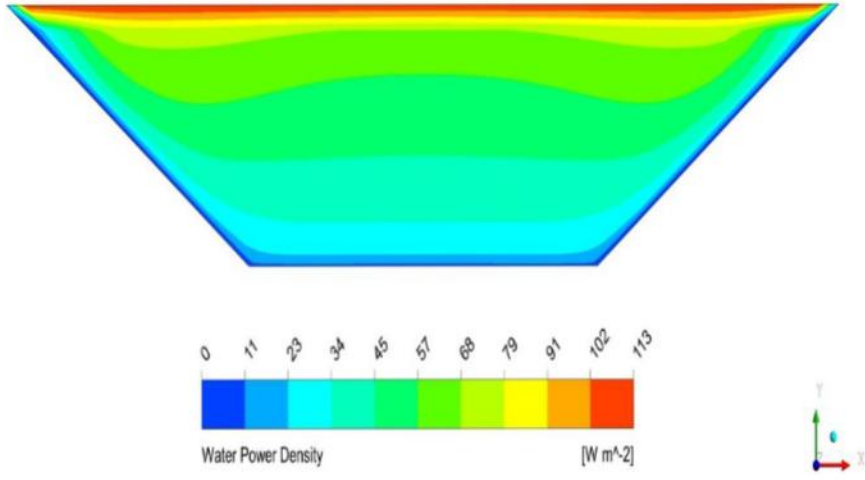
(a)


0 11 23 34 45 57 68 79 91 102 113
Water Power Density
[W m^-2]

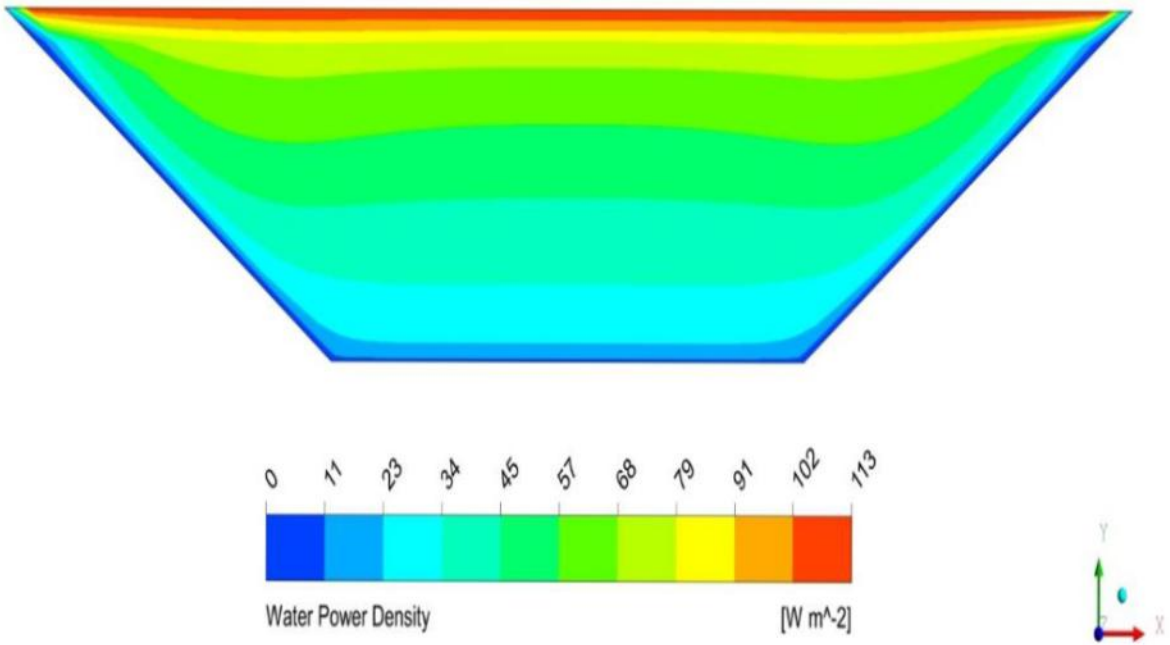
(b)


0 11 23 34 45 57 68 79 91 102 113
Water Power Density
[W m^-2]

(c)


0 11 23 34 45 57 68 79 91 102 113
Water Power Density
[W m^-2]

(d)



(e)

Fig. 3.17. Water power density for (a) $k-\varepsilon$ Standard, (b) $k-\varepsilon$ RNG, (c) $k-\varepsilon$ Realizable, (d) $k-\omega$ Standard and (e) $k-\omega$ SST.

3.4 Potential Region for Hydrokinetic Turbine Installation

Based on the various longitudinal velocity profiles along the width and depth, the $k-\omega$ SST models predict the better results with least errors at all locations. To identify the initial HKT study site among the various locations, the rectangular region of 1.8 m water depth (Y5 to Y2) and 6.5 m length (X2' to X2) was considered for potential site as shown in Fig. 3.18. In this region, the $k-\omega$ SST model predicts the maximum average velocity of 0.50 m/s while the experimental measured value was 0.42 m/s. As per the data measured throughout the year, the canal's water potential was accessible all year round [85]. There will be approximately 25% greater velocity available, i.e., 0.64 m/s, during periods of high demand which is higher than the HKTs preferred site installation velocity of 0.5 m/s [92]. Further, $k-\omega$ SST model suggests the secondary vector value of 0.0002 m/s in compare to the other region having 0.0005 m/s. This indicates that suggested potential region can allow complete free flow of water in longitudinal direction. In addition, the numerical simulation predicts that the available power density for potential region is found to be 63 W/m^2 with the power generation of 1.2 kW. Table 3.4 provides the details of the various HKT manufacturers installed across the world, their turbine types, rated power generation capacity and respective rated velocity. To install the same HKT at selected location, the number of turbines required needed is also appended in the Table 3.4.

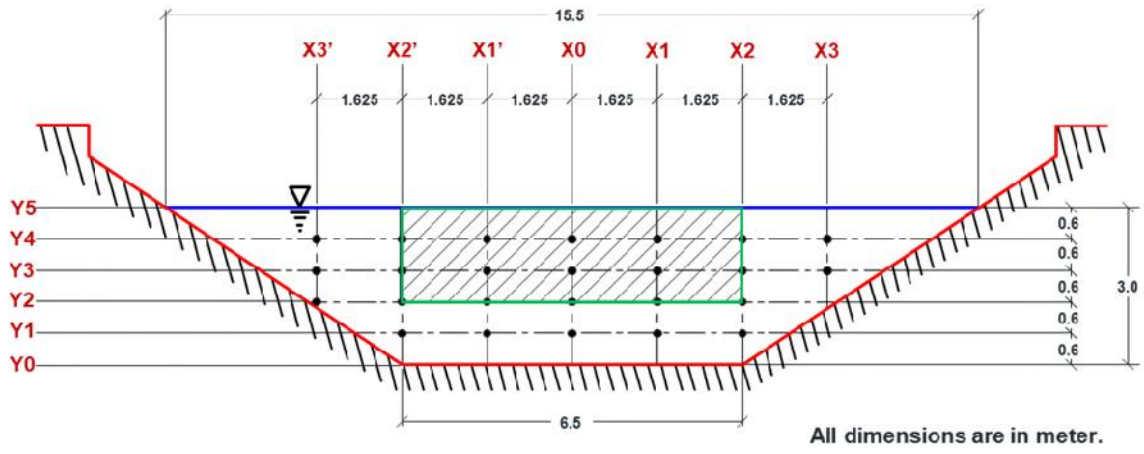


Fig. 3.18. The maximum potential region.

Table 3.4

Possible HKTs installation for given potential region.

Sr. No.	Manufacturer	Type of Flow	Type of Turbine	HKT Location	U_m (m/s)	$P_{turbine}$ (kW)	No. of Turbines Required at Potential Site for Required Power Generation	References
1	Smart Duo float	Axial	--	Neiva, Colombia	1.7	1.1	2	[93]
2	Smart Freestream	Axial	--	Roseheim, Germany	3.1	5	2	[93]
3	Guinard Energies	Axial	--	Gironde estuary, France	1	3.5	1	[94]
4	Hydro quest River	Cross	Darrieus	Paimpol-Bréhat, Brittany	3.1	40	3	[95]
5	Enviro Gen Series	Cross	H-Darrieus	Manitoba, Canada	3	5	1	[96]

Sr. No.	Manufacturer	Type of Flow	Type of Turbine	HKT Location	U_m (m/s)	$P_{turbine}$ (kW)	No. of Turbines Required at Potential Site for Required Power Generation	References
6	Instream Energy System	Cross	H-Darrieus	Yakima, Washington	3	25	3	[97]
7	ORPC Riv Gen	Cross	Darrieus	--	2.3	15	2	[98]
8	Waterotor Energy Tech	Cross	SHKT	Ottawa, Canada	0.8	1.1	1	[99]
9	Helios Altas	Cross	--	Balingasa, Philippine	1.8	0.5	1	[100]

3.5 Statistical Error Analysis

Error analysis is the study of evaluating the uncertainty associated with a various turbulence models to predict its effectiveness in relation to the experiment data. A variety of statistical error studies, including mean percentage error (MPE) and root mean square error (RMSE), were used in the current investigation in order to evaluate the effectiveness of the turbulence models. The following formulas are used to compute the errors [101]:

$$MPE\ (\%) = \frac{100}{n}\sum_{i=1}^{n}\left(\frac{U_{m_{model}} - U_{m_{exp}}}{U_{m_{exp}}}\right) \tag{3.18}$$

$$RMSE\ (\%) = \sqrt{\frac{1}{n}\sum_{i=1}^{n}\left(U_{m_{model}} - U_{m_{exp}}\right)^2} \tag{3.19}$$

The range of MPE errors for the different turbulence models is between 0.90% and 0.96%, while the range of RMSE errors among them is between 6.00% and 6.40%. The numerical results show that the $k-\omega$ SST turbulence model produces the close agreement between numerical and experimental results. The results from the $k-\omega$ SST turbulence model indicate that the MPE and RMSE are approximately 0.92% and 6.13%, respectively. The error range was reasonable with other research investigations that had been published in the literature [23,24,89,102]. Hence, there was an acceptable error in the good agreement between the numerical and experimental data. The individual error for each location prescribed in Fig. 3.6 is included in Appendix B.

In summary, this chapter presented the experimental field investigation and numerical analysis of the flow characteristics of the Ukai Left Bank Main Canal for identifying a suitable HKT installation site. The field measurements provided the velocity distribution and discharge characteristics of the canal, while the numerical investigation enabled a comparative assessment of different turbulence models. Among the considered models, the k–ω SST model provided comparatively better predictions of the measured flow

characteristics. Based on the velocity distribution, secondary flow behavior, and water power density, a potential region for HKT installation was identified. The selected site provided the representative canal flow conditions and hydrokinetic potential required for the subsequent investigation. Therefore, the obtained canal flow characteristics and selected HKT installation region are utilized in the next chapter for the comparative numerical analysis of the SHKT and MBHKT under canal flow conditions.

CHAPTER – 4

NUMERICAL STUDY OF HYDROKINETIC TURBINES BASED ON THE CANAL FLOW

In the second stage, using the obtained data of canal flow and preferred HKT study site, the comparative analysis of SHKT and MBHKT was carried out in a canal. Also, as discussed earlier, both HKTs are most viable for ease of fabrication and maintenance too. As well as they can perform and start easily under low velocity magnitude water streams.

4.1 Numerical Methodology

The numerical simulations were created in a similar step-by-step process. Initially, the "Design modeler" module is used to model the HKT and its flow domain, followed by the "Mesh module" for grid/mesh production. The third stage involves selecting a solution and applying boundary conditions to specify the HKT's operating conditions. The next step is to analyze the simulation results in the "CFD-post module". To carry out the numerical simulation, the approach used in this work is illustrated in a flow chart as shown in Fig. 4.1.

4.1.1 Geometry

The schematic of all the HKTs along with the geometrical parameters used in present study are shown in Fig. 4.2. These geometrical parameters were calculated for theoretical 1 kw power generation. The two bladed SHKT shown in Fig. 4.2 (a) has semi-circular blade profile with overlap ratio of 0.15. Earlier, many researchers have reported that two bladed SHKT shows better performance in compare to the three bladed SHKT [72,103,104]. Vertical axis MBHKT with total of eighteen circular blades were considered in this analysis as shown in Fig. 4.2 (b). The vertical axis MBHKT can reduce about 50% of total cost compare to the horizontal axis as it doesn't require mechanical and civil structures [47].

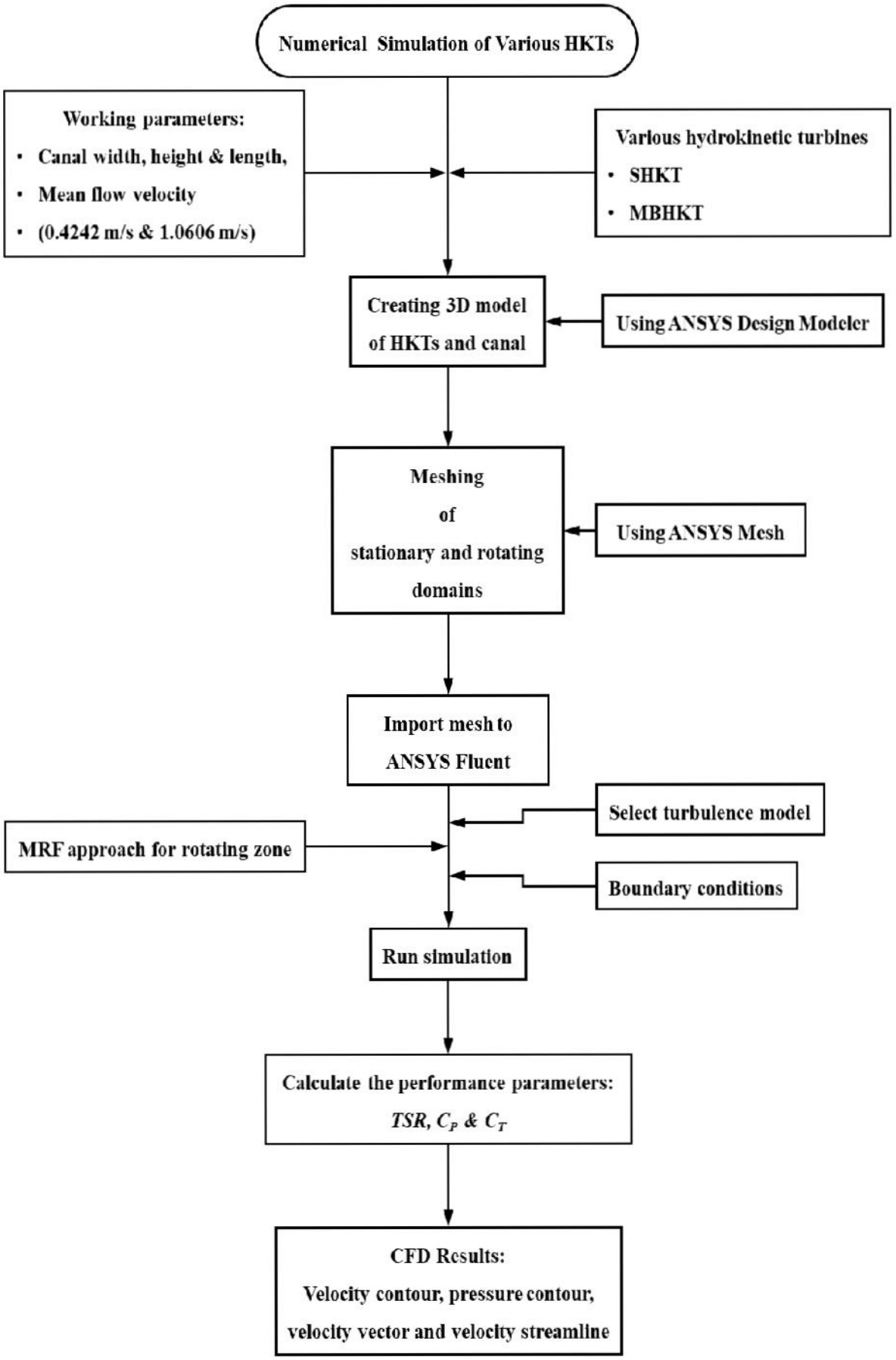
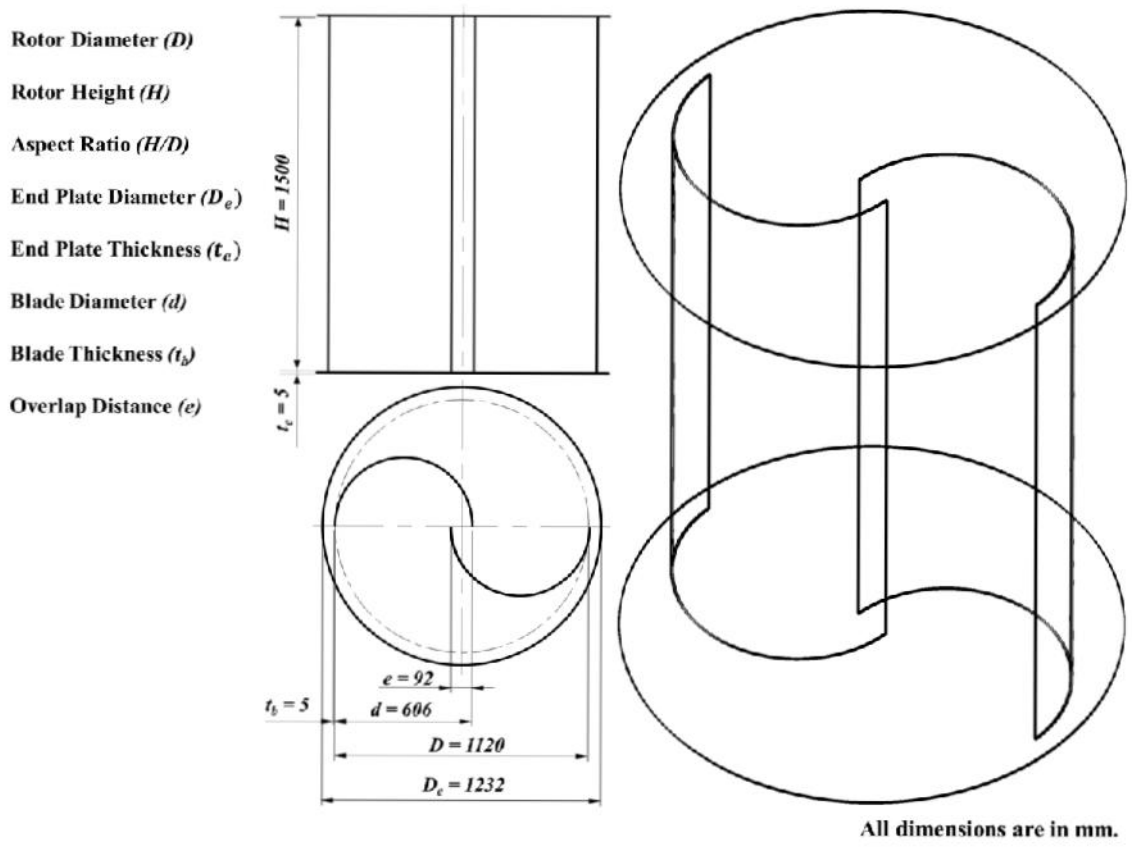
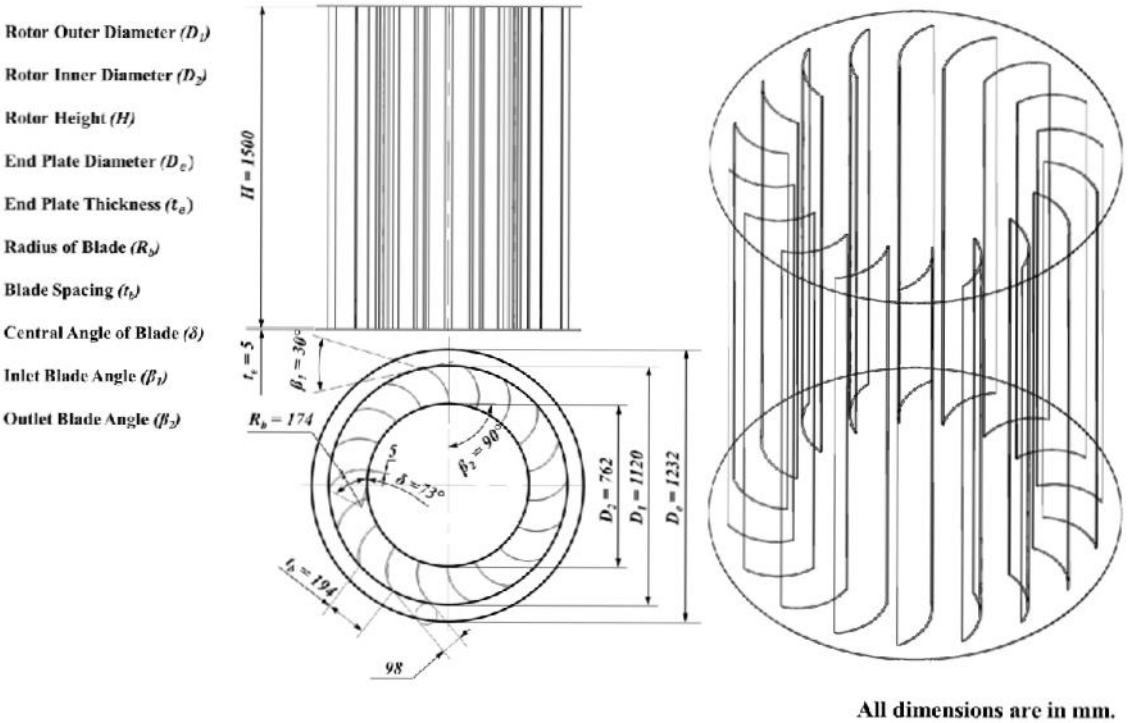


Fig. 4.1. Flow chart of approach used for HKTs analysis in canal.



(a)



(b)

Fig. 4.2. Schematic and geometrical parameters of (a) SHKT and (b) MBHKT.

4.1.2 Performance Parameters

The performance of a various HKTs with geometrical parameters taken into consideration is investigated numerically in the current work. Modelling and meshing of the computational domain are finished in order to fulfil the study's objectives, as described in the paper's preceding section. The performance of the HKTs is compared by the value C_T and C_P corresponds to TSR. The following equations are used to obtain characteristic curves (C_T vs. TSR and C_P vs. TSR) for various geometrical and flow parameters.

$$TSR = \frac{\omega D}{2U_m} \tag{4.1}$$

$$C_T = \frac{4T}{\rho {U_m}^3 D^2 H} \tag{4.2}$$

$$C_P = \frac{P_{turbine}}{P_{available}} = \frac{2T\omega}{\rho A_s {U_m}^3} = \frac{2T\omega}{\rho DH{U_m}^3} = C_T \times TSR \tag{4.3}$$

where ω is angular velocity in rad/s, T is torque in N·m, ρ is density in kg/m^3, $P_{turbine}$ is power developed by HKT in W, $P_{available}$ is hydraulic power available in W, A_S is HKT swept area in m^2. For the purpose of performance comparison, the same definition of reference area is adopted consistently for calculating the C_P. In the present study, the reference area (A_s) represents the projected swept area of the turbine rotor normal to the incoming flow. For the HKTs considered in this study, this area is calculated as $A_s = D \times H$, where D is the rotor diameter and H is the rotor height. Accordingly, the available $P_{turbine}$ is evaluated using the incoming U_m and the corresponding projected swept area. Therefore, the reported C_P represent the ratio of $P_{turbine}$ to the $P_{available}$ through the defined reference area under the specified operating conditions.

4.1.3 Computation Domain

In this study, ANSYS 2020 R1 "Design Modeller" was used to construct a 3-D model of SHKT and MBHKT as shown in Fig. 4.2. In order to carry out the rotating simulation,

HKTs have been enclosed by cylindrical volumes that have been created about the Y-axis so that, when subjected to numerical analysis, the HKTs can rotate at a specified angular velocity. In previous studies, the size of this rotating domain has been considered as 1.2 times of HKT diameter to 3 times of HKT diameter [105–107]. Under this study, diameter for the rotating domain is considered as 1.2 times of HKT diameter. To simulate the performance of the HKTs in a canal, a 3-D computational stationary domain has been modelled for numerical analysis. The canal is having trapezoidal section (side slope of 1.5:1) having top width of 15.5 m while bed width of 6.5 m for 65 m total length. The HKTs were considered to be submerged completely in the canal. This domain has a water surface similar to open channel flow; the standard water level in the channel is set at 3 m. The swept area of the rotor is 1.68 m^2 so that the rotor presented a channel blockage of 5%. Fernando and Modi [108] presented results which show that if blockage corrections vary from 5% to 20%, high increase in the power output of about 70% is observed. The interface is also created between the rotating zone and the stationary zone to ensure the continuity of the flow field. The complete 3-D computational domain, along with the rotational and stationary zones, is similar to submerged HKTs in a canal, as shown in Fig. 4.3. After the domain is constructed, the geometry is given the proper domain names to suit the respective boundary conditions. This process is called "physics module setup".

4.1.4 Meshing of Computation Domain

In the present study, a mesh for the whole flow domain is created by ANSYS MESH considering an unstructured grid of tetrahedral elements, as seen in Fig. 4.4 (a). The meshing of inner rotating zone containing various rotors such as SHKT and MBHKT is also depicted Fig. 4.4 (b) and (c). The mesh elements, ranging from 2.37 to 8.79 million, are generated for the inner rotating zone as well as a stationary zone. Grid independency test shown in Fig. 4.5 imparts that the expected number of grid elements for the SHKT and MBHKT is 4.02

and 6.30 million, beyond which any increase results in a negligible change in C_P. Also, the skewness of 0.28 with orthogonal quality of 0.86 was obtained for selected elements. An inflation layers was added to the rotor wall to gather the flow near the edges. Consequently, the y+ value in this research is regarded as being less than one.

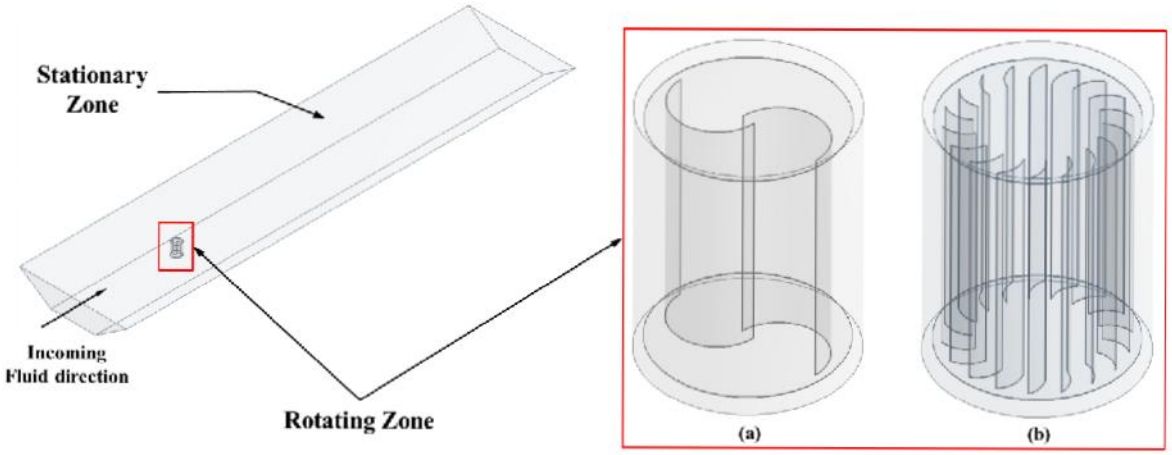
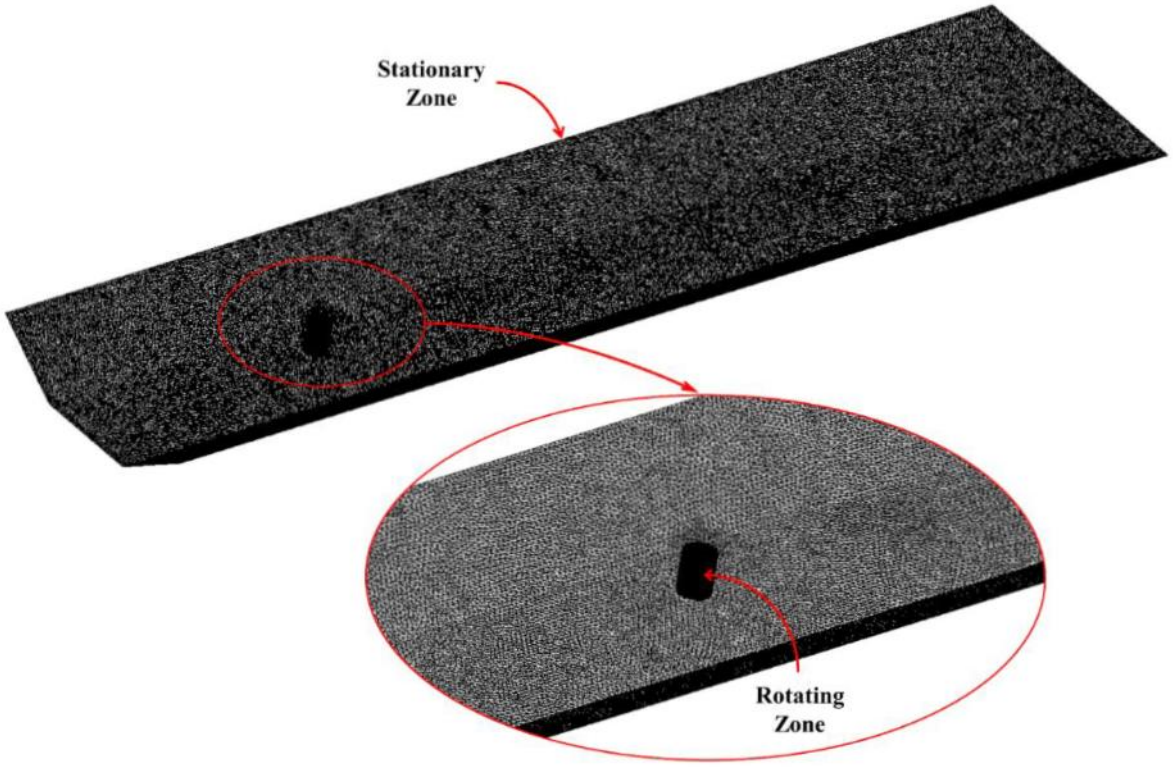


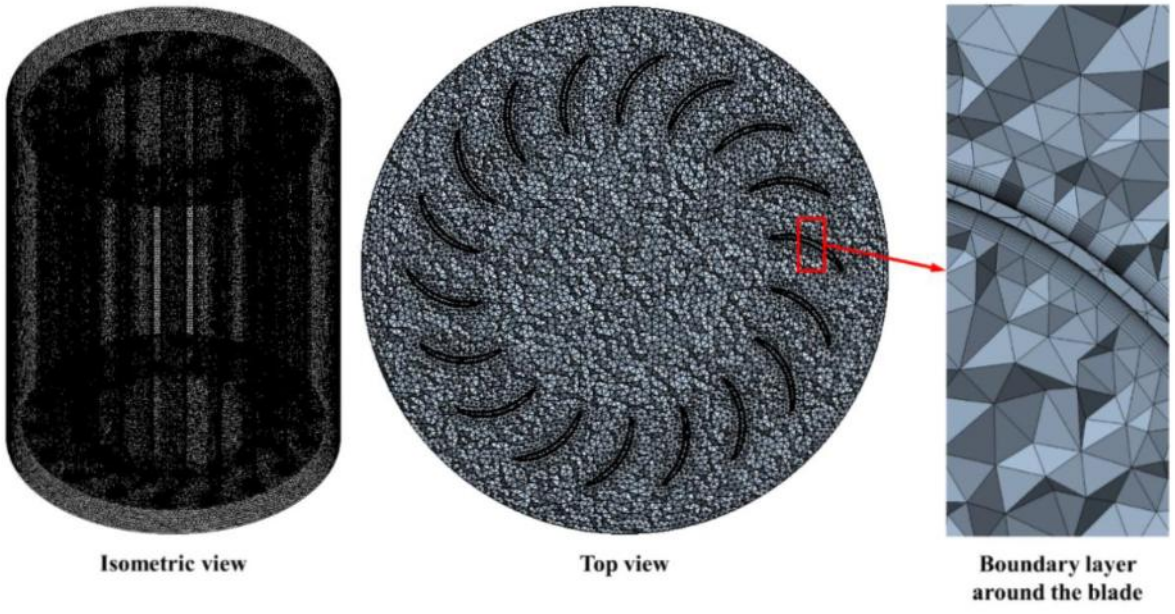
Fig. 4.3. 3-D computation domain of canal with stationary zone and rotating zone of (a) SHKT and (b) MBHKT.



(a)

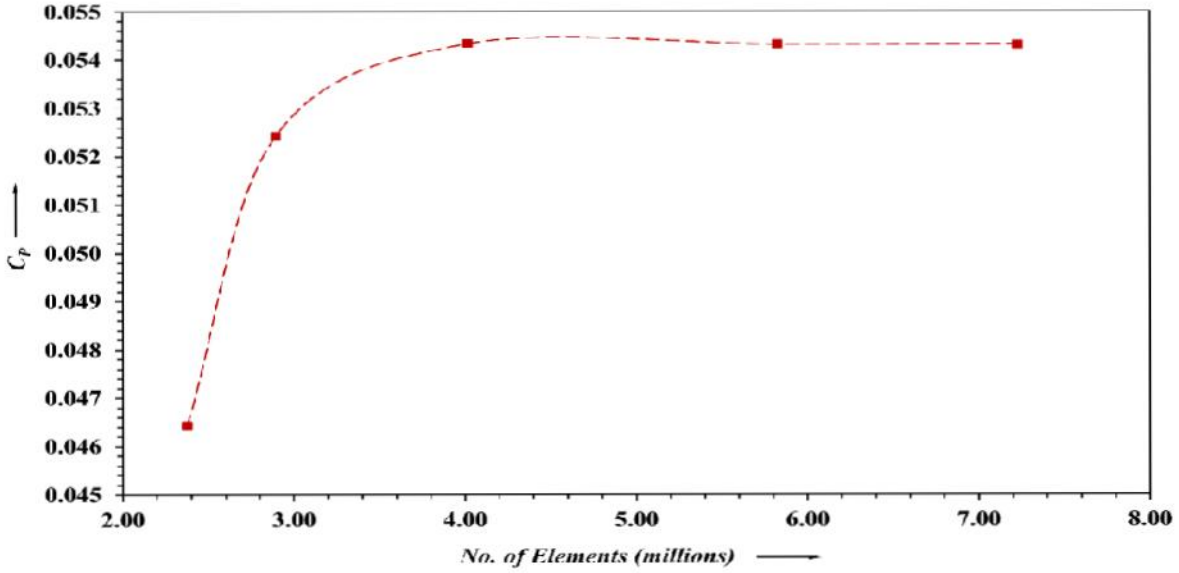


(b)

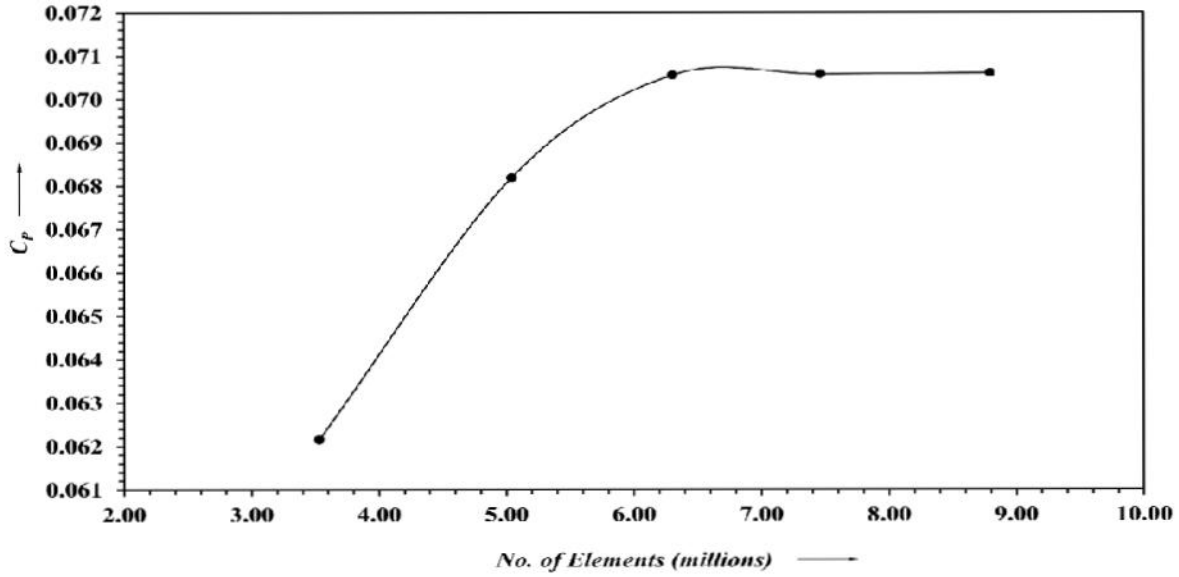


(c)

Fig. 4.4. Meshing of the computational fluid domain of (a) whole canal, (b) SHKT, and (c) MBHKT.



(a)



(b)

Fig. 4.5. Grid independency test for (a) SHKT and (b) MBHKT.

4.1.5 Boundary Conditions

Fig. 4.6 shows the boundary conditions taken into consideration for CFD analysis, which are listed in Table 4.1. A velocity inlet with a free stream velocity (Dirichlet boundary condition) and a pressure outlet condition are the configurations for the canal's inlet and outlet. Under the present investigation, two flow velocities are selected based on the experimental and site data. A velocity of 0.42 m/s was considered as the annual average flow velocity representing the mean velocity recorded throughout the year, whereas a velocity of

1.06 m/s was selected as the maximum flow velocity available at site. The canal bed and side wall are considered as stationary wall boundary conditions, while the HKT is provided with a rotating wall as a no-slip condition. The interface between the stationary and rotating zones is interconnected with a top, bottom, and lateral surface of cylindrical volume. The water surface of canal is assigned as a symmetry boundary condition [73,109]. The water surface's effect on the HKT's performance is negligible in this numerical analysis.

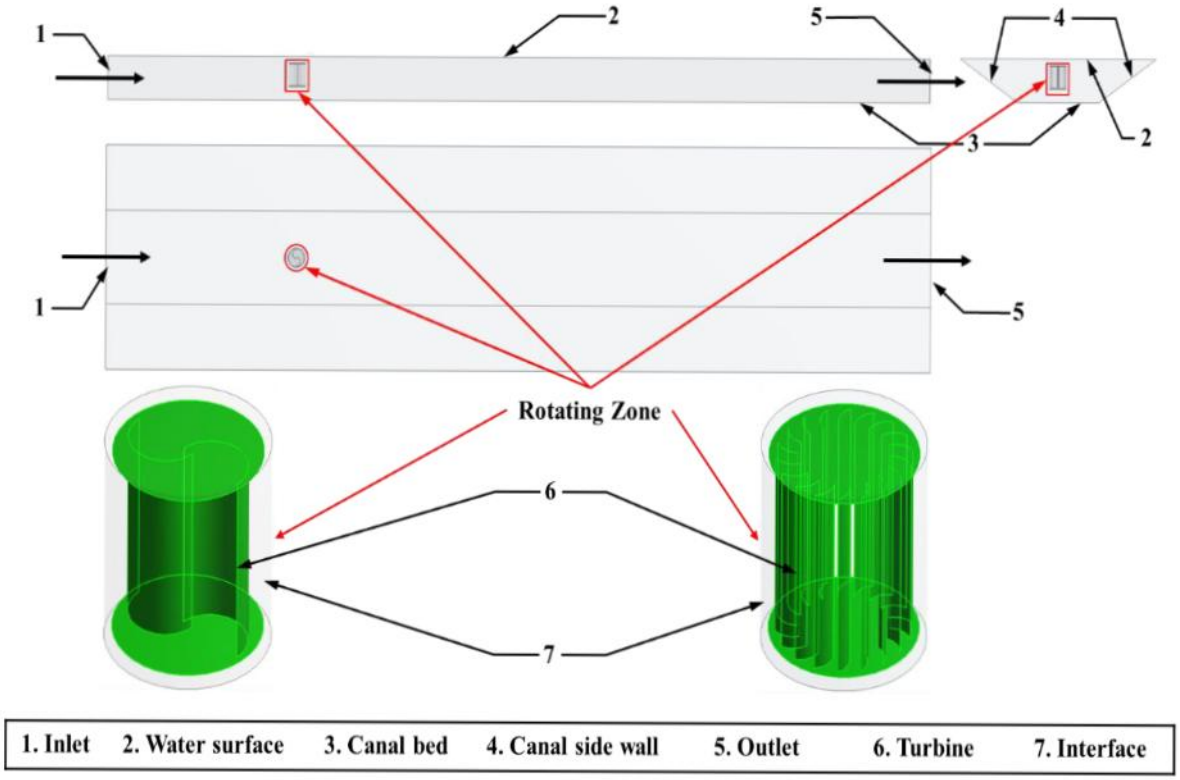


Fig. 4.6. Various boundary conditions for computational domain.

Table 4.1.

Boundary conditions for 3-D computational domain of canal.

Name	Boundary Type	Boundary Conditions
Inlet	Velocity inlet	0.42 m/s (annual average value) and 1.06 m/s (maximum available value), uniform flow
Water surface	Symmetry	Symmetry
Canal bed	Wall	Stationary

Name	Boundary Type	Boundary Conditions
Canal side wall	Wall	Stationary
Outlet	Pressure outlet	Pressure outlet
Turbine	No slip wall	Rotates at desired rpm

4.1.6 Validation

With the use of a finite volume discretization method, steady incompressible N-S equations were solved using ANSYS FLUENT, where the resulting mesh is imported, as a flow solver. In the case of water flow, turbulence was seen as critically important and needs to be properly accounted for. Several models are available to address the turbulence phenomena in the simulation. Therefore, choosing an appropriate turbulence model is necessary. For analysing all the gradients, the cell based least-squares approach is taken into consideration. For all residual of the momentum, continuity, and turbulence equations, the convergence conditions were set up as 1×10^{-5}. At the inlet of the canal, 2.2% turbulent intensity and 7.6 m hydraulic diameter was applied considering the fact that C_P decreases with increases above values [110]. In this investigation, $k-\varepsilon$ Standard, $k-\varepsilon$ RNG, $k-\varepsilon$ Realizable, $k-\omega$ Standard and $k-\omega$ SST turbulence models were employed. The findings of a previous experimental study conducted by Hayashi et al. [111] are used in order to choose an appropriate turbulence model for the current investigation. Their study's findings are displayed in Fig. 4.7, which shows how well CFD and experimental results for the $k-\omega$ SST turbulence model match. As a result, the present study has taken into consideration the $k-\omega$ SST turbulence model. It was proposed under prior studies [112–114] that $k-\omega$ SST turbulence model is better to simulate the rotating behavior of blades or aerofoil, flow through the channel, a boundary layer or isolated flows. Further, this model does not rely on the anticipated link between the Reynolds stress tensor and the strain rate tensor. In the $k-\omega$ SST model, the coefficient of the model is stated as a function of mean flow and turbulence

parameters, rather than considered to be constant as in the conventional model. Using a 2nd order upwind scheme for all convection terms, such as the momentum equation, turbulent dissipation rate, turbulent kinetic energy, and a SIMPLE pressure-velocity coupled solver, the CFD investigation was performed out in order to obtain results that are more accurate.

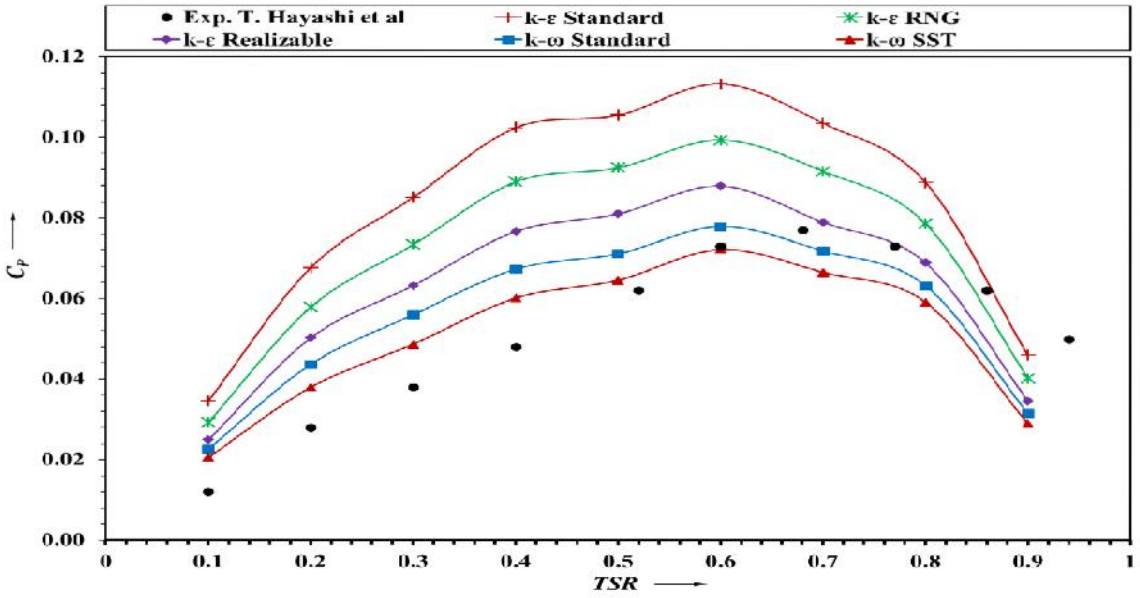


Fig. 4.7. Turbulence models comparison with previously published result by T. Hayashi et al.

4.2 Results and Discussion

This section presents comprehensive numerical results of SHKT and MBHKT for two velocities 0.42 m/s and 1.06 m/s for different values of TSR. For every value of the parameters taken into consideration, simulation results have been obtained. Nonetheless, the flow distribution surrounding the HKTs is explained correspondence to the $C_{P,max}$ value.

4.2.1 Performance Characteristics Curves

In this study, dimensionless parameters C_T, C_P and TSR stated in Section 4.1.2 are used to characterise the performance of HKTs. Using Eqs. (4.1) to (4.3), the performance characteristic curves were obtained for all HKTs. The variation of C_T and C_P with TSR for SHKT and MBHKT is shown in Fig. 4.8 (a) and (b), while comparative characteristic curve

for all the HKTs at two different velocities 0.42 m/s and 1.06 m/s is depicted in Fig. 4.9 (a) and (b). For a velocity of 0.42 m/s and 1.06 m/s, the $C_{P,max}$ obtained is 0.0648 and 0.0721 at 0.6 TSR for SHKT; and 0.1121 and 0.1249 at 0.4 TSR for MBHKT. Similarly, corresponding $C_{T,max}$ at respective TSR are 0.1081 and 0.1202 for SHKT; and 0.2802 and 0.3123 for MBHKT. Relative to the flow velocity of 0.42 m/s, $C_{P,max}$ increases by 11.26% and 11.42% for SHKT and MBHKT.

For SHKT and MBHKT, the value of C_T decreases as TSR increases. This behaviour can be understood as: For SHKT, the returning blade encounters more substantial negative drag and resistance as the turbine rotates faster at higher TSR, thereby opposing the advancing blade's positive torque and resulting in a decreased net driving force and torque. While for MBHKT, the blade speed is too fast in relation to the incoming jet, decreasing effective momentum transfer and lowering the attack angle which lowers the C_T for increasing TSR.

The value of C_P observes same behaviour for all the HKTs by increasing initially, reaching a $C_{P,max}$ for particular TSR and then reduces. This can be understood as: SHKT's C_P rises at low TSR due to the growing drag differential between the advancing and returning blades, peaks when the bucket speed equals the flow for the best momentum transfer, and then falls at high TSR due to the collapse of the drag differential, an increase in negative drag, and water slipping past the blades[115,116]. The value of C_P for a MBHKT rises at low TSR due to improved momentum transfer caused by the blade speed matching the incoming jet. At the ideal TSR, where incidence angle, flow attachment, and two-stage energy extraction are optimal, it peaks. After this, the rotor spins excessively quickly, which reduces effective power extraction by creating flow misalignment, separation, turbulence, and poor second-stage contact resulting in the fall of C_P.

Further, in compare to the 0.42 m/s, the value of C_T and C_P increases at 1.06 m/s flow

velocity for both HKTs. Additionally, these increases are larger at higher TSR and smaller at lower TSR. This can be understood by the underlying principles of fluid dynamics as well as turbine mechanics. The fluid's kinetic energy grows in direct proportion to the U_m. The HKT blades are subjected to a larger dynamic pressure as a result of this increase in kinetic energy, which increases torque generation. A notable increase in torque without a matching increase in flow resistance results in an improved C_T and C_P. Higher velocity further enhances the flow-turbine blade interaction, lowering turbulence and boundary layer separation losses. More effective energy transmission from the flow to the turbine is made possible by the higher relative velocity between the fluid and the revolving blades. Also, the rotor rotates slowly at low TSR, changes in flow velocity have little effect on the relative velocity or incidence angle on the blades; as a result, the rise in C_P is minimal. Any increase in flow velocity significantly alters the relative flow angle, momentum transfer, and hydraulic losses at higher TSR because the blade speed is similar to the flow speed. Due to these effects, variations in power extraction are amplified, resulting in a greater fluctuation in C_P at high TSR than at low TSR.

The comparative evaluation of SHKT and MBHKT based on their C_T and C_P reveals distinct performance behaviours governed by their underlying operating principles. The MBHKT's strong impulse-driven initiation capability is confirmed by its highest starting torque ($C_T > 0.55$ at TSR ≈ 0). Nevertheless, its C_T and C_P rapidly decrease with increasing TSR, with a modest peak C_P of ~ 0.11 at TSR $\approx$ 0.4–0.5, suggesting that its efficiency is limited to low rotational speeds. The SHKT, on the other hand, achieves just ~0.06 peak C_P at TSR = 0.6, which is consistent with drag-based turbine constraints where increasing TSR reduces the effective drag difference. It also produces moderate beginning torque and the lowest power extraction efficiency among the three HKTs. When compared to drag- or impulse-driven machines, this pattern represents the dominance of lift forces at optimal TSR,

resulting in much improved energy conversion. All things considered, the MBHKT has good self-starting qualities but poor high-speed performance, and the SHKT, despite its intrinsically low C_P, is still best suited for low-speed, high-torque applications.

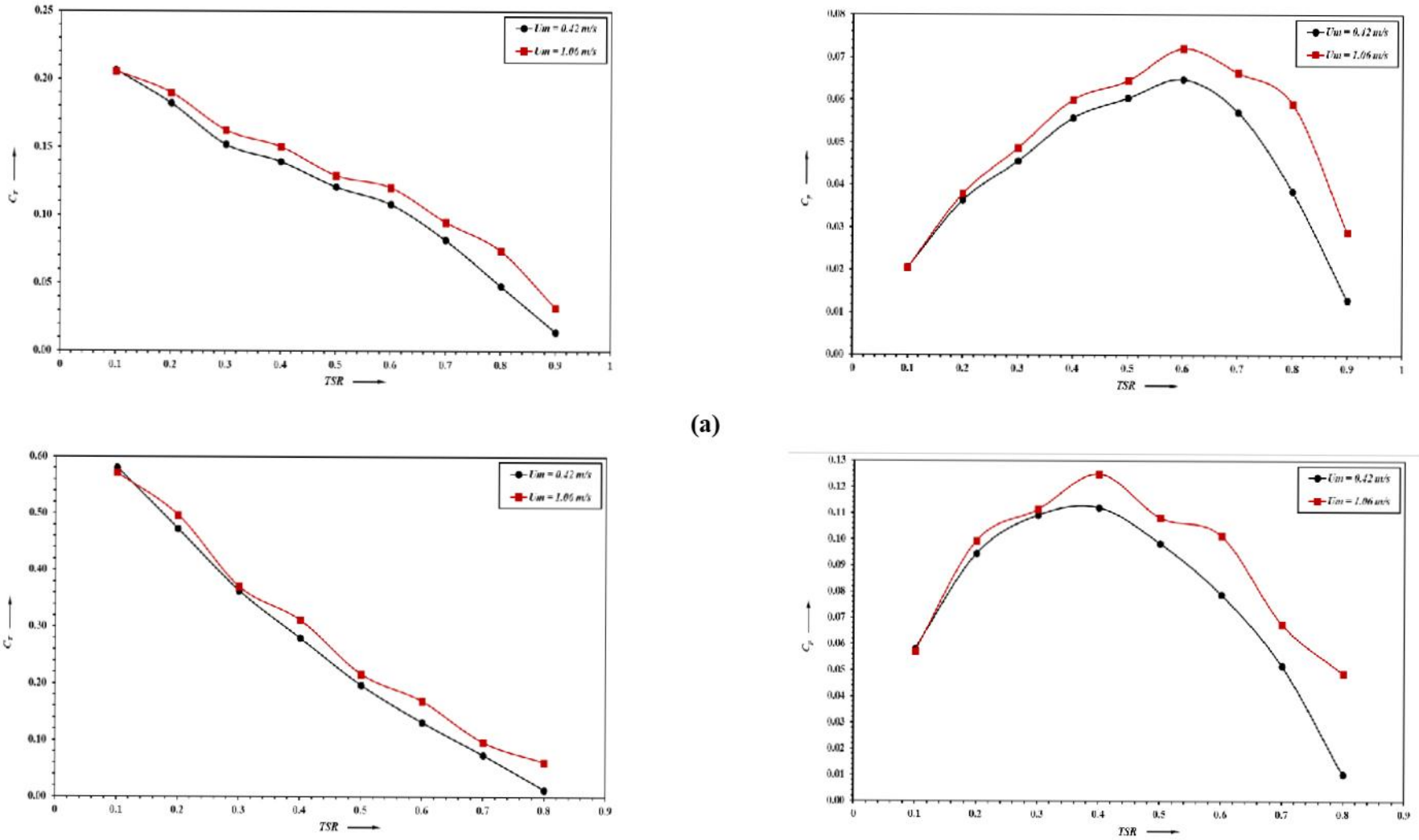


Fig. 4.8. Variation of C_T and C_P with TSR for (a) SHKT and (b) MBHKT.

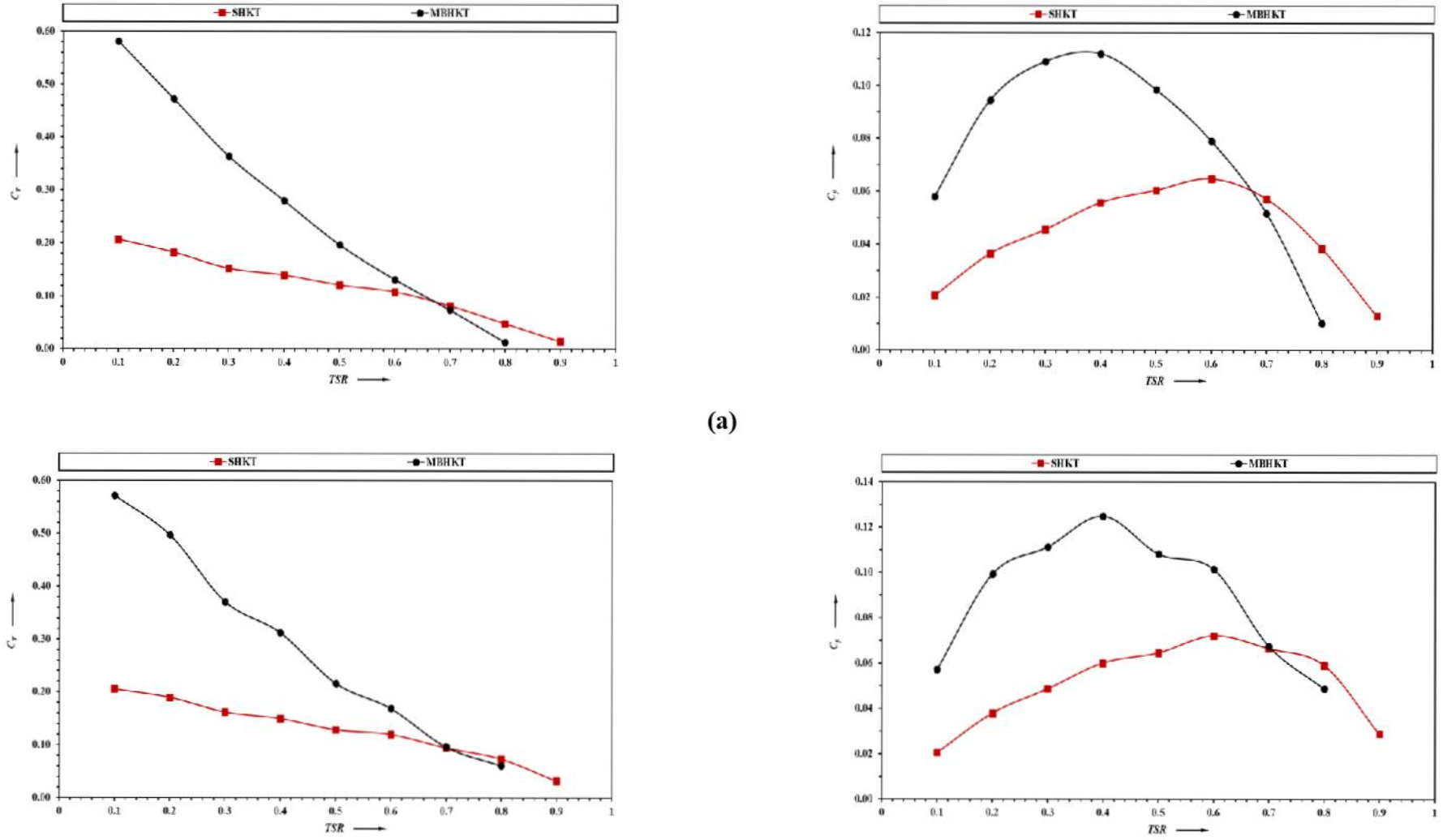


Fig. 4.9. Variation of C_T and C_P with TSR for all the HKTs at (a) U_m = 0.42 m/s and (b) U_m = 1.06 m/s.

4.2.2 Field Visualizations

To understand the complex dynamics of fluid motion, flow filed visualisations of SHKT and MBHKT are depicted in Fig. 4.10 and 4.12 at U_m = 0.42 m/s and in Fig. 4.11 and 4.13 at U_m = 1.06 m/s, respectively. Pressure contours, velocity contours, velocity vectors and velocity streamlines were studied thoroughly for in depth analysis of performance of all HKTs.

A noticeable intensification of the pressure differential across the SHKT with increasing flow velocity is revealed by the pressure contour comparisons (Fig. 4.10 (a) and 4.11 (a)). The concave side of the advancing blade encounters moderate positive pressure (orange–red zones, up to ~127 Pa) at 0.42 m/s, whereas the convex side suffers low negative pressure (blue–green zone, down to ~ –197 Pa). The torque of the rotor is produced by this slight but noticeable pressure asymmetry. The amplitude of both high- and low-pressure zones increases significantly as the flow velocity reaches to 1.06 m/s, with the suction region deepening to ~ –1244 Pa and the positive pressure on the advancing blade reaching ~770 Pa. The net pressure difference is greatly increased by the concave blade's stronger stagnation zone and the convex blade's increased separation, which suggests larger aerodynamic (hydrodynamic) forces and increased torque generation.

The velocity contours demonstrate how raising the flow velocity from 0.42 m/s to 1.06 m/s deepens shear around the blade tips and increases flow acceleration along the concave moving blade (Fig. 4.10 (b) and 4.11 (b)). At the greater velocity, peak speeds surpass 1.6 m/s, resulting in a longer wake and more powerful vortex formation, while at the lower velocity, the wake is compact with modest deceleration zones. Higher torque generation and improved momentum transfer are indicated by the steeper velocity gradients at 1.06 m/s, together with greater unstable hydrodynamic loading on the rotor.

As inlet velocity increases, the velocity vector fields demonstrate a strengthening of

flow circulation and shear around the SHKT blades (Fig. 4.10 (c) and 4.11 (c)). The vectors show modest acceleration on the approaching blade and substantial recirculation behind the retreating blade at the lower velocity. The wake region grows with more vortical motion as the flow rate increases, and the vectors along the concave moving blade become denser and more aligned, indicating greater flow attachment and higher local acceleration. Higher torque and power output are correlated with this improvement in flow circulation and directional coherence at 1.06 m/s, which indicates improved momentum exchange with the blades.

The velocity streamline patterns show how, as flow rate increases, vortical structures and flow acceleration around the SHKT get stronger (Fig. 4.10 (d) and 4.11 (d)). The streamlines exhibit a steady recirculation bubble behind the returning blade and a slight acceleration over the advancing blade at the lower velocity. Stronger circulation forms inside the rotor and sharper acceleration zones near the blade tips as the velocity increases, making the streamlines denser and more curved. Increased torque-producing flow-blade interaction and improved momentum exchange are indicated by the significant vortical core and noticeable streamline deflection at the higher flow rate.

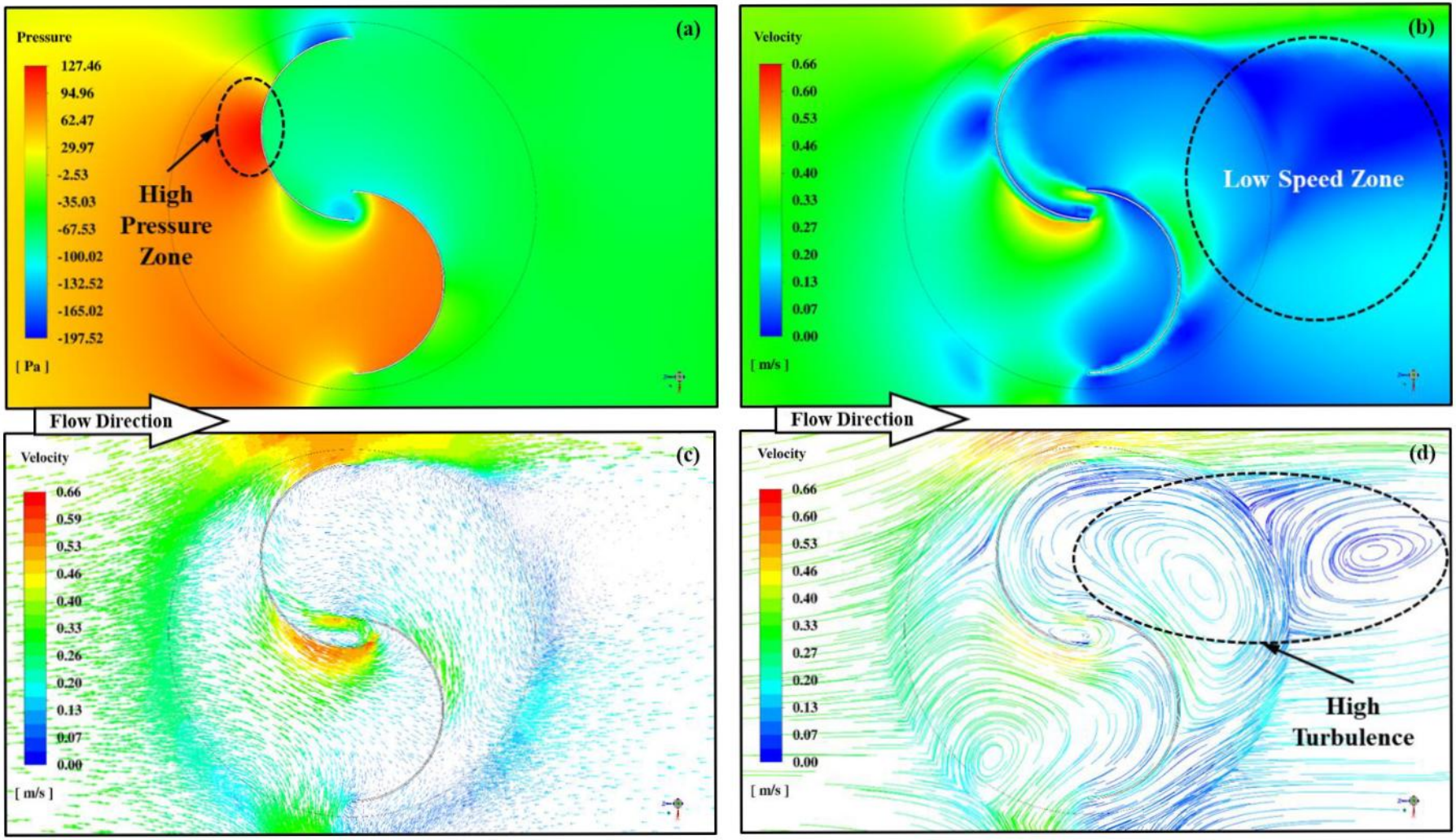


Fig. 4.10. Field visualizations for SHKT at U_m = 0.42 m/s (a) pressure contours, (b) velocity contours, (c) velocity vectors, and (d) velocity streamline.

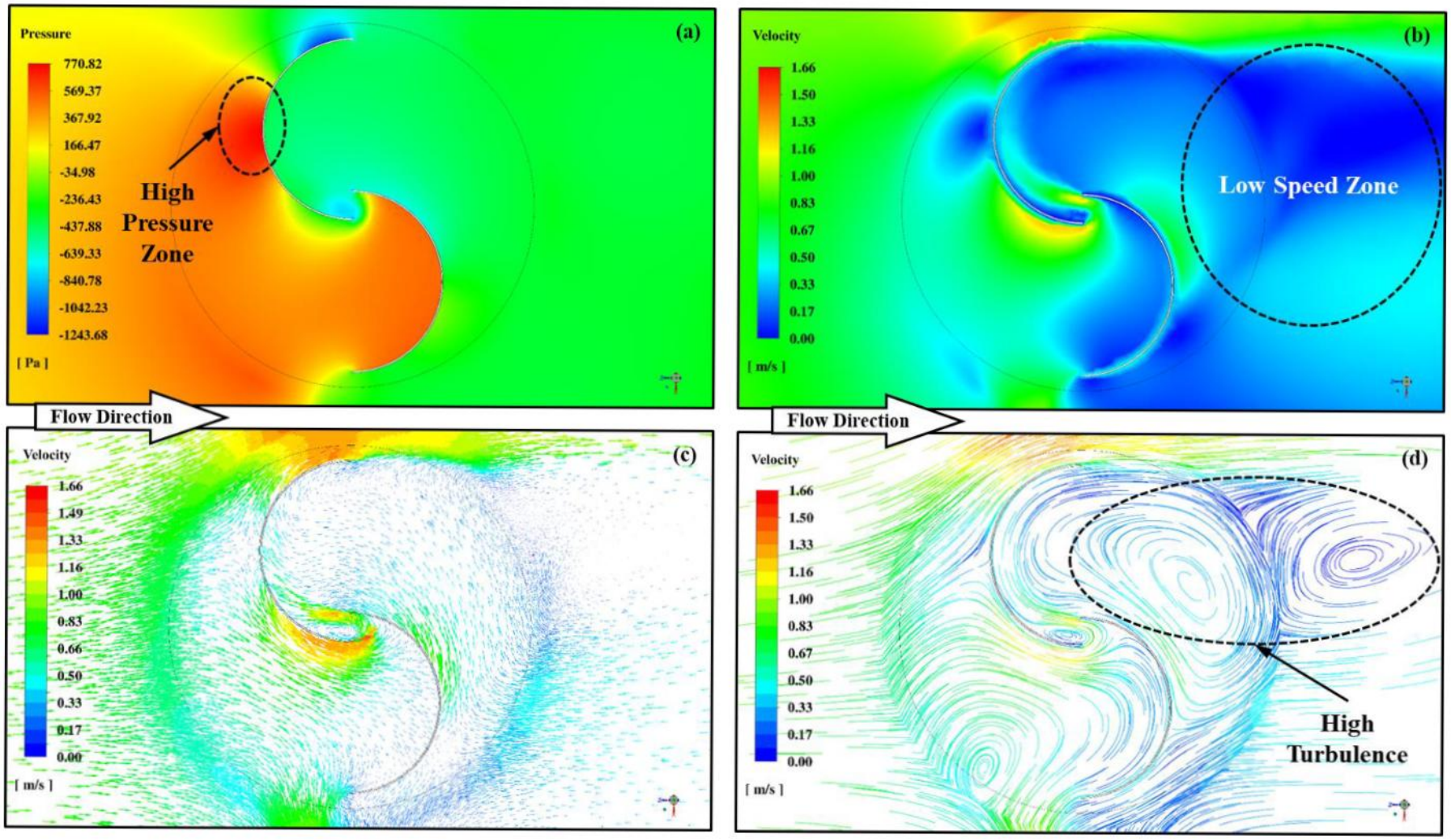


Fig. 4.11. Field visualizations for SHKT at U_m = 1.06 m/s (a) pressure contours, (b) velocity contours, (c) velocity vectors, and (d) velocity streamline.

The pressure contours for the MBHKT at intake velocities of 0.42 m/s and 1.06 m/s show that momentum transfer and hydraulic force clearly intensify with increasing flow velocity (Fig. 4.12 (a) and 4.13 (a)). High-pressure regions generated on the backside of the blade may also increase the pressure loading and flow resistance on it. If the pressure distribution is not favourable in the tangential direction, part of the resulting force may contribute to drag rather than useful torque. It can also promote stronger flow separation and pressure losses, potentially reducing the hydraulic efficiency of the turbine. At stage 1 and 2, a relatively high-pressure region over the blade surface is advantageous because it indicates that the incoming water flow and the blade are interacting efficiently. The higher pressure produces an advantageous pressure force across the blade, increasing torque production by contributing to the tangential component of hydrodynamic force. This pressure distribution supports higher rotational performance and efficient energy extraction by allowing for the effective transfer of momentum from the flowing water to the rotor.

The MBHKTs velocity contours demonstrate how internal flow interaction and flow coherence are stronger as inlet velocity rises (Fig. 4.12 (b) and 4.13 (b)). Region-1 shows a relatively higher and more distributed velocity field around the blade passage, indicating effective interaction between the incoming flow and the blades. As the flow passes through the rotor, its velocity changes because of the transfer of momentum to the blades. Region-2 represents the downstream blade-passage region, where the flow exhibits noticeable velocity variation and localised low-velocity zones. The prominent low-speed zone on the right side of the rotor is characterised by dark-blue contours, indicating reduced flow velocity and wake development after interaction with the turbine. The velocity reduction in this region reflects the extraction of kinetic energy from the water by the rotor.

The velocity vector fields at 0.42 m/s (Fig. 4.12 (c)) and 1.06 m/s (Fig. 4.13 (c)) demonstrate how flow momentum and organization clearly intensify as inlet velocity

increases. Power for the first stage (Region-1) is generated. The velocity vectors show the incoming flow approaching and interacting with the blades, with higher velocity vectors concentrated near the blade surfaces and leading-edge regions. This indicates strong flow–blade interaction and effective momentum transfer to the rotor. As the water passes through the blade passages, the velocity vectors change their direction and magnitude, demonstrating the turning of the flow and the transfer of its momentum to the rotating blades. The flow then went through the second stage power (Region-2) by crossing the vanless inside of the runner. The vectors indicate a substantial change in flow direction as the water exits the rotor, accompanied by localized higher and lower-velocity regions.

As inlet velocity rises, the streamline patterns at 0.42 m/s (Fig. 4.12 (d)) and 1.06 m/s (Fig. 4.13 (d)) clearly demonstrate a strengthening of internal flow circulation. The streamline pattern demonstrates effective flow turning and momentum transfer, which contributes to torque generation and energy extraction from the flowing water at Region-1 and 2. The recirculation zones visible around the rotor indicate localized flow separation and energy losses.

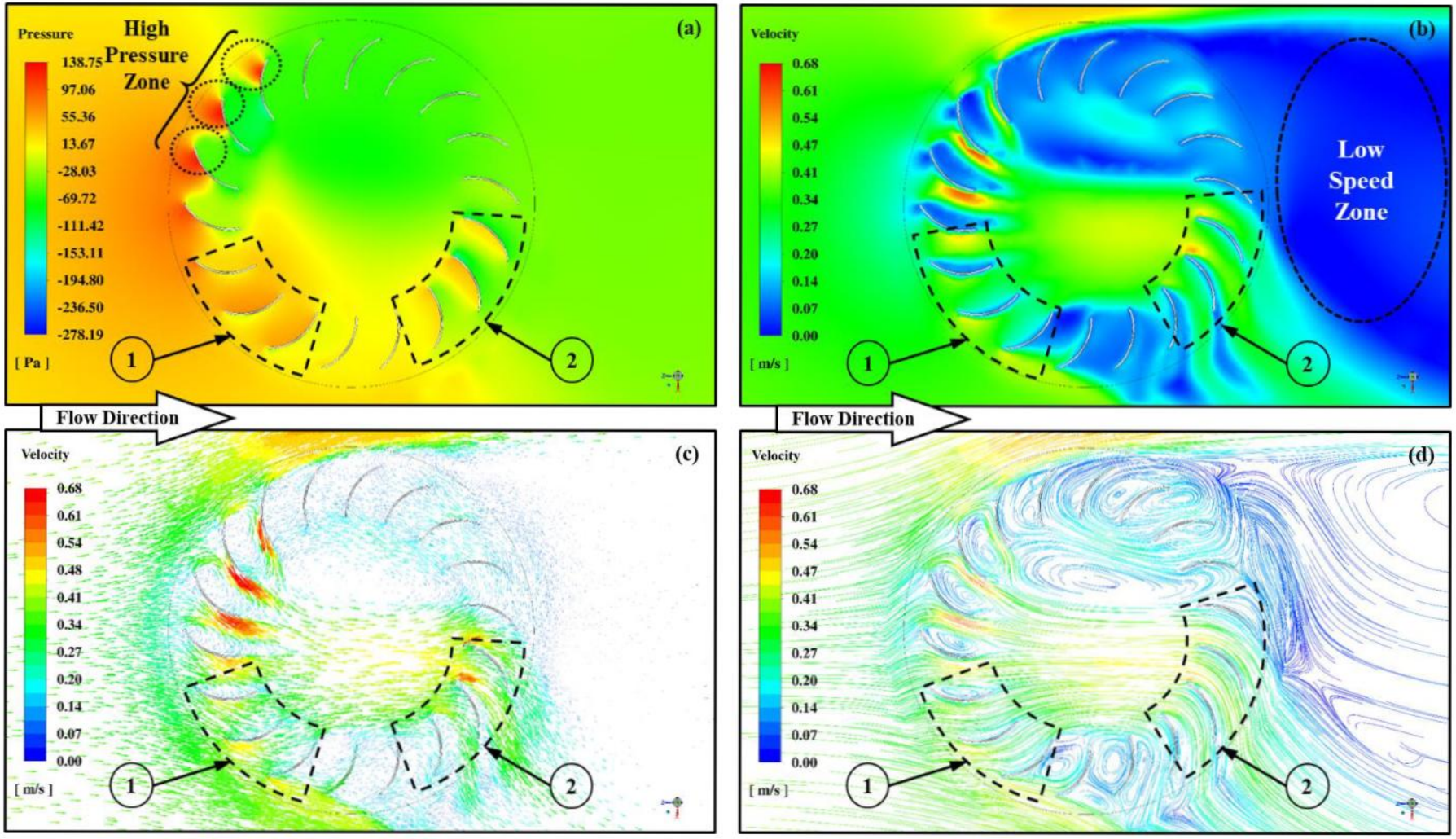


Fig. 4.12. Field visualizations for MBHKT at U_m = 0.42 m/s (a) pressure contours, (b) velocity contours, (c) velocity vectors, and (d) velocity streamline.

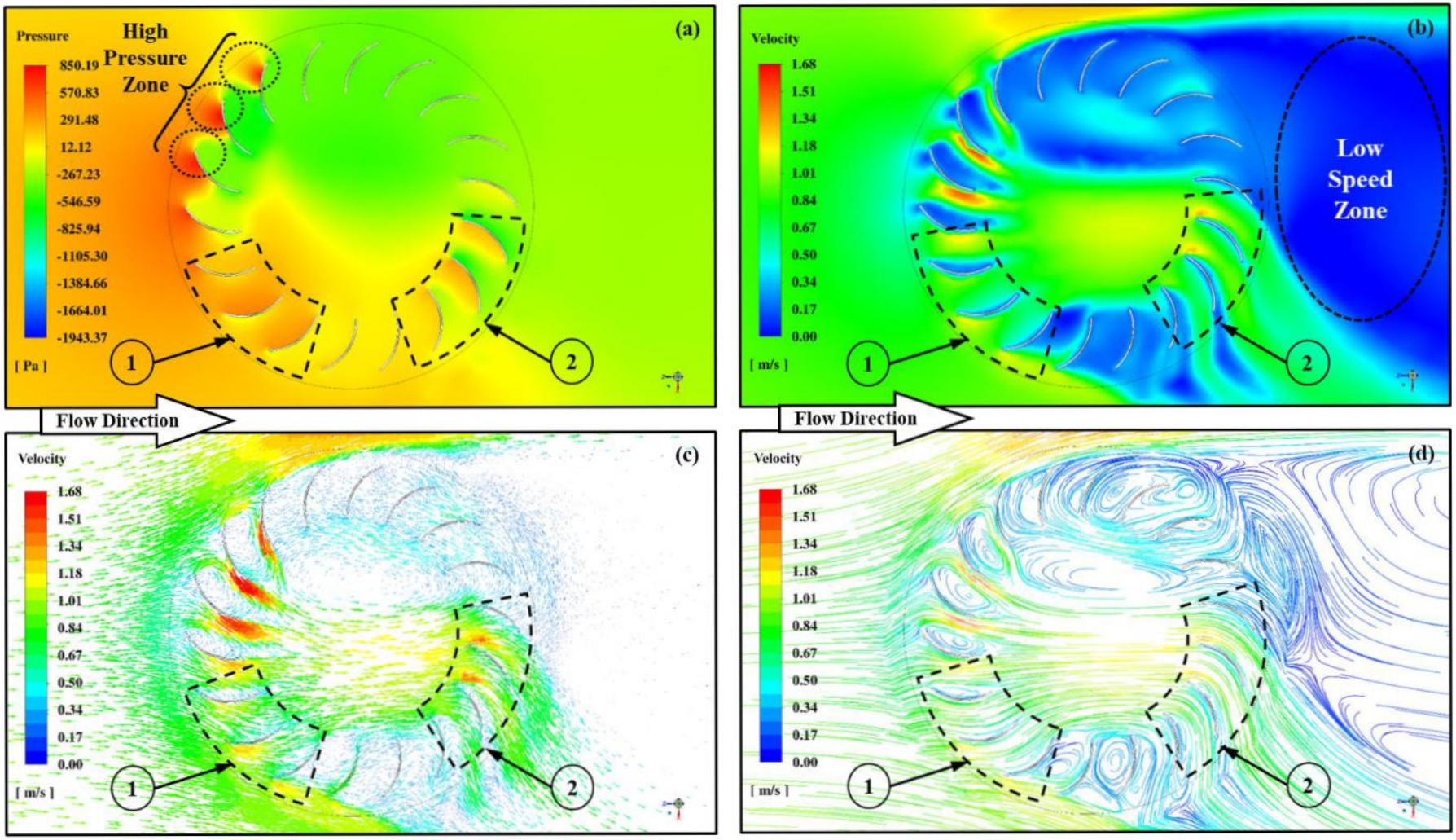


Fig. 4.13. Field visualizations for MBHKT at U_m = 1.06 m/s (a) pressure contours, (b) velocity contours, (c) velocity vectors, and (d) velocity streamline.

CHAPTER – 5

EXPERIMENTAL AND NUMERICAL STUDY OF MICHELL-BANKI HYDROKINETIC TURBINE IN OPEN CHANNEL

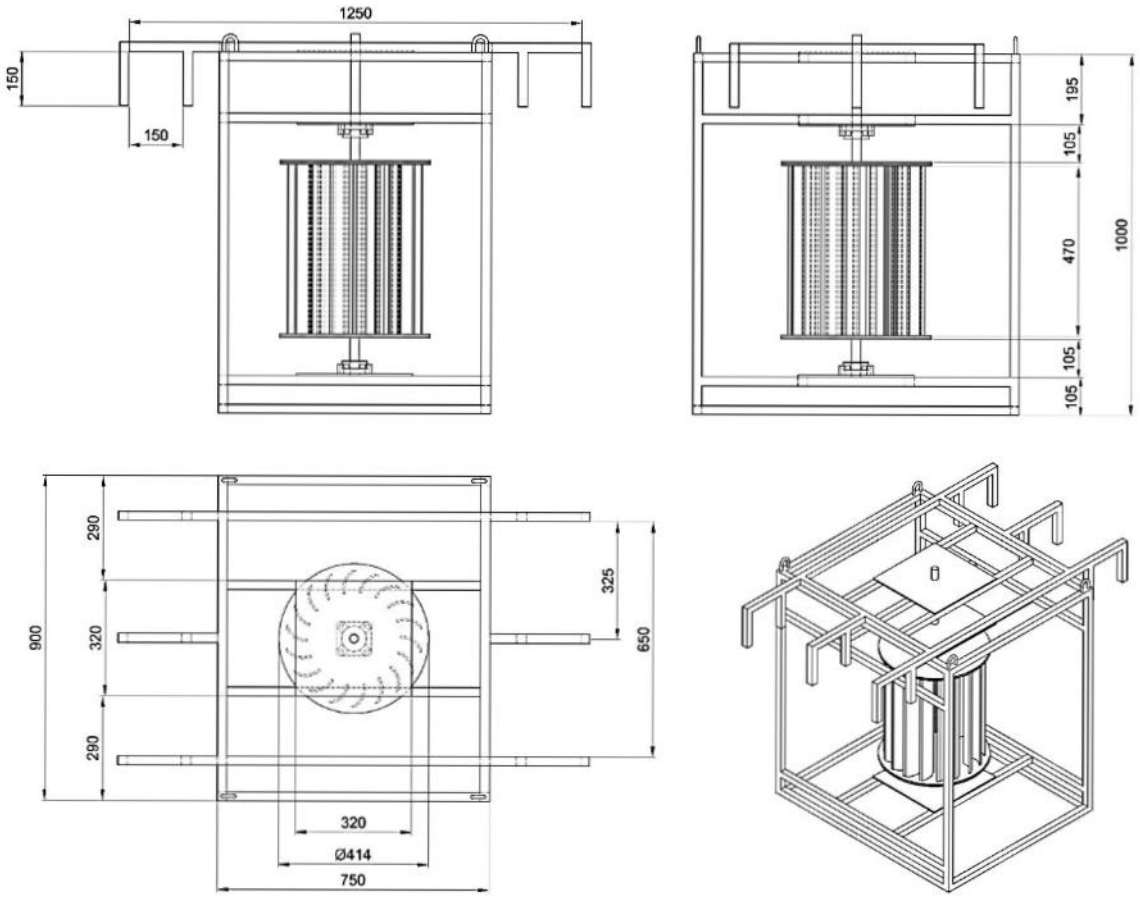
5.1 Experimental Work

5.1.1 Fabrication of Michell-Banki Hydrokinetic Turbine

Based on the results obtained from various HKTs performance in Canal as explained in Chapter 4, the MBHKT performance was investigated at open channel testing facility established at Fluid Mechanics and Fluid Machine Laboratory, Sardar Vallabhbhai National Institute of Technology, Surat, Gujarat, India. Fig. 5 (a) shows the photographic view of the employed MBHKT with its dimensions, while Fig. 5 (b) shows the schematic view of the MBHKT.

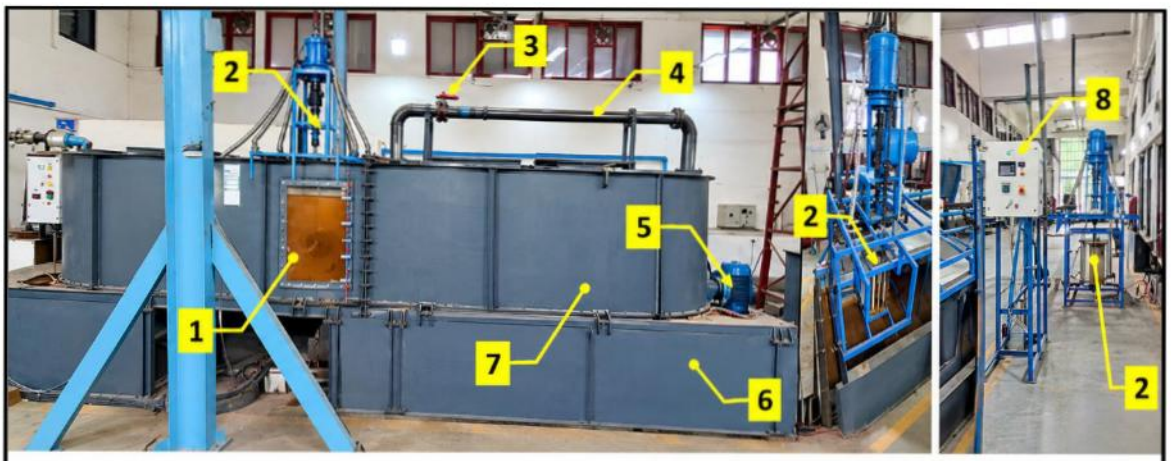


(a)



(b)

Fig. 5.1. (a) Photographic view and (b) Schematic view of the MBHKT.



Part No.	Part Name	Part No.	Part Name
1	Glass window for turbine visual	5	Assembly of motor and Centrifugal pump
2	Turbine setup	6	Base of the setup
3	Flow Control Valve	7	Open channel
4	Delivery Pipe	8	Control panel

Fig. 5.2. Photographic view of the experimental test setup.

5.1.2 Experimental Test Rig

A testing facility was set up at the Fluid Mechanics and Fluid Machine Laboratory, Sardar Vallabhbhai National Institute of Technology, Surat, Gujarat, India, to assess an MBHKT's performance. Fig. 5.2 depicts the photographic view of the experimental testing facility, which includes the MBHKT test bed, flow control, and measuring system. The open loop circuit in the lab is mostly used to test real HKT models.

5.1.3 Instrumentation Details

The following section contains information on key test-rig instruments and equipment. For the measurement of velocity the PCM described in subsection 3.2 was utilised. An inductive proximity sensor POWER M18 PNP shown in Fig. 5.3 is used to gauge the MBHKT's speed. This sensor works on the basis of electromagnetic induction, in which an electromotive force is created in the rotating shaft by a fluctuating current. This non-contact sensing technique is perfect for ongoing monitoring in experimental setups since it guarantees great endurance and reliability.



Fig. 5.3. Proximity sensor.



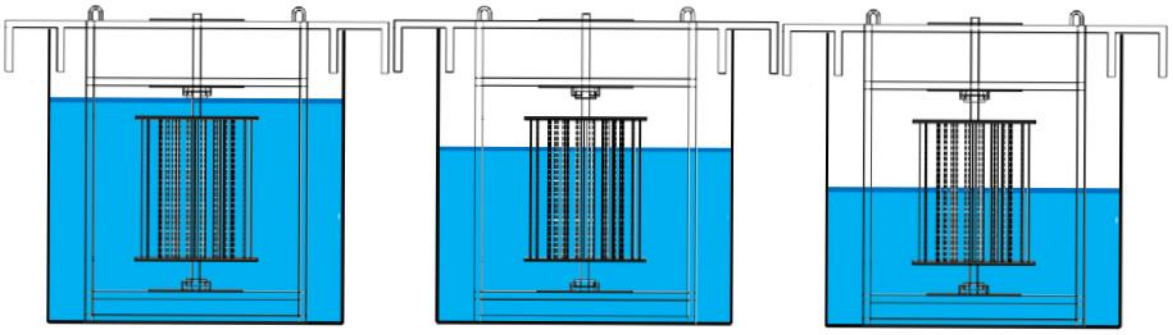
Fig. 5.4. Torque sensor.

The MBHKTs output torque was precisely measured using the Honeywell Model 1703 torque sensor with 0.02 N·m to 1500 N·m capacity range (Fig. 5.4). It may be used in both laboratory and industrial applications because to its small size and variety of mounting

choices. It guarantees exact monitoring of the MBHKT's functioning and enables correct assessment of power transfer and efficiency by recording torque data in real-time and turning it into electrical signals.

5.1.4 Methodology

The experimental investigation was conducted under controlled laboratory conditions to evaluate the effect of flow conditions and turbine immersion level on MBHKT performance. Prior to the experiment, the MBHKT and all measuring instruments were assembled, inspected, and calibrated to ensure accurate measurements. The water circulation system was then operated until a stable flow condition was achieved before data collection commenced. The experiment was performed by varying two main parameters: flow control setting and turbine immersion level. Three turbine immersion conditions were achieved: (i) fully submerged (100% immersion), (ii) partially submerged at 75% immersion, and (iii) partially submerged at 50% immersion as shown in Fig. 5.5. For each immersion condition, the flow rate was adjusted using three valve opening positions: 90° opening (fully open), 70° opening (approximately 78% open), and 50° opening (approximately 56% open). This resulted in a total of nine experimental conditions. For each test condition, the MBHKT was positioned at the required immersion level and the desired valve opening was set to establish the corresponding flow condition. After allowing the system to reach steady-state operation, the required experimental parameters were measured and recorded. The measurements included flow characteristics and turbine operating parameters such as rotational speed, torque, power output, and efficiency, depending on the available instrumentation. The same procedure was repeated for all combinations of immersion levels and valve openings to ensure consistency and reliability of the experimental data. The collected data were subsequently analysed to evaluate the performance characteristics of the MBHKT under different operating conditions.



Turbine fully submerged (100% Immersion) | **Turbine partially submerged (75% Immersion)** | **Turbine partially submerged (50% Immersion)**

Fig. 5.5. MBHKT immersion conditions for experiments.

5.1.5 Uncertainty Analysis

"Uncertainty" is the range of potential measurement values for physical quantities that includes the true values of physical quantities or the domain of approximated parameter values. There are two types of errors: random and systematic. When same environmental circumstances are used for the research, random errors fluctuate but systematic errors do not. Random errors can be minimized by the complete experimental procedure and the operating conditions, but systematic errors are inevitable and cannot be averted. Type A (internal uncertainty) and Type B (external uncertainty) are the two main types of uncertainty, according to these errors. Internal uncertainty (Type A), which is calculated for every experiment parameter by statistical analysis, is associated with random errors.

During the experiments, physical attributes such as velocity, flow, torque, etc. were measured using instruments with inherent uncertainty, which is reflected in the accuracy of the devices. External uncertainty (Type B), which can be computed using the information from the individual data books or calibration reports of the instruments, is associated with systematic errors.

5.1.5.1 Statistical Uncertainty

In the experiments, the internal uncertainties are derived from statistical analysis of

repeated measurements at each prescribed time-period. Data for a specified measurement for number of repetitive experiments have been considered and approximate individual uncertainties has been calculated.

$$\%\ Uncertainity = \frac{U_l}{Average\ of\ \bar{X}} \tag{6.1}$$

For each prescribed point of the system, estimated quantity X is arithmetic mean $\overline{X}$ of N number of observations X_i and internal uncertainty is the standard deviation σ of mean $\bar{X}$, that can be calculated by,

$$U_l = \sqrt{\frac{\sigma_1^2 + \sigma_2^2 + \sigma_3^2 + \cdots \sigma_N^2}{N^2}} \tag{6.2}$$

where,

$$\sigma = \sqrt{\frac{\sum_{i=1}^{N}(X_i - \bar{X})^2}{N}} \tag{6.3}$$

$$\bar{X} = \frac{\sum_{i=1}^{N} X_i}{N} \tag{6.4}$$

The internal uncertainties of individual parameters have been stated in Table 5.1 using statistical analysis mentioned above.

Table 5.1.

Statistical uncertainty at different immersion levels.

Immersion Level	**Valve Opening Position**	U_m **(m/s)**	**Internal Uncertainty (%)**	
			Torque	**rpm**
100% immersion	50°	0.51	0.0799	0.1410
	70°	0.61	0.2653	0.1316
	90°	0.72	0.0953	0.1125
75% immersion	50°	0.45	3.3670	3.0798
	70°	0.51	1.0846	0.6684

Immersion Level	Valve Opening Position	U_m (m/s)	Internal Uncertainty (%)	
			Torque	rpm
50% immersion	90°	0.65	1.0538	0.5900
	50°	0.37	4.1685	2.1925
	70°	0.45	3.5172	0.7469
	90°	0.51	3.2161	1.5025

5.1.5.2 Experimental Uncertainty

A more precise method of evaluating uncertainty in experimental data has been established by Kline and McClintock [117]. The approach is based on a careful characterisation of the uncertainties in the main experimental measurements. In the analysis, let the result R is a given function of the independent variables $x_1, x_2, x_3, \dots, x_n$ and $\omega_1, \omega_2, \omega_3, \dots, \omega_n$ be the uncertainties associated with the independent variables then ω_R the resultant uncertainty can be calculated as,

$$\omega_R = \sqrt{\left(\frac{\partial R}{\partial x_1}\omega_1\right)^2 + \left(\frac{\partial R}{\partial x_2}\omega_2\right)^2 + \cdots + \left(\frac{\partial R}{\partial x_n}\omega_n\right)^2} \tag{6.5}$$

Based on the systemic errors of each instrument, the experimental uncertainty analysis was carried out for the performance parameters stated in subsection 4.2.2. The obtained experimental uncertainties are depicted in Table 5.2.

Table 5.2.

Experimental uncertainty at different immersion levels.

Immersion Level	Valve Opening Position	U_m (m/s)	Experimental Uncertainty (%)	
			C_T	C_P
100% immersion	50°	0.51	0.8916	1.0555
	70°	0.61	0.2640	0.2461

Immersion Level	Valve Opening Position	U_m (m/s)	Experimental Uncertainty (%)	
			C_T	C_P
	90°	0.72	0.2221	0.1893
75% immersion	50°	0.45	1.4823	1.4944
	70°	0.51	0.8897	0.9278
	90°	0.65	0.3485	0.3219
50% immersion	50°	0.37	4.2808	3.3565
	70°	0.45	2.0516	1.5843
	90°	0.51	1.1380	0.8488

5.2 Numerical Methodology

The numerical methodology explained in Section 4.1 is same followed for the performance analysis of MBHKT at laboratory. To carry out the numerical simulation, the approach used in this work is illustrated in a flow chart as shown in Fig. 5.6.

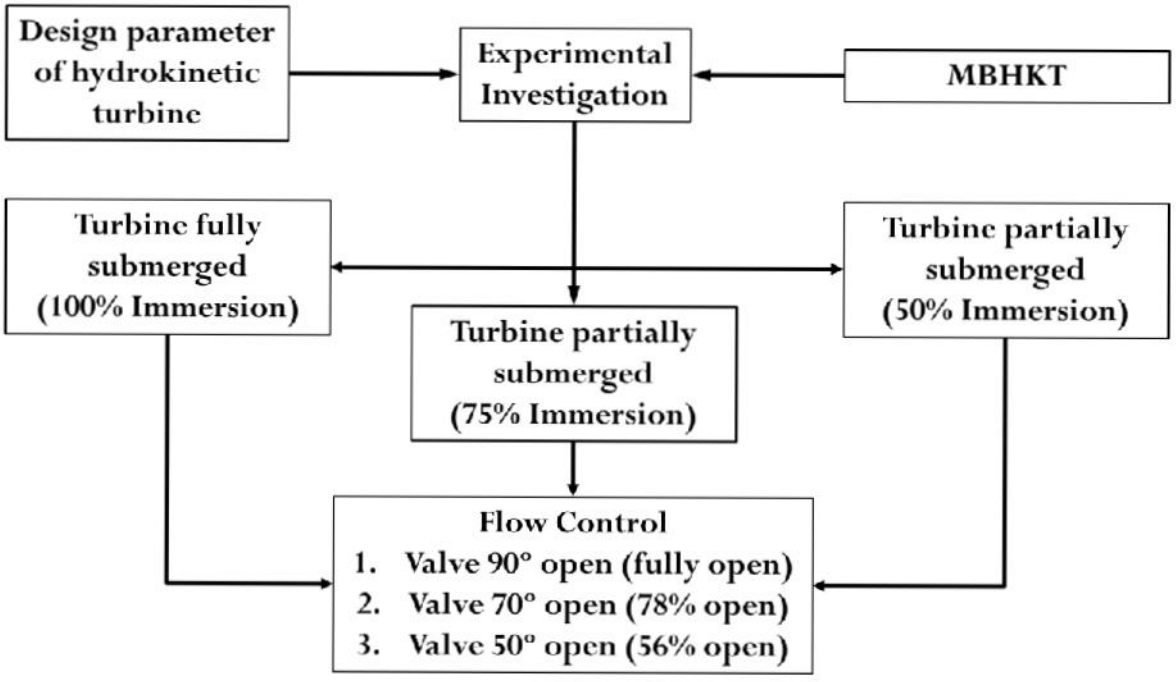


Fig. 5.6. Flow chart of approach used for MBHKT analysis in laboratory.

The geometry of MBHKT used for the analysis in Subsection 4.1.1 is used for the construction of 3-D computational domain of all the immersions as depicted in Fig. 5.7. Also, the boundary conditions used for the CFD analysis are tabulated in Table 5.3.

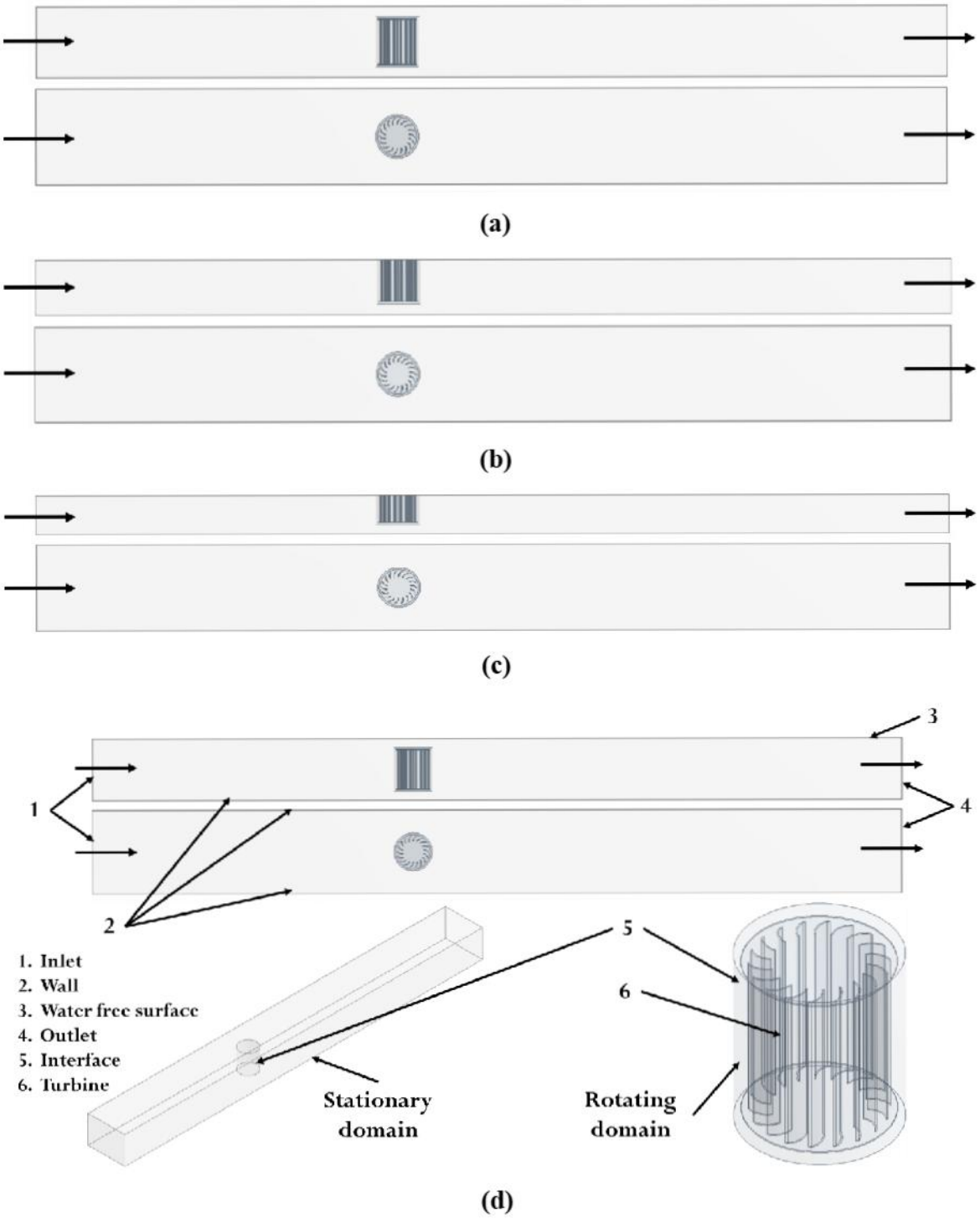


Fig. 5.7. 3-D computation domain of MBHKT at (a) fully submerged (100% immersion), (b) partially submerged at 75% immersion, and (c) partially submerged at 50% immersion (d) the whole domain.

Table 5.3.

Boundary conditions for 3-D computational domain of MBHKT.

Name	Boundary Type	Boundary Conditions
Inlet	Velocity inlet	Uniform flow
Open channel wall	Wall	Stationary
Water free surface	Symmetry	Symmetry
Outlet	Pressure outlet	Pressure outlet
Turbine	No slip wall	Rotates at desired rpm

5.3 Results and Discussion

This section presents comprehensive experimental and numerical results of MBHKT for different valve openings at various MBHKT immersions. For every value of the parameters taken into consideration, simulation results have been obtained. Nonetheless, the flow distribution surrounding the MBHKT is explained correspondence to the $C_{P,max}$ value.

5.3.1 Performance Characteristics Curves

The flow velocity and TSR obtained for different immersion levels at various valve openings are tabulated in Table 5.4. Also, the values of C_T, C_P and $P_{turbine}$ are also included in the table for respective valve openings.

Table 5.4.

Performance parameters values at different immersion levels.

Immersion Level	**Valve Opening Position**	U_m **(m/s)**	***TSR***	**Experimental**			**Numerical**		
				C_T	C_P	$P_{turbine}$ **(W)**	C_T	C_P	$P_{turbine}$ **(W)**
100% immersion	50°	0.51	1.2353	0.1467	0.1813	2.1246	0.1637	0.2023	2.3709
	70°	0.61	1.0328	0.1788	0.1846	3.7029	0.2198	0.2270	4.5527
	90°	0.72	0.8750	0.1391	0.1217	4.0145	0.1615	0.1413	4.6596
75% immersion	50°	0.45	1.1812	0.1097	0.1296	1.0433	0.1275	0.1506	1.2130
	70°	0.51	1.0809	0.1409	0.1523	1.7851	0.1594	0.1723	2.0197
	90°	0.65	0.9692	0.0954	0.0924	2.2428	0.1082	0.1049	2.5454
50% immersion	50°	0.37	0.8513	0.1593	0.1356	0.6069	0.1900	0.1618	0.7242
	70°	0.45	0.7875	0.1810	0.1425	1.1476	0.2107	0.1659	1.3361
	90°	0.51	0.7334	0.1086	0.0797	0.9338	0.1318	0.0966	1.1327

The variation in C_T with TSR for MBHKT at all three immersion conditions is depicted in Fig. 5.8. It can be observed that C_T increases with increasing TSR until an optimum point and then decreases gradually beyond that region. The $C_{T,max}$ values are observed for the fully immersed turbine condition, while reduced immersion conditions show comparatively lower C_T. Higher torque generation at full immersion is associated with greater momentum transfer between the incoming flow and MBHKT blades. The CFD predictions reproduce the overall experimental trend; however, the numerical results generally overpredict the measured performance parameters. The degree of discrepancy varies with the operating and immersion conditions and is discussed further in the numerical–experimental validation analysis. This difference may arise from simplifications in the numerical model and uncertainties associated with experimental measurements. The close agreement between experimental and numerical trends validates the computational approach for predicting the hydrodynamic performance of MBHKT systems.

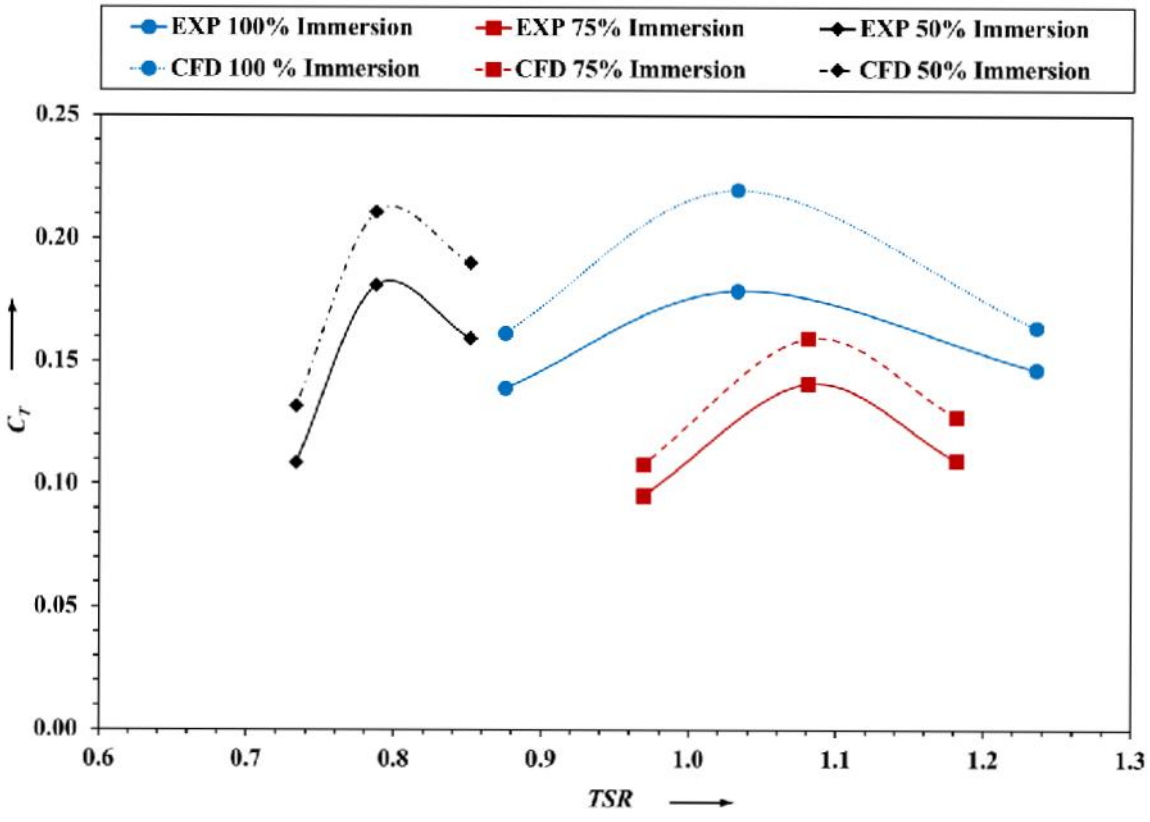


Fig. 5.8. Variation of C_T with TSR for different immersion conditions.

Similarly, the variation in C_P with TSR for MBHKT at all three immersion conditions is shown in Fig. 5.9. The variation of C_P with TSR indicates that the performance of the MBHKT strongly depends on the operating TSR and immersion level. For all immersion conditions, both experimental and CFD results show an initial increase in C_P with TSR, reaching a peak value and then decreasing slightly at higher TSR values. The 100% immersion condition exhibits the $C_{P,max}$ among all cases, indicating energy extraction capability due to maximum interaction between the turbine blades and the water stream. The $C_{P,max}$ occurs approximately around TSR ≈ 1.05-1.10, suggesting the optimum operating range of the MBHKT. The simulation results consistently predict slightly higher values compared to the experimental observations, which can be attributed to idealized assumptions in numerical simulations and unavoidable experimental losses such as mechanical friction, turbulence fluctuations, and flow non-uniformity. Lower immersion conditions (75% and 50%) demonstrate reduced C_P because of the reduced effective flow area and lower water force on the rotor blades.

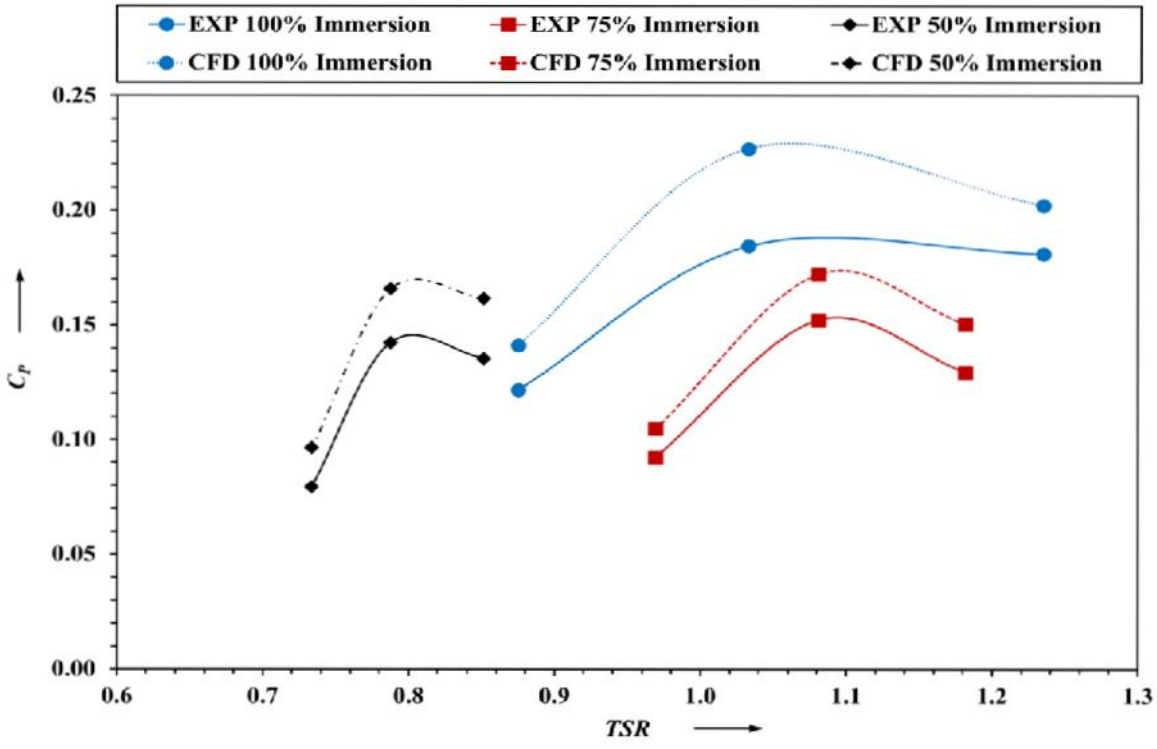


Fig. 5.9. Variation of C_P with TSR for different immersion conditions.

The variation of $P_{turbine}$ with incoming Um, shown in Fig. 5.10, indicates that the influence of flow velocity on the generated power depends on the turbine immersion condition. For the 100% and 75% immersion conditions, the experimental and numerical results show an overall increase in turbine power with increasing incoming velocity. This behavior is associated with the increase in the available kinetic energy of the flowing water and the resulting enhancement in momentum transfer to the turbine blades.

However, a different trend is observed experimentally at 50% immersion. The turbine power increases from 0.6069 W at U_m = 0.37 m/s to 1.1476 W at U_m = 0.45 m/s, but subsequently decreases to 0.9338 W at U_m = 0.51 m/s. This indicates that, under partial immersion, an increase in incoming flow velocity does not necessarily result in a proportional increase in useful power extraction. At 50% immersion, only a reduced portion of the rotor interacts effectively with the incoming flow. The reduced submerged blade area and the proximity of the rotor to the free surface can lead to non-uniform flow interaction, increased flow disturbances, and unstable hydrodynamic loading on the blades. Consequently, at the higher velocity, the increase in available flow energy may not be effectively converted into turbine power, resulting in the observed reduction in the experimental power output.

The numerical results for the 50% immersion condition show a continuous increase in $P_{turbine}$ with increasing U_m. The difference between the experimental and numerical trends may be attributed to the idealized representation of the flow and turbine system in the numerical model, whereas the experimental condition is affected by additional physical phenomena, including free-surface disturbances, non-uniform flow interaction, mechanical losses, and flow fluctuations. The higher uncertainties associated with the 50% immersion experiments may also contribute to the observed variation in the measured results.

Overall, the results demonstrate that increasing incoming velocity generally enhances

turbine power under higher immersion conditions; however, at 50% immersion, the reduced and non-uniform interaction between the flow and the turbine limits the effective conversion of the available kinetic energy. The fully immersed condition provides the most favourable and stable operating condition, producing the highest power output.

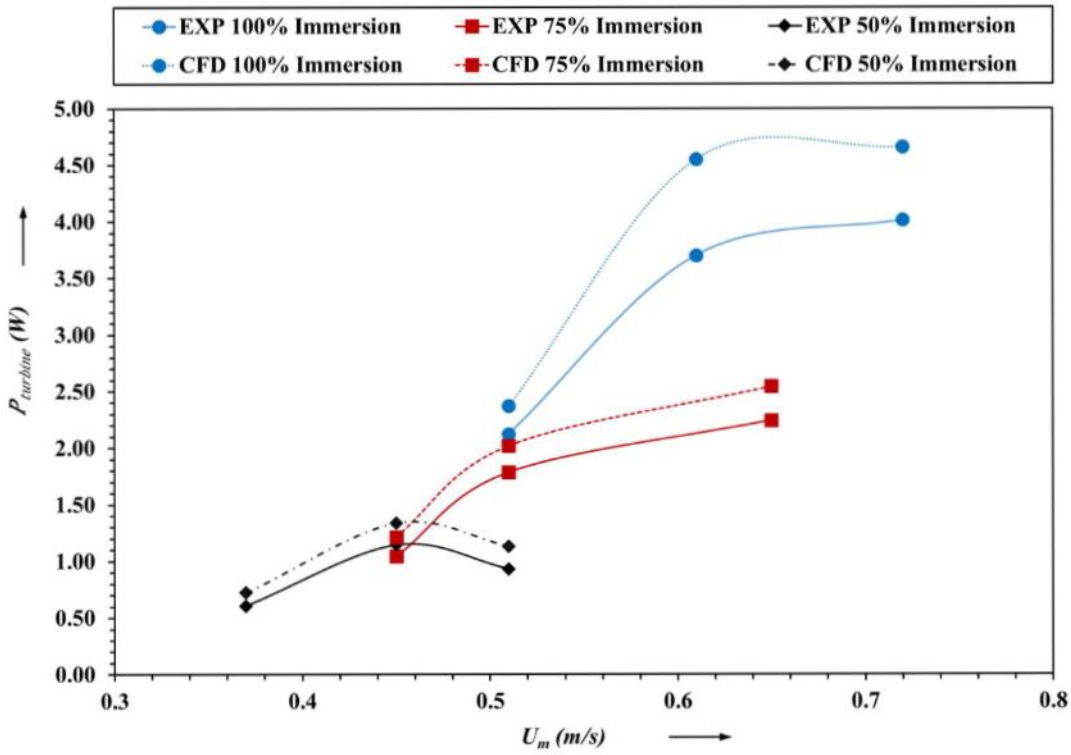


Fig. 5.10. Variation of $P_{turbine}$ with U_m for different immersion conditions.

Overall, the numerical and experimental results show reasonable agreement in capturing the general variation of MBHKT performance under different immersion conditions, although the numerical model generally overpredicts the measured performance parameters. The discrepancies can be attributed to the idealized assumptions in the numerical model and the practical effects present during the experiments, including flow non-uniformity and fluctuations, mechanical losses, and additional free-surface disturbances under partial immersion. The reported uncertainty values further indicate that the experimental results are comparatively more sensitive at lower immersion conditions, particularly at 50% immersion. However, as some numerical–experimental differences exceed the reported uncertainty range, the discrepancies cannot be attributed solely to

measurement uncertainty. Overall, the validation supports the use of the numerical model for predicting the general performance trends and conducting comparative analyses, while recognizing its tendency to over predict the absolute performance values under the investigated operating conditions.

5.3.2 Field Visualizations

The flow distribution surrounding the MBHKT is explained correspondence to the $C_{P,max}$ value which is obtained at 70° opening (approximately 78% open) for all the immersion cases. Figs. 5.11 to 5.13 represent the flow-field characteristics of the MBHKT at 100%, 75%, and 50% immersion conditions, respectively.

The pressure distribution surrounding the rotor is comparatively consistent at 100% immersion (Fig. 5.11 (a)), with a distinct pressure differential between the upstream and downstream areas. Stable pressure development and gentler pressure gradients are the outcome of the totally submerged situation, which permits the incoming flow to interact with the turbine over an entire blade area. Under 75% immersion (Fig. 5.12 (a)), the pressure contours begin to exhibit a less uniform pattern. Regions of elevated pressure become more concentrated near the blade surfaces directly exposed to the incoming stream, while pressure reduction behind the rotor appears more localized. The reduction in submergence alters the incoming flow structure and introduces moderate disturbances around the turbine. While for the 50% immersion case (Fig. 5.13 (a)), the pressure field displays stronger non-uniformity with more concentrated pressure zones near the upstream side of the rotor. The decrease in submerged blade area limits the interaction between the flow and the turbine, causing uneven pressure loading and more pronounced flow disturbances downstream.

Velocity contours at 100% immersion (Fig. 5.11 (b)) shows a clearly defined wake region extends behind the turbine. The lower velocity area downstream suggests that a significant amount of kinetic energy is extracted from the incoming flow. The larger wake

structure reflects stronger momentum transfer from the fluid to the rotating rotor. In the 75% immersion condition (Fig. 5.12 (b)), the wake region remains identifiable but becomes relatively shorter and narrower compared with the fully submerged case. Although effective interaction between the flow and rotor continues to occur, the decrease in submergence reduces the extent of energy extraction. The 50% immersion configuration (Fig. 5.13 (b)) exhibits a weaker and more dispersed wake structure. Faster recovery of flow velocity downstream indicates that a greater portion of the incoming flow bypasses the turbine without contributing effectively to rotor motion. This behaviour suggests reduced momentum exchange between the fluid and the rotating blades.

The velocity vector graphs provide additional information about the local flow behaviour and rotational impacts surrounding the turbine. For 100% immersion (Fig. 5.11 (c)), the vector distribution shows relatively smooth and orderly flow patterns around the rotor. The downstream flow direction progressively shifts, demonstrating a wake pattern and stable circulation caused by rotor motion. With 75% immersion (Fig. 5.12 (c)), various instabilities appear in the vector field. Localized recirculation zones are seen around the blade region, indicating the start of flow separation due to altered input conditions. Under 50% immersion (Fig. 5.13 (c)), the flow vectors show more directional variance and less orderly movement around the turbine. Reduced submergence causes stronger disruptions in the top flow region, resulting in unstable flow structures and higher recirculation effects.

Among the three operating conditions, 100% immersion has the preferable flow characteristics, with smoother pressure gradients, stronger wake production, and more orderly circulation patterns. The 75% immersion condition exhibits intermediate flow behaviour, whereas the 50% immersion instance exhibits weaker fluid-rotor interaction, increased flow instability, and decreased wake formation. The findings imply that increasing the immersion level enhances the MBHKT's overall hydrodynamic response under the 70°

valve opening condition, perhaps contributing to increased energy extraction capabilities. In the final stage of the current research work, the 100% immersion case of MBHKT with different blade profiles and augmentation systems was studied.

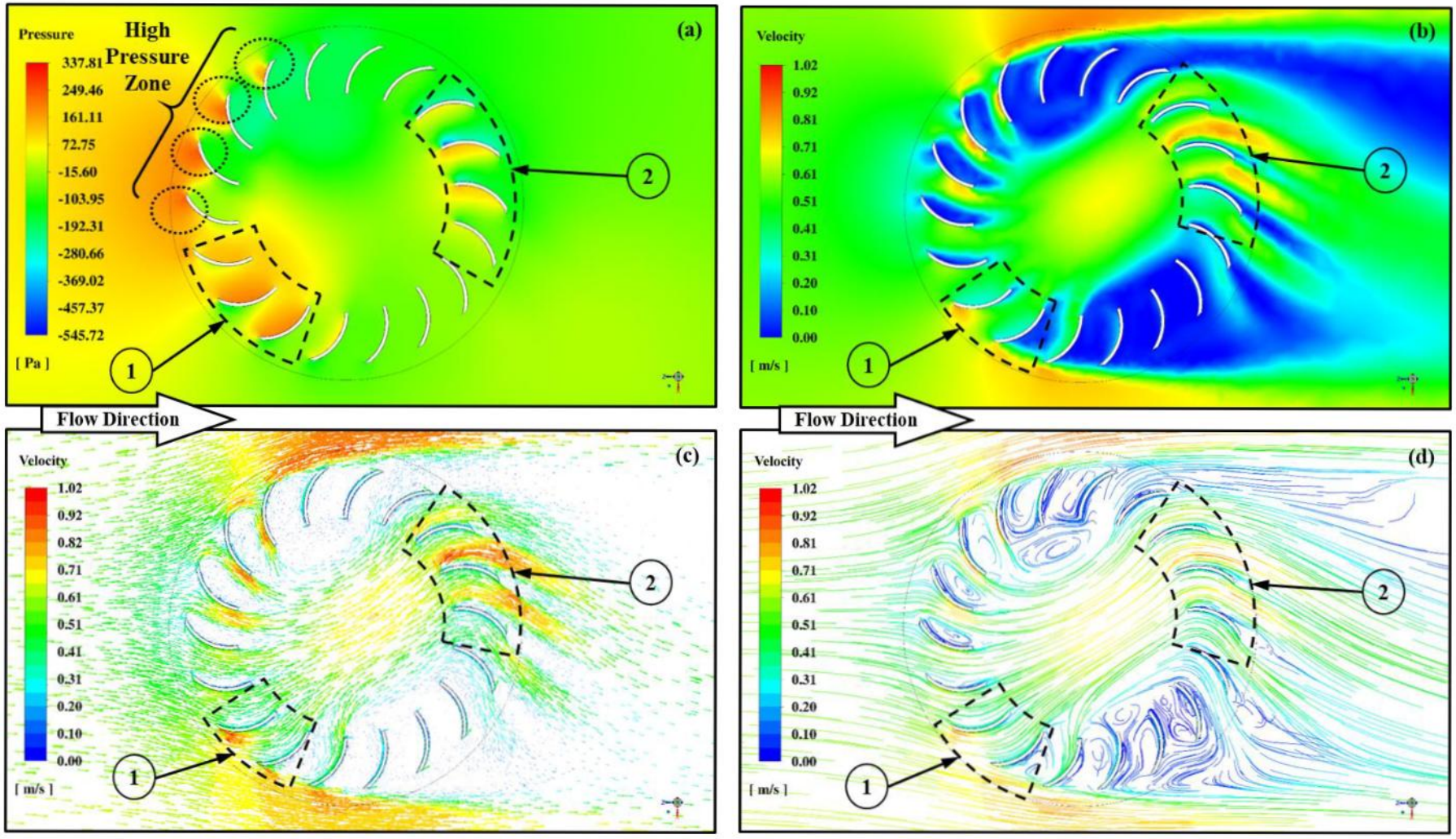


Fig. 5.11. Field visualizations for MBHKT at 100% immersion (a) pressure contours, (b) velocity contours, (c) velocity vectors, and (d) velocity streamline.

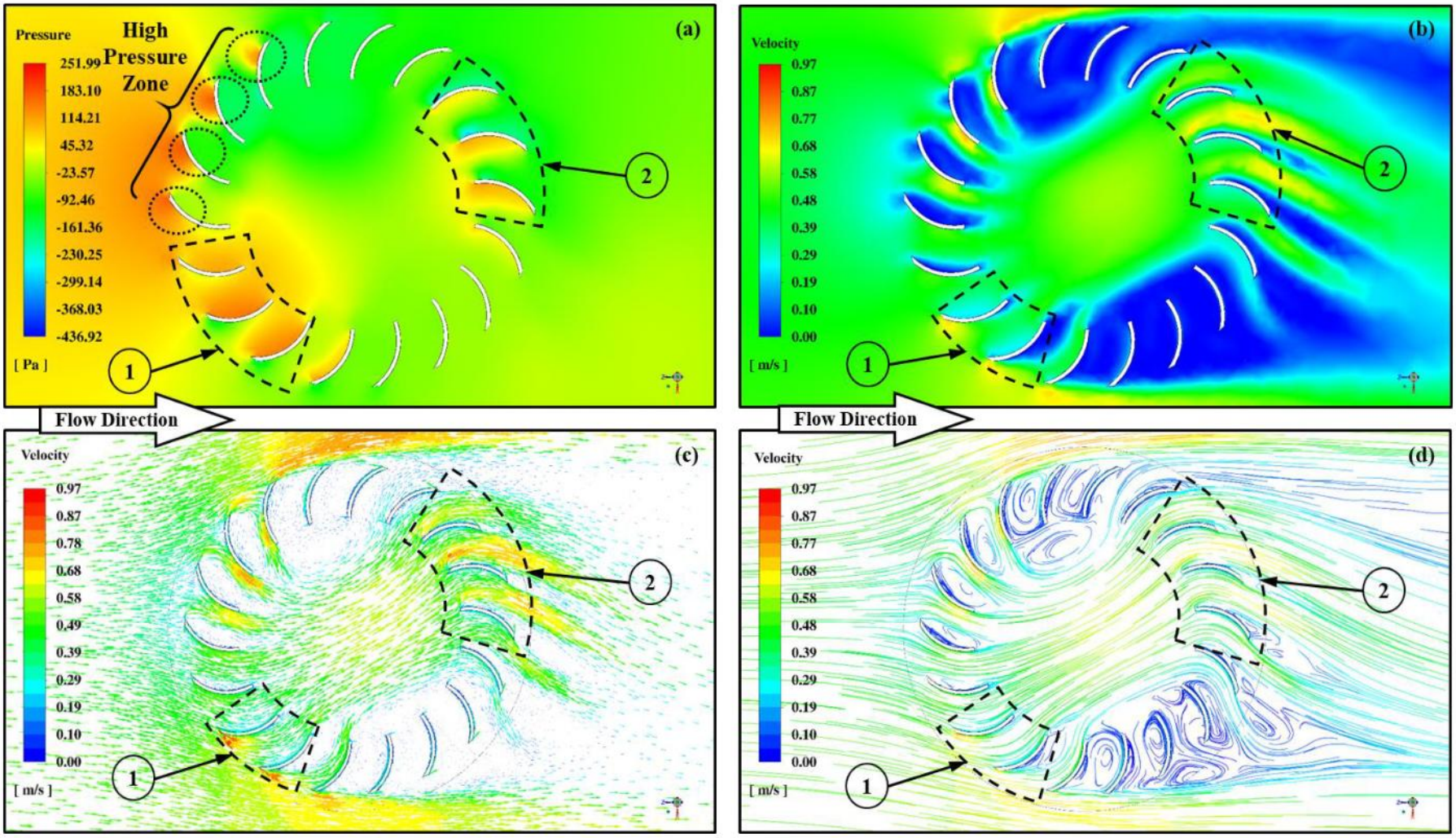


Fig. 5.12. Field visualizations for MBHKT at 75% immersion (a) pressure contours, (b) velocity contours, (c) velocity vectors, and (d) velocity streamline.

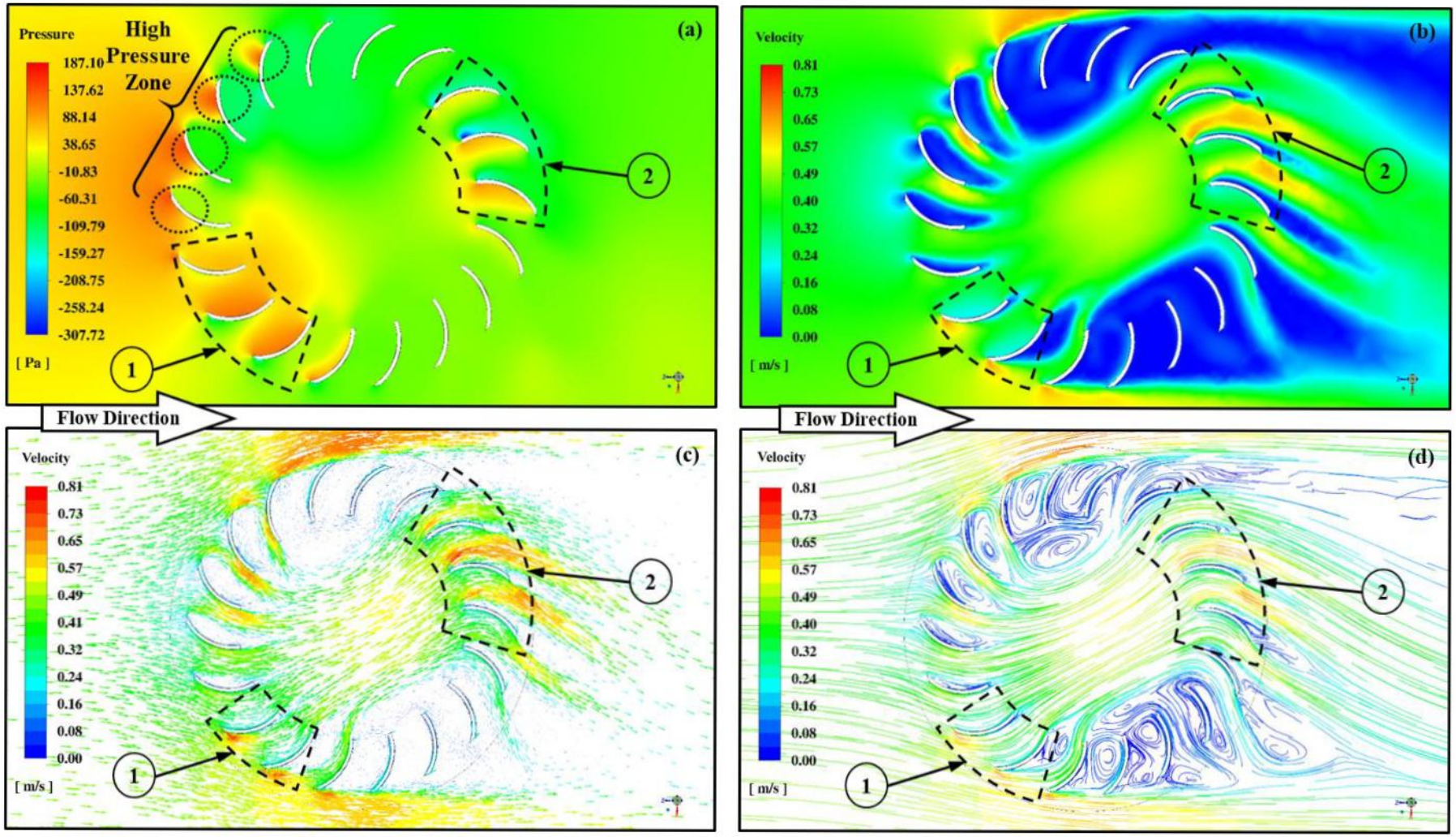


Fig. 5.13. Field visualizations for MBHKT at 50% immersion (a) pressure contours, (b) velocity contours, (c) velocity vectors, and (d) velocity streamline.

CHAPTER – 6

OPTIMIZATION AND AUGMENTATION OF MICHELL-BANKI HYDROKINETIC TURBINE IN OPEN CHANNEL BY NUMERICAL APPROACH

In the fourth and final stage of the present investigation, the optimization of three different blade profiles of MBHKT for fully submerged turbine (100% immersion) was numerically performed. Additionally, based on the optimum blade profile obtained the various augmentations combining the nozzle and diffuser were also simulated to find out the optimum design of augmentation which helps to develop the modular structure.

6.1 Numerical Methodology

To carry out the investigation of MBHKT optimization and augmentation, the approach used in this work is illustrated in a flow diagram as shown in Fig. 6.1. The same numerical methodology elaborated in Section 4.1 is followed for the performance analysis.

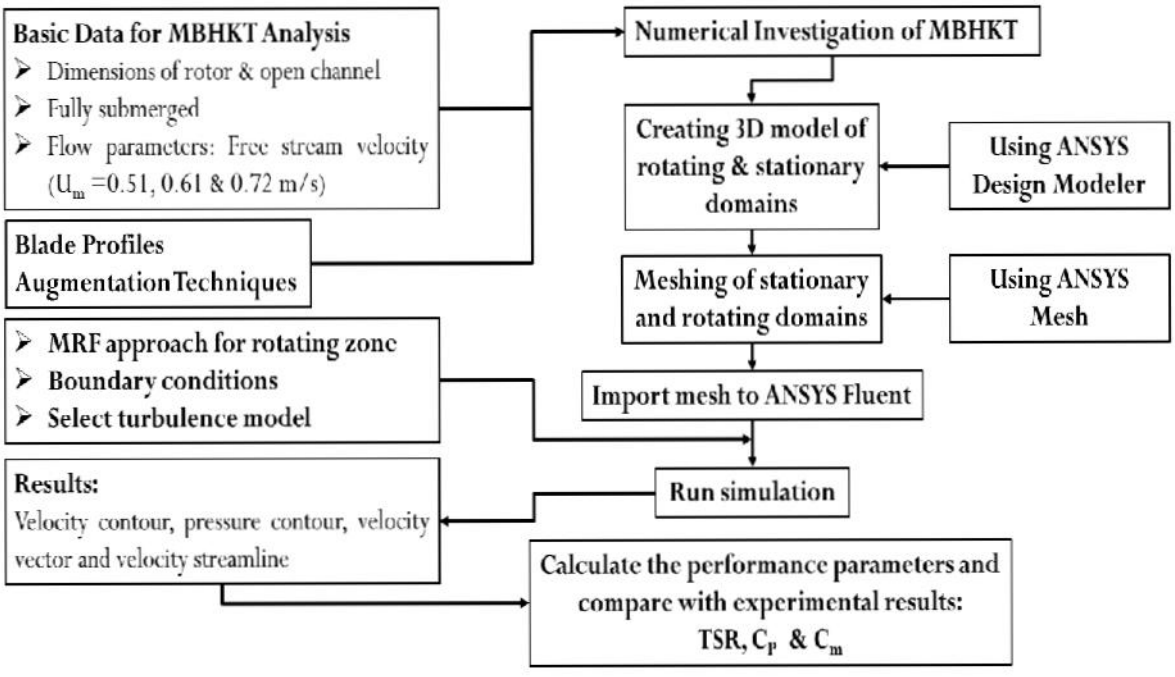


Fig. 6.1. Flow chart of approach used for MBHKT optimization and augmentation.

The 3-D computational domain of each blade profile shown in Fig. 6.2 is constructed using the MBHKT geometry utilized for the study in Subsection 4.1.1. The three different blade profiles of MBHKT are blade profile-1 – flat, blade profile-2 – round and blade profile-3 – sharp edged. The design of various augmentations combining the nozzle and diffuser namely, augmentation system-1 to augmentation system-4 is shown in Fig. 6.3. It represents four alternative augmentation geometries developed for a MBHKT, where the objective is to modify and accelerate the incoming flow before it reaches the turbine runner. The system consists of three primary regions: Section 1, representing the inlet augmentation passage; Section 2, representing the turbine runner with a diameter of Ø466 mm; and Section 3, representing the outlet or diffuser section. The red arrows indicate the direction of water flow through the augmented turbine arrangement. The geometries differ in terms of transition angle, flow passage dimensions, and the use of curved profiles around the turbine region, allowing comparison of their influence on flow acceleration and guidance into the runner.

The augmentation system-1 utilizes straight-walled inlet and outlet passages with a transition angle of 32° and a width of 483 mm. The inlet and outlet regions converge directly toward the MBHKT runner with linear boundaries, forming relatively abrupt geometric transitions where the flow passage meets the circular runner profile. In MBHKT application, this design acts as a basic augmentation arrangement intended to concentrate and direct water toward the runner. However, the sudden intersection between the flow passage and the runner boundary may generate localized flow disturbances and non-uniform velocity distribution at the runner inlet, potentially affecting energy extraction efficiency.

The augmentation system-2 maintains the same transition angle (32°) and dimensional characteristics but introduces curved surfaces around the turbine runner. Instead of allowing direct intersections between the runner and the augmentation walls, the passage smoothly wraps around the circular geometry. This curved transition is intended to guide the incoming

water more gradually toward the runner and reduce abrupt directional changes in the flow field. For a MBHKT, smoother flow guidance can improve the uniformity of water entry into the runner blades, potentially reducing flow separation and increasing energy transfer efficiency.

The third configuration, augmentation system-3 reduces the transition angle from 32° to 20° and increases the transition length to 795 mm, resulting in a wider augmentation channel (745 mm). The smaller transition angle creates a more gradual flow contraction and expansion process. Such a configuration may reduce losses associated with rapid acceleration or deceleration of the flow. However, similar to Design 1, the turbine runner still intersects directly with the surrounding passage boundaries, which can create localized disruptions near the runner interface. Although the gentler angle may improve flow stability, the geometric discontinuities may still influence the incoming flow characteristics.

The final augmentation system-4 combines the advantages of both modifications by incorporating a reduced transition angle (20°) and smooth curved connections around the turbine runner. This arrangement creates the most continuous flow path among the four designs. The longer transition region allows gradual acceleration of water, while the curved surfaces guide the flow around the runner with minimal abrupt changes in direction. For a MBHKT augmentation system, this design is expected to provide the most favorable hydraulic behavior by improving flow uniformity at the runner inlet, minimizing recirculation regions, and reducing hydraulic losses. Consequently, it may lead to enhanced turbine performance and higher power extraction efficiency.

The 3-D computational domain of all the augmentation systems is depicted in Fig. 6.4 with Table 6.1 containing a tabulation of the boundary conditions used in the CFD analysis.

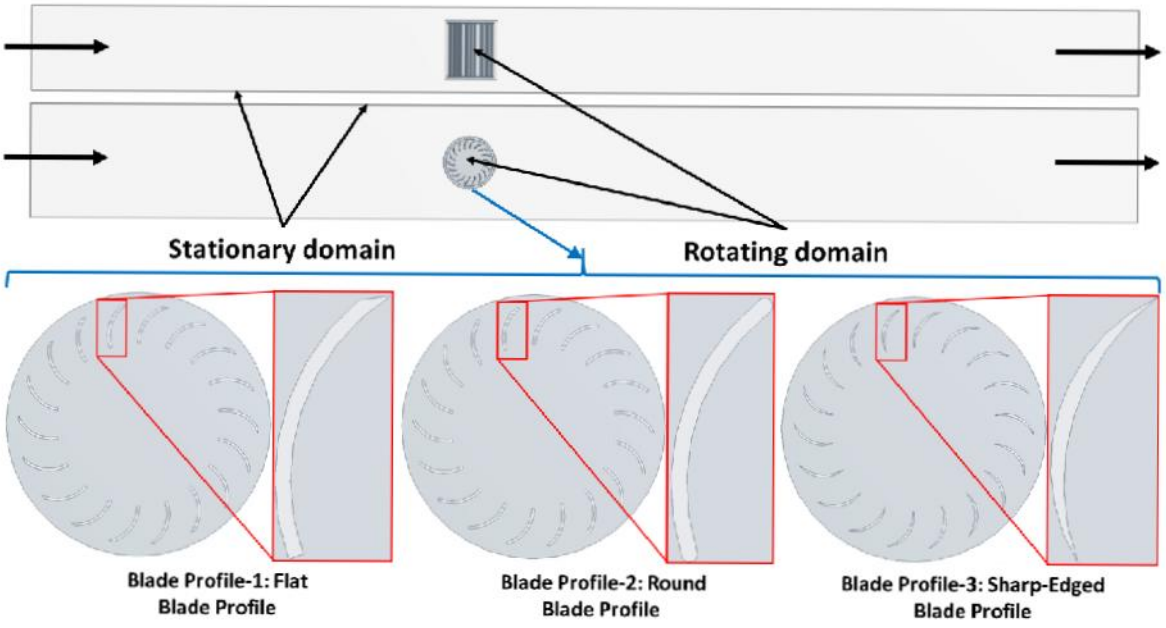


Fig. 6.2. Computation domain of MBHKTs with different blade profiles.

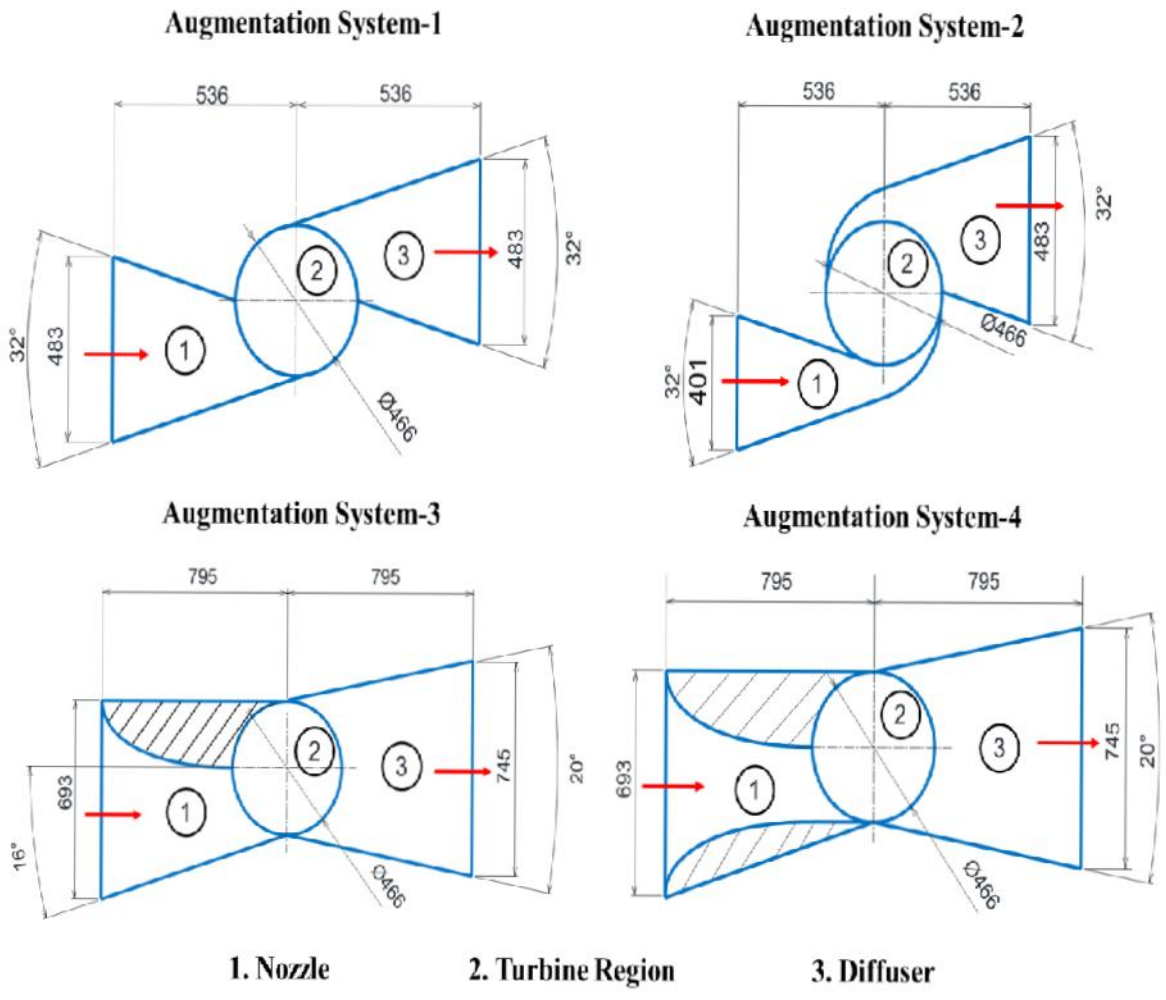


Fig. 6.3. Augmentation systems of MBHKT.

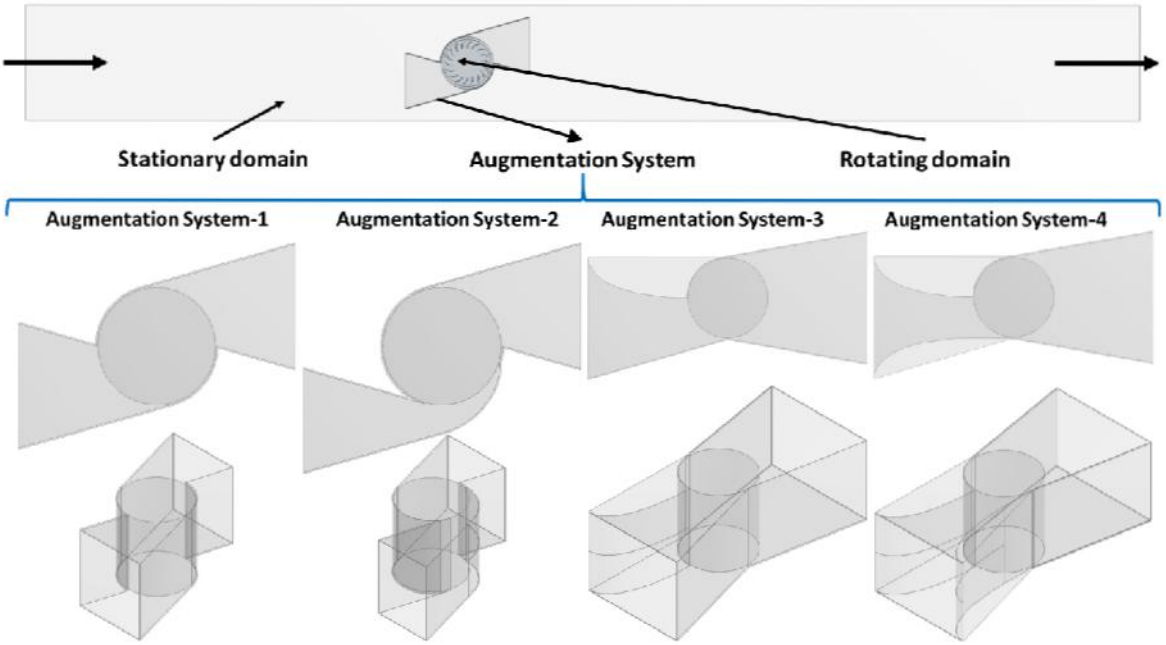


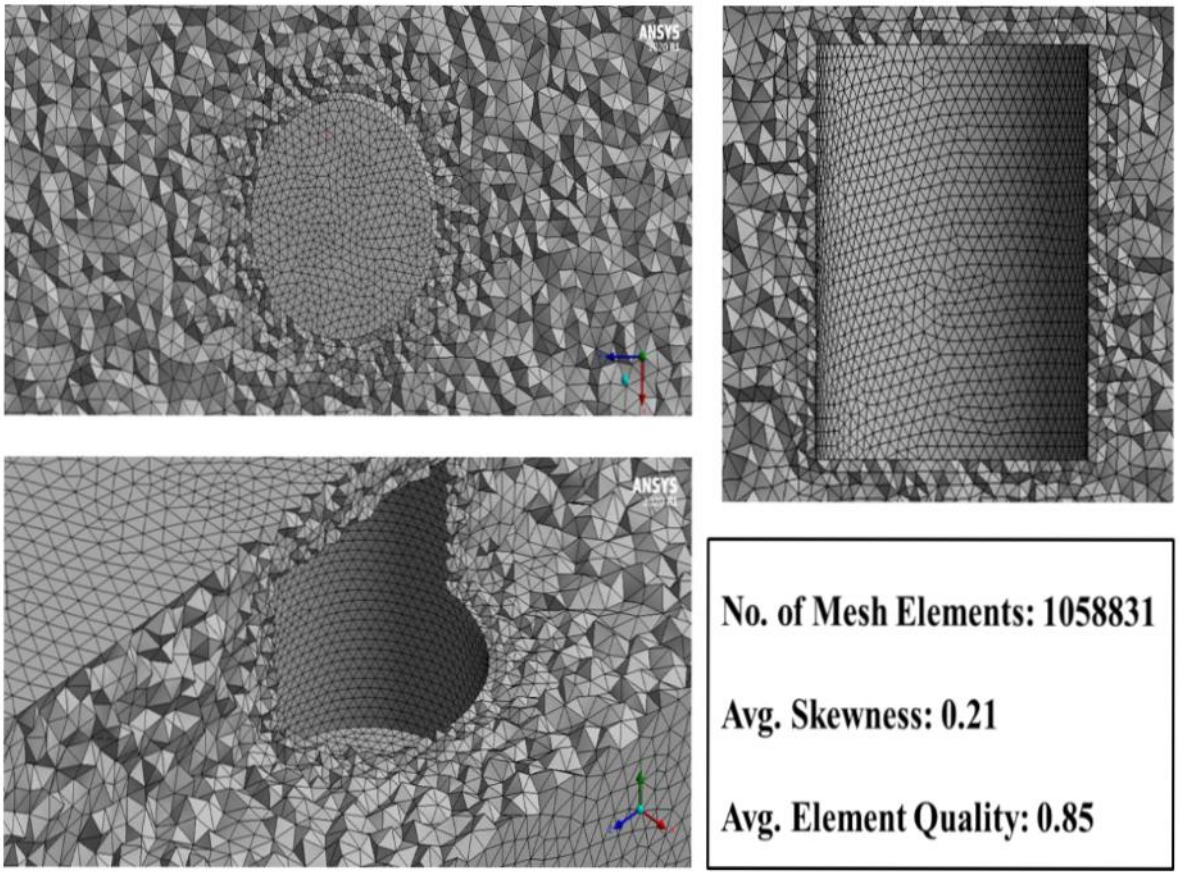
Fig. 6.4. Computation domain of various augmentation systems of MBHKT.

Table 6.1.

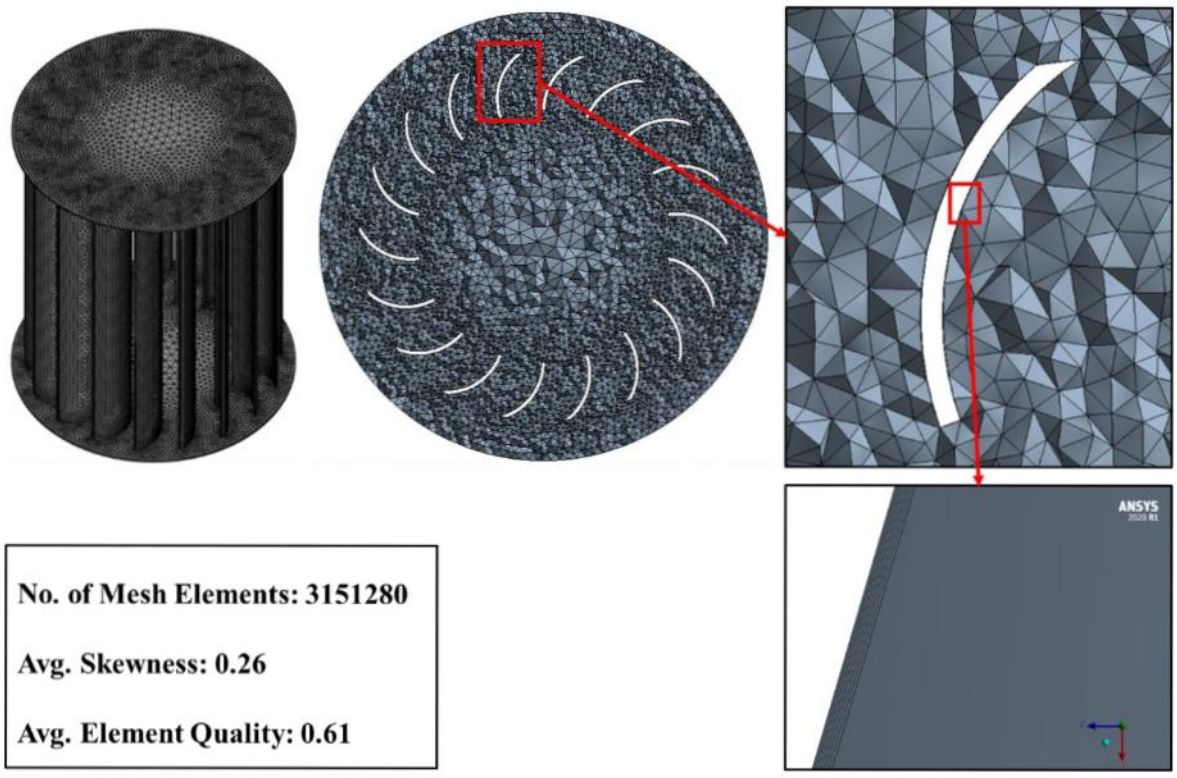
Boundary conditions for 3-D computational domain of various blade profiles and argumentation systems of MBHKT.

Name	Boundary Type	Boundary Conditions
Inlet	Velocity inlet	Uniform flow
Open channel wall	Wall	Stationary
Water free surface	Symmetry	Symmetry
Outlet	Pressure outlet	Pressure outlet
Turbine	No slip wall	Rotates at desired rpm

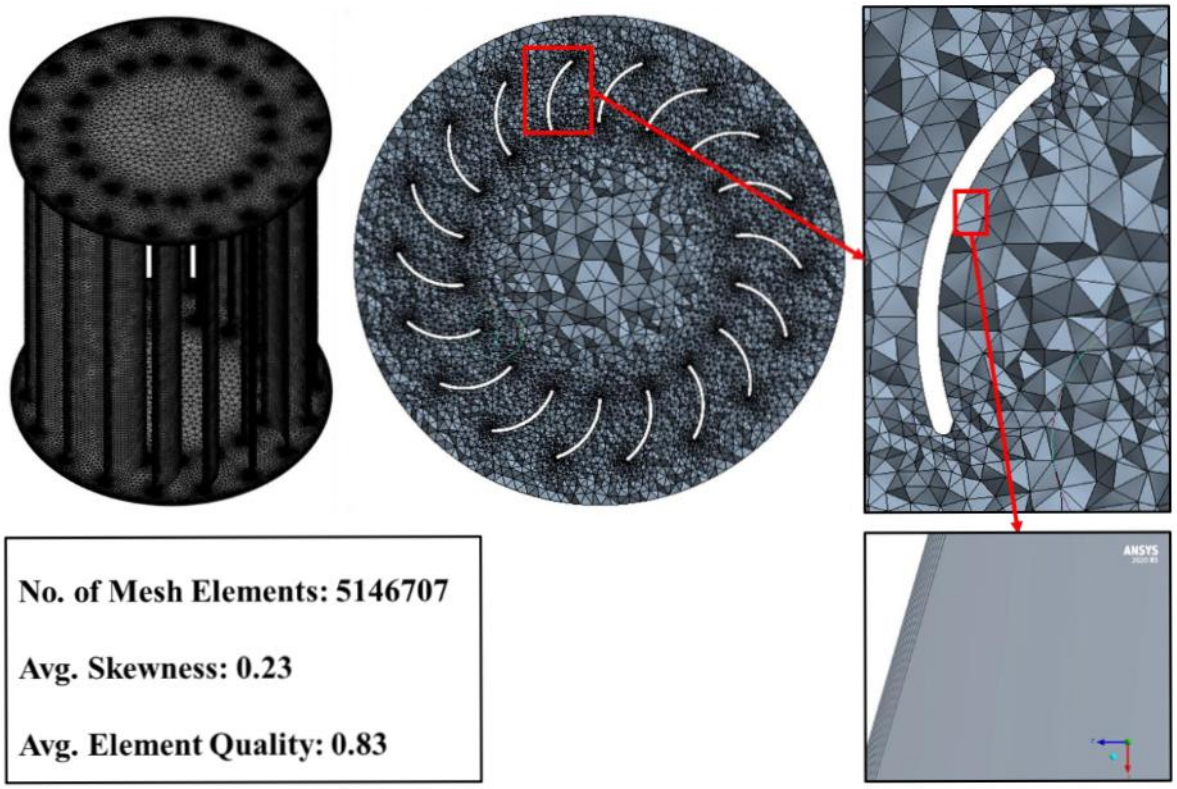
For the meshing of stationary and rotating domain, an unstructured grid of tetrahedral elements is used by ANSYS MESH. Fig. 6.5 (a) shows the meshing of stationary domain while Fig. 6.5 (b), (c), and (d) depicts the rotating domain of blade profile-1, blade profile-2 and blade profile-3, respectively. Similarly, meshing of stationary domain of augmentation system-1 to augmentation system-4 is illustrated in Fig. 6.6.


No. of Mesh Elements: 1058831
Avg. Skewness: 0.21
Avg. Element Quality: 0.85

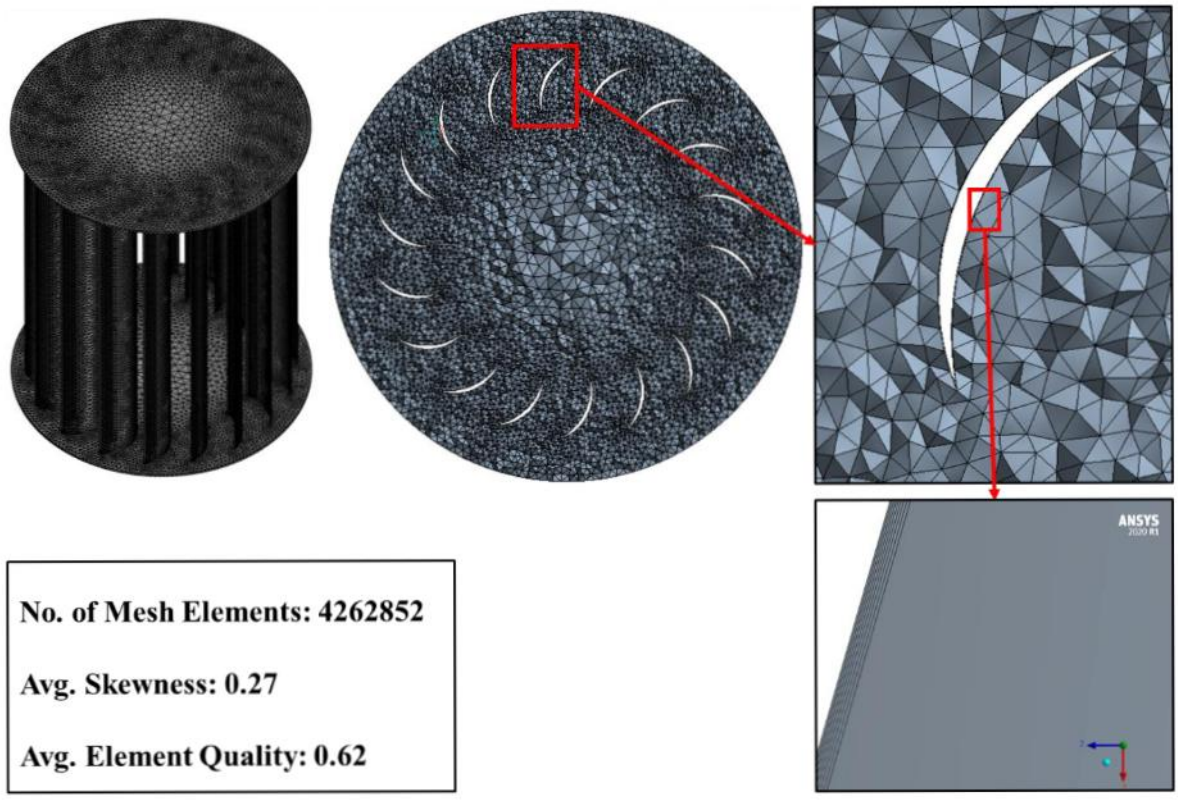
(a)


No. of Mesh Elements: 3151280
Avg. Skewness: 0.26
Avg. Element Quality: 0.61

(b)



(c)



(d)

Fig. 6.5. Meshing of the computational fluid domain of (a) stationary domain, (b) blade profile-1, (c) blade profile-2, and (d) blade profile-3.

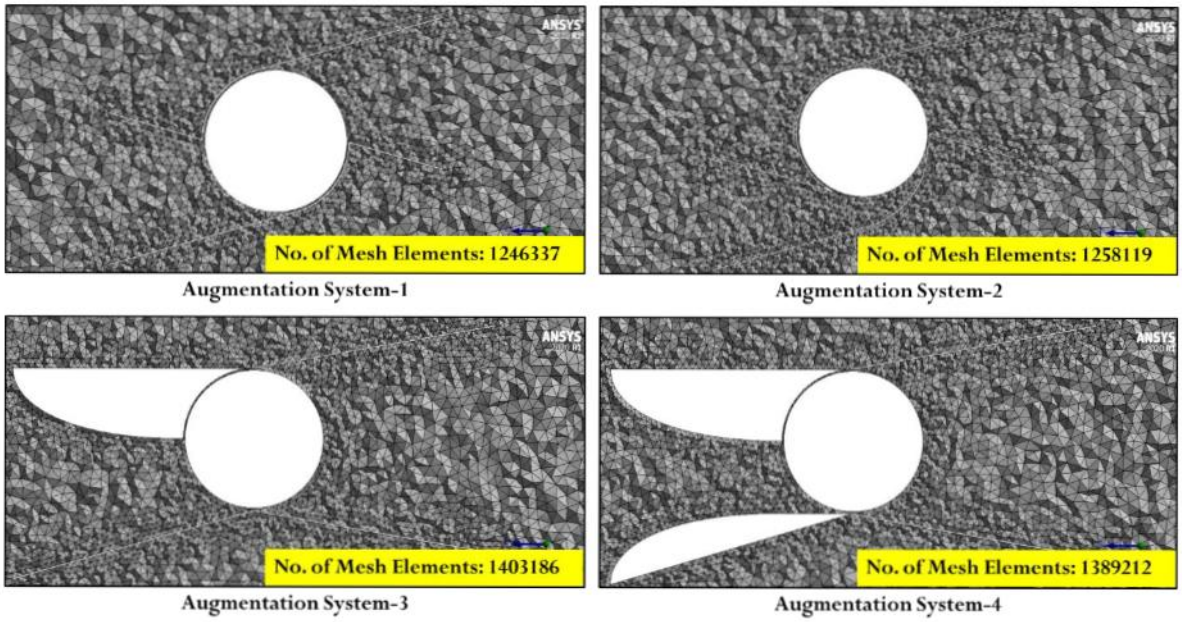


Fig. 6.6. Meshing of the computational fluid domain of various augmentation systems.

6.2 Results and Discussion

The simulation results for different blade profiles and augmentation systems are discussed in this section. The performance of sharp-edged profile is found to be the optimum among all three blades in terms of $C_{P,max.}$ Using the optimum blade profile-3, various augmentation systems were designed and studied. The flow field visualisations corresponding to the $C_{P,max}$ provide better idea about the enhancement.

6.2.1 Blade Profiles

The variation of C_T with TSR depicted in Fig. 6.7 reveals notable differences among the blade profiles. Similar to the C_P trend, the sharp-edged blade profile generates the $C_{T.max}$, reaching a maximum of approximately 0.2438 at TSR of 1.0328. Higher torque generation indicates stronger hydrodynamic forces acting on the rotor, which contributes to improved power extraction capability. The flat blade profile exhibits a trend closely matching the experimental data, with moderate thrust values throughout the TSR range. The round blade profile produces the lowest torque coefficients and shows a continuous reduction with increasing TSR. This reduction indicates weaker momentum exchange between the fluid

stream and the rotor blades. Although higher torque generally enhances energy capture, it may also increase structural loading on the turbine system. Therefore, blade profile optimization should consider both energy extraction.

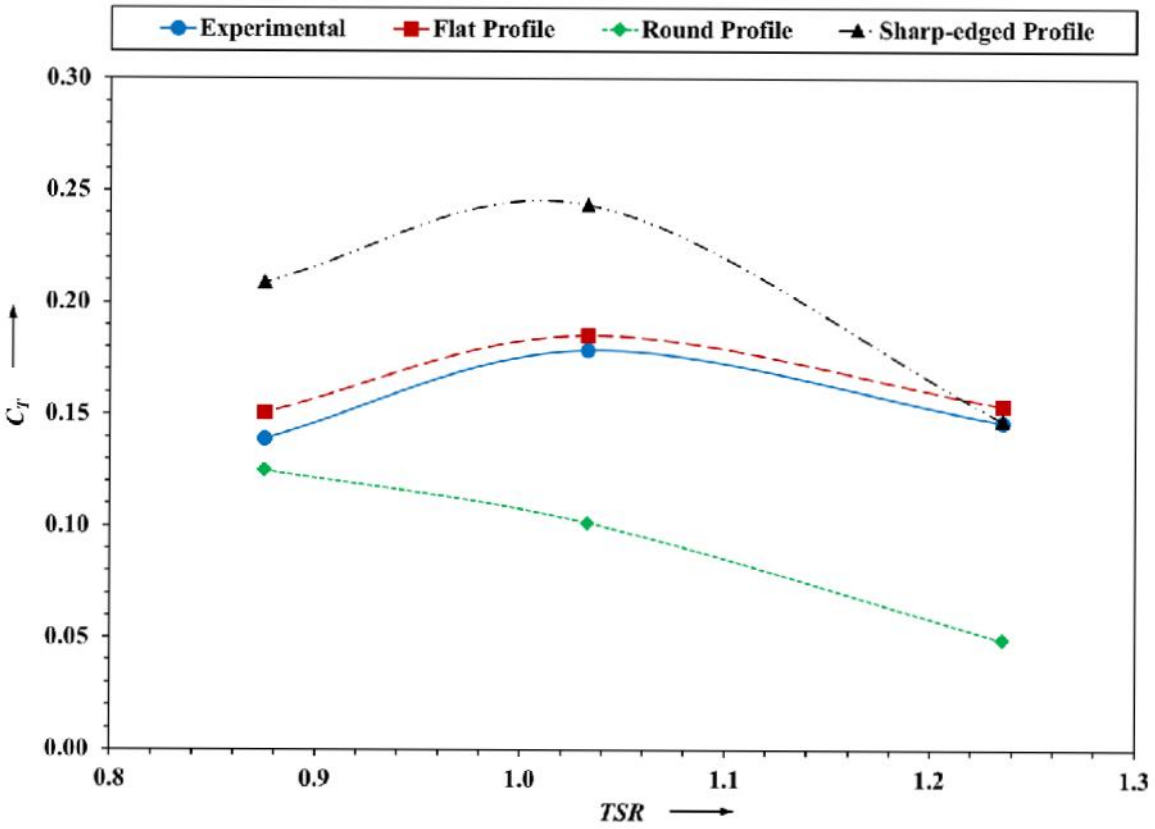


Fig. 6.7. Variation of C_T with TSR for different blade profiles.

The variation of C_P with TSR for different blade profiles shown in Fig. 6.8 demonstrates a significant influence of blade geometry on MBHKT performance. Among the investigated blade configurations, the sharp-edged profile exhibits the $C_{P,max}$ throughout the operating range, reaching a peak value of approximately 0.2517 at TSR of 1.0328. This indicates that the sharp-edged blade profile possesses superior energy extraction capability due to more effective interaction with the incoming flow and improved momentum transfer characteristics. The flat blade profile shows performance very close to the experimental results, with the $C_{P,max}$ around 0.1915 near the optimum TSR region. In contrast, the round blade profile demonstrates the lowest power coefficient values, showing a gradual reduction in performance at higher TSR values. The lower performance of the round profile may be

attributed to increased flow separation and less efficient hydrodynamic loading on the blade surfaces. Overall, the results suggest that blade edge geometry has a direct influence on turbine efficiency, with sharp-edged blades providing the most favorable power extraction characteristics.

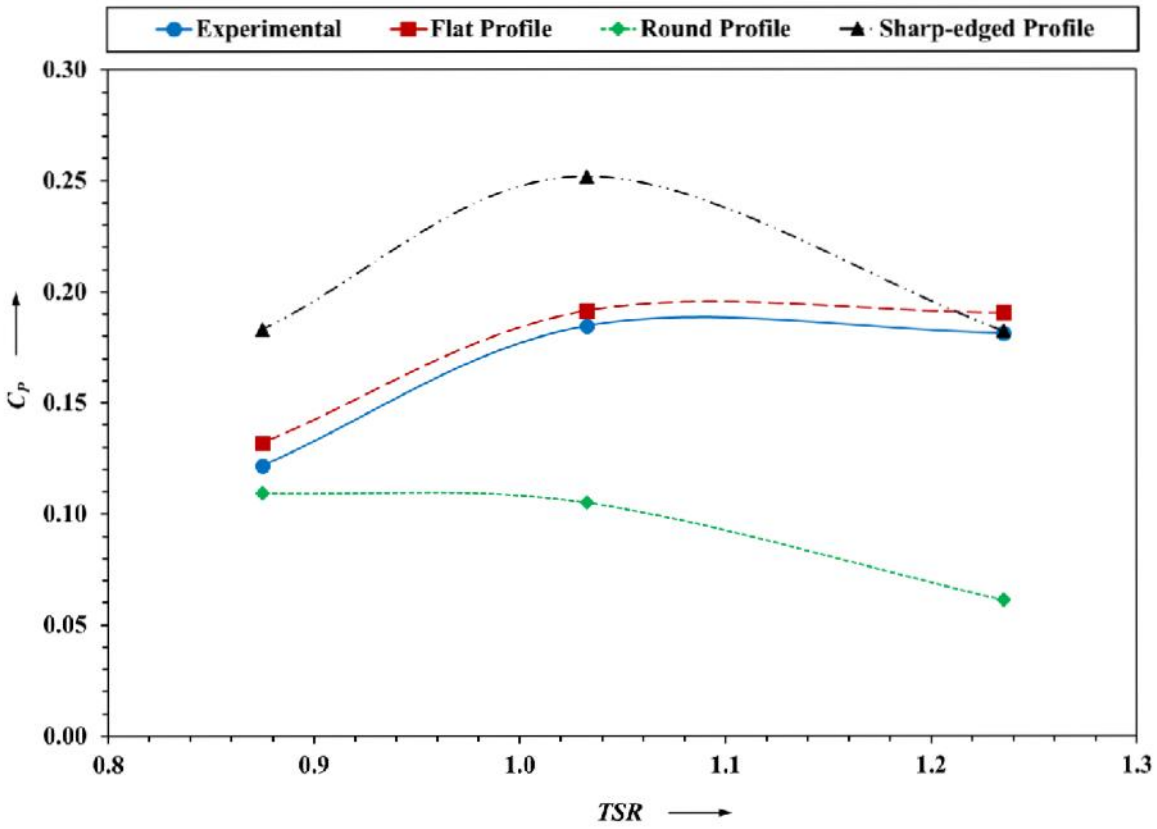


Fig. 6.8. Variation of C_P with TSR for different blade profiles.

The variation of $P_{turbine}$ with U_m for different blade profiles indicates that generated power increases significantly with increasing flow velocity for all cases as shown in Fig. 6.9. The sharp-edged blade profile consistently produces the highest $P_{turbine}$, reaching approximately 6.0329 W at a velocity of around 0.72 m/s. The flat blade profile follows a trend similar to the experimental results and generates moderate power values, while the round profile exhibits the lowest power output across the entire velocity range. The increase in power with flow velocity is expected because the available kinetic energy in flowing water increases rapidly with increasing velocity. The better performance of the sharp-edged profile can be attributed to its ability to create stronger hydrodynamic interactions and improved

pressure differentials around the blade surfaces. Conversely, the smoother curvature of the round profile may reduce effective flow interception, leading to lower energy conversion efficiency. The performance parameters values for different blade profiles are tabulated in Table 6.2.

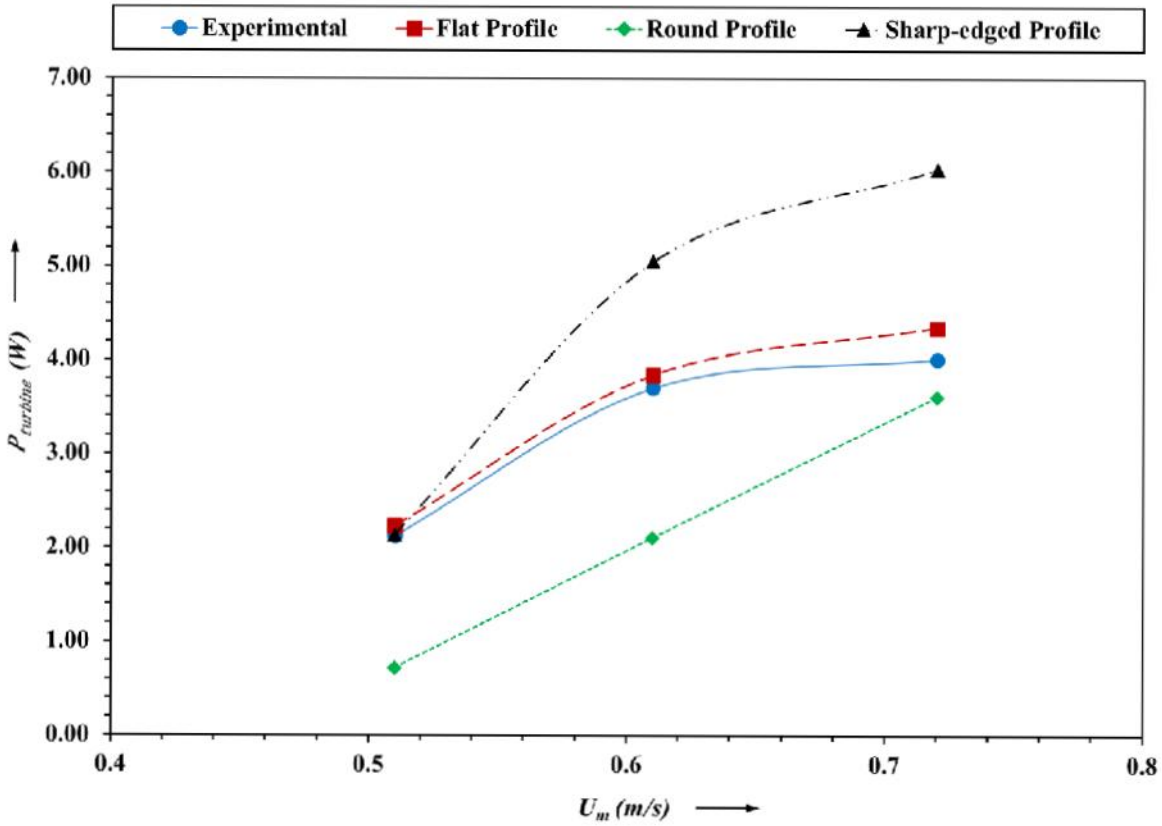


Fig. 6.9. Variation of $P_{turbine}$ with TSR for different blade profiles.

Table 6.2.

Performance parameters values for different blade profiles.

Methodology	Blade Profile	U_m (m/s)	TSR	C_T	C_P	$P_{turbine}$ (W)
Experimental	Blade profile-1	0.51	1.2353	0.1467	0.1813	2.1246
	(Flat profile)	0.61	1.0328	0.1788	0.1846	3.7029
		0.72	0.8750	0.1391	0.1217	4.0145
Numerical	Blade profile-1	0.51	1.2353	0.1904	0.1541	2.2315
	(Flat profile)	0.61	1.0328	0.1915	0.1854	3.8413

Methodology	Blade Profile	U_m (m/s)	TSR	C_T	C_P	$P_{turbine}$ (W)
		0.72	0.8750	0.1319	0.1507	4.3496
Numerical	Blade profile-2	0.51	1.2353	0.0495	0.0612	0.7168
	(Round profile)	0.61	1.0328	0.1016	0.1050	2.1051
		0.72	0.8750	0.1250	0.1094	3.6064
Numerical	Blade profile-3	0.51	1.2353	0.1474	0.1821	2.1343
	(Sharp-edged	0.61	1.0328	0.2438	0.2517	5.0490
	profile)					
		0.72	0.8750	0.2091	0.1829	6.0329

Flow field analysis was carried out to better understand how the shape of blade profiles influences performance. The flow distribution around the MBHKT is discussed in relation to the $C_{P,max}$ value, which is obtained at 1.0328 TSR for all blade profiles. Figs. 6.10 to 6.12 show the flow-field characteristics of the MBHKT for flat, round, and sharp-edged profiles, respectively.

For flat blade profile, the entering flow generates an extended high-pressure region at the blade entry zone (Fig. 6.10 (a)). The higher-pressure concentration on the leading side implies direct flow impact on the blade surface, which causes increased localized loading. Simultaneously, a somewhat broad low-pressure area develops within the rotor interior, indicating a significant pressure drop as the fluid transfers energy to the rotating system. In round blade profile, the pressure contours are smoother over the blade surfaces (Fig. 6.11 (a)). The rounded design encourages a more progressive shift in flow direction, resulting in a gradual pressure transition around the rotor. Localized pressure accumulation is reduced, and the pressure field seems more evenly distributed than with the flat blade shape. The pressure field in sharp-edged blade profile shows concentrated high-pressure regions around

the leading edge of the blade surfaces (Fig. 6.12 (a)). Because of the acute geometry, fluid accelerates quickly around these locations, resulting in higher local pressure gradients. The pressure change across the rotor becomes steeper than in the circular profile.

The velocity contours for flat blade profile depicted in Fig. 6.10 (b) indicate multiple low-velocity zones both within and behind the rotor. A significantly larger wake forms downstream, suggesting significant energy extraction from the flow. However, the wake indicates higher flow disruption near the blade passageways. The round blade design creates a more consistent velocity pattern around the turbine (Fig. 6.11 (b)). Flow acceleration is more gradual along the blade channels, reducing sudden changes in velocity magnitude. The wake zone behind the rotor seems more compact and orderly, reflecting a decrease in energy losses caused by flow instability. Localized acceleration becomes more evident in the sharp-edged blade profile around the blade tips and edges as shown in Fig. 6.12 (b). Because of the quick flow redirection, these locations exhibit higher velocity gradients. Although there is strong fluid interaction, isolated disturbances might form within the flow field.

For the flat blade profile, the velocity vector in patterns show considerable variations in flow direction as the fluid flows through the turbine (Fig. 6.10 (c)). Some sections of the rotor have unusual vector orientations, indicating the presence of localized recirculation and disrupted flow behaviour. On the hand, the round blade profile as per Fig. 6.11 (c) leads to a more orderly vector arrangement. The flow travels more smoothly through the blade channels, which improves directional consistency and reduces flow disturbance. In sharp-edged profile, the vectors have more local interactions with the blade surfaces (Fig. 6.12 (c)). Although the flow remains active along the blade edges, localized circulation regions occur in particular spots due to abrupt geometric transitions.

As shown in Fig. 6.10 (d), the flat blade profile has many recirculation zones and flow separation sections visible inside the rotor. These formations suggest the presence of

localized turbulence. While, in round blade profile shown in Fig. 6.11 (d), the streamlines have smoother curvature and minor interruptions in flow direction. Reduced separation areas suggest that the fluid is held in place on the blade surface for a longer period of time, increasing momentum transfer efficiency. Furthermore, the sharp-edged blade profile illustrates the stronger rotational features around specific blade areas (Fig. 6.12 (d)). Although the flow remains highly intense, localized vortex generation is more visible near sharp geometric features.

A study of the three different blade profiles reveals that blade profile is essential in defining the hydrodynamic response of the MBHKT system. The flat blade profile has larger pressure variations and stronger recirculation effects, whereas the sharp-edged shape causes higher local flow interactions and velocity gradients. The round blade design allows for smoother pressure variation and more steady flow development around the rotor.

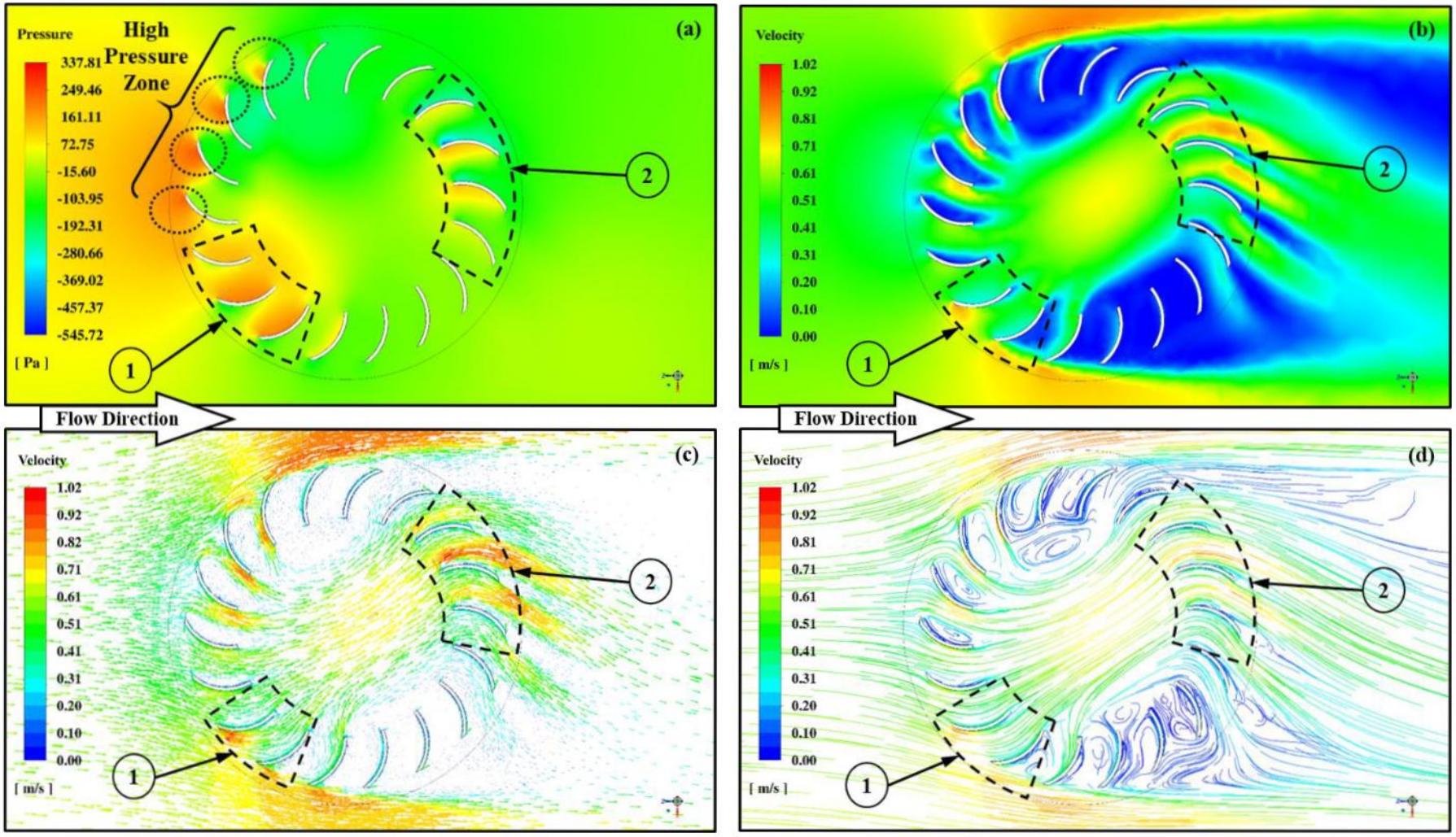


Fig. 6.10. Field visualizations for blade profile-1 (flat profile) of MBHKT (a) pressure contours, (b) velocity contours, (c) velocity vectors, and (d) velocity streamline.

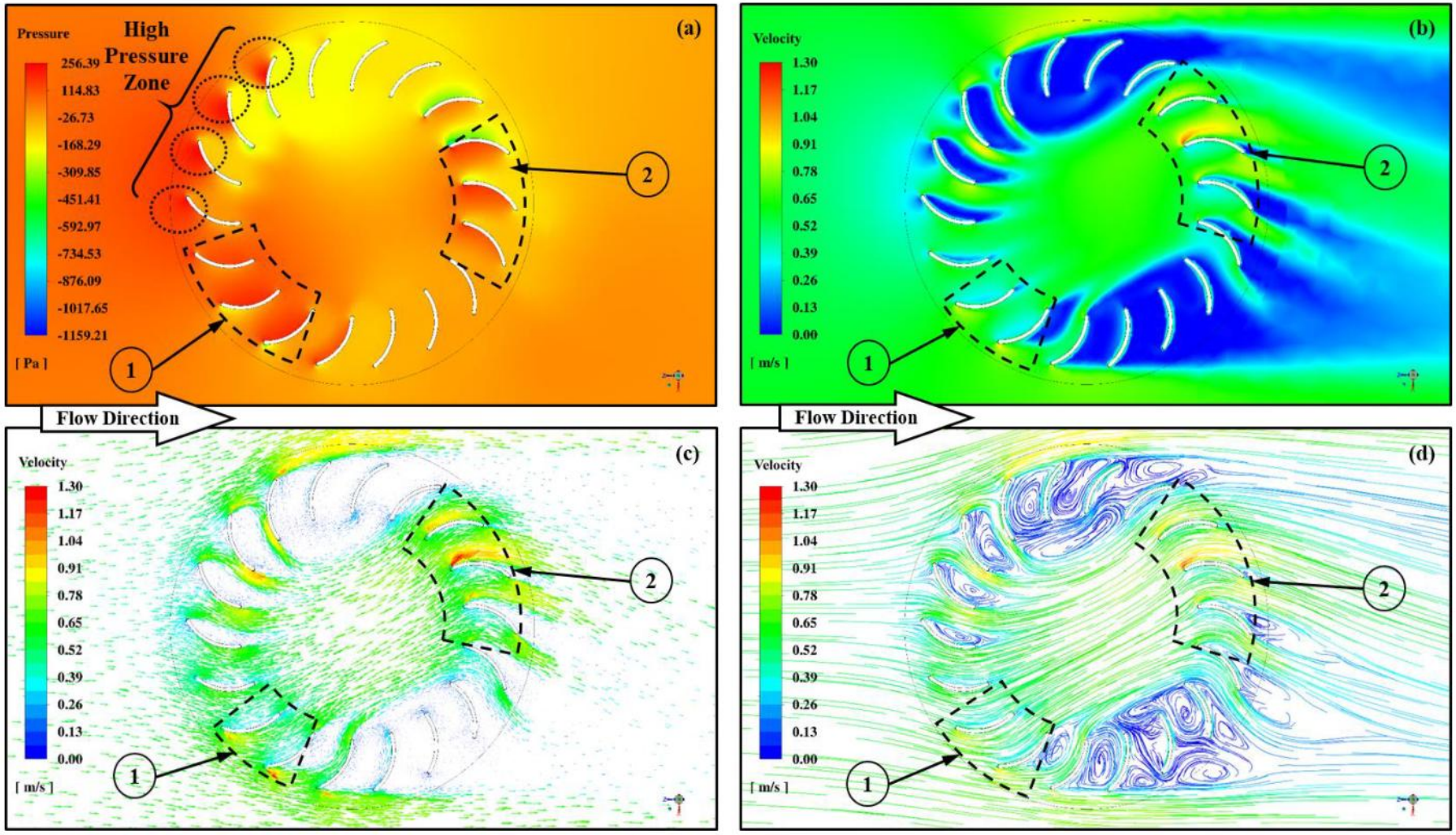


Fig. 6.11. Field visualizations for blade profile-2 (round profile) of MBHKT (a) pressure contours, (b) velocity contours, (c) velocity vectors, and (d) velocity streamline.

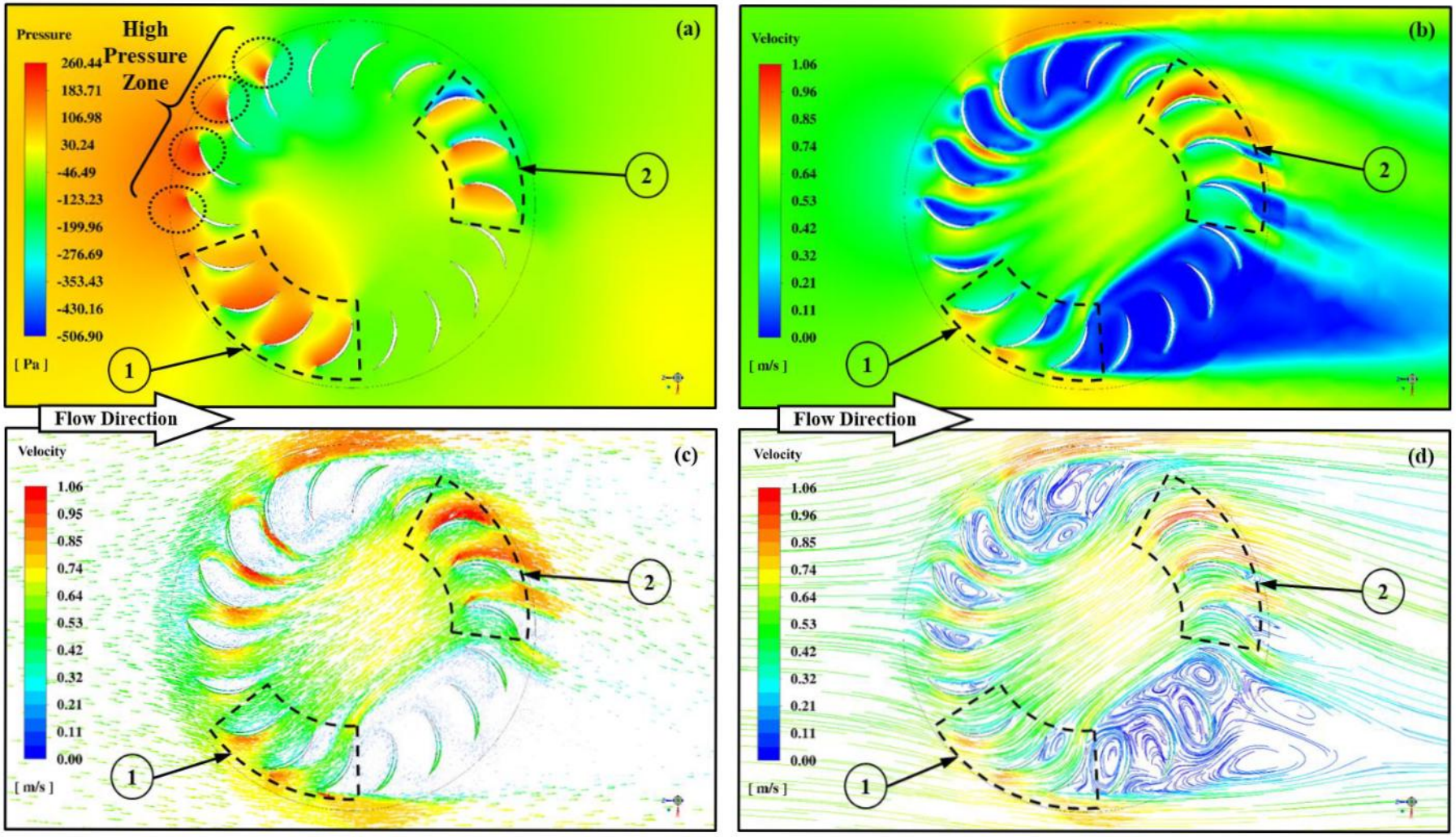


Fig. 6.12. Field visualizations for blade profile-3 (sharp-edged profile) of MBHKT (a) pressure contours, (b) velocity contours, (c) velocity vectors, and (d) velocity streamline.

6.2.2 Augmentation Systems

In the previous section, the optimum results obtained with the blade profile-3 (sharp edged blade profile). In this section, the various argumentation systems were designed using the same blade profile. The fluctuation in C_T with TSR depicted in Fig. 6.13 shows that C_T first increases with TSR and reaches a maximum around the optimum working point, after which it decreases slightly at higher TSR values. Augmentation system-4 produces the $C_{T,max}$ = 0.5345 of any design due to increased flow acceleration around the rotor. Increased torque indicates a stronger hydrodynamic interaction between the entering flow and the turbine blades, which results in better momentum transfer and energy conversion. Augmentation system-3 has intermediate torque characteristics, whereas systems 1 and 2 produce relatively low torque values. Although higher torque generally enhances power extraction capability, it also adds structural load to the turbine and support system.

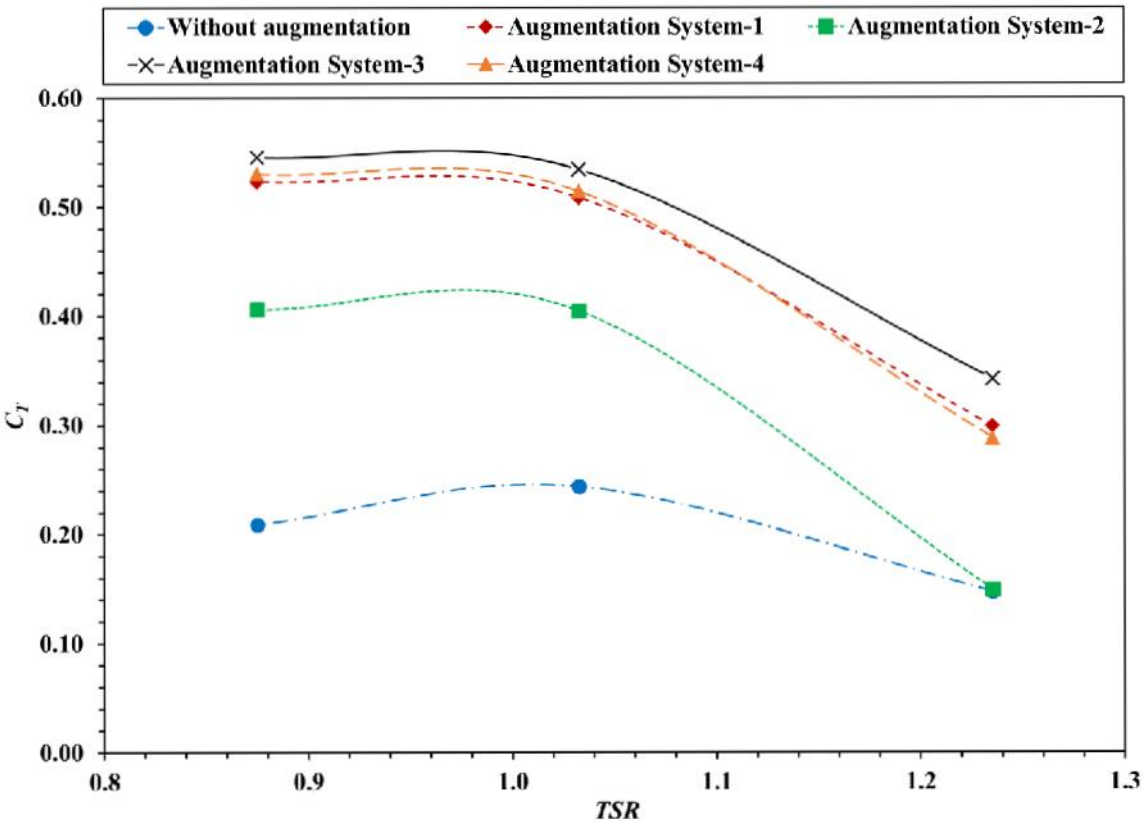


Fig. 6.13. Variation of C_T with TSR for different augmentation systems.

The change of C_P with TSR for various augmentation systems shown in Fig. 6.14 depicts how flow-guiding structures affect the MBHKT's hydrodynamic performance. It is noticed that all augmentation systems show an increase in C_P as TSR increases until they reach an optimum operating zone, at which point they gradually decrease. Augmentation system-3 has the $C_{P,max}$ of 0.5520 across the working range, suggesting optimal flow acceleration and concentration toward the turbine rotor. The curved guide sections in this configuration appear to reduce flow separation and direct a higher mass flow rate toward the turbine blades, increasing energy extraction. Augmentation system-4 outperforms simpler designs to its changed inlet profile and smoother flow guidance characteristics. Augmentation systems 1 and 2 have lower C_P, implying that simpler geometrical configurations produce less effective flow concentration. The results show that optimal augmentation geometry improves turbine efficiency by enhancing local flow velocity near the rotor.

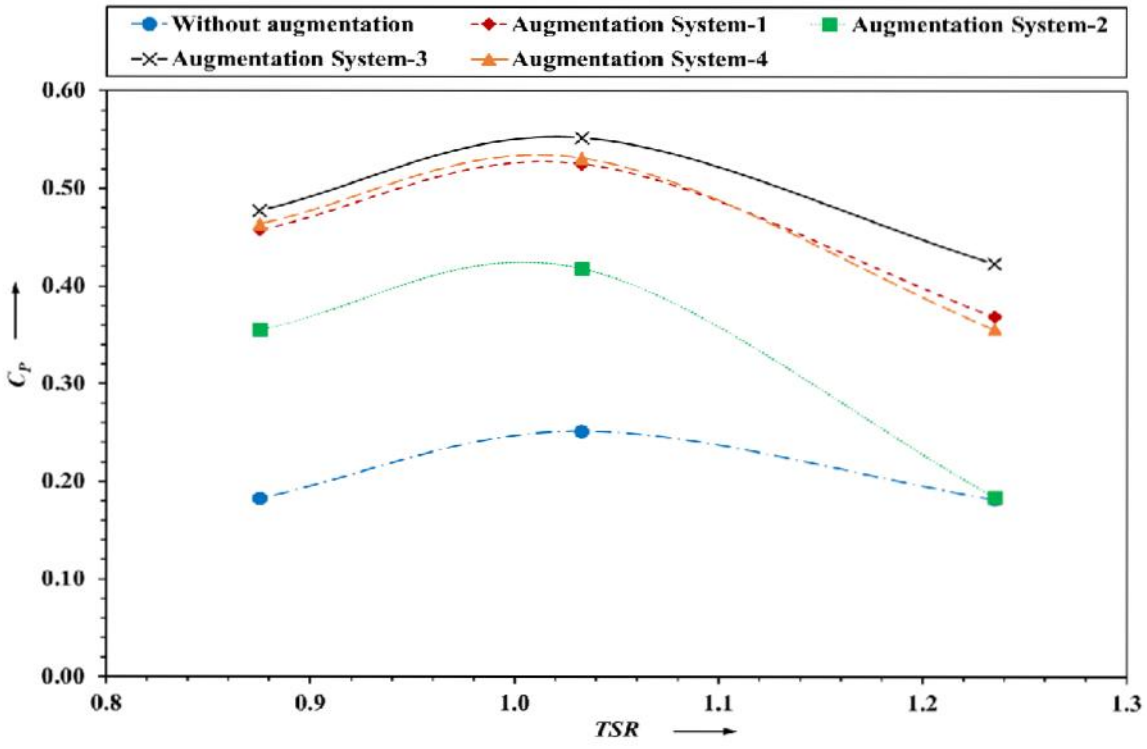


Fig. 6.14. Variation of C_P with TSR for different augmentation systems.

The relationship between $P_{turbine}$ and U_m shown in Fig. 6.15 clears a steady rise in generated power with increasing flow velocity for all augmentation setups. This pattern is expected given that the available kinetic energy in flowing water grows dramatically as velocity increases. Among all tested designs, Augmentation system-3 produces the maximum power output over the velocity range, suggesting its greater capacity to improve local flow conditions around the rotor. The revised flow-guiding system effectively enhances flow velocity and guides a higher mass flow rate into turbine blades, resulting in increased power generation. Augmentation systems 1, 2, and 4 have lower power outputs due to less efficient flow manipulation features. Table 6.3 shows the performance parameters values for different augmentation systems.

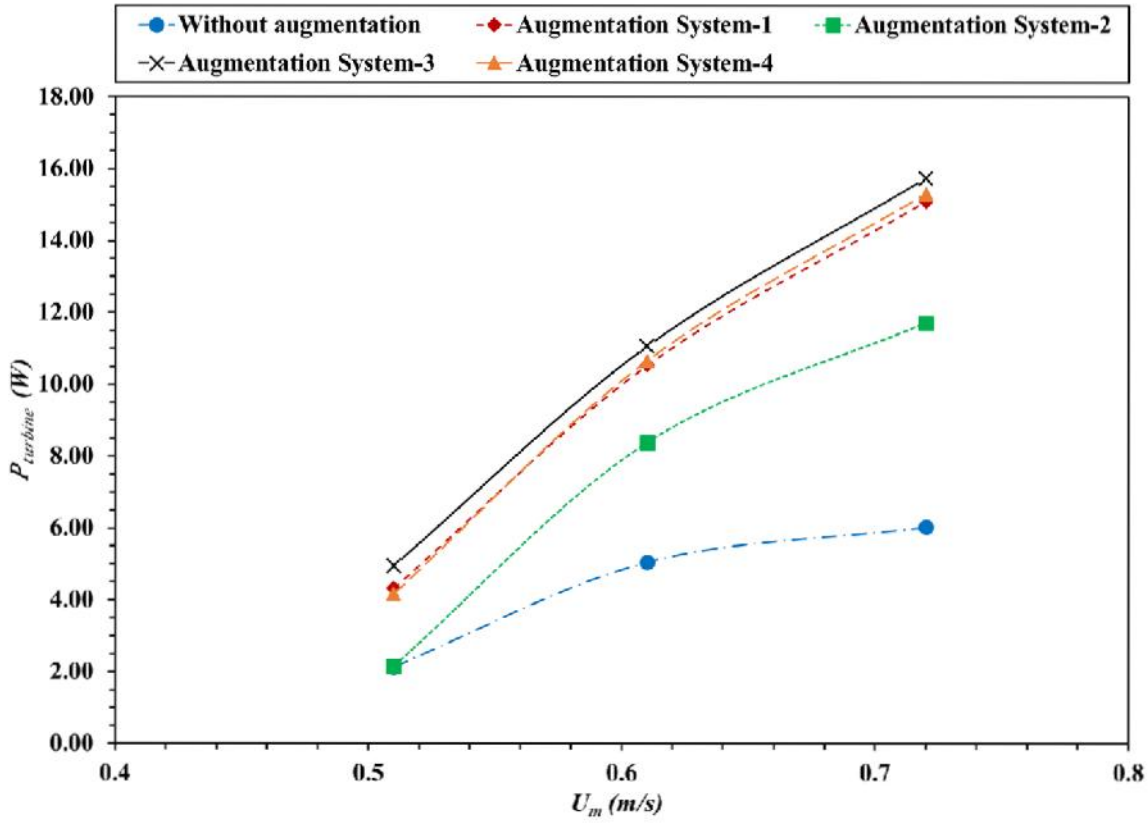


Fig. 6.15. Variation of $P_{turbine}$ with U_m for different augmentation systems.

Table 6.3.

Performance parameters values for various augmentation systems.

Augmentation	U_m (m/s)	TSR	C_T	C_P	$P_{turbine}$ (W)
Without Augmentation	0.51	1.2353	0.1474	0.1821	2.13
	0.61	1.0328	0.2438	0.2517	5.05
	0.72	0.8750	0.2091	0.1829	6.03
Augmentation System-1	0.51	1.2353	0.1492	0.1843	2.16
	0.61	1.0328	0.4048	0.4180	8.38
	0.72	0.8750	0.4061	0.3554	11.72
Augmentation System-2	0.51	1.2353	0.2988	0.3691	4.33
	0.61	1.0328	0.5085	0.5252	10.53
	0.72	0.8750	0.5230	0.4576	15.09
Augmentation System-3	0.51	1.2353	0.3425	0.4231	4.96
	0.61	1.0328	0.5345	0.5520	11.07
	0.72	0.8750	0.5456	0.4774	15.74
Augmentation System-4	0.51	1.2353	0.2881	0.3559	4.17
	0.61	1.0328	0.5145	0.5314	10.66
	0.72	0.8750	0.5303	0.4640	15.30

Figs. 6.16 to 6.19 present the pressure contours, velocity contours, velocity vectors, and velocity streamline patterns of the MBHKT integrated with four different augmentation systems. The introduction of augmentation systems modifies the incoming flow characteristics and consequently affects the hydrodynamic interaction occurring around the turbine rotor.

A thorough investigation of the pressure contours reveals that the augmentation systems' shape affects the pressure field surrounding the rotor region. In augmentation

system-1 (Fig. 6.16 (a)), the pressure distribution shows relatively large, with an extended upstream high-pressure region before the water reaches the turbine. The pressure gradient around the rotor progressively increases, indicating steady flow direction toward the blade passageways. When considering augmentation system-2 (Fig. 6.17 (a)), the pressure field becomes more concentrated at the rotor entry. The improved shape guides the incoming flow more effectively into the turbine, resulting in a greater pressure differential throughout the rotor zone. The pressure variation appears to be more confined than that reported in system-1. Further, the pressure distribution surrounding the turbine is more concentrated and well-organized for augmentation system-3 as shown in Fig. 6.18 (a). In order to ensure smoother transitions around the rotor and encourage a stronger pressure gradient, the entering fluid is directed toward the blade region. Improved energy transfer conditions between the fluid and the revolving blades are suggested by the concentration of the pressure field. Although the pressure field shows more extension into the surrounding domain in augmentation system-4 (Fig. 6.19 (a)), pressure concentration is still apparent near the entrance location. In comparison to system-3, the dispersion seems less concentrated near the turbine, despite the continued presence of severe flow interaction.

Evaluation of the velocity contours demonstrates that the augmentation systems influence both flow acceleration and wake development behind the turbine. For system-1 (Fig. 6.16 (b)), the flow experiences moderate acceleration as it approaches the rotor, while the wake region downstream remains relatively broad. The larger wake structure indicates the presence of greater flow disturbance after passing through the turbine. A different trend becomes apparent in system-2 (Fig. 6.17 (b)), where the incoming fluid is guided more effectively toward the rotor. The wake region decreases in size compared with system-1, indicating improved momentum transfer and more organized downstream flow characteristics. Unlike the previous configurations, system-3 generates a highly concentrated

flow region around the rotor and produces a more coherent velocity field through the blade passages (Fig. 6.18 (b)). The downstream wake appears comparatively narrower and more stable, suggesting that the augmentation structure contributes to stronger interaction between the fluid and blades of the turbine. By comparison, as shown in Fig. 6.19 (b), system-4 also enhances flow acceleration around the turbine; however, certain regions within the flow domain exhibit broader areas of disturbed flow. The wake recovery pattern appears less uniform than that observed in system-3.

Further details on the directional behaviour of the fluid surrounding the turbine can be obtained by examining the vector fields. The vectors in system-1 shown in Fig. 6.16 (c) depicts how localized disturbances around the rotor along with variations in flow direction close to the augmentation boundaries. These differences suggest decreased flow coherence and the existence of secondary flow effects. The vectors illustrated in Fig. 6.17 (c) for system-2 shows how they align more closely with the direction of incoming flow. Smoother flow development in the rotor region is the outcome of the fluids seemingly more ordered direction toward the turbine. On the other hand, a more structured vector arrangement is observed in system-3 (Fig. 6.18 (c)), where the flow enters the turbine with improved directional consistency. The vectors surrounding the rotor demonstrate stronger alignment and reduced lateral disturbances, suggesting more efficient momentum transport toward the blade passages. Conversely, system-4 displays organized vector behaviour in several regions; however, some flow irregularities remain visible near the downstream region (Fig. 6.19 (c)). These disturbances indicate that the flow experiences additional redistribution after passing through the rotor.

Observation of the streamline patterns further highlights the differences among the augmentation systems. In system-1 shown in Fig. 6.16 (d), many recirculation zones observed around the rotor and downstream regions. These flow structures indicate local

energy dissipation and flow separation effects. As the augmentation geometry changes in system-2, the streamline paths become smoother and demonstrate reduced recirculation intensity (Fig. 6.17 (d)). The fluid follows a more continuous route around the rotor, indicating improved flow guidance. Among all configurations, system-3 has the most structured streamline structure (Fig. 6.18 (d)). The flow remains linked to the surrounding surfaces for a longer period of time, resulting in fewer large-scale vortices. Reduced separation and enhanced streamline continuity imply that the incoming fluid is more efficiently directed toward the turbine. Unlike system-3, system-4 still has notable vortex patterns in the downstream region as depicted in Fig. 6.19 (d). Although flow concentration occurs near the rotor, extra recirculation zones persist and contribute to local flow disturbances.

Based on a combined interpretation of pressure contours, velocity fields, vector distributions, and streamline characteristics, the augmentation systems exhibit various hydrodynamic responses. System-1 has larger wake structures and strong recirculation, but system-2 improves flow organization and decreases disturbances around the rotor. Although system-4 improves flow concentration, certain downstream anomalies persist to affect the flow structure. Among the investigated systems, augmentation system-3 has the optimum flow characteristics. The pressure field stays evenly distributed around the rotor, the velocity contours indicate a more concentrated flow region, vector alignment improves, and streamline patterns show less separation and recirculation effects. These characteristics indicate a stronger fluid-rotor contact and more efficient use of the incoming flow. The results indicate that the optimized augmentation configuration provides improved performance under the simulated conditions. However, its practical feasibility and field applicability require further experimental validation.

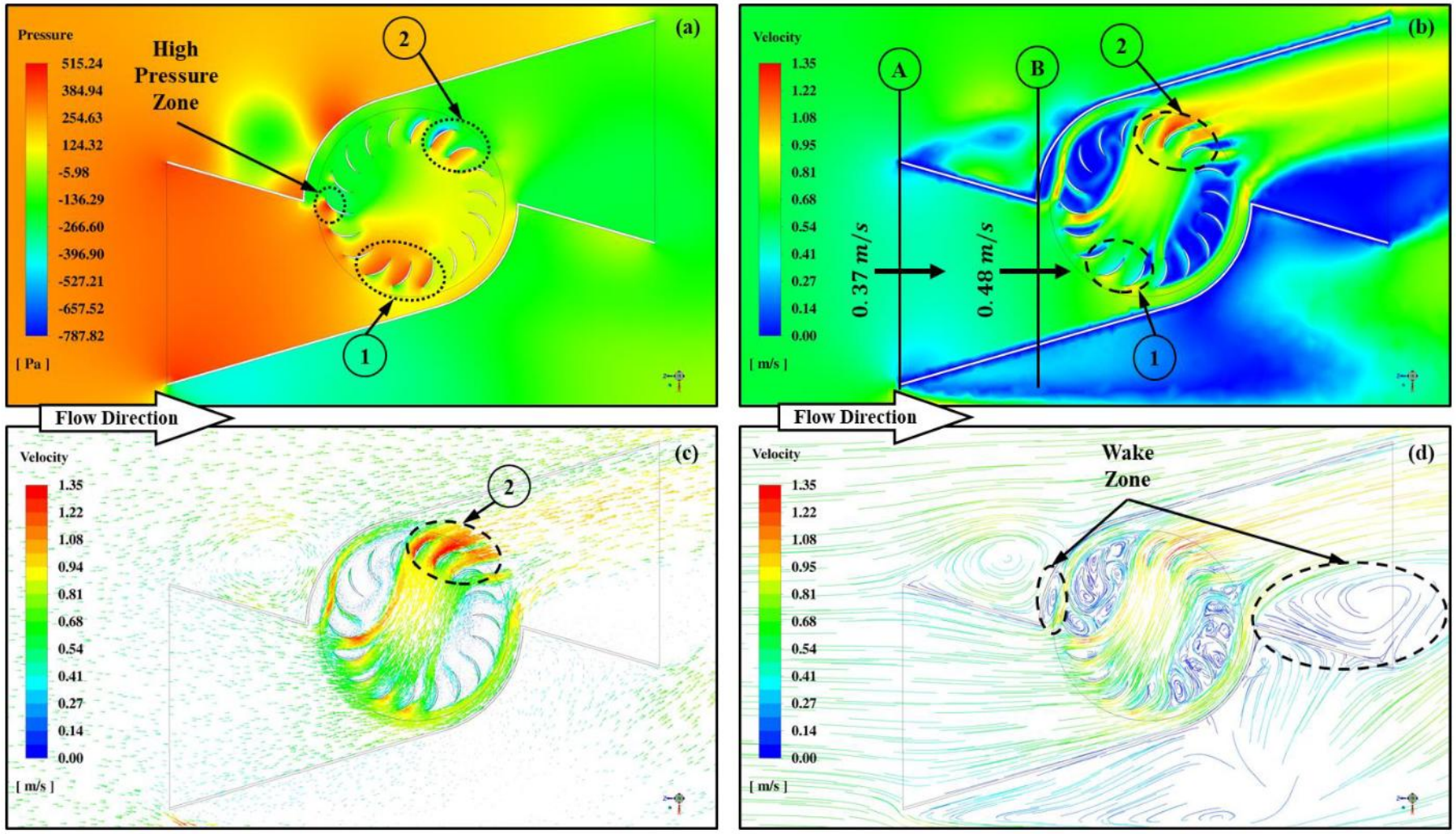


Fig. 6.16. Field visualizations for augmentation system-1 (a) pressure contours, (b) velocity contours, (c) velocity vectors, and (d) velocity streamline.

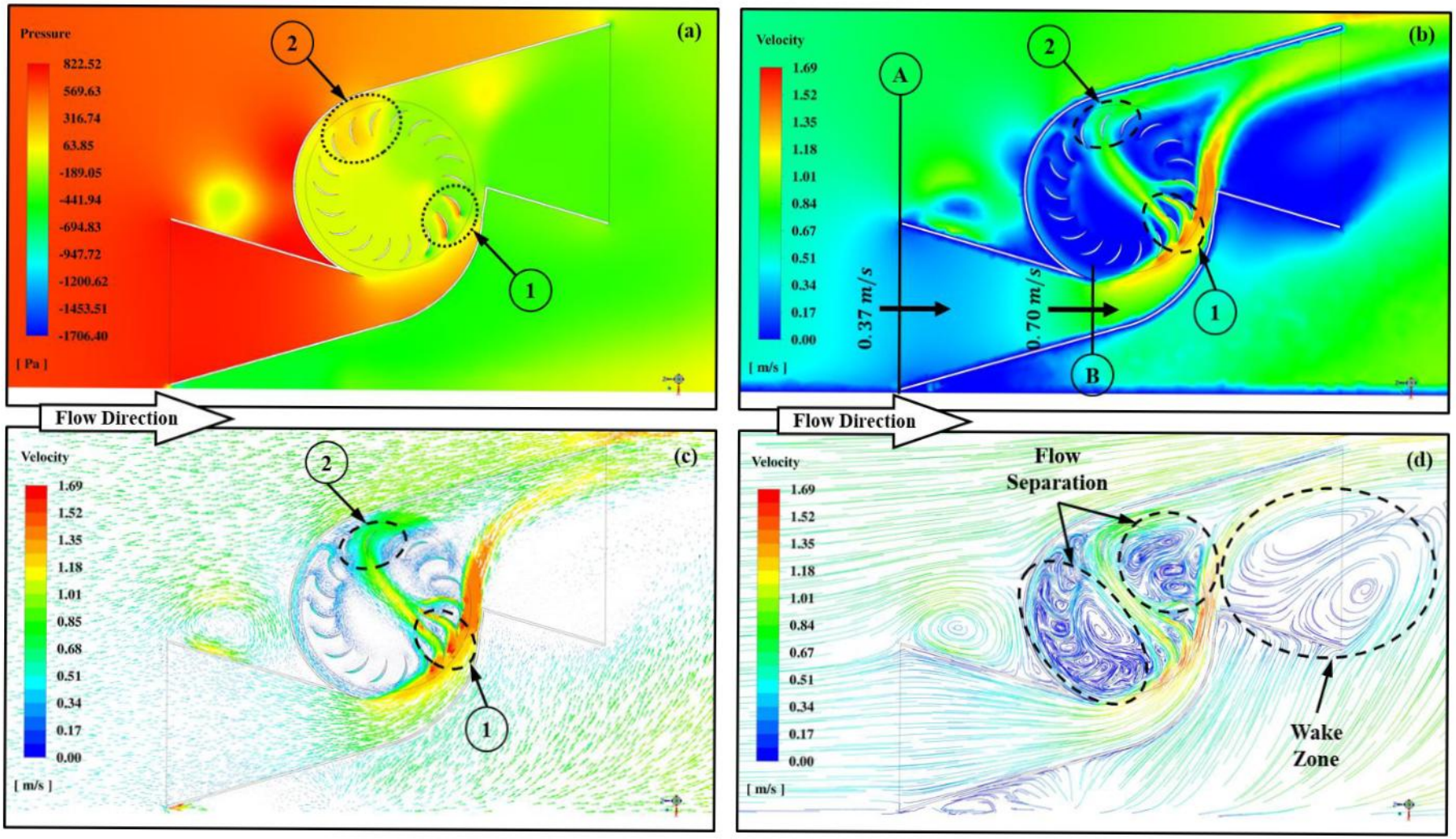


Fig. 6.17. Field visualizations for augmentation system-2 (a) pressure contours, (b) velocity contours, (c) velocity vectors, and (d) velocity streamline.

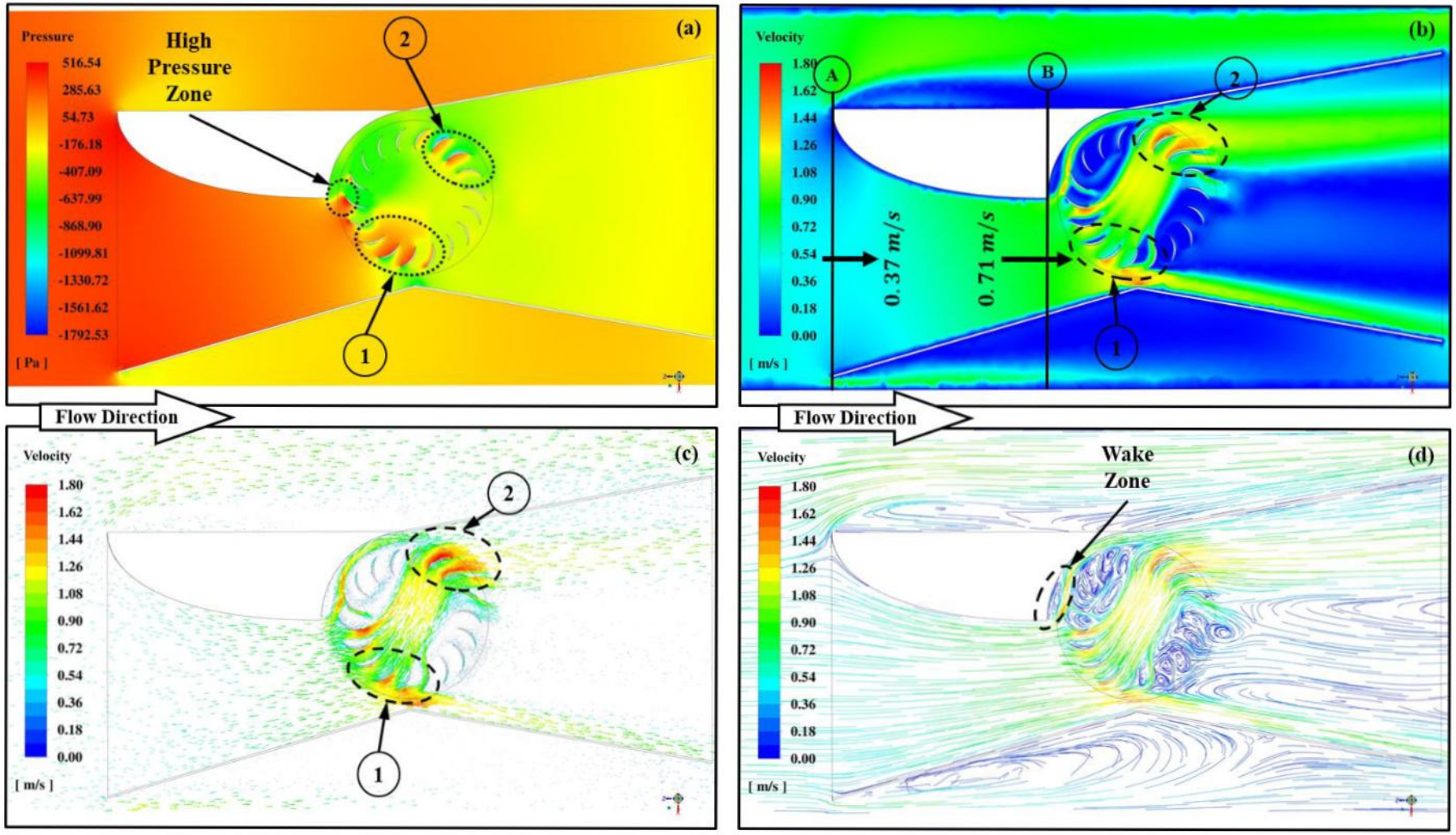


Fig. 6.18. Field visualizations for augmentation system-3 (a) pressure contours, (b) velocity contours, (c) velocity vectors, and (d) velocity streamline.

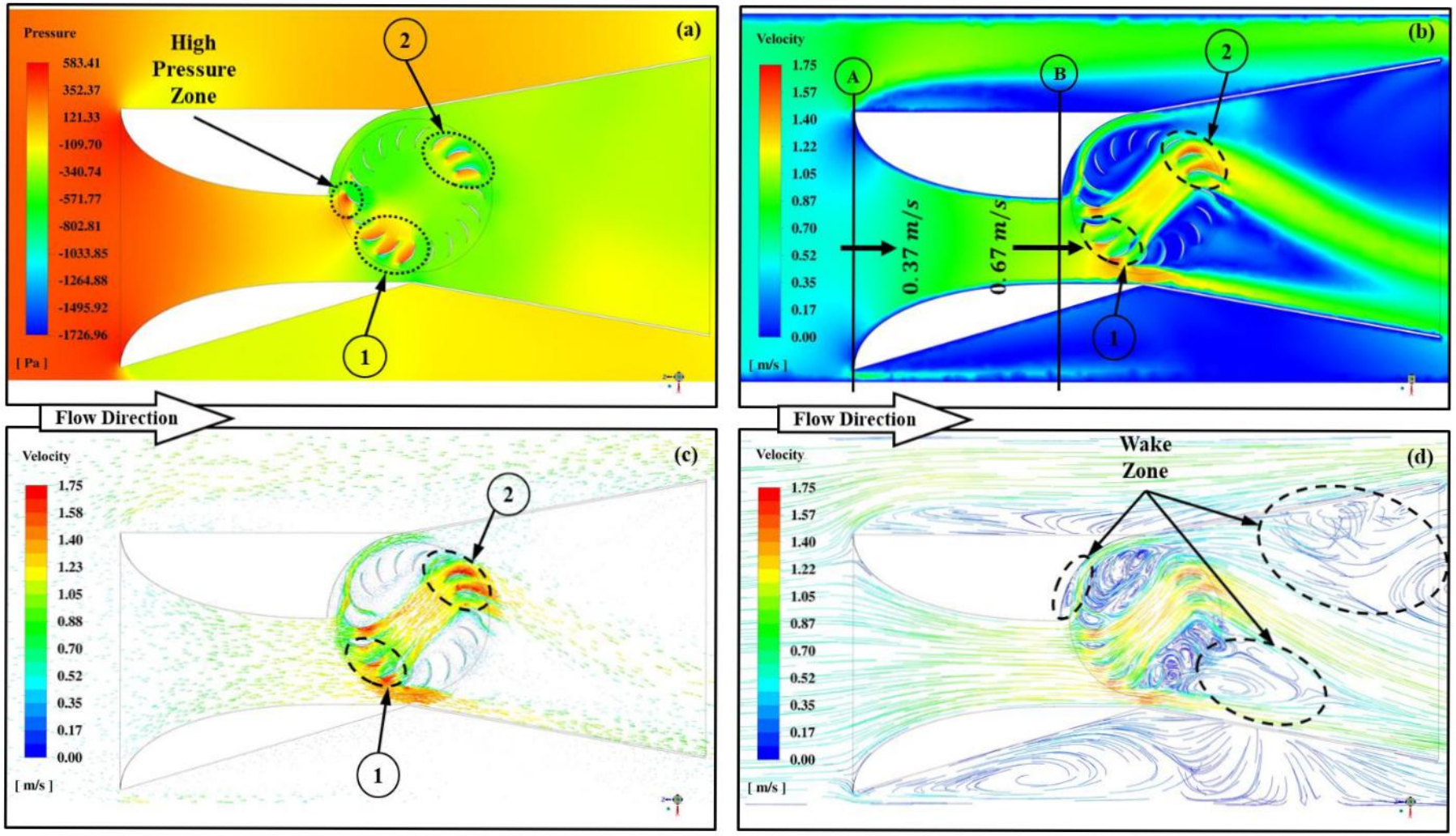


Fig. 6.19. Field visualizations for augmentation system-4 (a) pressure contours, (b) velocity contours, (c) velocity vectors, and (d) velocity streamline.

CHAPTER – 7

CONCLUSION

To meet the power demand of various locations across the world, HKT can be a cost-effective solution. In the first stage of this research work, an identification of a potential HKT study site and a comparative assessment of various turbulence models was carried out at trapezoidal open canal situated on Tapi River, Surat, Gujarat, India. Based on the obtained results and data of the canal flow, in the second stage comparative analysis of SHKT and MBHKT was carried out. In the third stage, experimental study of MBHKT was performed at open channel testing facility established at Fluid Mechanics and Fluid Machine Laboratory, Sardar Vallabhbhai National Institute of Technology, Surat, Gujarat, India. The simulation results were validated with the experimental results for MBHKT at different velocities. In the final and forth stage, the numerical optimization of three different blade profiles (profile 1 – flat, profile 2 – round and profile 3 – sharp edged) was performed. Additionally, based on the optimum blade profile obtained the various augmentations combining the nozzle and diffuser were also numerically investigated to find out the optimum design of augmentation, which helps to develop the modular structure.

The concluding remarks of the current study are as follows:

- Among the five possible locations at canal, Location-2 was identified for comprehensive analysis of HKT study having about 495 cusecs (average annual discharge) available throughout the year. The maximum discharge is 1236 cusec at a study site.
- Among the five turbulence models evaluated, the $k-\omega$ SST model demonstrated the best overall agreement with the experimental results and provided comparatively better accuracy in predicting the canal-flow parameters at the investigated locations.

- Secondary flow vectors that resist the longitudinal flow were found to be least near the canal's centre, notably in the direction of the right side (X2') from the mid-section (X0). Due to the water's resistance, the lowest values of velocity and water power density were found along the canal side walls and bed, while the highest values were found close to the free surface.
- The rectangular region of 1.8 m water depth (Y5 to Y2) and 6.5 m length (X2' to X2) was finalised for potential site of HKT site. Numerical results in agreement with the experimental observations supports that this site can be capable enough to generate 1.2 kW using HKT throughout a year as a single unit.
- $C_{T,max}$ enhances by 11.19% and 11.46% for 1.06 m/s in compare to the 0.42 m/s for SHKT and MBHKT corresponding $C_{P,max}$ at respective TSR. Similarly, the $C_{P,max}$ improves by 11.26% and 11.42% for 1.06 m/s in compare to the 0.42 m/s for SHKT and MBHKT.

  Improvement in $C_{T,max}$ and $C_{P,max}$ for MBHKT at optimum TSR was found to be 159.02% and 72.99% for 0.42 m/s and 159.82% and 73.23% for 1.06 m/s flow velocity, respectively.
- SHKT shows the lesser power extraction efficiency, with performance limited by drag-based operation. MBHKT offers the best self-starting capability due to its high starting torque making it suitable for low-speed operation.
- The pressure differential, flow circulation, and vortex strength surrounding the SHKT blades are intensified by increasing the inlet flow velocity. This leads to much greater torque generation and better momentum transfer for increased power extraction. Stronger shear, deeper suction zones, and larger hydrodynamic force are produced by higher velocities, which indicate more effective energy conversion but also put more structural strain on the SHKT rotor blades.

- With deeper suction zones, sharper impact pressures, and stronger flow striking the blade, the MBHKT changes from a weakly engaged, low-energy impulse device to a much more forcefully driven turbine with rising inlet velocity. With well-defined high-speed flow, greater recirculation, and more ordered wake formation, the internal flow structure becomes considerably more coherent and energetic at higher velocities for MBHKT.
- From the experimental results at the fully submerged (100% immersion) condition shows an enhancement in C_T and C_P of 26.90% and 21.21%, respectively, compared to 75% immersion, while compared to 50% immersion, the C_T slightly decreases by 1.22% whereas C_P increases by 29.54%. Similarly, for the numerical results at the 100% immersion condition exhibits improvements in C_T and C_P of 37.89% and 31.75%, respectively, relative to 75% immersion, whereas compared to 50% immersion, the enhancements are 4.32% and 36.83%, respectively.
- The fully submerged (100% immersed) MBHKT intensifies the pressure differential and hydrodynamic interaction around the rotor blades, leading to improved momentum transfer and enhanced power extraction capability.

Higher immersion levels generate stronger hydraulic loading and improved flow attachment around the turbine blades, resulting in more effective energy conversion along with increased structural loading on the rotor. With stronger flow circulation, better wake organization, and improved fluid penetration through the rotor, the internal flow field under fully submerged conditions becomes more coherent and energetic compared to partially submerged conditions.

- For a blade profile-3 (sharp-edged), at a TSR of 1.03, the values of C_T and C_P increase by 65.40% and 38.22% in compared with the 1.24 TSR flow condition. While in

comparison to the 0.87 TSR, the 1.03 TSR flow velocity exhibits an enhancement of 16.59% and 37.62% in C_T and C_P.

- A blade profile-3 (sharp-edged) exhibits an enhancement of 27.31% and 35.76% in C_T and C_P, compared with blade profile-1 (flat profile) at 1.03 TSR.
- Relative to blade profile-2 (round profile), blade profile-3 shows significant improvements of 139.96% and 139.71% in C_T and C_P.
- The blade profile-3 (sharp-edged) intensifies local pressure gradients and fluid interaction near blade surfaces, leading to stronger momentum transfer and improved energy extraction capability.
- The augmentation system-3 exhibits an enhancement of 119.24%, and 119.23% in C_T and C_P compared with the without augmentation configuration at 1.03 TSR.
- Relative to augmentation system-1, augmentation system-3 shows improvements of 32.04% and 32.06%, while in comparison with augmentation system-2, augmentation system-3 provides an enhancement of 5.11% and 5.10% in C_T and C_P.

  Similarly, in compared with augmentation system-4, augmentation system-3 demonstrates increase of 3.89% and 3.87% in C_T and C_P.
- For augmentation system-3, at a TSR of 1.03, the values of C_T and C_P increase by 56.06% and 30.46%, compared with the 1.24 TSR and 2.03% and 15.63% relative to the 0.87 TSR.
- Augmentation system-3 creates more structured flow structures with fewer recirculation zones and better streamline continuity, resulting in more efficient use of incoming flow energy.

  With greater flow concentration, stronger vector alignment, and narrower wake creation, augmentation system-3 creates a more coherent and stable internal flow structure surrounding the MBHKT, resulting in better turbine performance.

Summarizing, this study thoroughly investigated the site selection, design optimization, and performance enhancement of HKTs for sustainable energy extraction from canal flows. The site assessment found an appropriate installation zone within the canal, capable of producing roughly 1.2 kW from a single HKT. A comparison of the SHKT and MBHKT revealed that the MBHKT had more energy extraction capability, owing to improved self-starting characteristics, higher torque generation, and a significantly improved power coefficient. During an experiments found that immersion depth and flow control conditions had a considerable influence on turbine performance, with full immersion producing the best hydrodynamic behaviour and energy conversion efficiency. Furthermore, blade profile optimization and augmentation experiments have shown that sharp-edged blade geometries significantly increase pressure distribution, momentum transfer, and power extraction performance. Overall, the findings show that appropriate site selection, optimized operating conditions, and turbine design can significantly improve hydrokinetic energy harvesting, making it a technically feasible and environmentally sustainable solution for decentralized renewable power generation in irrigation canal networks. The findings of the present study provide a numerical and experimental basis that may support the future design and development of modular hydrokinetic turbine systems for suitable canal-flow conditions. In particular, the numerical results obtained for the optimized blade profile and augmentation system provide useful guidance for improving turbine performance. However, the practical feasibility, scalability, environmental suitability, and field deployment of the final optimized augmentation configuration require further experimental and field-scale investigation before practical implementation can be established.

CHAPTER – 8

SCOPE OF FUTURE WORK

The present CFD investigations provide useful insight into the flow characteristics and comparative performance of the investigated HKT configurations; however, certain engineering limitations should be recognized. The numerical approach is based on the specified operating conditions and does not fully represent transient canal-flow variations, detailed unsteady flow behaviour, or all free-surface effects. Practical field conditions may also involve fluctuating water levels, sediment transport, debris accumulation, and other site-specific disturbances that can influence turbine performance and operation. Furthermore, the present analysis primarily considers individual turbine configurations, and the hydrodynamic interaction between multiple turbines in an array requires further investigation. Future studies should therefore incorporate unsteady and more detailed free-surface simulations, together with experimental and field-scale investigations of sediment/debris effects, fluctuating canal conditions, and turbine-array interactions.

Future studies may focus on:

- The interaction effects of multiple turbines arranged in an array may also be examined to determine the optimum spacing and arrangement for maximizing overall power generation.
- Furthermore, the optimized MBHKT with augmentation system can be experimentally tested under actual canal or river conditions by considering practical factors such as sediment transport, fluctuating water levels, and debris effects.
- Evaluating the performance of different HKT configurations such as Darrieus, Gorlov, helical, and hybrid turbines under similar open-channel flow conditions to identify more efficient systems.

- Advanced numerical approaches such as transient CFD and Large Eddy Simulation (LES) can be employed to better capture complex unsteady flow behaviour, turbulence characteristics, and wake dynamics.
- Additionally, the influence of different geometrical parameters including blade number, blade curvature, blade thickness, overlap ratio, and rotor aspect ratio can be investigated for further enhancement of MBHKT performance.
- Artificial intelligence and optimization techniques such as ANN, ANFIS, genetic algorithms, and machine learning methods can also be integrated for performance prediction and automated optimization of HKT systems.

REFERENCES

[1] Forbes. GDP of India: Current and historical growth rate, India's rank in the world. Forbes India 2023:1–5.

[2] International Energy Agency (IEA). India Energy Outlook 2021. 2021.

[3] US. EIA. International Energy Outlook 2023 - U.S. Energy Information Administration (EIA). Paris: 2023.

[4] U.S. Energy Information Administration. Global primary energy consumption by region. 2019.

[5] Welsby D, Price J, Pye S, Ekins P. Unextractable fossil fuels in a 1.5 °C world. Nature 2021;597:230–4. https://doi.org/10.1038/s41586-021-03821-8.

[6] Whiteman A, Rinke T, Esparrago J, Elsayed S. Renewable Capacity Statistics. Abu Dhabi: 2016.

[7] Bilgili M, Bilirgen H, Ozbek A, Ekinci F, Demirdelen T. The role of hydropower installations for sustainable energy development in Turkey and the world. Renew Energy 2018;126:755–64. https://doi.org/10.1016/j.renene.2018.03.089.

[8] Lata-García J, Jurado F, Fernández-Ramírez LM, Sánchez-Sainz H. Optimal hydrokinetic turbine location and techno-economic analysis of a hybrid system based on photovoltaic/hydrokinetic/hydrogen/battery. Energy 2018;159:611–20. https://doi.org/10.1016/j.energy.2018.06.183.

[9] EVG-250T — New Energy Corporation n.d. https://www.newenergycorp.ca/250kw-turbine (accessed April 20, 2025).

[10] Kusakana K, Vermaak HJ. Hydrokinetic power generation for rural electricity supply: Case of South Africa. Renew Energy 2013;55:467–73.

https://doi.org/10.1016/j.renene.2012.12.051.

[11] Henri van Els R, Vélez S, Brasil Junior A. Hydrokinetic Energy Conversion-State of the Art and Perspectives in Brazil. Environmental impact of hydrokinetic turbines View project. 1st Lat. Am. Conf. Sustain. Dev. Water Energy Environ. Syst. Lat. Am. SDEWES-LA, Rio de Janeiro: 2018, p. 1–14.

[12] Khan MJ, Iqbal MT, Quaicoe JE. River current energy conversion systems: Progress, prospects and challenges. Renew Sustain Energy Rev 2008;12:2177–93. https://doi.org/10.1016/j.rser.2007.04.016.

[13] Khan MJ, Bhuyan G, Iqbal MT, Quaicoe JE. Hydrokinetic energy conversion systems and assessment of horizontal and vertical axis turbines for river and tidal applications: A technology status review. Appl Energy 2009;86:1823–35. https://doi.org/10.1016/j.apenergy.2009.02.017.

[14] Sood M, Singal SK. Development of hydrokinetic energy technology: A review. Int J Energy Res 2019;43:5552–71. https://doi.org/10.1002/er.4529.

[15] Fleming PD, Probert SD, Tanton D. Designs and performances of flexible and taut sail savonius-type wind-turbines. Appl Energy 1985;19:97–110. https://doi.org/10.1016/0306-2619(85)90065-0.

[16] Quaranta E, Perrier JP, Revelli R. Optimal design process of crossflow Banki turbines: Literature review and novel expeditious equations. Ocean Eng 2022;257. https://doi.org/10.1016/j.oceaneng.2022.111582.

[17] Elbatran AH, Yaakob OB, Ahmed YM, Shehata AS. Numerical and experimental investigations on efficient design and performance of hydrokinetic Banki cross flow turbine for rural areas. Ocean Eng 2018;159:437–56. https://doi.org/10.1016/j.oceaneng.2018.04.042.

[18] Alvarez-Alvarez E, Corominas EL, Rico-Secades M, Huerta-Medina N, Aitor-Fernandez J, Fernandez-Francos J. A proposal of a modular hydroKinetic smart grid. Int. Power Electron. Congr. - CIEP, vol. 2016- Augus, 2016, p. 271–6. https://doi.org/10.1109/CIEP.2016.7530769.

[19] Lassabatere L, Pu JH, Bonakdari H, Joannis C, Larrarte F. Velocity Distribution in Open Channel Flows: Analytical Approach for the Outer Region. J Hydraul Eng 2013;139:37–43. https://doi.org/10.1061/(asce)hy.1943-7900.0000609.

[20] Sahoo A, Samantaray S, Bikram Singh R. Analysis of velocity profiles in rectangular straight open channel flow. Pertanika J Sci Technol 2020;28:1–18.

[21] Santos IFS dos, Camacho RGR, Tiago Filho GL, Botan ACB, Vinent BA. Energy potential and economic analysis of hydrokinetic turbines implementation in rivers: An approach using numerical predictions (CFD) and experimental data. Renew Energy 2019;143:648–62. https://doi.org/10.1016/j.renene.2019.05.018.

[22] Qasim RM, Mohammed AA, Abdulhussein IA. An Investigating of the Impact of Bed Flume Discordance on the Weir-Gate Hydraulic Structure. HighTech Innov J 2022;3:341–55. https://doi.org/10.28991/HIJ-2022-03-03-09.

[23] Khuntia JR, Devi K, Das BS, Khatua KK. Turbulence Characteristics in a Rough Open Channel Under Unsteady Flow Conditions 2022:143–55. https://doi.org/10.1007/978-3-030-81768-8_12.

[24] Tajnesaie M, Jafari Nodoushan E, Barati R, Azhdary Moghadam M. Performance comparison of four turbulence models for modeling of secondary flow cells in simple trapezoidal channels. ISH J Hydraul Eng 2020;26:187–97.

https://doi.org/10.1080/09715010.2018.1469053.

[25] Shnipov FD. Three-dimensional kinematic structure of a flow in trapezoidal channels. Hydrotechnical Constr 1989;23:557–63. https://doi.org/10.1007/BF01432069.

[26] Yang S-Q, Tan S-K, Lim S-Y. Velocity Distribution and Dip-Phenomenon in Smooth Uniform Open Channel Flows. J Hydraul Eng 2004;130:1179–86. https://doi.org/10.1061/(asce)0733-9429(2004)130:12(1179).

[27] Yang SQ, Lim SY. Boundary shear stress distributions in trapezoidal channels. J Hydraul Res 2005;43:98–102. https://doi.org/10.1080/00221680509500114.

[28] Kang H, Choi SU. Turbulence modeling of compound open-channel flows with and without vegetation on the floodplain using the Reynolds stress model. Adv Water Resour 2006;29:1650–64. https://doi.org/10.1016/j.advwatres.2005.12.004.

[29] Bonakdari H, Larrarte F, Lassabatere L, Joannis C. Turbulent velocity profile in fully-developed open channel flows. Environ Fluid Mech 2008;8:1–17. https://doi.org/10.1007/s10652-007-9051-6.

[30] Absi R. An ordinary differential equation for velocity distribution and dip-phenomenon in open channel flows. J Hydraul Res 2011;49:82–9. https://doi.org/10.1080/00221686.2010.535700.

[31] Kamel B, Ilhem K, Ali F, Abdelbaki D. 3D simulation of velocity profile of turbulent flow in open channel with complex geometry. Phys Procedia 2014;55:119–28. https://doi.org/10.1016/j.phpro.2014.07.018.

[32] Holanda P da S, Blanco CJC, Mesquita ALA, Brasil Junior ACP, de Figueiredo NM, Macêdo EN, et al. Assessment of hydrokinetic energy resources downstream of

hydropower plants. Renew Energy 2017;101:1203–14.
https://doi.org/10.1016/j.renene.2016.10.011.

[33] Fouz DM, Carballo R, López I, Iglesias G. A holistic methodology for hydrokinetic energy site selection. Appl Energy 2022;317.
https://doi.org/10.1016/j.apenergy.2022.119155.

[34] Wang J, Liu X, Min F, Dai J, Jiang X. Turbulence structure and longitudinal velocity distribution of open channel flows with reedy emergent vegetation. Ecohydrology 2022;15.
https://doi.org/10.1002/eco.2352.

[35] Singh PK, Khatua KK. Lateral dissemination of depth-averaged velocity, boundary shear stress and stage-discharge curves for compound channels. ISH J Hydraul Eng 2021;27:253–66.
https://doi.org/10.1080/09715010.2018.1549962.

[36] Song X, Chen Y, Huang H, Xu H, Bai Y, Zhang J. Turbulent flow simulations in a simplified channel bend model of Dragon style rivers with constant curvature and different single-short-branch characteristics. Eng Appl Comput Fluid Mech 2023;17.
https://doi.org/10.1080/19942060.2023.2234019.

[37] Gorji S, Seddighi M, Ariyaratne C, Vardy AE, O'Donoghue T, Pokrajac D, et al. A comparative study of turbulence models in a transient channel flow. Comput Fluids 2014;89:111–23.
https://doi.org/10.1016/j.compfluid.2013.10.037.

[38] Shahheydari H, Nodoshan EJ, Barati R, Moghadam MA. Discharge coefficient and energy dissipation over stepped spillway under skimming flow regime. KSCE J Civ Eng 2015;19:1174–82.
https://doi.org/10.1007/s12205-013-0749-3.

[39] Hosseini K, Nodoushan EJ, Barati R, Shahheydari H. Optimal design of labyrinth spillways using meta-heuristic algorithms. KSCE J Civ Eng 2016;20:468–77. https://doi.org/10.1007/s12205-015-0462-5.

[40] Fadafan MA, Moghaddam MA, Barati R, Arami-Fadafan M. Reduce Spillways Cavitation Damages Through Accurate Prediction of Bottom Air Concentration 2018.

[41] Benoumessad K, Fourar FZ, Fourar A, Massouh F. Modeling Turbulent Flow Velocity Profiles in Irregularly shaped Open Channels: A 3D Approach. Eng Technol Appl Sci Res 2025;15:22203–8. https://doi.org/10.48084/etasr.9251.

[42] Kumar A, Saini RP. Performance analysis of a Savonius hydrokinetic turbine having twisted blades. Renew Energy 2017;108:502–22. https://doi.org/10.1016/j.renene.2017.03.006.

[43] Kumar A, Saini RP. Performance analysis of a single stage modified Savonius hydrokinetic turbine having twisted blades. Renew Energy 2017;113:461–78. https://doi.org/10.1016/j.renene.2017.06.020.

[44] Talukdar PK, Sardar A, Kulkarni V, Saha UK. Parametric analysis of model Savonius hydrokinetic turbines through experimental and computational investigations. Energy Convers Manag 2018;158:36–49. https://doi.org/10.1016/j.enconman.2017.12.011.

[45] Chaudhari VN, Shah SP. Numerical investigation on the performance of an innovative Airfoil-Bladed Savonius Hydrokinetic Turbine (ABSHKT) with deflector. Int J Thermofluids 2023;17. https://doi.org/10.1016/j.ijft.2023.100279.

[46] T G S, C M S, Gumtapure V, Madav V. Numerical analysis of Savonius hydrokinetic turbine performance in straight and curved channel configurations. Energy Nexus

2025;17.
https://doi.org/10.1016/j.nexus.2025.100382.

[47] Mereke NB, Ancha VR, Hendrick P. Numerical modeling and CFD simulation of diffuser augmented dual vertical axis hydrokinetic Banki-Michell turbine. Heliyon 2024;10.
https://doi.org/10.1016/j.heliyon.2024.e26970.

[48] Lukeš R, Honus S, Blejchař T, Balco M. Reaction cross-flow turbine for small hydropower plants: Flow profile design and CFD analysis. Renew Energy 2025;252.
https://doi.org/10.1016/j.renene.2025.123560.

[49] Jeeva B, Sandeep SJ, Ramsundram N, Prasanth M, Praveen B. Experimental Investigation of Three Bladed Inclined Savonius Hydrokinetic Turbine by using Deflector Plate. IOP Conf Ser Mater Sci Eng 2021;1146:012009.
https://doi.org/10.1088/1757-899x/1146/1/012009.

[50] Shashikumar CM, Hindasageri V, Madav V. CFD investigation of unsteady three-dimensional savonius hydrokinetic turbine in irrigation channel with varying positions for hydro power application. AIP Conf Proc 2021;2316.
https://doi.org/10.1063/5.0036472.

[51] Nag AK, Sarkar S. Performance analysis of Helical Savonius Hydrokinetic turbines arranged in array. Ocean Eng 2021;241.
https://doi.org/10.1016/j.oceaneng.2021.110020.

[52] Patel VK, Shah K, Rathod V. Performance Enhancement of Savonius Hydrokinetic Turbine with a Unique Vane Shape: An Experimental Investigation 2021:1453–63.
https://doi.org/10.1007/978-981-15-5955-6_138.

[53] Alizadeh H, Jahangir MH, Ghasempour R. CFD-based improvement of Savonius type hydrokinetic turbine using optimized barrier at the low-speed flows. Ocean Eng

2020;202.
https://doi.org/10.1016/j.oceaneng.2020.107178.

[54] Anthony AZ, Roy S. Performance analysis of a modified Savonius hydrokinetic turbine blade for rural application. IOP Conf Ser Mater Sci Eng 2020;943.
https://doi.org/10.1088/1757-899X/943/1/012034.

[55] Mosbahi M, Elgasri S, Lajnef M, Mosbahi B, Driss Z. Performance enhancement of a twisted Savonius hydrokinetic turbine with an upstream deflector. Int J Green Energy 2021;18:51–65.
https://doi.org/10.1080/15435075.2020.1825444.

[56] Ramadan A, Nawar MAA, Mohamed MH. Performance evaluation of a drag hydro kinetic turbine for rivers current energy extraction - A case study. Ocean Eng 2020;195.
https://doi.org/10.1016/j.oceaneng.2019.106699.

[57] Alipour RR, Alipour RR, Fardian F, Koloor SSR, Petrů M. Performance improvement of a new proposed Savonius hydrokinetic turbine: a numerical investigation. Energy Reports 2020;6:3051–66.
https://doi.org/10.1016/j.egyr.2020.10.072.

[58] Zhang Y, Kang C, Ji Y, Li Q. Experimental and numerical investigation of flow patterns and performance of a modified Savonius hydrokinetic rotor. Renew Energy 2019;141:1067–79.
https://doi.org/10.1016/j.renene.2019.04.071.

[59] Nag AK, Sarkar S. Experimental and numerical study on the performance and flow pattern of different Savonius hydrokinetic turbines with varying duct angle. J Ocean Eng Mar Energy 2020;6:31–53.
https://doi.org/10.1007/s40722-019-00155-6.

[60] Kerikous E, Thévenin D. Optimal shape and position of a thick deflector plate in front of a hydraulic Savonius turbine. Energy 2019;189. https://doi.org/10.1016/j.energy.2019.116157.

[61] Mosbahi M, Ayadi A, Chouaibi Y, Driss Z, Tucciarelli T. Performance study of a Helical Savonius hydrokinetic turbine with a new deflector system design. Energy Convers Manag 2019;194:55–74. https://doi.org/10.1016/j.enconman.2019.04.080.

[62] Goundar JN, Ahmed MR, Lee YH. Design and optimization of a ducted marine current savonius turbine for Gun-Barrel passage, Fiji. J Offshore Mech Arct Eng 2019;141. https://doi.org/10.1115/1.4041459.

[63] Thakur N, Biswas A, Kumar Y, Basumatary M. CFD analysis of performance improvement of the Savonius water turbine by using an impinging jet duct design. Chinese J Chem Eng 2019;27:794–801. https://doi.org/10.1016/j.cjche.2018.11.014.

[64] Patel V, Eldho TI, Prabhu S V. Velocity and performance correction methodology for hydrokinetic turbines experimented with different geometry of the channel. Renew Energy 2019;131:1300–17. https://doi.org/10.1016/j.renene.2018.08.027.

[65] Patel V, Eldho TI, Prabhu S V. Theoretical study on the prediction of the hydrodynamic performance of a Savonius turbine based on stagnation pressure and impulse momentum principle. Energy Convers Manag 2018;168:545–63. https://doi.org/10.1016/j.enconman.2018.04.065.

[66] Elbatran AH, Ahmed YM, Shehata AS. Performance study of ducted nozzle Savonius water turbine, comparison with conventional Savonius turbine. Energy

2017;134:566–84.
https://doi.org/10.1016/j.energy.2017.06.041.

[67] Thiyagaraj J, Rahamathullah I, Prabu PS. Experimental investigations on the performance characteristics of a modified four bladed Savonius hydro-kinetic turbine. Int J Renew Energy Res 2016;6:1530–6.
https://doi.org/10.20508/ijrer.v6i4.4798.g6943.

[68] Basumatary M, Biswas A. Numerical simulation of two-bladed Savonius water turbine with deflector. Int J Renew Energy Technol 2016;7:383.
https://doi.org/10.1504/ijret.2016.080115.

[69] Vimal Patel, Ganapathi Bhat, T. I. Eldho, S. V. Prabhu. Influence of overlap ratio and aspect ratio on the performance of Savonius hydrokinetic turbine. Int J Energy Res 2016.

[70] Sharma S, Sharma RK. Performance improvement of Savonius rotor using multiple quarter blades – A CFD investigation. Energy Convers Manag 2016;127:43–54.
https://doi.org/10.1016/j.enconman.2016.08.087.

[71] Harries T, Kwan A, Brammer J, Falconer R. Physical testing of performance characteristics of a novel drag-driven vertical axis tidal stream turbine; With comparisons to a conventional Savonius. Int J Mar Energy 2016;14:215–28.
https://doi.org/10.1016/j.ijome.2016.01.008.

[72] Kumar A, Saini RP. Numerical investigation and novel designing of multi-stage savonius rotor for harnessing hydro power. 12th IEEE Int Conf Electron Energy, Environ Commun Comput Control (E3-C3), INDICON 2015 2016.
https://doi.org/10.1109/INDICON.2015.7443835.

[73] Sarma NK, Biswas A, Misra RD. Experimental and computational evaluation of Savonius hydrokinetic turbine for low velocity condition with comparison to

Savonius wind turbine at the same input power. Energy Convers Manag 2014;83:88–98. https://doi.org/10.1016/j.enconman.2014.03.070.

[74] Kailash G, Eldho TI, Prabhu S V. Performance study of modified savonius water turbine with two deflector plates. Int J Rotating Mach 2012;2012. https://doi.org/10.1155/2012/679247.

[75] Golecha K, Eldho TI, Prabhu S V. Influence of the deflector plate on the performance of modified Savonius water turbine. Appl Energy 2011;88:3207–17. https://doi.org/10.1016/j.apenergy.2011.03.025.

[76] Al-Quraishi MBZY, Sarip S, Mad Kaidi H, Ardila-Rey JA, Muhammad-Sukki F. A CFD Analysis for Novel Close-Ended Deflector for Vertical Water Turbines. Sustain 2022;14. https://doi.org/10.3390/su14052790.

[77] Elbatran AHA, Yaakob OB, Ahmed YM. Experimental Investigation of a Hydraulic Turbine for Hydrokinetic Power Generation in Irrigation/Rainfall Channels. J Mar Sci Appl 2021;20:144–55. https://doi.org/10.1007/s11804-020-00152-4.

[78] Gaba VK, Bhowmick S. A CFD-based study of cross-flow turbine for tidal energy extraction. Sustain Eng Prod Manuf Technol 2019:177–86. https://doi.org/10.1016/B978-0-12-816564-5.00007-4.

[79] Elbatran AH, Yaakob OB, Ahmed YM, Jalal MR. Novel approach of bidirectional diffuser-augmented channels system for enhancing hydrokinetic power generation in channels. Renew Energy 2015;83:809–19. https://doi.org/10.1016/j.renene.2015.05.038.

[80] Goundar JN, Chettiar N, Narayan S, Deo A, Prasad D. Design of a Ducted Cross Flow

Turbine for Fiji. Appl Mech Mater 2015;772:561–5. https://doi.org/10.4028/www.scientific.net/amm.772.561.

[81] Kim KP, Ahmed MR, Lee YH. Efficiency improvement of a tidal current turbine utilizing a larger area of channel. Renew Energy 2012;48:557–64. https://doi.org/10.1016/j.renene.2012.06.018.

[82] Government of India Ministry of Power Central Electricity Authority. Report Of The Committee To Study The Concept & Commercial Applications Of Hydro Kinetic Turbine Developed By M/S Maclec New Delhi. 2021.

[83] Puertas-Frías CM, Willson CS, García-Salaberri PA. Design and economic analysis of a hydrokinetic turbine for household applications. Renew Energy 2022;199:587–98. https://doi.org/10.1016/j.renene.2022.08.155.

[84] Niebuhr CM, van Dijk M, Neary VS, Bhagwan JN. A review of hydrokinetic turbines and enhancement techniques for canal installations: Technology, applicability and potential. Renew Sustain Energy Rev 2019;113. https://doi.org/10.1016/j.rser.2019.06.047.

[85] Narmada, Water Resources WS and KD. Narmada, Water Resources, Water Supply and Kalpsar Department (Water Resources Division). 2010.

[86] British Standards Institution. Field acceptance tests to determine the hydraulic performance of hydraulic turbines, storage pumps and pump-turbines BS EN 60041:1995 1995.

[87] ISO. ISO 748:2007. Hydrometry-Measurement of liquid flow in open channels using current-meters or floats. Hydrom Liq Flow Open Channels Using Curr or Floats 2007;3:48.

[88] Nash S, Phoenix A. A review of the current understanding of the hydro-environmental

impacts of energy removal by tidal turbines. Renew Sustain Energy Rev 2017;80:648–62.
https://doi.org/10.1016/j.rser.2017.05.289.

[89] Ghani U, Ali S, Arif S. Comparison of Different Turbulence Models in Open Channels with Smooth-Rough Bedforms 2013;32:623–30.

[90] Mohammadi B, Pironneau O. Analysis of the K-Epsilon Turbulence Model. Res Appl Math 1994:194.

[91] Sahoo S, Khuntia JR, Devi K, Prasad BSS, Khatua KK. Turbulence modelling for depth-averaged velocity and boundary shear stress of a dense rigid grass bed open channel. Aqua Water Infrastructure, Ecosyst Soc 2023;72:1748–69.
https://doi.org/10.2166/aqua.2023.093.

[92] Kumar A, Saini RP, Gandhi BK, Srivastava RK, Chandra P, Dubey AK. Experiences in discharge measurements at Small Hydropower Stations in India. Flow Meas Instrum 2019;69.
https://doi.org/10.1016/j.flowmeasinst.2019.101605.

[93] SHP. Smart hydro power. Munich: Smart Hydro Power 2016.
http://www.smart-hydro.de/decentralized-rural-electrification-projectsworldwide/%0Anigeria-rural-electrification/#project. (accessed May 11, 2025).

[94] Guinard Energies. P66 hydrokinetic turbine 2018.
https://www.guinard-energies.bzh/en/our-products/p66-hydrokinetic-turbine-3-%0A5-kw (accessed May 11, 2025).

[95] Hydroquest. Hydroquest, smart power solutions. WwwHydroquestNet/Fr 2015.
http://www.hydroquest.net/the-benefits-of-river-current-turbines/?lang=en (accessed May 11, 2025).

[96] New Energy Corporation. Power Generation Units 2018. https://www.newenergycorp.ca/power-generation-units.html (accessed May 11, 2025).

[97] Corp. 2019 Instream Energy Systems. Instream Energy Systems. Instream 2019. https://www.instreamenergy.com/technology (accessed May 11, 2025).

[98] ORPC. Ocean renewable Power Company. 2015.

[99] Waterotor. Waterotor Energy Technologies Inc. 2024. https://waterotor.com/products/ (accessed May 11, 2025).

[100] Case Study Balingasag-Philippine Hybrid Micro-Grid 2018. https://www.heliosaltas.com/projects/ (accessed May 11, 2025).

[101] Anderson AM. Experimental methods for engineers. vol. 9. New York, United States of America: McGraw-Hill; 1994. https://doi.org/10.1016/0894-1777(94)90118-x.

[102] Meana-Fernández A, Fernández Oro JM, Argüelles Díaz KM, Velarde-Suárez S. Turbulence-model comparison for aerodynamic-performance prediction of a typical vertical-axis wind-turbine airfoil. Energies 2019;12. https://doi.org/10.3390/en12030488.

[103] Zhao Z, Zheng Y, Xu X, Liu W, Hu G. Research on the improvement of the performance of savonius rotor based on numerical study. 1st Int Conf Sustain Power Gener Supply, SUPERGEN '09 2009. https://doi.org/10.1109/SUPERGEN.2009.5348197.

[104] Saha UK, Thotla S, Maity D. Optimum design configuration of Savonius rotor through wind tunnel experiments. J Wind Eng Ind Aerodyn 2008;96:1359–75. https://doi.org/10.1016/j.jweia.2008.03.005.

[105] Marsh P, Ranmuthugala D, Penesis I, Thomas G. Three-dimensional numerical

simulations of straight-bladed vertical axis tidal turbines investigating power output, torque ripple and mounting forces. Renew Energy 2015;83:67–77. https://doi.org/10.1016/j.renene.2015.04.014.

[106] Ghosh A, Biswas A, Sharma KK, Gupta R. Computational analysis of flow physics of a combined three bladed Darrieus Savonius wind rotor. J Energy Inst 2015;88:425–37. https://doi.org/10.1016/j.joei.2014.11.001.

[107] McTavish S, Feszty D, Sankar T. Steady and rotating computational fluid dynamics simulations of a novel vertical axis wind turbine for small-scale power generation. Renew Energy 2012;41:171–9. https://doi.org/10.1016/j.renene.2011.10.018.

[108] FERNANDO M, MODI V. A numerical analysis of the unsteady flow past a Savonius wind turbine 1988. https://doi.org/10.2514/6.1988-755.

[109] Kolekar N, Banerjee A. Performance characterization and placement of a marine hydrokinetic turbine in a tidal channel under boundary proximity and blockage effects. Appl Energy 2015;148:121–33. https://doi.org/10.1016/j.apenergy.2015.03.052.

[110] Vicente AJ, Antonio VH, Prisco PA. A review on the performance of Savonius wind turbines. Renew Sustain Energy Rev 2012.

[111] Hayashi T, Li Y, Hara Y. Wind tunnel tests on a different phase three-stage Savonius rotor. JSME Int Journal, Ser B Fluids Therm Eng 2005;48:9–16. https://doi.org/10.1299/jsmeb.48.9.

[112] Chen Y, Lian Y. Numerical investigation of vortex dynamics in an H-rotor vertical axis wind turbine. Eng Appl Comput Fluid Mech 2015;9:21–32.

https://doi.org/10.1080/19942060.2015.1004790.

[113] Mohamed MH. Impacts of solidity and hybrid system in small wind turbines performance. Energy 2013;57:495–504. https://doi.org/10.1016/j.energy.2013.06.004.

[114] Mohamed MH, Ali AM, Hafiz AA. CFD analysis for H-rotor Darrieus turbine as a low speed wind energy converter. Eng Sci Technol an Int J 2015;18:1–13. https://doi.org/10.1016/j.jestch.2014.08.002.

[115] Hassan Saeed HA, Nagib Elmekawy AM, Kassab SZ. Numerical study of improving Savonius turbine power coefficient by various blade shapes. Alexandria Eng J 2019;58:429–41. https://doi.org/10.1016/j.aej.2019.03.005.

[116] Bian PX, Yang ZH, Wang Y, Ma PL, Wang SY. Hydrodynamic performance of Savonius water turbine. Zhejiang Daxue Xuebao (Gongxue Ban)/Journal Zhejiang Univ (Engineering Sci 2018;52:268–72. https://doi.org/10.3785/j.issn.1008-973X.2018.02.009.

[117] Kline S, McClintock F. Describing uncertainties in single-sample experiments. vol. 75. 1953.

[118] Epinette J, Sutton K. User ′ s Guide 2003:1–44.

LIST OF RESEARCH PUBLICATION

1. **Amit U. Mehta** and Pankaj P. Gohil, "A comparative study of turbulence models in a trapezoidal open channel for potential turbine installation site selection.", ISH Journal of Hydraulic Engineering, pp. 1–26, 2026. **[ESCI Index]**
2. **Amit U. Mehta** and Pankaj P. Gohil, "Performance analysis of Savonius Hydrokinetic Turbine in Open Channel", Multidisciplinary, Scientific Work and Management Journal, Volume 36 (1), pp. 4650-4655, 2026. **[Scopus Index]**
3. **Amit U. Mehta** and Pankaj P. Gohil, "Survey of India's Small Hydro Power Plants Using Hydro Turbines", Journal of Research in Engineering and Applied Sciences, Volume 11 (01), pp. 1-9, 2026.
4. Pankaj P. Gohil, Vimal K. Patel, **Amit U. Mehta**, "Computationally Investigate Low Velocity Hydrokinetic Turbines with Variant Systems", Journal of Applied Fluid Mechanics, Volume 18 (3), pp. 769-786, 2024. **[SCIE Index]**
5. Dr. Pankajkumar P. Gohil and **Amit U. Mehta**, "Twin Supportive Area Box Type Telescopic Water Current Meter Structure", Design Patent No.:357333-001, Dt: 16/03/2023, the Patent Office, Government of India. **[Design Patent]**
6. Dr. Pankajkumar P. Gohil and **Amit U. Mehta**, "Water Current Meter Structure", Design Patent No.:357334-001, Dt: 07/06/2023, the Patent Office, Government of India. **[Design Patent]**

APPENDICES

Appendix A: Turbulence Models

The N-S equation for a turbulent flow of an incompressible Newtonian fluid is as follows:

The mass conservation continuity equation:

$$\frac{\partial u_i}{\partial x_j} = 0 \tag{A.1}$$

The momentum conservation equation:

$$\frac{\partial u_i}{\partial t} + \frac{\partial}{\partial x_i}(u_i u_j) = \frac{-1}{\rho}\frac{\partial p}{\partial x_i} + \frac{1}{\rho}\frac{\partial \tau_{ij}}{\partial x_i} \tag{A.2}$$

where $u_i (i = 1,2,3)$ represents the components of instantaneous velocity, $\tau_{ij} (i = 1,2,3)$ represents the viscous stress tensor components, p is the instantaneous pressure, and ρ is the fluid density.

The Reynolds decomposition technique may be used to represent the components of pressure and instantaneous velocity as an average value (P, U_i) with a fluctuating random component (p', u_i') to compensate for turbulence. The RANS equations are obtained by using Reynolds' decomposition principle, and the N-S equations (Eqs. (A.1) and (A.2)) are time averaged as follows:

$$\frac{\partial U_i}{\partial x_i} = 0 \tag{A.3}$$

$$\frac{\partial U_i}{\partial t} + U_j \frac{\partial U_i}{\partial x_j} = \frac{-1}{\rho}\frac{\partial p}{\partial x_i} + \frac{\partial}{\partial x_j}\left[\nu\left(\frac{\partial U_i}{\partial x_j} + \frac{\partial U_j}{\partial x_i}\right)\right] - \frac{\partial}{\partial x_j}\left(\overline{u_i' u_j'}\right) \tag{A.4}$$

➢ *The $k - \varepsilon$ Model*

One of the turbulence models that is used the most commonly in CFD is the $k - \varepsilon$ model. The transport equations for k and ε are comparable in all three models. Since its proposal by Launder and Spalding (1974), the standard $k - \varepsilon$ model in FLUENT, which

belongs to this family of turbulence models, has emerged as the mainstay of engineering flow computations in practice. The standard equations for the $k-\varepsilon$ model are given as follows [118]:

$$\frac{\partial k}{\partial t}+U_j\frac{\partial k}{\partial x_j}=P_k-\varepsilon+\frac{\partial}{\partial x_j}\left(\frac{v_t}{\sigma_k}\frac{\partial k}{\partial x_j}\right) \tag{A.5}$$

$$\frac{\partial \varepsilon}{\partial t}+U_i\frac{\partial \varepsilon}{\partial x_j}=\frac{\varepsilon}{k}(C_{\varepsilon 1}P_k-C_{\varepsilon 2}\varepsilon)+\frac{\partial}{\partial x_j}\left(\frac{v_t}{\sigma_\varepsilon}\frac{\partial \varepsilon}{\partial x_j}\right) \tag{A.6}$$

$$v_t=C_\mu\left(k^{1/2}\right)\left(\frac{k^{3/2}}{\varepsilon}\right)=C_\mu\frac{k^2}{\varepsilon} \tag{A.7}$$

$$P_k=v_t\left(\frac{\partial U_i}{\partial x_j}+\frac{\partial U_j}{\partial x_i}\right)\frac{\partial U_i}{\partial x_j} \tag{A.8}$$

where, v_t is the turbulent eddy viscosity in m²/s, P_k is the turbulence kinetic energy [118] production by mean shear, and $C_{\varepsilon 1}$, $C_{\varepsilon 2}$, C_μ, σ_k and σ_ε, are the model constants.

- *The $k-\omega$ Model*

The equations for the standard $k-\omega$ model are presented as follows:

$$\frac{\partial k}{\partial t}+U_j\frac{\partial k}{\partial x_j}=v_t\left(\frac{\partial U_i}{\partial x_j}+\frac{\partial U_j}{\partial x_i}\right)\frac{\partial U_i}{\partial x_j}=\beta^* k\omega+\frac{\partial}{\partial x_j}\left[(v+\sigma^* v_t)\frac{\partial k}{\partial x_j}\right] \tag{A.9}$$

$$\frac{\partial \omega}{\partial t}+U_j\frac{\partial \omega}{\partial x_j}=\alpha\frac{\omega}{k}v_t\left(\frac{\partial U_i}{\partial x_j}+\frac{\partial U_j}{\partial x_i}\right)\frac{\partial U_i}{\partial x_j}-\beta\omega^2+\frac{\partial}{\partial x_j}\left[(v+\sigma v_t)\frac{\partial \omega}{\partial x_j}\right] \tag{A.10}$$

$$v_t=\frac{k}{\omega} \tag{A.11}$$

where $\alpha, \beta, \beta^*, \sigma\ and\ \sigma^*$ are known as closure coefficients.

The following lists the $k-\omega$ SST model's auxiliary and governing equations:

Turbulent kinetic energy:

$$\frac{\partial k}{\partial t}+U_j\frac{\partial k}{\partial x_j}=P_k-\beta^* k\omega+\frac{\partial}{\partial x_j}\left[(v+\sigma_{\sigma k}v_t)\frac{\partial k}{\partial x_j}\right] \tag{A.12}$$

Specific dissipation rate:

$$\frac{\partial \omega}{\partial t} + U_j \frac{\partial \omega}{\partial x_j} = \alpha S^2 - \beta \omega^2 + \frac{\partial}{\partial x_j}\left[(v + \sigma_\omega v_t)\frac{\partial \omega}{\partial x_j}\right] + 2(1 - F_1)\sigma_{\omega 2}\frac{1}{\omega}\frac{\partial k}{\partial x_i}\frac{\partial \omega}{\partial x_i} \quad \text{(A.13)}$$

Blending function:

$$F_1 = \tanh\left\{\left\{min\left[max\left(\frac{\sqrt{k}}{\beta^* \omega Y}, \frac{500v}{Y^2 \omega}\right), \frac{4\sigma_{\omega 2} k}{CD_{k\omega} Y^2}\right]\right\}^4\right\} \quad \text{(A.14)}$$

Kinematic eddy viscosity:

$$v_t = \frac{a_1 k}{max(a_1 \omega, SF_2)} \quad \text{(A.15)}$$

Second blending function:

$$F_2 = \tanh\left[\left[max\left(\frac{2\sqrt{k}}{\beta^* \omega Y}, \frac{500v}{Y^2 \omega}\right)\right]\right] \quad \text{(A.16)}$$

Production limiter:

$$P_k = min\left(\tau_{ij}\frac{\partial U_i}{\partial x_j}, 10\beta^* k\omega\right) \quad \text{(A.17)}$$

Appendix B: Statistical Error Analysis

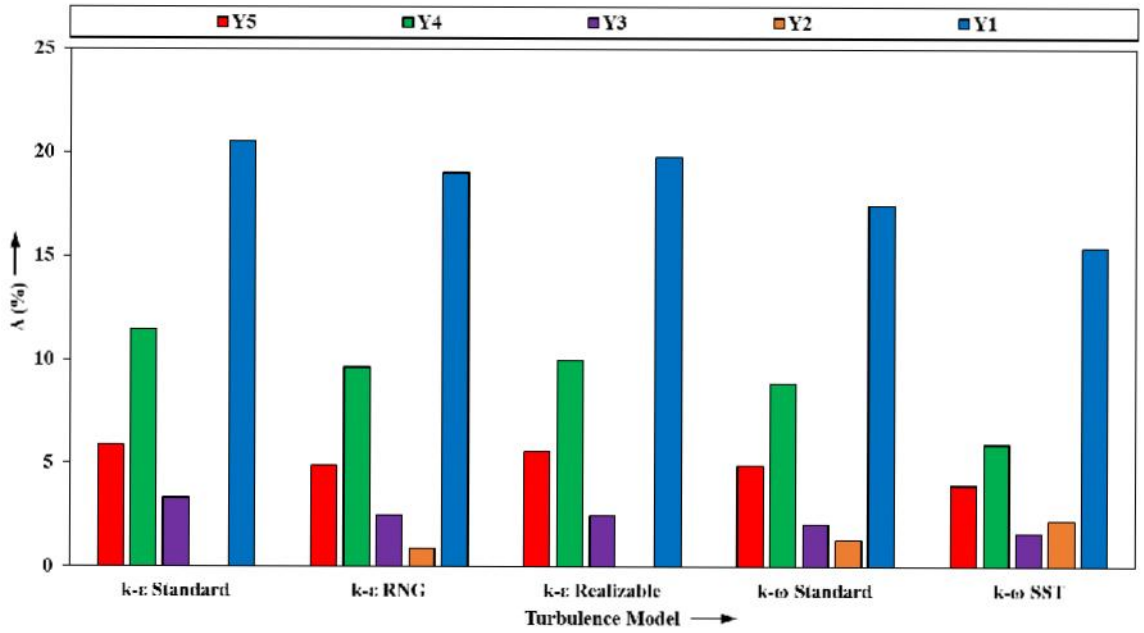


Fig. B.1. % error in local velocity at location X0 along the water depth.

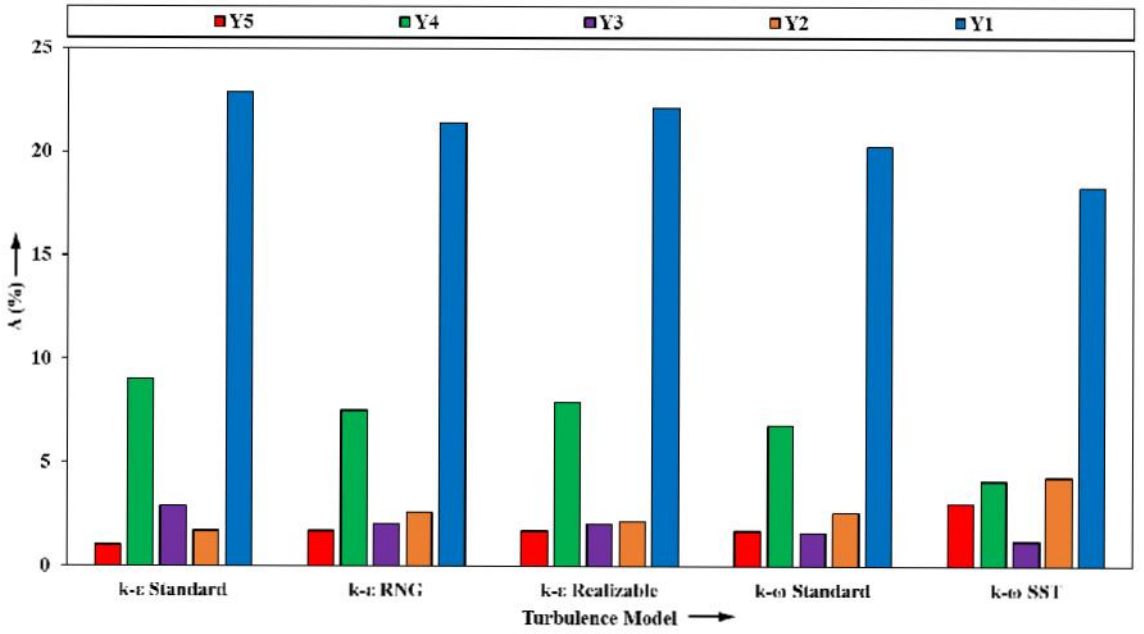


Fig. B.2. % error in local velocity at location X1' along the water depth.

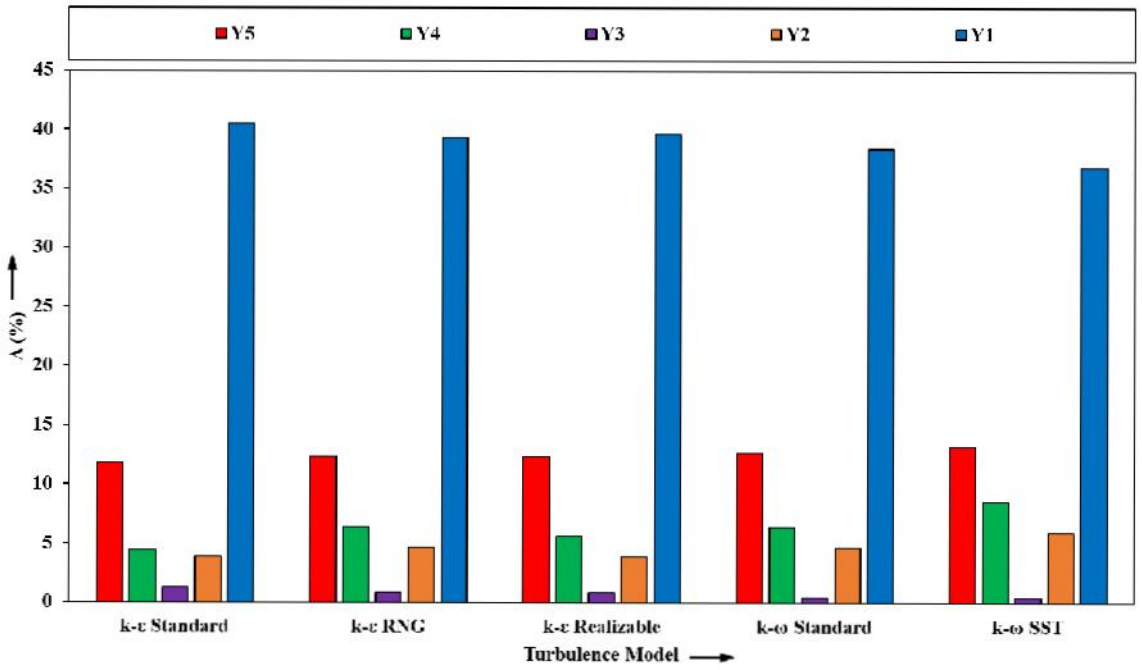


Fig. B.3. % error in local velocity at location X2' along the water depth.

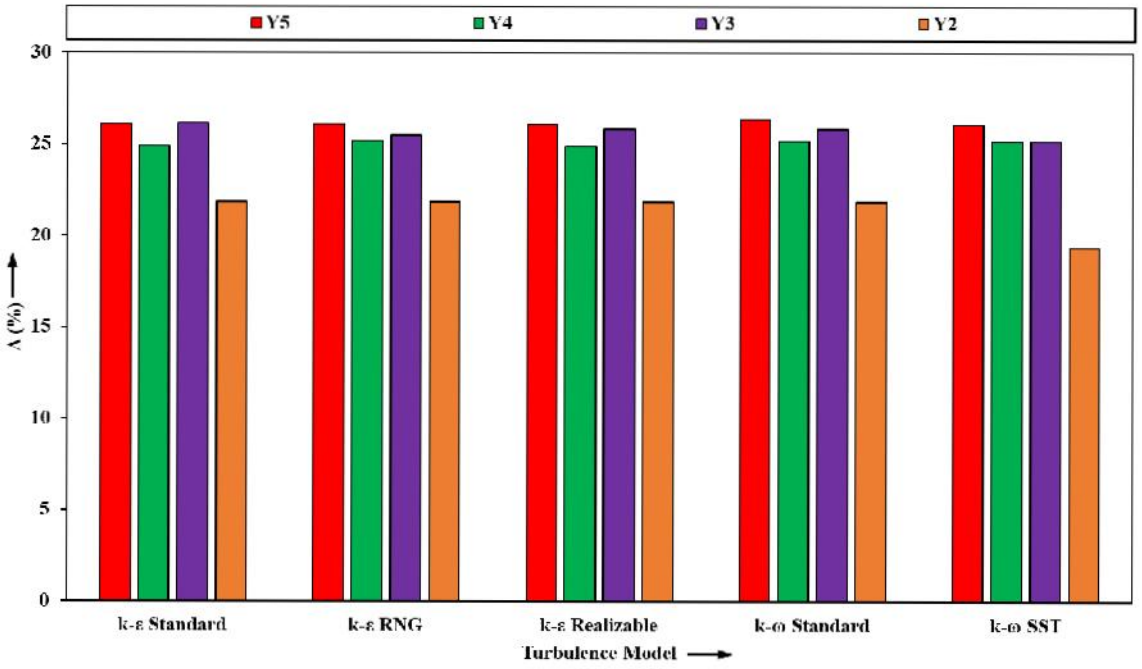


Fig. B.4. % error in local velocity at location X3' along the water depth.

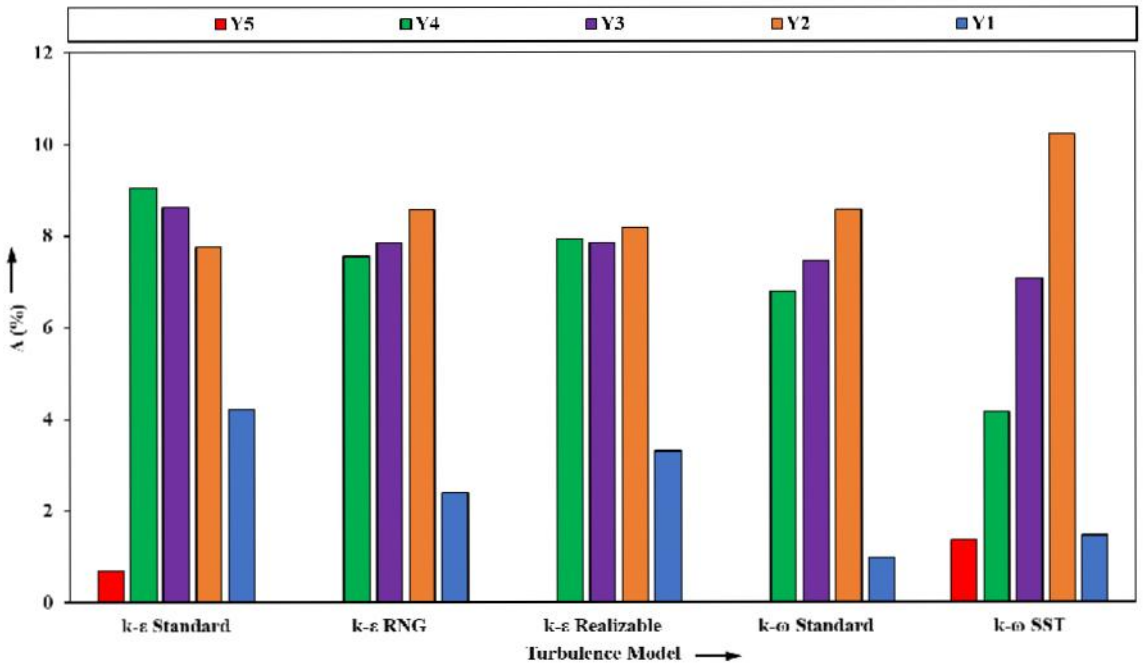


Fig. B.5. % error in local velocity at location X1 along the water depth.

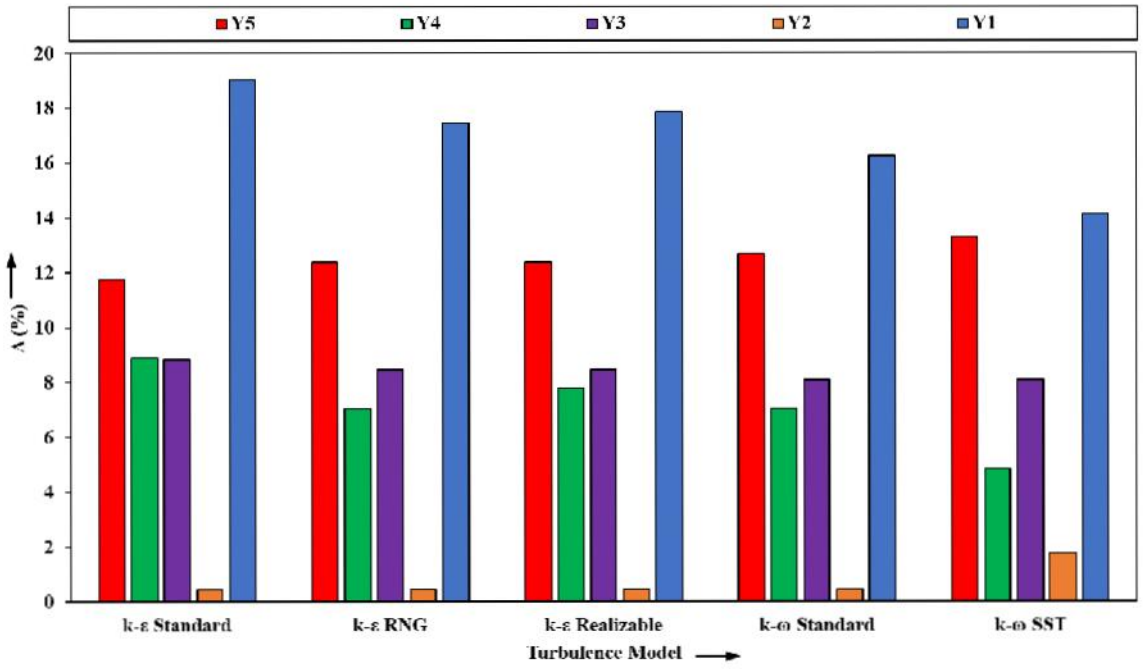


Fig. B.6. % error in local velocity at location X2 along the water depth.

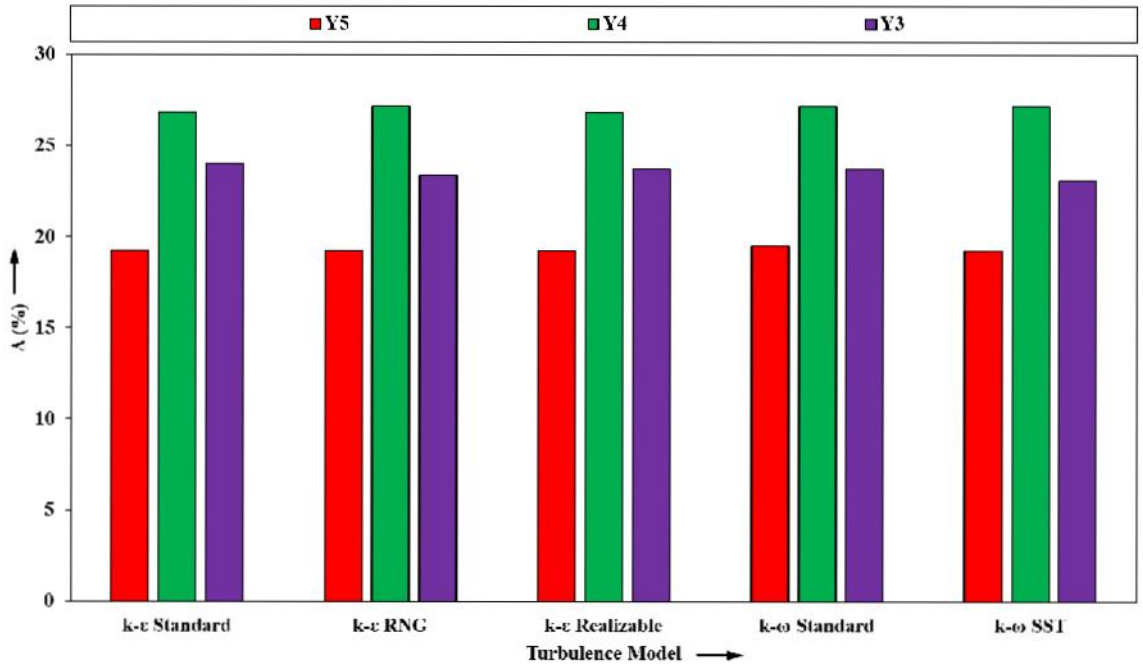


Fig. B.7. % error in local velocity at location X3 along the water depth.

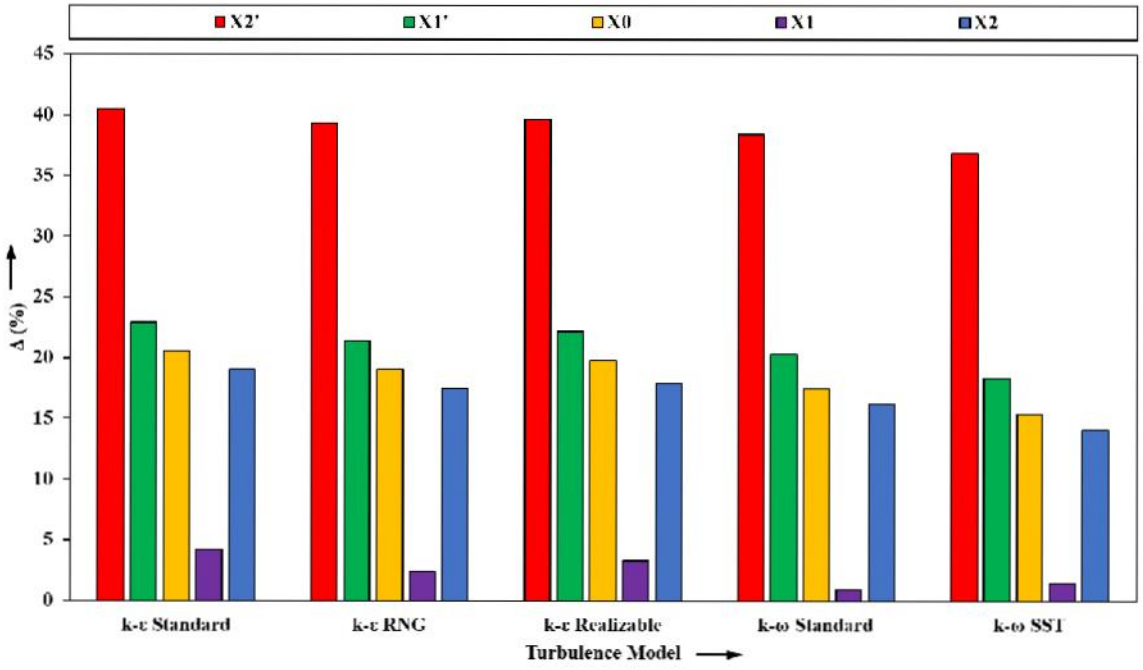


Fig. B.8. % error in local velocity at location Y1 along the canal width.

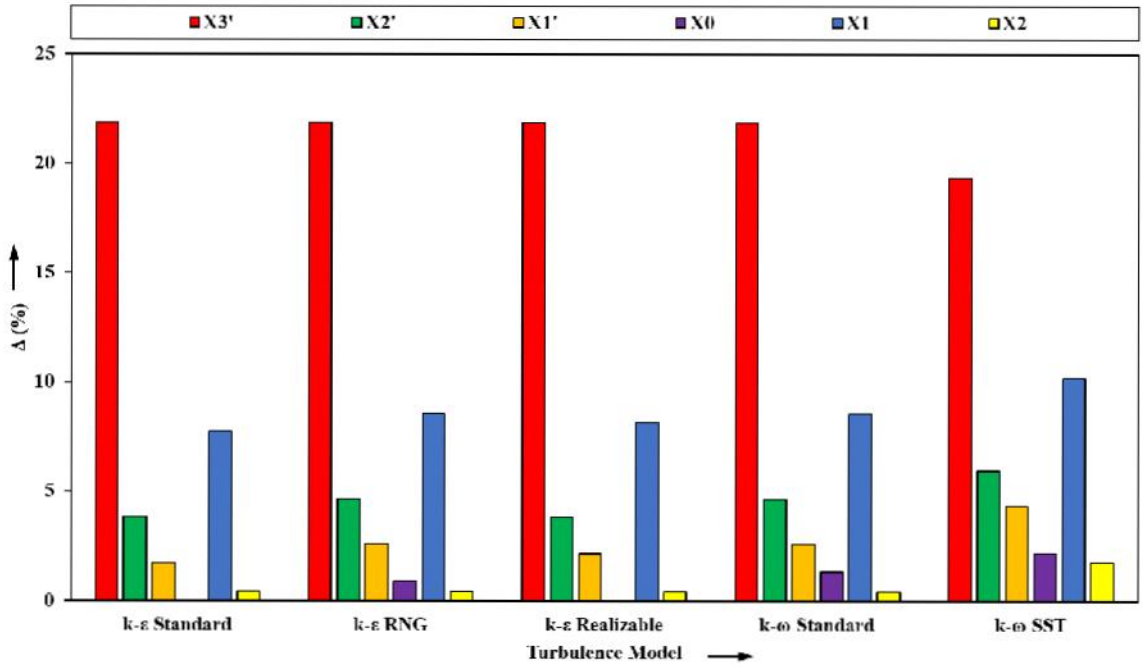


Fig. B.9. % error in local velocity at location Y2 along the canal width.

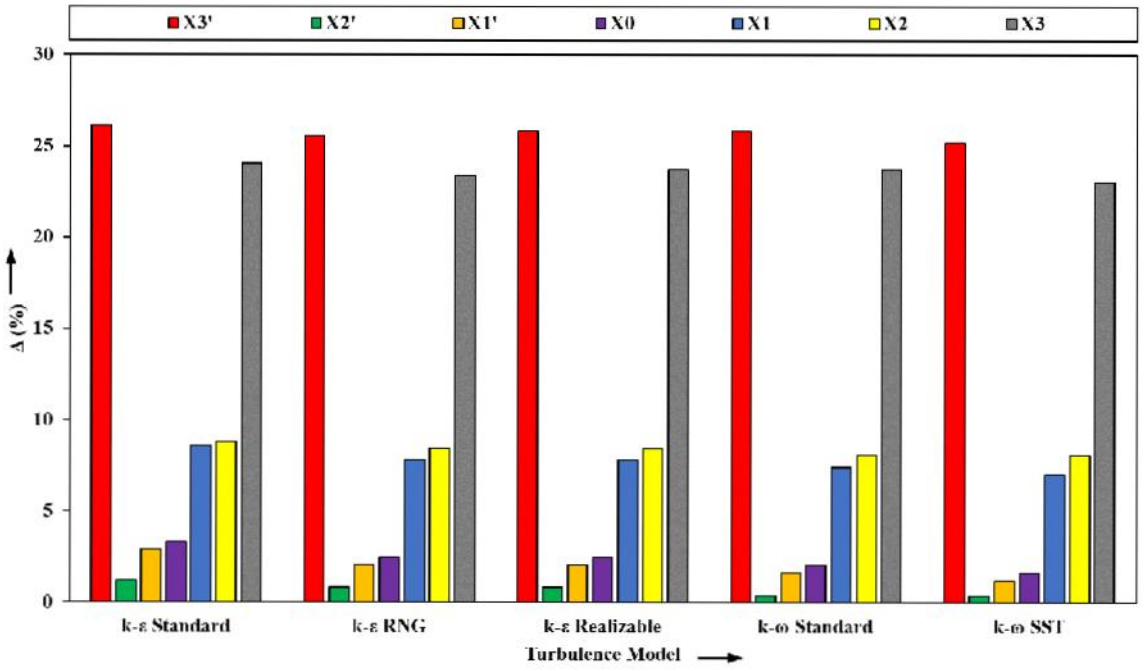


Fig. B.10. % error in local velocity at location Y3 along the canal width.

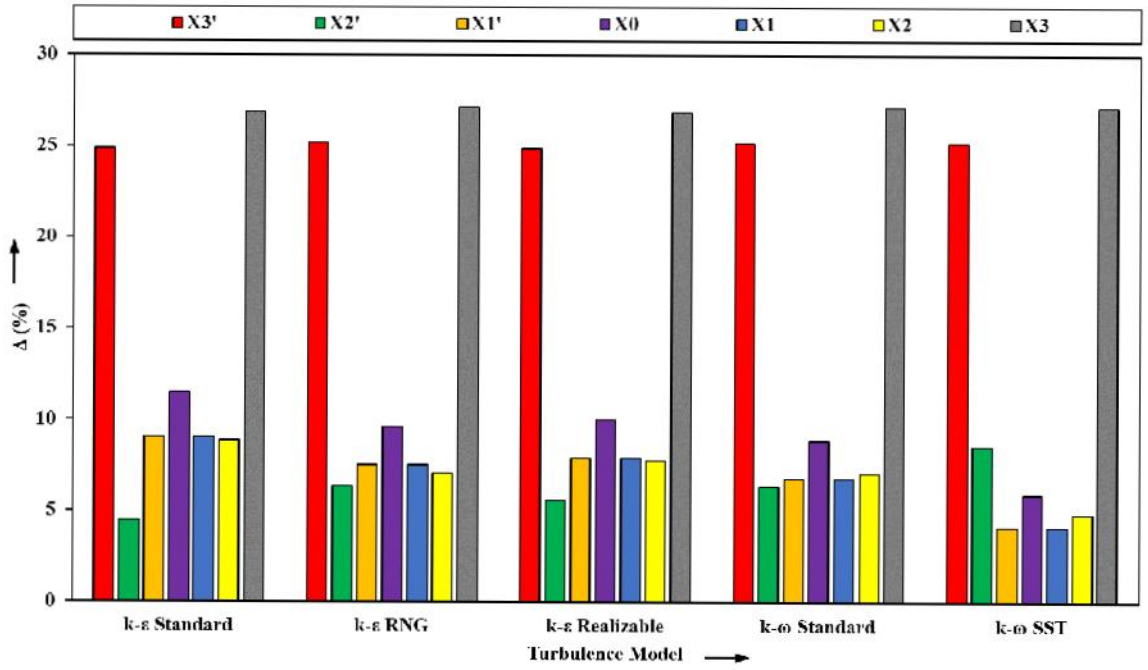


Fig. B.11. % error in local velocity at location Y4 along the canal width.

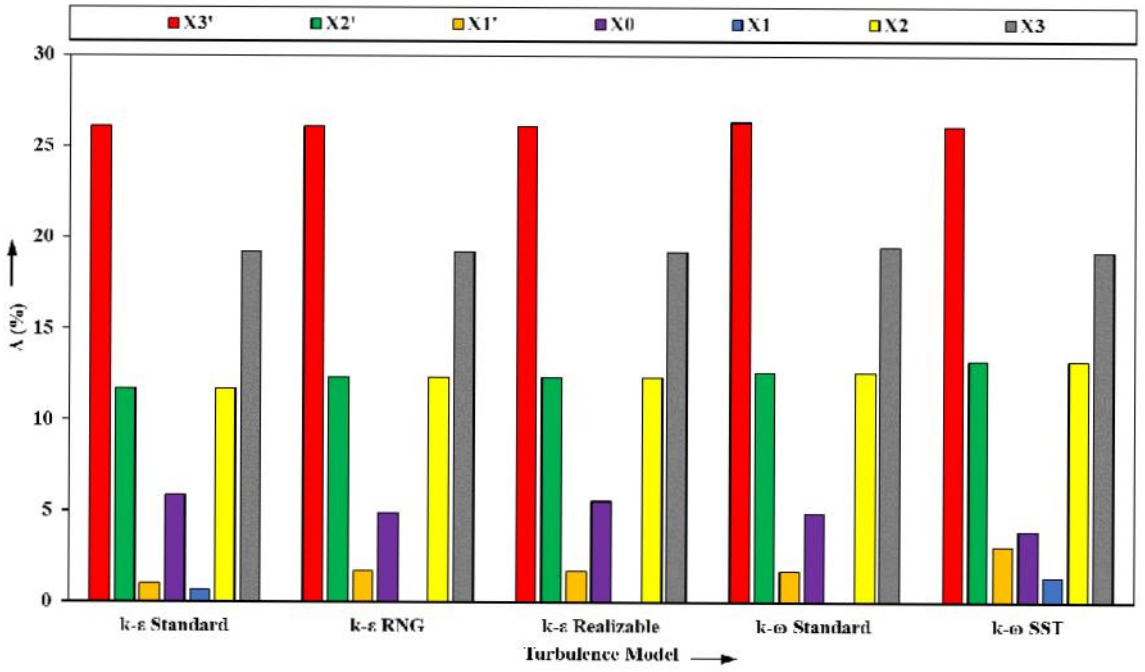


Fig. B.12. % error in local velocity at location Y5 along the canal width.